Characterization of the Autoignition of Single Droplets of Fischer-Tropsch Fuels and Development of Surrogates

Vom Fachbereich Produktionstechnik

der

UNIVERSITÄT BREMEN

zur Erlangung des Grades
Doktor-Ingenieur
genehmigte

Dissertation

von

Dipl. Ing. Manfredo Reimert

Gutachter:
Prof. Dr.-Ing. Hans J. Rath
Prof. Dr.-Ing. Friedrich Dinkelacker

Tag der mündlichen Prüfung: 9. März, 2012

Abstract

The autoignition behavior of single droplets of synthetic fuels produced by the Fischer-Tropsch process, such as GTL-Diesel and GTL-Kerosene, is the main focus of this study. For this, experiments are carried out under microgravity and normal gravity conditions with single droplets with an initial diameter of 0,7 mm in a high-temperature high-pressure chamber. Ignition delay times are determined for ambient pressures between 0,1 MPa < p < 1 MPa and ambient temperatures between 550 K < T < 950 K with the aid of a Michelson interferometer setup. The experimental data is fitted with two-term Arrhenius-type functions that represent the two main reaction mechanisms, the cool and hot flame. Furthermore the development of suitable surrogate fuels for these fuels is performed and the selection and formulation procedure for the components is shown. Surrogate fuels enable numerical calculations with detailed chemical reaction kinetics. The obtained data on the characterization of the aforementioned fuels is compared with data of related fuels, such as their mineral variants and other surrogates.

Zusammenfassung

Der Schwerpunkt dieser Arbeit ist die Charakterisierung des Selbstzündverhaltens von Einzeltropfen synthetischer Kraftstoffe, die mit dem Fischer-Tropsch Prozess hergestellt werden, in diesem Fall GTL-Diesel und GTL-Kerosin. Dafür werden Experimente mit Einzeltropfen unter normaler und kompensierter Gravitationsumgebung mit einem Anfangsdurchmesser von 0,7 mm in einer Druckkammer durchgeführt. Zündverzugszeiten werden für Umgebungsdrücke zwischen 0,1-1,0 MPa und Umgebungstemperaturen zwischen 550-950 K mit Hilfe eines Michelson Interferometers bestimmt. Zu den experimentellen Messdaten werden Zweiterm-Arrhenius-Fitfunktionen, die die zweistufigen Reaktionsmechanismen (Cool und Hot Flame) nachbilden, ermittelt. Außerdem werden geeignete Ersatzkraftstoffe entwickelt und die Selektionsprozedur vorgestellt. Ersatzkraftstoffe erlauben numerische Simulationen mit detaillierten chemischen Reaktionsmechanismen. Die gewonnen Experimentdaten der vorhergenannten Kraftstoffe werden Daten ähnlicher Kraftstoffe, wie Mineralölvarianten, gegenübergestellt und verglichen.

Acknowledgements

This study was performed at ZARM Uni-Bremen. I want to thank Prof. Dr.-Ing. Hans J. Rath for being my main supervisor of this dissertation and for giving me the opportunity of writing my thesis at ZARM. I also want to thank Prof. Dinkelacker for being the second corrector and for his interest in my work.

I want to specially thank Christian Eigenbrod for his continuous support and for providing me with a very good working atmosphere. I want to thank also Peter Rickmers for the rich discussions and suggestions, and of course, for proofreading this thesis.

I am greatly thankful to Günther Marks, who helped me to conduct many of the experimental campaigns and for keeping the apparatus in good shape.

I want also thank my students Sebastian Wagner and Chris Nordmann for their work and helping hands.

I want to express my gratitude to the ZARM-FAB Team for their competence, support and patience and for helping us to carry out many experimental campaigns successfully.

I want to thank my family, Nicola Plathner, Eva Striebeck and Katrin Stöver for their love and support.

This work is dedicated to my family.

This work originated as part of the CPS (Combustion Properties of Partially Premixed Spray Systems) project funded by ESA and the BioSpray (Bestimmung der Selbstzündeigenschaften von Tropfen eines aus Biomasse durch Fischer-Tropsch Synthese gewonnenen Diesel-Brennstoffes durch Mikrogravitationsexperimente und Entwicklung einer Spray-Zündsimulation) project funded by DLR. The GTL-Diesel and GTL-Kerosene fuel samples were provided by Shell Co.

Table of Contents

Abbreviations, Nomenclature and Symbols

Abbreviations

AMN	Alphamethylnaphthalene or 1-Methylnaphthalene
BCH	Bicyclohexyl
Bio-SNG	Bio-Synthetic Natural Gas or Bio-Substitute Natural Gas
BTL	Biomass-to-liquid (fuel)
CAS Nr.	Chemical Abstracts Service, Chemical Numerical Identifier
CCS	Capsule Control System
CFD	Computational Fluid Dynamics
COC	Cyclooctane
CTL	Coal-to-liquid (fuel)
DLR	Deutsches Zentrum für Luft- und Raumfahrt (German Aerospace Center)
DME	Dimethylether
DMM	Dimethoxymethane
DMO	2,2-Dimethyloctane
EU	European Union
FAME	Fatty Acid Methyl Ester
FBP	Final Boiling Point
FT	Fischer-Tropsch Synthesis/Process
GCMS	Gas Chromatography and Mass Spectrometry
GTL	Gas-to-liquid (fuel)
HMN	2,2,4,4,6,8,8-Heptamethylnonane
IBP	Initial Boiling Point
ISS	International Space Station
LHV	Lower Heating Value
mg, µg	Microgravity
Mtoe	Million tons of oil equivalent
ND	Not defined
NDC	n-Decane
NDD	n-Dodecane
NHD	n-Hexadecane
normal-g	Normal gravity, 1g
NTC	Negative Temperature Coefficient
NTD	n-Tetradecane
PCH	Propylcyclohexane
ppm	Parts per million
RME	Rape-Seed Methyl Ester
RT	Room Temperature
SASOL	South African Synthetic Oil Limited
SPS	Speicherprogrammierbare Steuerung (Programmable Logic Controller or PLC)
TCH	1,3,5-Trimethylcyclohexane
TMB	1,2,4-Trimethylbenzene
TSI	Threshold Sooting Index
UHV	Upper Heating Value
VI	Virtual Instrument
ZARM	Zentrum für angewandte Raumfahrttechnologie und Mikrogravitation (Centre for Applied Space Technology and Microgravity)
ZTC	Zero Temperature Coefficient

Nomenclature and Symbols

a	Phase shift
A	Empirical constant Arrhenius equation
A	Component specific constant Antoine equation
A_k	Coefficient of production rate of k-reaction
B	Component specific constant Antoine equation
B_i^{CN}	Blend Value of molecule i
c_{pi}	Heat capacity of species i

C	Component specific constant Antoine equation
CI	Cetane Index
CN	Cetane Number
D	Diffusion coefficient
d_f	Flame diameter
d_s	Droplet diameter
E	Global activation energy during the induction period
E_k	Coefficient of production rate of k-reaction
f	Fugacity
FP	Flash Point
g	Gravitational acceleration
Gr	Grashof number
$\bar{h} = \sum h_i Y_i$	Enthalpy of mixture
h_i	Specific enthalpy of species i
Δh_C	Heat of combustion
ΔH_v	Enthalpy of vaporization
l	Object size
L	Characteristic length
m	Mass
m	Empirical constant Arrhenius equation
n	Empirical constant Arrhenius equation
n	Refractive index
n_k	Coefficient of production rate of k-reaction
p	Pressure
r	Radius (in spherical coordinates)
r_s	Coordinate of liquid-gas boundary (droplet radius)
R^0	Universal gas constant
R^2	1-SSE/SST, Square of the multiple correlation coefficient and the coefficient of multiple determination
$R_i = R^0/\mu_i$	Gas constant of specie i
SSE	Sum of Squares due to Error
SST	Sum of Squares about the mean
t	Time
$\boldsymbol{u}$	Velocity
$\boldsymbol{u}_{Di}$	Diffusion velocity of species i
$v'_{i,k}, v''_{i,k}$	Stoichiometric coefficients of species I by chemical reaction k as an educt and as a product
$\dot{w}_i$	Rate of production of species i by chemical reactions (mass per volume per time)
T	Temperature
X_i	Mole fraction of species i
Y_i	Mass fraction of species i
Z	Compressibility factor
λ	Thermal conductivity
λ	Wavelength
$\bar{\mu} = \sum \mu_i X_i$	Molecular weight of mixture
μ_i	Molecular weight of species i
ρ	Density
τ_1	First induction time (syn. First ignition delay)
τ_2	Second induction time (syn. Second ignition delay)
τ_C	Hot flame combustion duration
τ_t	Total induction time (syn. Total ignition delay)
τ_{Lt}	Droplet lifetime
φ	Fuel-air ratio of mixture
ϕ	Fugacity coefficient
Φ	Equivalence ration

Conventions

In this work all units are strictly based on the SI system {m, kg, s, A, K, cd, mol}. The decimal marker is the comma {,}. All cited graphics and diagrams have been formatted and adapted to the general layout in this work.

1. Introduction and Motivation

Energy, and the demand for it, is directly linked to the development of our civilization and societies. The world's total primary energy demand amounts currently to about 11400 Mtoe (477 EJ) per year. The following figure depicts the different sources of energy and their contribution to satisfying the energy demands. As can be seen, fossil sources, such as oil, coal and gas, account for 81% of the total. Renewable sources account for 13%, with biomass dominating this sector.

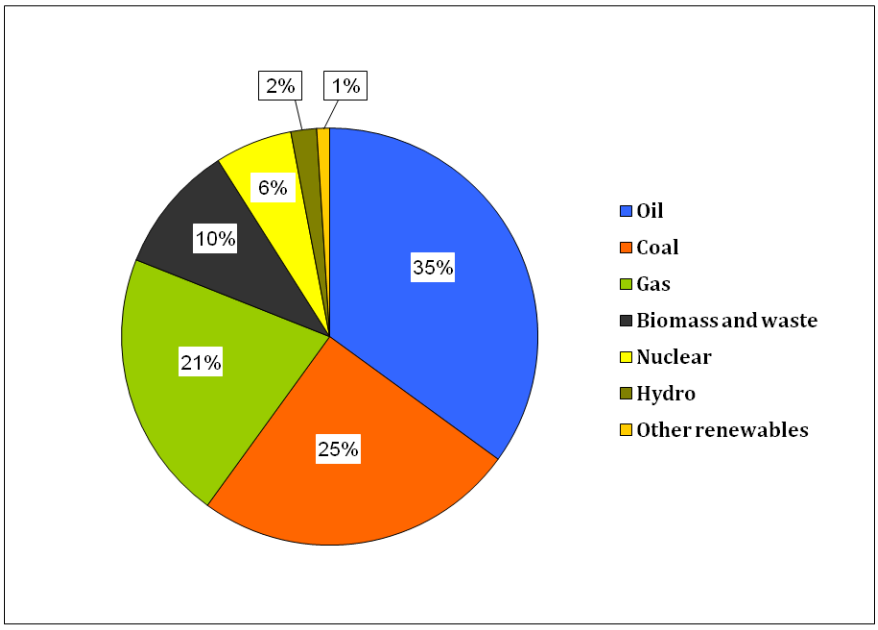

Fig. 1 – World primary energy demand by source, 2007 [1]

The use of fossil energy sources and its coupled CO_2 emissions and other greenhouse gases has increased over the past 250 years since the dawn of industrialization. Although the major greenhouse gases occur naturally, the dramatic increase and its effects on the global climate have been linked directly to human activities [2]. **Figure 2** depicts the greenhouse emissions for the different sectors of our economy. The focus of this study is the use of liquid fuels in the transportation sector. As can be seen, this sector has a share of 13,1% of the total greenhouse gas emissions. **Figure 3** shows the CO_2 emissions caused by the main types of transportation activities (see, air, road) and the projected amounts till 2050.
Efforts on reducing these emissions, increasing oil prices, dwindling oil resources, paired with the need for energy supply independence, have boosted the interest in renewable energy sources. In the transportation sector, fuels developed from biological feedstocks hold the promise of fulfilling these goals.

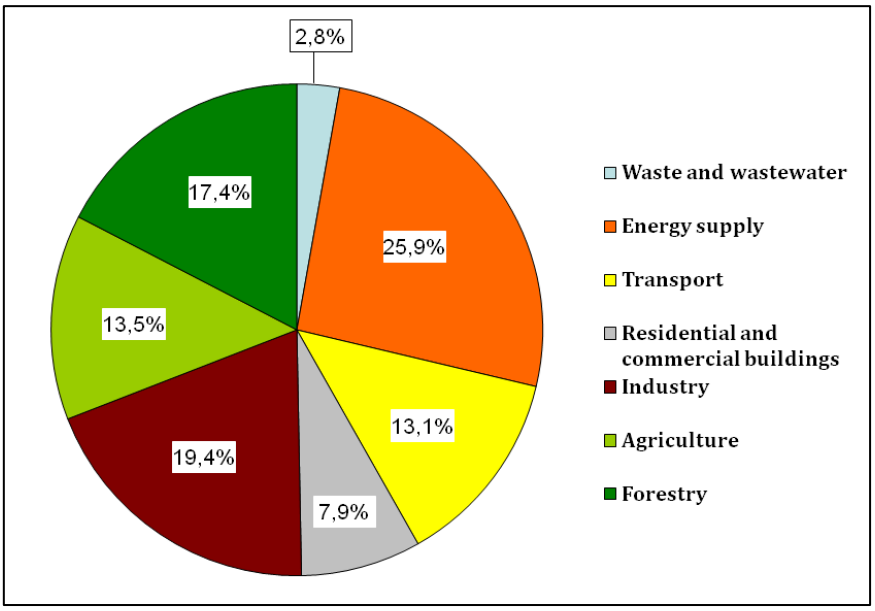

Fig. 2 – Greenhouse gas emissions by sector in 2004 [3]

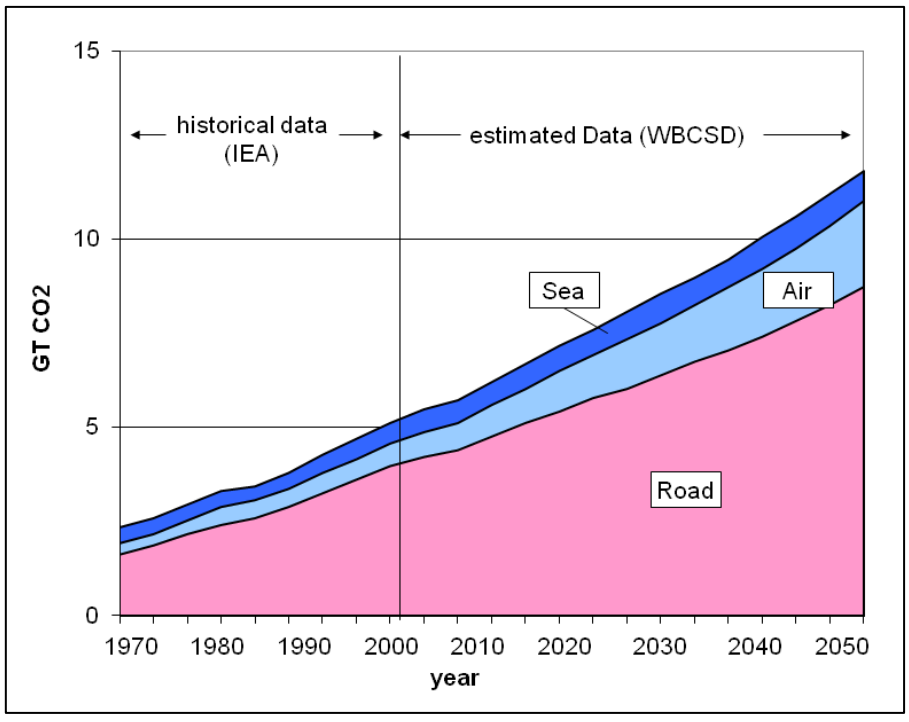

Fig. 3 – Historical and projected CO2 emissions from transport [3]

Biofuels can be classified according to the state in which they are used. Solid fuels such as fuelwood, charcoal and animal dung constitute by far the largest segment of the bioenergy sector, representing over 90% of all biofuels. Liquid biofuels, such as ethanol and Bio-Diesel, play a much more limited role in global energy supply and account for only 1,9% of total bioenergy. Their significance lies mainly in the transport sector, but even here they supplied only 0,9% of total transport fuel consumption (2005). Gaseous biofuels, such as biogas, can be used for heat and power generation and some applications for transportation have been also considered. A basic distinction is also made between primary (unprocessed) and secondary (processed) biofuels:

- **Primary biofuels:** Organic material is used essentially in its natural form, as harvested. Such fuels are directly combusted, usually to supply cooking fuel, heating or electricity production needs in small- and large-scale industrial applications.
- **Secondary biofuels:** Solids (e.g. charcoal), liquids (e.g. ethanol, Bio-Diesel), gaseous (e.g. biogas, synthesis gas, hydrogen) can be used for a wider range of applications, including transport and high-temperature industrial processes.

In this work the focus lies mainly on liquid biofuels for transportation uses. A general distinction has been made between first and second generation biofuels.

- **First generation biofuels:** This type of biofuels is available on the market today. Typical fuels are ethanol (sugarcane, corn), Bio-Diesel and straight vegetable oil (SVO).
- **Second generation biofuels:** These biofuels are produced from cellulose, hemicelluloses or lignin. Examples are cellulosic ethanol and Fischer-Tropsch (FT) fuels. FT-fuels based on biomass are called Biomass-to-liquid (BTL) fuels. (FT-fuels using mineral feedstock sources such as natural gas or coal are called Gas-to-liquid (GTL) and Coal-to-liquid (CTL) fuels.)

The share of liquid biofuels has increased in the past years and the growth is projected to continue, as shown in the following figure. In this scenario biofuels will cover a modest 3 to 3,5% of the total demand for transport energy.

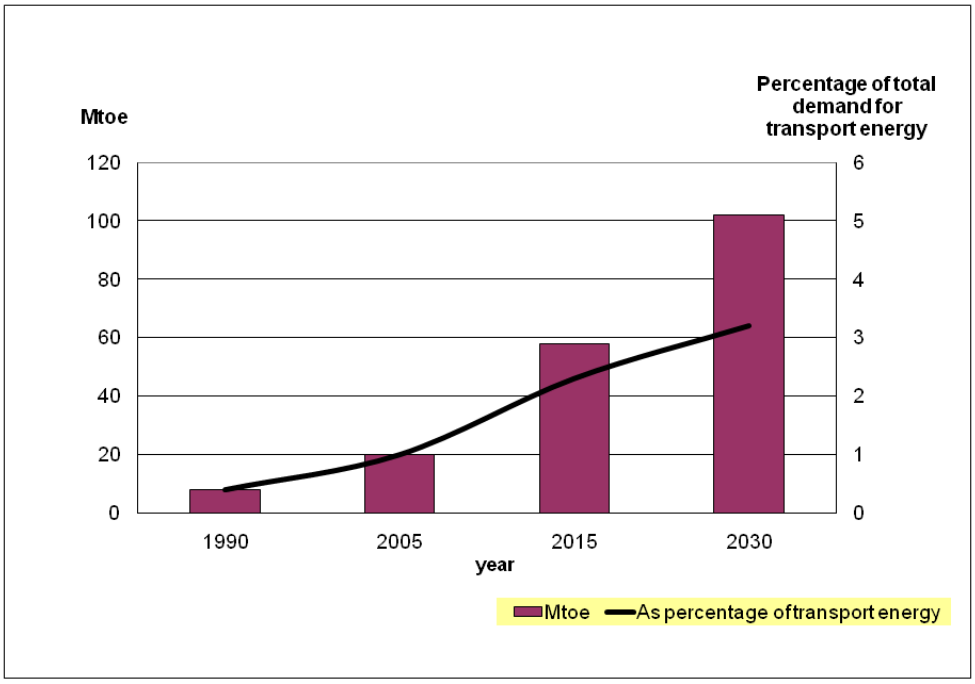

Fig. 4 – Trends in consumption of transport biofuels [1, 4]

Other scenarios from the IEA [4, 5] model future energy demand in light of a global long-term CO_2 concentration in the atmosphere of 450 ppm and a total energy demand of 14389 Mtoe (604 EJ) and projects, a share of around 9% (11,7 EJ) for biofuels of the total transport fuel demand (126 EJ) in 2030. Further studies have extended this analysis to the year 2050, where biofuels provide 26% (29 EJ) of total transportation fuel (112 EJ), with second-generation biofuels accounting for roughly 90% of all biofuels.

The most significant biofuels currently in production are ethanol and Bio-Diesel. Ethanol can be obtained from any feedstock containing substantial amounts of sugar, or materials that can be converted into sugar such as starch or cellulose. The use of biomass containing sugar that can be fermented directly is the simplest way of producing ethanol, with sugar cane being the most widely used feedstock. Currently no commercial production of ethanol from cellulosic biomass exists, but substantial research is being conducted in this area [6]. Bio-Diesel is produced by combining vegetable oil or animal fat with an alcohol and a catalyst through the process of transesterification. Oil for Bio-Diesel production can be extracted from almost any oilseed crop, with rapeseed (EU) and soybean (US and Brazil) being the most popular sources. Also straight vegetable oil SVO is a potential fuel for Diesel engines that can be produced from oilseed crops, used cooking oil from restaurants and animal fat from meat-processing industries. **Figure 5** depicts the conversion of agricultural feedstocks into liquid biofuels of the first generation.

According to the FAO report [1], the impact of biofuels on greenhouse gas emissions, which is one of the key motivations underlying support to the biofuels sector, differs according to feedstock, location, agricultural practice and conversion technology. The contribution of biofuels to energy supply depends both on the energy content of the biofuels and on the energy going into its production. The latter includes the energy required to cultivate, harvest, process and transport the feedstock and the resulting biofuels. The fossil energy balance, as shown in **figure 6** expresses the ratio of energy contained in the biofuels relative to the fossil energy used in its production. It reveals wide variations in the estimated fossil energy balances across feedstocks and fuels. A ratio of 1,0 means that 1 liter of biofuel requires the equivalent of 1 liter of fossil fuel to produce it. A ratio of 2,0 means that a liter of biofuel contains twice the amount of energy required for its production.
One of the prevailing arguments for biofuels is their potential for carbon neutrality. Biofuels are made from biomass. Therefore, in theory, they should be carbon neutral, as their combustion only returns to the atmosphere the carbon that was sequestered from the atmosphere by the plant during its growth, unlike fossil fuels, which release carbon that has been stored for millions of years beneath the earth's surface. This is shown for different crops in different countries in **figure 7**. Assessing the net effect of biofuels on greenhouse gas emissions requires analysis of emissions throughout the life cycle of the biofuel, as mentioned previously and depicted in **figure 8**. Fossil energy balances are only one of several determinants of the emissions impact of biofuels. Also critical factors related to the agricultural production process have to be considered and include, among others: fertilizing, pesticide use, irrigation technology and soil treatment.
In many cases the net effect is unfavorable, due to land-use change (converting forest land to crop land) and deforestation. This can lead to the release of large quantities of carbon dioxide that would take years to recover through the emission reductions achieved by substituting biofuels for fossil fuels. Also the environmental impact can be negative, caused by increased need of water resources and decreasing biodiversity.

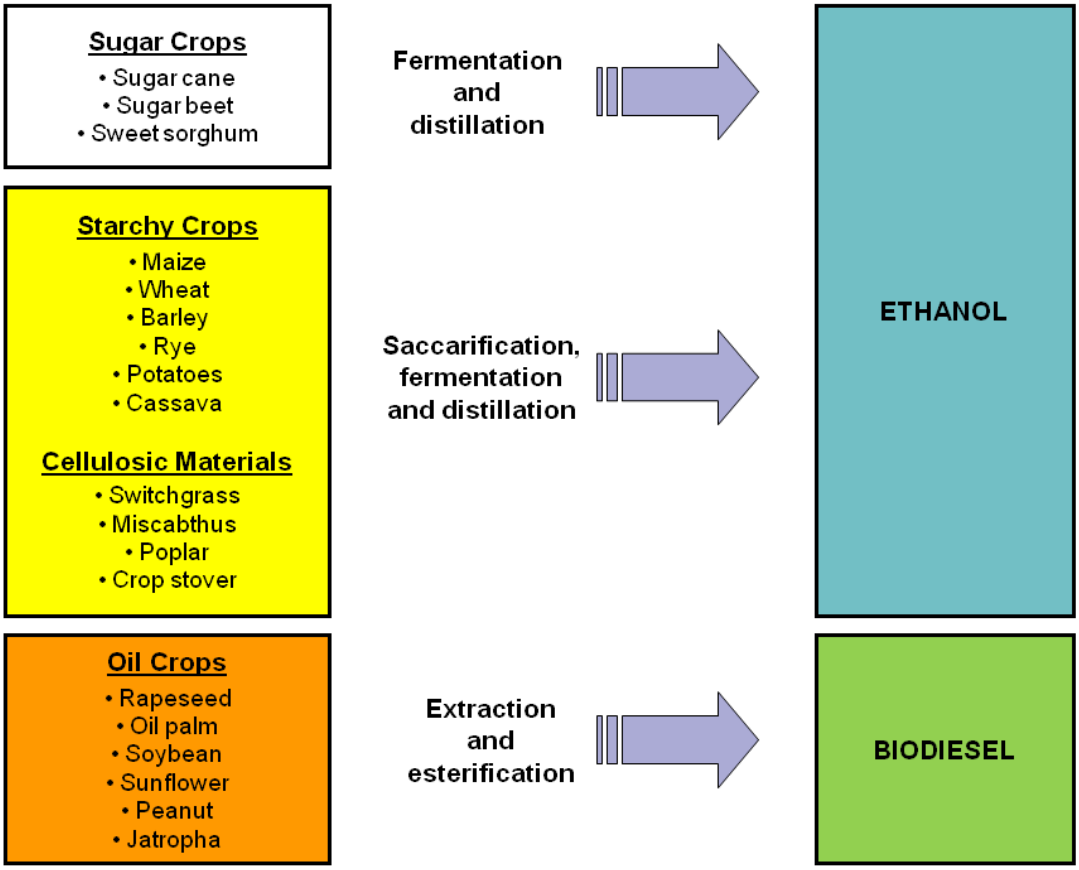

Fig. 5 – Conversion of agricultural feedstocks into liquid biofuels, First generation biofuels [1]

The introduction of second generation biofuels based on lignocellulosic feedstocks can counteract these drawbacks and improve the potential of biofuels. Cellulosic biomass is the most abundant biological material. The successful development of commercially viable second generation biofuels cellulose-based biofuels could significantly expand the volume and variety of feedstocks that can be used for production, such as cellulosic wastes from agriculture, forestry, processing (straw, stalks, leaves, nut shells, bagasse, sawdust, etc.). Cellulosic biomass is more resistant to being broken down or hydrolyzed than starch, sugar and oils, making the conversion technology more expensive, although the cost of the cellulosic feedstock itself is lower compared to the feedstock used in first generation biofuels. The use of cellulosic wastes and dedicated feedstocks that have higher energy yields per hectare could dramatically reduce life-cycle greenhouse gas emissions.

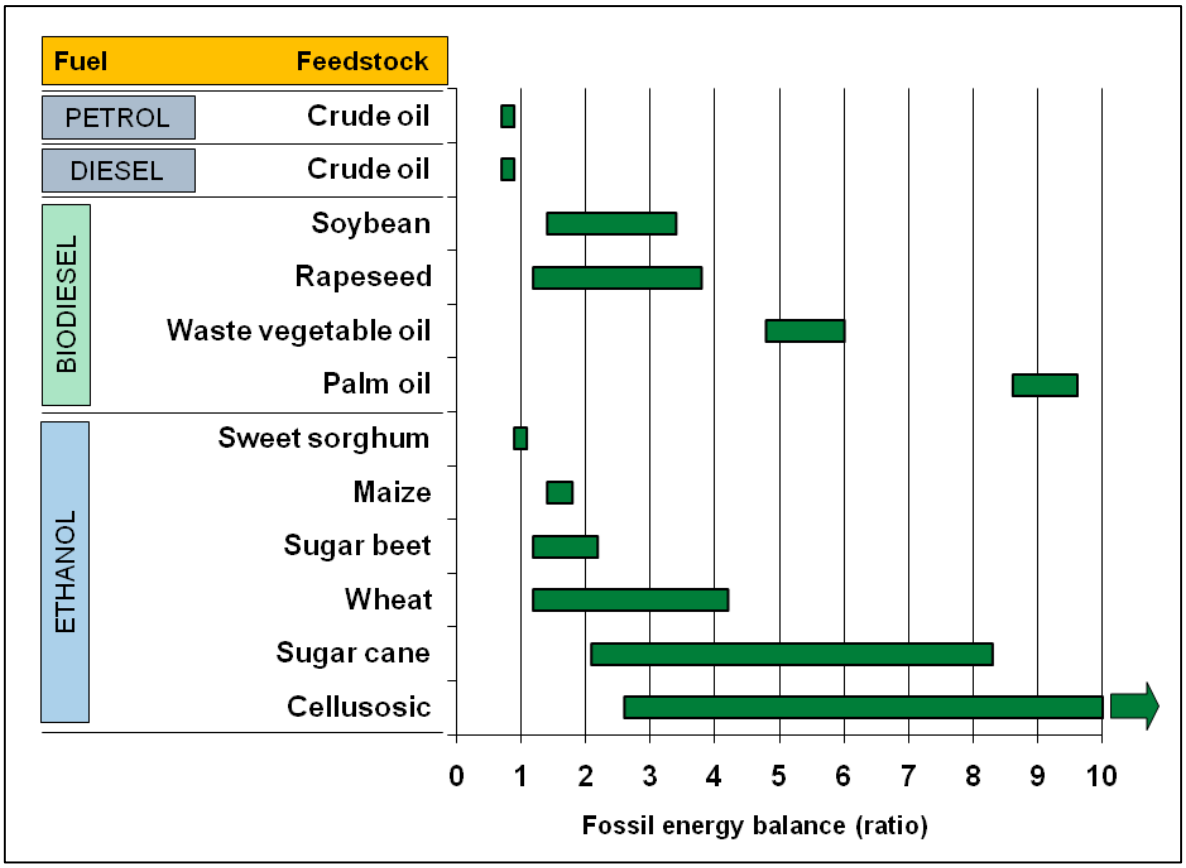

Fig. 6 – Estimated ranges of fossil energy balances of selected fuel types [1]

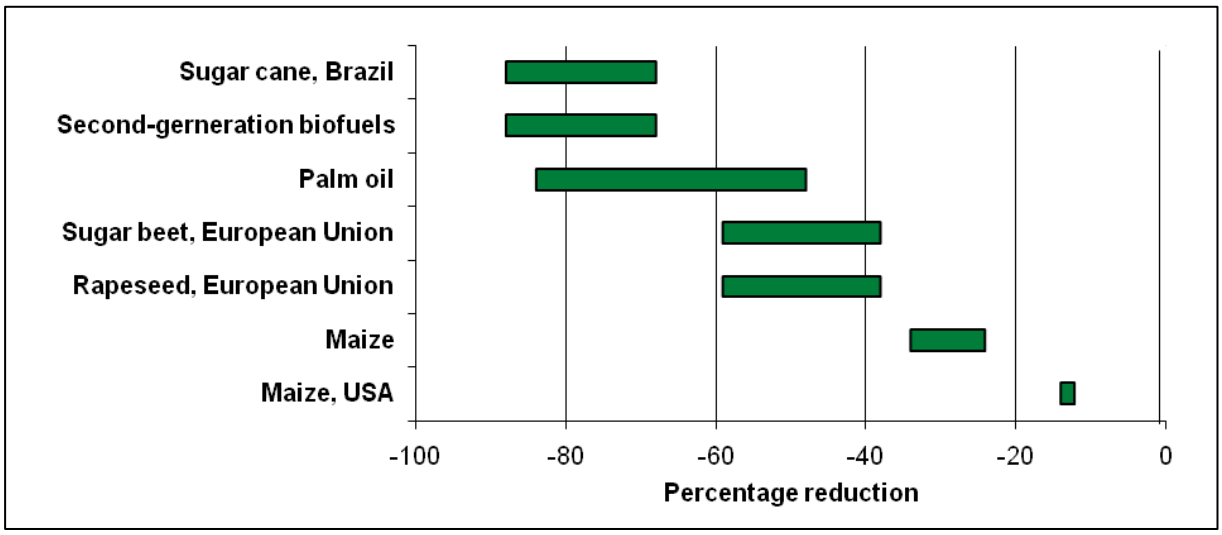

Fig. 7 – Reduction in greenhouse gas emissions of selected biofuels relative to fossil fuel. Effects of land-use change are excluded [1]

In spite of the overall better appeal of the second generation fuels, large-scale production of biofuels implies large land requirements for feedstock production. Liquid biofuels can therefore be expected to displace fossil fuels for transport to only a very limited extent. Exemplarily, calculations conducted by Rajagopal et al. [7] estimate that even with the use of 25% of the main cereal and sugar crops (wheat, rice, maize, sorghum, sugar cane, cassava, sugar beet) that represent 42% of the entire cropland, using common conversion efficiencies, only 14% of petrol consumption would be replaced by the obtained biofuel.

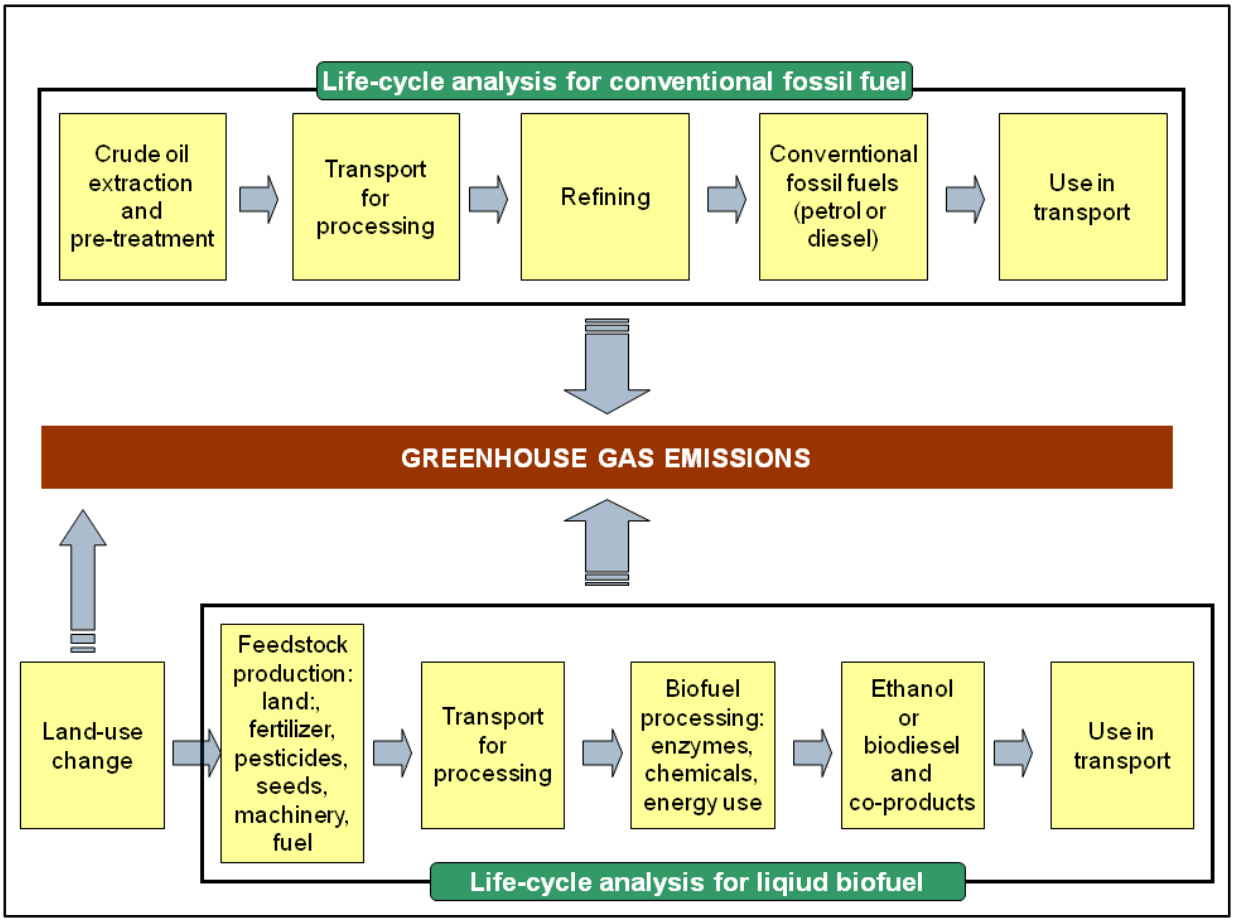

Fig. 8 – Example for life-cycle analysis for greenhouse gas balances of different fuels [1]

In summary, current biofuels have been developed with the aim of [4]:

- Mitigating greenhouse gas emissions
- Strengthening of the energy supply security
- Reducing oil imports
- Supporting agricultural industries and rural communities

First generation biofuels fulfill partially some of the aims, but some drawbacks and concerns have been reported as previously stated, as they:

- Contribute to higher food prices due to competition with food crops.
- Are an expensive option for energy security taking into account total production costs excluding government grants and subsidies.
- Provide limited greenhouse gas reduction benefits (with the exception of sugarcane ethanol).
- Do not meet claimed environmental benefits due to unsustainable biomass feedstock production.
- Contribute to acceleration of deforestation.
- Potentially have a negative effect on biodiversity.
- Compete in some regions for scarce water resources.

Second generation biofuels address many of the problems listed previously by using agricultural and forest residues, non-food crops as a feedstock. The production of these fuels is still in a development stage. With research underway, the promises of increased production and cost reduction can make these fuels a commercially viable alternative. The following

figure shows the projected transition between biofuels from the 1st- and 2nd generation over time till the year 2050.

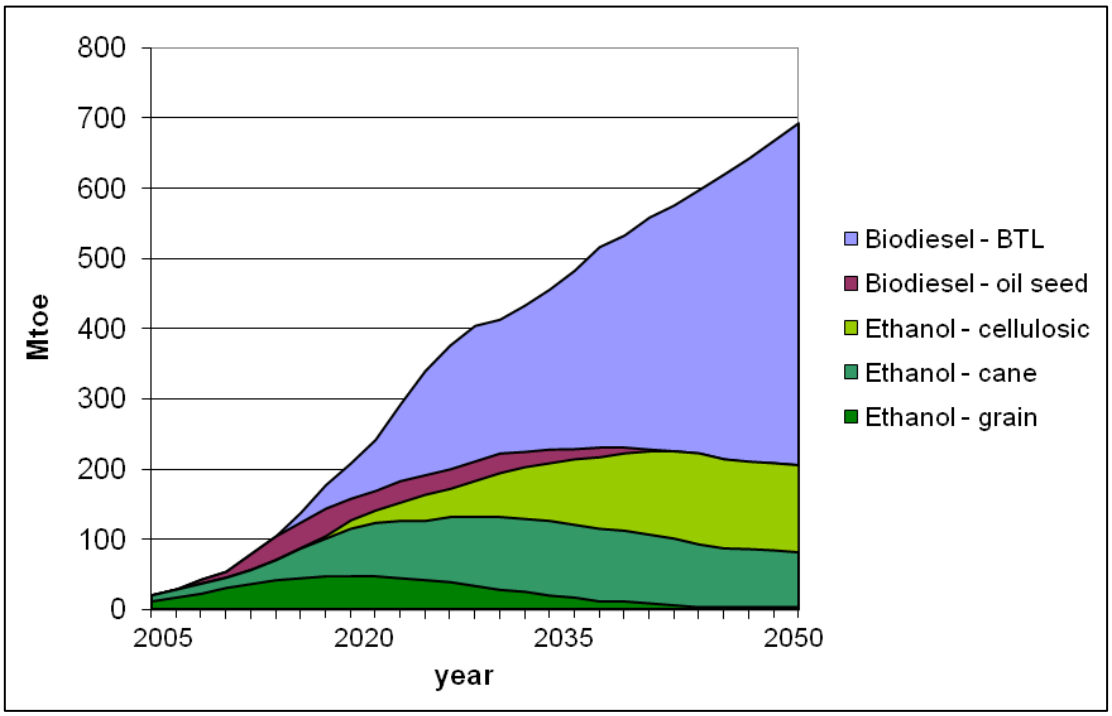

Fig. 9 – Projected transition between biofuels from the 1st- and 2nd- generation [6]

Alternatives are becoming available for light vehicles, besides the previously described biofuels, such as hybrid, electric motors and fuels cells. Such alternatives are less likely for airplanes, boats, ships and heavy trucks, which will continue to rely on liquid fuels.

The introduction and spread of biofuels has also socio-economic implications in our societies. The extraction and processing of petroleum requires a relatively small amount of highly skilled labor, compared to the large amount of farm labor needed for obtaining the required feedstock for biofuels, such as cellulosic biomass, which is abundant but widespread. Thus job creation is an important driver in emerging and developing countries to promote second-generation biofuels. Not only farm labor, but also new jobs for highly skilled labor in biofuel production plants and where dedicated energy crops are cultivated, would be fomented.

The costs of biofuel production will depend strongly on the costs of biomass supply, the aforementioned labor costs and the biomass conversion efficiency of the biofuel production plant, which includes also annual full-load hours of operation and capital requirements.

The costs of biomass feedstock, as stated by [4], strongly depend on regional specific conditions, such us the available infrastructure, labor costs and potential biomass production of the region. Currently there aren't any established markets for most of the primary agricultural residues; therefore no reliable data for biofuel feedstock costs is available. Nonetheless these costs should vary significantly between the different emerging and developed countries, due to available supply logistics and demand.
Compared to petroleum, biomass has a much lower volumetric energy density, so one important factor for the costs of biofuel production is the biomass conversion efficiency of the production plants.

1.1. State of the Art / Motivation

This section is intended to offer brief answers to general questions concerning the motivation of this work and the methods used.

Why are autoignition experiments needed?

As mentioned before, many research activities and governmental efforts are being invested in order to fulfill the goals of reducing the emission of greenhouse gases. One way of accomplishing these goals is to develop fuels based on sustainable renewable biological feedstock. Another possibility is to improve the technical devices and the combustion processes associated. High temperature combustion processes, mainly above 1550 K, create nitric oxides or NO_x as products through the thermal or Zeldovich-NO_x formation process. NO_x are, compared to CO_2, about 300 times more effective as greenhouse gases.
One way to reduce the emission of these compounds into the atmosphere is keeping combustion processes at lower temperatures. Lean-prevaporized-premixed combustion is the most promising approach for reducing NO_x emissions. However, an intrinsic problem to be treated in the design of prevaporizing/premixing combustors is the potential inadvertent autoignition of the fuel-air mixture prior to injection into the primary combustion zone. This means, if the residence time of the fuel-air mixture is sufficiently long, ignition and flame stabilization could occur in the premixing passage and not in the combustor. Consequently, mixing and vaporization must be completed rapidly. Therefore, a precise knowledge of the autoignition behavior and the associated ignition delay or induction times of the fuels used are required. This information can be gained by characterizing the autoignition behavior of the fuels used and then consequently optimization of the technical device where they are applied.

Why are autoignition/evaporation experiments in microgravity needed?

Generally speaking, the intrusion of gravitational forces is a greater impediment to combustion studies than most other areas of science. By its nature, combustion involves chemical energy release which typically cause the temperature of reactive mixtures to increase from an unreacted ambient state of roughly 300 K to totally reacted states at 2000-3000 K. These large temperature differences yield corresponding density differences, which in the presence of gravity invariably cause buoyant motions that vastly complicate, both the execution and interpretation of experiments. Buoyant motion also prevents the observation of phenomena at a fundamental level, such as 1D-configurations, e.g. spherical droplets, which are the intended case in this study. Microgravity conditions enable studies in a buoyancy-free environment. A more detailed discussion on single droplet autoignition experiments in microgravity is given in section 2.2.2.

Why are surrogate fuels needed?

Common fuels are complex mixtures or blends of many hydrocarbon species. In common Diesel, for example, over 100 compounds can be found. For numerical simulations of the autoignition behavior of droplets and sprays, detailed chemical kinetic mechanisms are needed. These have been developed and are still in development individually for each species containing, for a single molecule, hundreds of reactions. Simulating all the components of a common fuel, including their interactions and its behavior as a mixture is currently, for the available computing power, prohibitive. Simulations and good results can still be accomplished with the aid of a simplified fuel, a surrogate. This fuel is composed of one or

two species and is intended to represent certain characteristics and behaviors of the targeted fuel. Current surrogate fuels are only valid for representing one specific process. Thus there are specific surrogates for representing the autoignition behavior, other surrogates for NOx formation, other for soot formation, and so on. An overview of surrogate mixtures and surrogate formulation procedures found in literature is given in section 2.1.5.

1.2. Objectives and Outline

The main objective of this work is to characterize the autoignition behavior of BTL-Kerosene and BTL-Diesel, two fuels derived from biomass and synthesized via the Fischer-Tropsch process. (As mentioned before, FT-fuels can also be derived from mineral feedstocks (GTL and CTL). These are chemically identical to BTL and only distinguishable through C_{14} analysis.) For this work, GTL-fuels were readily available and the subsequent analysis has been performed on these fuels. The characterization of the autoignition behavior is accomplished by conducting experiments with single droplets under normal-g and microgravity conditions. Based on this data, a surrogate fuel is developed and experimentally validated. Finally, the experimental data is used for validation of numerical codes developed by the Aerospace Combustion Engineering research group at ZARM for the simulation of the autoignition of single fuel droplets and subsequently of sprays. The general interest of this type of studies is rooted primarily in the development of computational codes that enable the prediction of the behavior of a technical system. This is performed through simulations of events based on thermokinetic models representing the detailed chemistry and its associated heat release, and the coupling of these with complex fluid mechanics models representing the gas dynamics in the system. The following figure shows the general context of the studies conducted at ZARM, the general roadmap of the research activities and the contextual positioning of this work.

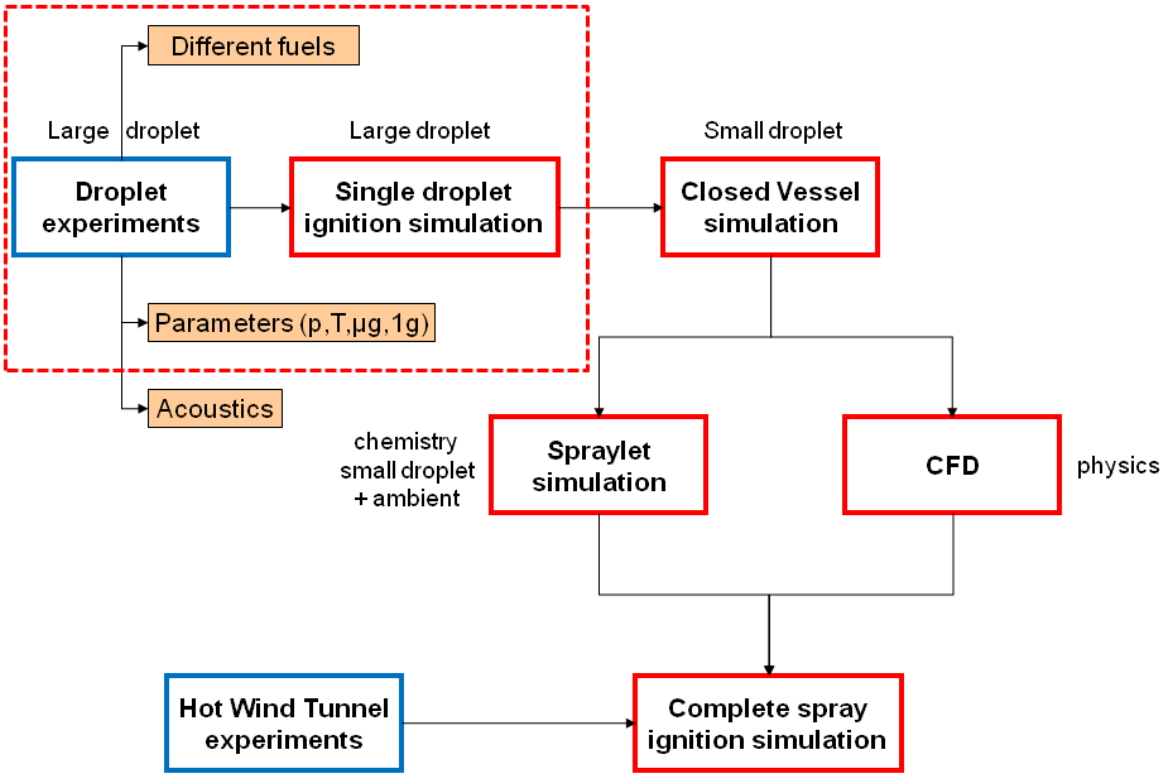

Fig. 10 – Research context of this study

The experimental activities (blue) provide data for the numerical codes (red). The drop tower experimental apparatus provides autoignition and evaporation data of single fuel droplets and is described in more detail in section 3.2 of this study. The Hot Wind Tunnel provides experimental data concerning the autoignition of fuel sprays in machine-like conditions [8, 9]. As can be seen, the goal of the research activities is to develop an experimentally validated numerical code for the prediction of the autoignition of fuel sprays. This goal is preceded by several development stages shown in the graphic. The Single Droplet Ignition Simulation describes the autoignition behavior of spherically symmetric large droplets (~ tenths of mm) in absence of natural convection. Studies and validation of this code for other fuels have been conducted in dependency of pressure and temperature [10-20]. The Closed Vessel Simulation (CVS) takes this development further and simulates a monodisperse equidistant spray. This code enables the simulation of technical sized (tenths of μm) droplets. The next step, currently in development, is a single droplet simulation with variable gas boundary conditions and the coupling of these results with characteristic trajectories of single droplets from a CFD simulation, leading to a Complete Spray Ignition Simulation.

The general working procedure of this work is depicted in the following diagram. This study is composed of five chapters, with three main sections dealing with theory, experiments and simulations. After the current introductory segment, Chapter 2 of this work gives an overview of the theory related to autoignition of liquid hydrocarbon fuels. Also a description of the general properties of these fuels is given. A subsection concerning the selection criteria and the determination of appropriate surrogate fuels closes this chapter.
The third Chapter deals with the experimental studies. A description of the apparatus used for the experiments on autoignition and evaporation of single fuel droplets, the experiments and the obtained results is given. For each analyzed fuel, a discussion of the results is conducted. Also a comparison of the autoignition experimental results of related fuels is presented.
In Chapter 4 a comparison between the obtained experimental data and the results of the numerical code developed at the Aerospace Combustion Engineering Group at ZARM is presented. Finally, in the last section of this study a summary of the results obtained is given and conclusions are drawn. An outlook for future work closes this study.

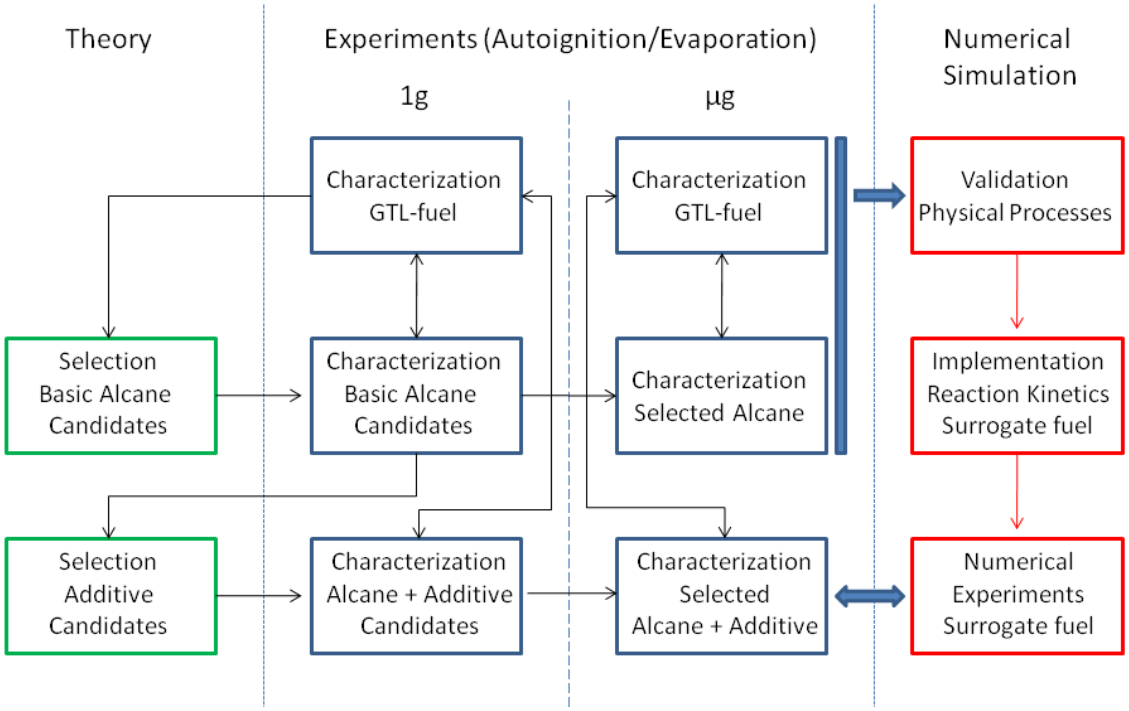

Fig. 11 - Work flow of the thesis

Publications

Reimert, M., Marks, G., Eigenbrod, C., „Diesel, Bio-Diesel, GTL-/BTL-Diesel, n-Heptane and n-Tetradecane / AMN: Experimental Comparison of the spontaneous ignition of single droplets", 24. Deutscher Flammentag, 16-17 September 2009, Bochum, Germany

Eigenbrod, C., Reimert, M., Rickmers, P., Rath, H.J., „Autoignition of Droplets and Sprays",4th China-Germany Workshop on Microgravity and Space Life Sciences, 2009, Shanghai, China

Eigenbrod, C., Reimert, M., Marks, G., Rickmers, P., Klinkov, K., Moriue, O., „Experiments on Induction Times of Diesel-Fuels and its Surrogates", 9th Drop Tower Days, COSPAR 2010, Bremen, Germany

Eigenbrod, C., Reimert, M., Marks, G., Klinkov, K., „Induction Times of a Gas-to-Liquid (GTL) Kerosene and Definition of a Simple Model Fuel", 4th International Symposium on Physical Sciences in Space, ISPS4, 11-15 July 2011, Bonn-Bad Godesberg, Germany

2. Theoretical Background

In this chapter the terminology and concepts used throughout this work are presented. It is divided into two main sections, the first one focuses on the general properties of liquid hydrocarbon fuels, especially Diesel and Kerosene; the second section deals with the single droplet ignition phenomenon.

2.1. Liquid Hydrocarbon Fuels

The objective of this section is to define the terminology used throughout this work concerning the fuels studied. Also a brief review of the current state-of-the-art is presented.

2.1.1. General Properties of Liquid Hydrocarbon Fuels

General Physical Properties

Density: Definition and measurement procedure normed under EN ISO 3675 and EN ISO 12185 and given in kg/m^3 at 15 °C. Density is measured under this norm with the aid of an oscillating U-tube. The density of the fuel in a compression engine affects, in the case of a fixed injection volume, the engine's performance, fuel consumption and particle emissions. [21]

Kinematic viscosity: Definition and measurement procedure normed under EN ISO 3104 and given in mm^2/s at 40 °C. Viscosity is measured under this norm with the aid of an Ubbelohde viscometer. With decreasing temperature and increasing pressure viscosity increases. This property influences the flow and pumping behavior of fuels in an engine, such as the spray formation during the injection process. In the case of compression engines, a too high viscosity can disturb the pumpability and cause cold start problems at low ambient temperatures. On the other hand, a too low viscosity can hinder the hot start of an engine, reduce the performance and increase the wearing of the pumping system. [21]

Heating value: The heat of combustion $\Delta \boldsymbol{h_C}$, also known as the heating value, is numerically equal to the enthalpy of reaction, but with the opposite sign. The upper or higher heating value, HHV, is the heat of combustion calculated assuming that all of the water in the products has condensed to liquid. In this scenario, the reaction liberates the most amount of energy. The lower heating value, LHV, corresponds to the case where none of the water is assumed to condense. [22] The method of determination is standardized under DIN 51900.

Boiling/Distillation curve: Definition and measurement procedure normed under EN ISO 3405 and ASTM D86. This test method covers the atmospheric distillation of petroleum products using a laboratory batch distillation unit to determine quantitatively the boiling range characteristics of such products as light and middle distillates, automotive spark-ignition engine fuels with or without oxygenates, aviation gasolines, aviation turbine fuels, Diesel fuels, Bio-Diesel blends up to 20%, marine fuels, special petroleum spirits, naphthas, white spirits, kerosenes, and Grades 1 and 2 burner fuels.

From this test several properties can be gained:

- **Boiling curve:** This diagram shows the relation between boiling temperature and condensate volume. (See next figure)
- **Initial boiling point (IBP):** Defined as the temperature where the first condensate is obtained.
- **Boiling points:** Defined as the temperature where a certain amount of fluid is evaporated. Common points are T_5, T_{10}, T_{50}, T_{90}, T_{95}, where T stands for temperature and the adjacent value describes the volume that has evaporated.
- **Final boiling point (FBP):** Defined as the temperature where the analyzed volume completely evaporates.
- **Condensate volumes:** Defined as the volume of condensate obtained at a certain temperature. Common volumes are E_{70}, E_{100}, E_{150}, E_{205}, E_{250}, E_{350}. E is an abbreviation for "evaporated" and the adjacent value specifies the temperature in °C.
- **Residues:** Defined as the residual volume in the apparatus after the distillation process.
- **Losses:** Defined as the difference between the initial volume and the residues.

The distillation (volatility) characteristics of hydrocarbons have an important effect on their safety and performance, especially in the case of fuels and solvents. The boiling range gives information on the composition, the properties, and the behavior of the fuel during storage and use. Volatility is the major determinant of the tendency of a hydrocarbon mixture to produce potentially explosive vapors. The distillation characteristics are critically important for both automotive and aviation gasolines, affecting starting, warm-up, and tendency to vapor lock at high operating temperature or at high altitude, or both. The presence of high boiling point components in these and other fuels can significantly affect the degree of formation of solid combustion deposits. [23]

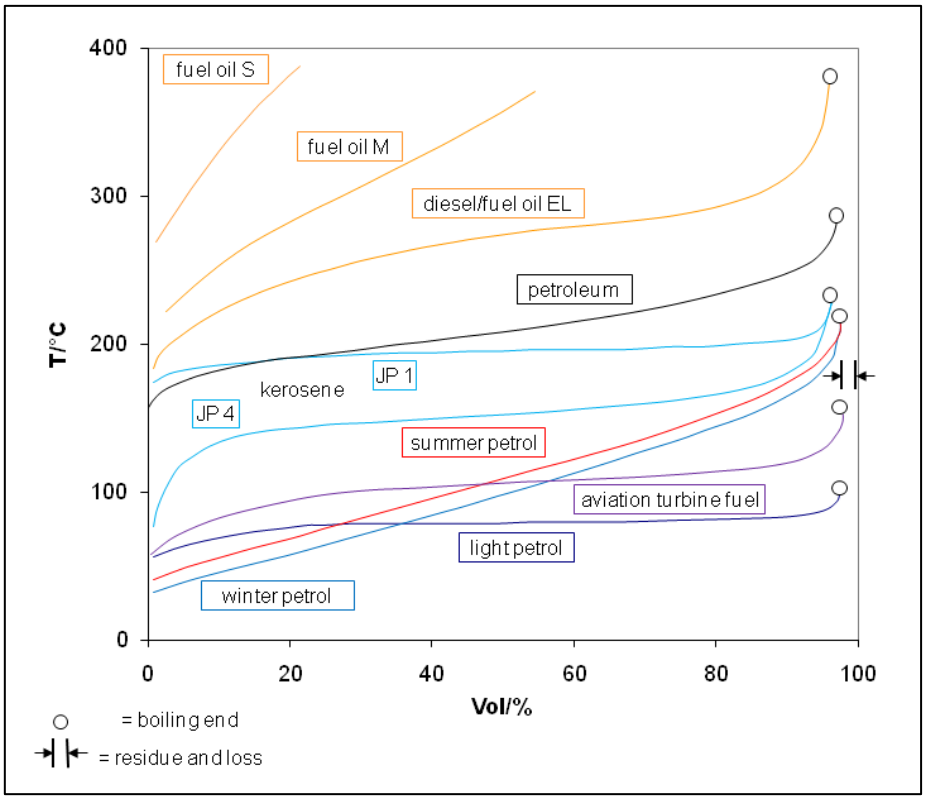

Fig. 12 – Qualitative boiling curves of different common fuels [24]

Heat of evaporation or enthalpy of vaporization ΔH_v: Defined as the energy required for vaporizing a given quantity of a substance into a gas at a given pressure (often atmospheric pressure) and is given in kJ/kg.

Flash point: Definition and measurement procedure normed under EN 22719 and ISO 2719 and given in °C [21, 25]. The flash point of a volatile liquid is the lowest temperature at which it can vaporize to form an ignitable mixture in air at normal pressure. Measuring the flash point of a liquid requires an ignition source. At the flash point, the vapor may cease to burn when the source of ignition is removed. The flash point is not to be confused with the autoignition temperature, which does not require an ignition source. The fire point, a higher temperature, is defined as the temperature at which the vapor continues to burn after being ignited. Neither the flash point nor the fire point is related to the temperature of the ignition source or of the burning liquid, which are much higher. The flash point is often used as a descriptive characteristic of a liquid fuel, and it is also used to help characterize the fire hazards of liquids. It refers to both flammable liquids and combustible liquids. There are various standards for defining each term. Commonly, liquids with a flash point less than 60,5 °C are flammable, and liquids with a flash point above those temperatures are combustible.
Exemplarily, Diesel fuel flash points vary between 52 °C and 96 °C. Diesel is designed for use in a high-compression engine where air is compressed until it has been heated above the autoignition temperature of Diesel. Fuel is then injected as a high-pressure spray, keeping the fuel-air mix within the flammable limits of Diesel. No ignition source is used. Therefore, Diesel is required to have a high flash point and a low autoignition temperature.
On the other hand, spark ignition engines use fuels (such as gasoline) that are required to have a low flash point and a high autoignition temperature. The fuel is intended to be premixed with air within its flammable limits and heated above its flash point, then ignited by the spark plug. The fuel should not pre-ignite in the hot engine.
Jet fuel flash points vary greatly. Both Jet A and Jet A-1 have flash points between 38 °C and 66 °C, close to that of off-the-shelf Kerosene. Yet both Jet B and FP-4 have flash points between -23 °C and -1 °C.

The flash point can be approximated by the following correlation [21]:

Eq. 1

$$FP = 0{,}654 t_{10\%} - 0{,}537(t_{10\%} - t_{IBP}) - 60{,}7$$

FP is the flash point in °C, $t_{10\%}$ is the temperature at 10% volume recovered (during the distillation) in °C and t_{IBP} is the temperature at the initial boiling point in °C.

General Chemical Properties

Cetane Number (CN): Similar to the octane number for gasoline, the cetane (trivial name for n-Hexadecane) number uses n-Hexadecane as a reference compound for describing the ignition and combustion quality of Diesel fuels in compression ignition engines. For n-Hexadecane, the assigned cetane number is 100. On the other end of the scale, alpha-methylnaphthalene (AMN) has an assigned cetane number of 0. Currently AMN, due to its slight toxicity, is no longer used. Branched compounds exhibit lower cetane numbers (and lower melting points) compared to n-Hexadecane, as exemplified by iso-cetane (or 2,2,4,4,6,8,8,-Heptamethylnonane (HMN)), which has a cetane number of 15. A low cetane

number means a fuel component is relatively resistant to ignition in a Diesel engine while a high cetane number indicates it is easily ignited. This definition implies:

Eq. 2

$$CN = (\%\, n - Hexadecane) + 0{,}15(\%\, HMN)$$

Basically two methods for measuring the cetane number exist. The first one involves burning the fuel in a Diesel engine called Cooperative Fuel Research (CFR), or in Europe, BASF engine, under standard test conditions. The operator of the CFR engine uses a hand-wheel to increase the compression ratio (and therefore the peak pressure within the cylinder) of the engine until the time between fuel injection and ignition is 2,407 ms. The resulting cetane number is then calculated by determining which mixture of cetane and iso-cetane will result in the same ignition delay. The other method uses an apparatus called Ignition Quality Tester (IQT) [26]. This instrument applies a simpler, more robust approach to CN measurement than the CFR. Fuel is injected into a constant volume combustion chamber in which the ambient temperature is approximately 575 °C. The fuel ignites, and the high rate of pressure change within the chamber defines the start of combustion. The ignition delay of the fuel can then be calculated as the time difference between the start of fuel injection and the start of combustion. The fuel's derived cetane number can then be calculated using an empirical inverse relationship to ignition delay. The industry standards for measuring cetane number are ASTM D-613, ISO 5165, and DIN 51773 for the CFR engine and ASTM D-6890 for the IQT.

The following figures show the CNs for pure components for different hydrocarbon families: n-alkanes have the highest CNs and they increase with the number of carbon atoms, or the longer the backbone chain the higher the CN. Addition of branches decreases the CN, shown by the difference between iso- and n-alkanes. The CN decreases with the degree of branching. The position of the branches plays a role, although rather secondary. If the branching is concentrated at one end of the molecule, leaving a long chain at the other end, then such iso-alkanes tend to have higher CNs. Compared to iso-alkanes, alkenes (olefins) have higher CNs and follow closely the alkanes trend. Aromatics and cyclo-alkanes typically have lower CNs, unless they have a long n-alkane side chain. Multi-ring structures have lower CNs compared to the corresponding single ring structures, as shown in the figure in the case of cyclo-alkanes and decalins.

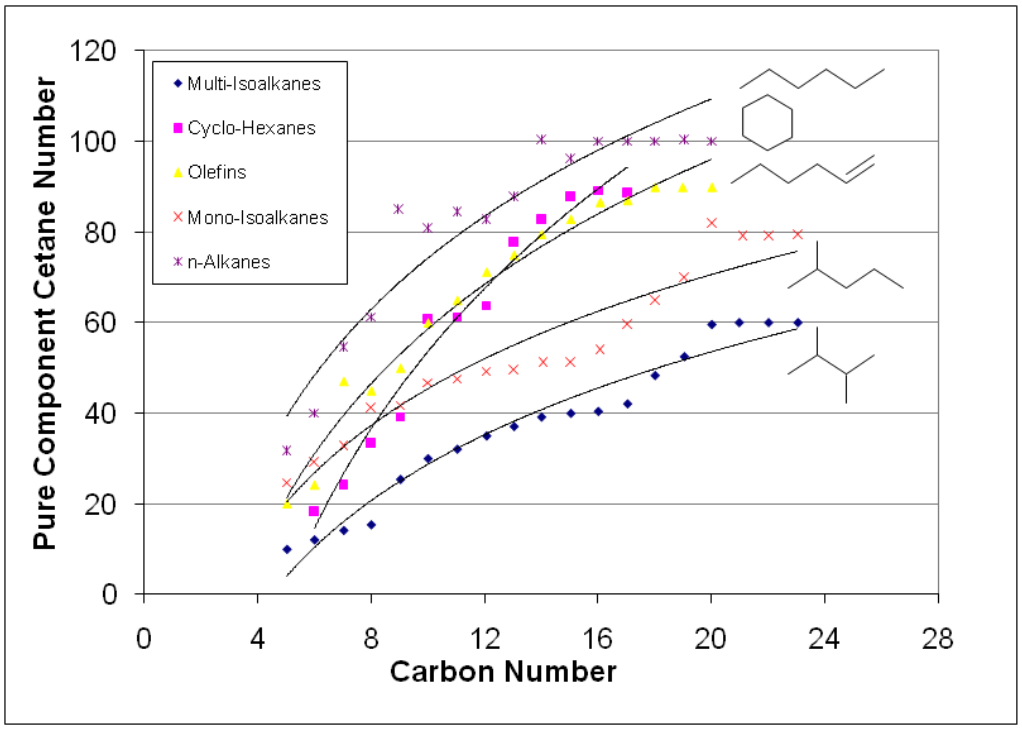

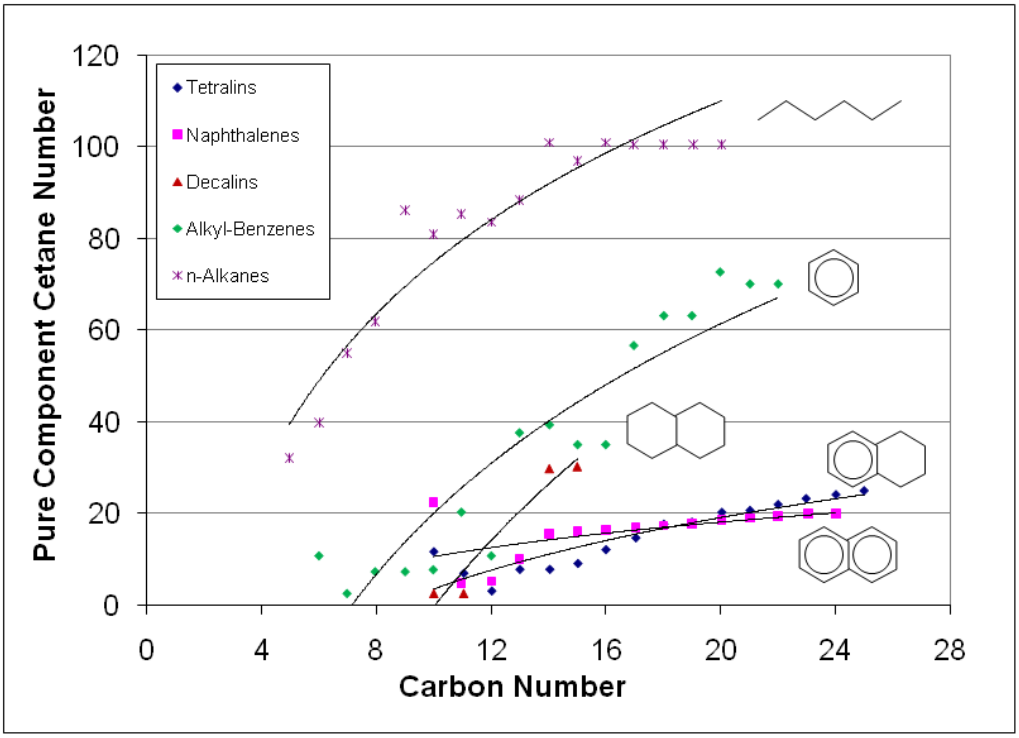

Fig. 13 – Pure component Cetane Numbers for different hydrocarbon compound families [27]

The CN of a multi-component fuel can be predicted by using a simple composition-based model developed by Ghosh and Jaffe [28]. This model is described by the following equations:

Eq. 3

$$CN = \sum_i v_i B_i^{CN}$$

By definition, CN is a linear volumetric blend of the blend contributions of all of the different molecules present in the fuel. v_i is the volume fraction of molecule *i* in the fuel, B_i^{CN} is the blend value, which is the molecule's contribution to the CN of the fuel. This means, that a molecule does not necessarily contribute its pure component CN to the fuel's CN. Thus the blend value of a molecule depends on the overall composition of the fuel it is part of. Assuming that the blend value B_i^{CN} of molecule *i* in a fuel varies linearly with the CN of the fuel, then

Eq. 4

$$B_i^{CN} = a_i^{(0)} + a_i^{(1)} CN$$

B_i^{CN} has two parameters, a slope $a_i^{(1)}$ and an intercept $a_i^{(0)}$, thereby implying a linear variation of blend values with the composition of the fuel. This does not however, imply a linear relationship of the fuel composition to its CN.
The boundary condition for this model is for the case where the fuel is composed of a single component, thus CN equals B_i^{CN} equals CN_i (the pure component CN). Applying this boundary condition we obtain:

Eq. 5

$$CN_i = a_i^{(0)} + a_i^{(1)} CN_i$$
$$\rightarrow a_i^{(0)} = \left(1 - a_i^{(1)}\right) CN_i$$

By defining $\beta_i = 1 - a_i^{(1)}$, the previous equation can be rewritten as:

Eq. 6

$$a_i^{(0)} = \beta_i CN_i$$

Based on the previous equations, the final form of the prediction model is:

Eq. 7

$$CN = \frac{\sum_i v_i \beta_i \, CN_i}{\sum_i v_i \beta_i} = \frac{\sum_{lumps} v_i \beta_i \, CN_i}{\sum_{lumps} v_i \beta_i}$$

The summation index *i* is intended to run over all molecules present in the fuel, rendering it impractical for technical applications. Therefore some merging or lumping of molecules is necessary for a realistic and practical model. A lump defines the compositional level of abstraction that the model uses. Ghosh and Jaffe [28] define a total of 129 molecular lumps belonging to 9 different hydrocarbon classes. The defined classes are shown in the following table. For a detailed listing of the molecular lumps and their correspondent CN_i values, please refer to [28]. The values for the fitting parameter β found by Ghosh and Jaffe [28] are listed on the table as well.

Molecular class	**Carbon number range**	***β***
n-alkanes	nC_5 to nC_{16+}	0,5212
i-alkanes Monobranched i-alkanes Multibranched i-alkanes	iC_5 to iC_{25+}	7,3717
Naphthenes Alkylcyclohexanes Decalins	 Cyclohexane to C_{10+} cyclohexanes Decalin to C_{4+} decalins	0,0727

Aromatics Alkylbenzenes Naphthalenes Tetralins	 Benzene to C_{14+} benzenes Naphthalene to C_{13+} naphthalenes Tetralin to C_{15+} tetralins	3,1967
Olefins/Cyloolefins	C_5 to C_{18+} olefins	0,3597

Tab. 1 – Molecular lumps and parameter values for the cetane number prediction model [28]

Cetane Index (CI): Is a calculated number based on the density and distillation range of the fuel. Currently the international standards (DIN EN ISO 4264:2007 and ASTM D4737) use the "4-point method", based on density, 10% 50% and 90% recovery temperatures. The outdated '2-point method' is defined in ASTM D976, and uses just density and the 50% recovery temperature. This 2-point method tends to over-estimate the cetane index and is not recommended. Cetane index calculations cannot account for cetane improver additives and therefore do not represent the total cetane number for additized Diesel fuels. Diesel engine operation is primarily related to the actual cetane number and the cetane index is simply an estimation of the base, unadditized cetane number. The empirical formula for the determination of CI [21] is as follows:

Eq. 8

$$CI = 45{,}2 + 0{,}0892T_{10N} + (0{,}131 + 0{,}901B)T_{50N} + (0{,}0523 - 0{,}420B)T_{90N} + 0{,}00049(T_{10N}^2 - T_{90N}^2) + 107B + 60B^2$$

Where

Eq. 9

$$B = \left[e^{(-0{,}0035D_N)}\right] - 1$$

D is the density at 15 °C in kg/m^3 and $D_N = D - 850$

T_{10} is the temperature in °C where 10 Vol% of the fluid is evaporated and $T_{10N} = T_{10} - 215$

T_{50} is the temperature in °C where 50 Vol% of the fluid is evaporated and $T_{50N} = T_{50} - 260$

T_{90} is the temperature in °C where 90 Vol% of the fluid is evaporated and $T_{90N} = T_{90} - 310$

General Operational Properties

Lubricity: Definition and measurement procedure normed under ISO 12156-1. Lubricity is the measure of the reduction in friction of a lubricant. In a modern Diesel engine, the fuel is part of the engine lubrication process. Fossil Diesel fuel naturally contains sulfur compounds that provide good lubricity, but because of regulations in many countries (such as the US and the EU) sulfur must be removed. Reformulated Diesel fuel has a lower lubricity and requires lubricity improving additives to prevent excessive engine wear. Lubricity is measured with a high frequency reciprocating rig or HFRR, which is a friction and wear test composed of a sphere with 6mm diameter, which is pressed with a defined force on a steel vane with specified surface roughness. The sphere is partially submerged in the fluid to be analyzed

(T=60 °C) and the vane is moved back and forth. After 75 min the flattening of the sphere is measured and is given in μm.

Low-Temperature-Operability: Several parameters are used, defined and tested under EN 116 and EN 23015. [21]

> **Cloud point (CP):** Temperature in °C at which first visible crystals form upon cooling a fuel and at which therefore problems such as fuel filter plugging could result.
>
> **Cold filter plugging point (CFPP):** Lowest temperature, expressed in °C, at which a given volume of Diesel type of fuel still passes through a standardized filtration device in a specified time when cooled under certain conditions. This test gives an estimate for the lowest temperature that a fuel will give trouble-free-flow in certain fuel systems. This is important as in cold temperate countries a high cold filter plugging point will clog up vehicle engines more easily.
>
> **Pour Point (PP):** Lowest temperature at which a fuel will still pour or flow under prescribed conditions. It is a rough indication of the lowest temperature at which a liquid is readily pumpable.

Compressibility: Compressibility is a measure of the relative volume change of a fluid or solid as a response to a pressure (or mean stress) change. In the context of engine operability, the compressibility of a fuel is an important parameter for the design and function of fuel injection systems.

Electrical conductivity: In order to avoid electrostatic charging during rapid pumping, fuels have to possess a minimal electrical conductivity defined in Germany under BGR132 "Vermeidung von Zündgefahren infolge elektrostatischer Aufladungen". The values of paraffines found in Diesel and Kerosene are in the order of 0,01-0,02 pS/m and usually are sufficient for the pumping rates commonly used. [21]

Elastomer compatibility, corrosion effect on metals: Elastomers are used as basic materials for tubing and other components of the fuel system of an engine. E.g. aromates can cause shrinkage of certain elastomers and esters can cause degradation of acrylnitril-based materials. Fuels come in contact with air and moisture and degrade metallic components.

Composition: The composition of the fuels is a basic parameter for describing a fuel. This topic is treated in subsequent sections of this study. In this overview a brief description of the allowed amount of residues is given.

> **Ash content, carbon residue, total contamination:** General composition parameters are defined specifically for each fuel. The ash content describes the allowed amount of inorganic material in the fuel. Testing is defined under EN ISO 6245. Carbon residue quantities are defined under EN ISO 10370. Total contamination is defined as the total allowed amount of unsolvable impurities and its testing is normed by EN 12662.
>
> **Oxidative stability:** Definition and testing procedure normed under EN ISO 12205. Stored fuels can degrade through oxidation and polymerization, which can enhance filter clogging. Additives are used to counteract these processes. The amount of unsolvable residues is given in g/m^3

2.1.2. Fossil Diesel and Bio-Diesel

In the transportation industry, on-road transport of goods is mainly done by Diesel engine powered transporters because of their advantages regarding fuel efficiency compared to other types of engines. Compared to spark ignition engines, Diesel engines or compression ignition engines have the disadvantage of emitting higher amounts of NO_x and soot particles. Continuously stricter pollutant emission values and regulations force manufacturers to integrate more complex injection, combustion, exhaust gas recirculation and aftertreatment systems into their engines. Such complex engine systems are designed, calibrated and optimized to work with a specific fuel. Contrasting the technical demand for fuels with defined properties in order to fulfill the aforementioned emission targets, there is a societal demand for alternative fuels in order to reduce crude oil dependency.

The Diesel family of fuels is mainly divided into two groups:

- Fossil Diesel. Also known as conventional, mineral, Petrodiesel, Diesel or Diesel fuel is derived from petroleum and is defined by the standards ASTM D975 in the US and EN 590 in Europe
- Alternative Diesel fuels. Mainly four types of fuel alternatives for compression ignition engines are currently in use, as stated by Soltic et al. [29]:

    1. Bio-Diesel made from fatty acid methyl ester (FAME) from vegetable oils or animal fats and standardized in the US under ASTM D6751 and in Europe under EN 14214.
    2. Neat vegetable oil standardized under DIN V 51605.
    3. Recycled waste oil from fossil or biogenic sources.
    4. Fuels synthesized from fossil or biogenic gas (GTL or BTL) or coal (CTL) via the Fischer-Tropsch process.

The latter type will be described in section 2.1.4.

Fossil Diesel

Fossil Diesel is a very complex mixture composed of mainly four types of chemical compounds: n-alkanes, branched alkanes or iso-alkanes, cycloalkanes and aromatics. Aromatics comprise a large fraction of fossil Diesel, at about 30-35 % by weight on average. Most of these aromatics are compounds with one aromatic ring, or monoaromatics, with alkyl substitutions. Benzene itself is not present at any significant level in fossil Diesel fuel. [30] As stated in the general properties section, compared to alkanes, branched compounds exhibit lower cetane numbers (and lower melting points) as exemplified by iso-cetane or 2,2,4,4,6,8,8,-heptamethylnonane, having a cetane number of 15. Alkylaromatics and alkylcycloalkanes also possess low melting points and lower cetane numbers which increase with increasing side chain length.
The following image depicts the general composition of fossil Diesel.

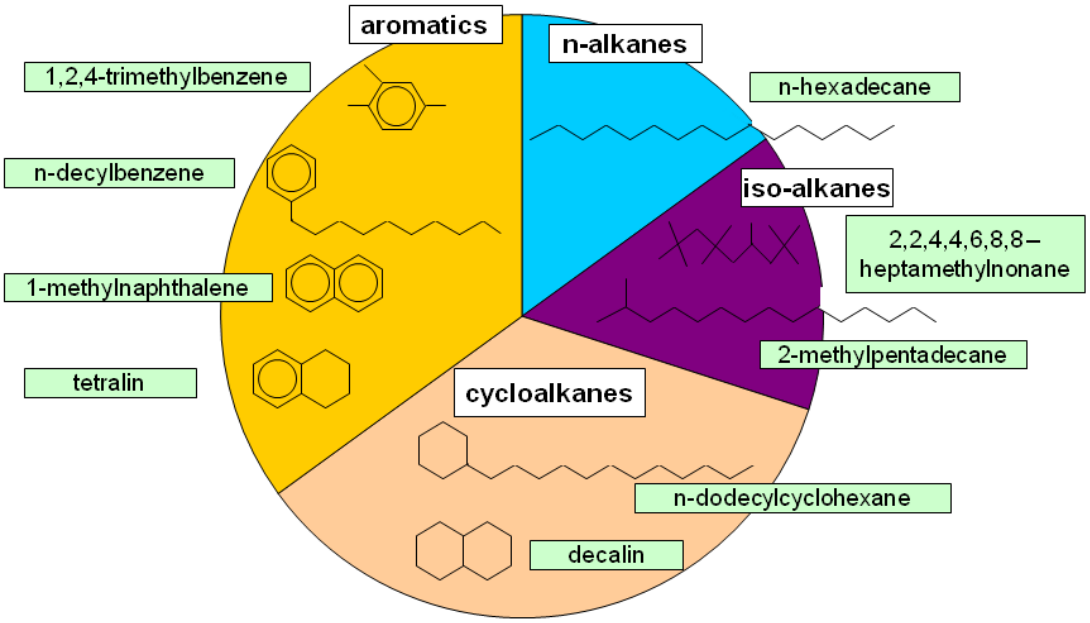

Fig. 14 Relative amounts of chemical classes present in fossil Diesel and possible representative candidates for a surrogate fuel [30]

Bio-Diesel and alternative Diesel fuels

The term Bio-Diesel defines a fuel comprised of mono-alkyl esters of long-chain fatty acids derived from vegetable oils or animal fats, designated "B100" as formulated in the Bio-Diesel standard ASTM D6751, with the European Bio-Diesel standard EN 14214 referring to fatty acid methyl esters (FAME) as fuel. Bio-Diesel is obtained by transesterifying oil or fat with alcohol and obtaining glycerol as co-product. The major components are straight chain fatty acids, the most common containing 16 and 18 carbon atoms. Minor constituents are among others intermediary mono- and diacylglycerols and residual triacylglycerols, sterols and sterol glucosides. Transesterification reduces the viscosity, ranging prior to the process in the order of 28-40 mm^2/s to 4-5 mm^2/s which is closer to that of fossil Diesel, thus reducing operational problems in Diesel engines. The cetane number of fatty esters depends on chain length and degree of unsaturation. The presence of polyunsaturated fatty esters is the cause of oxidative problems with Bio-Diesel and the presence of higher amounts of saturated fatty esters is the cause of cold flow problems.

Knothe [31] points out, that Bio-Diesel, when produced with methanol as alcohol component, contains only approximately 95% carbon atoms that are "bio". The reason is that methanol, although it can be obtained from renewable resources, is most commonly derived from non-renewable natural gas. In the case of ethyl esters, Bio-Diesel is completely "bio" as ethanol is commonly derived from renewable resources such as corn and sugarcane. However, the prefix "bio" can be applied to the observation that Bio-Diesel fuel is readily biodegradable. In any case, this definition of Bio-Diesel is generally accepted internationally. More recently, the term Bio-Diesel has sometimes been used in the compound phrase "second-generation Bio-Diesel", usually in conjunction with Bio-Diesel derived from "alternative" feedstocks such as inedible oils or algae. Knothe denotes that this marketing-slogan-like term is misleading and should not be used as it implies that Bio-Diesel derived from such feedstocks may have superior fuel properties, which is not necessarily the case. For example, Bio-Diesel derived

from jatropha contains in the range of 20-25% C16 and C18 saturated fatty acid methyl esters and thus possesses poorer cold flow properties than Bio-Diesel derived from soybean or rapeseed (canola) oil, which contain lower amounts of saturated esters. Virtually no literature reports exist on the fuel properties of algae-derived Bio-Diesel fuels. Therefore terms such as "algae-derived Bio-Diesel" or "jatropha Bio-Diesel" appear preferable. Furthermore, the phrase "second-generation Bio-Diesel" has also been applied to fossil Diesel-like fuels derived from biological feedstocks such as lipids and in this case it is even more misleading because the resulting fuel does not even meet the definition of Bio-Diesel as mono-alkyl esters. Knothe [31] makes a distinction between Bio-Diesel and "renewable" Diesel which is derived from lipid feedstocks and processed via cracking, pyrolysis or hydrodeoxygenation. Renewable Diesel is also often referred to as hydrotreated vegetable oil or HVO. Renewable Diesel resembles in its chemical composition more fossil Diesel than Bio-Diesel, being mainly a mixture of hydrocarbons compared to fatty acid alkyl esters. The following caption depicts the typical material flow for the transformation of lipid materials to fuels to products of engine combustion:

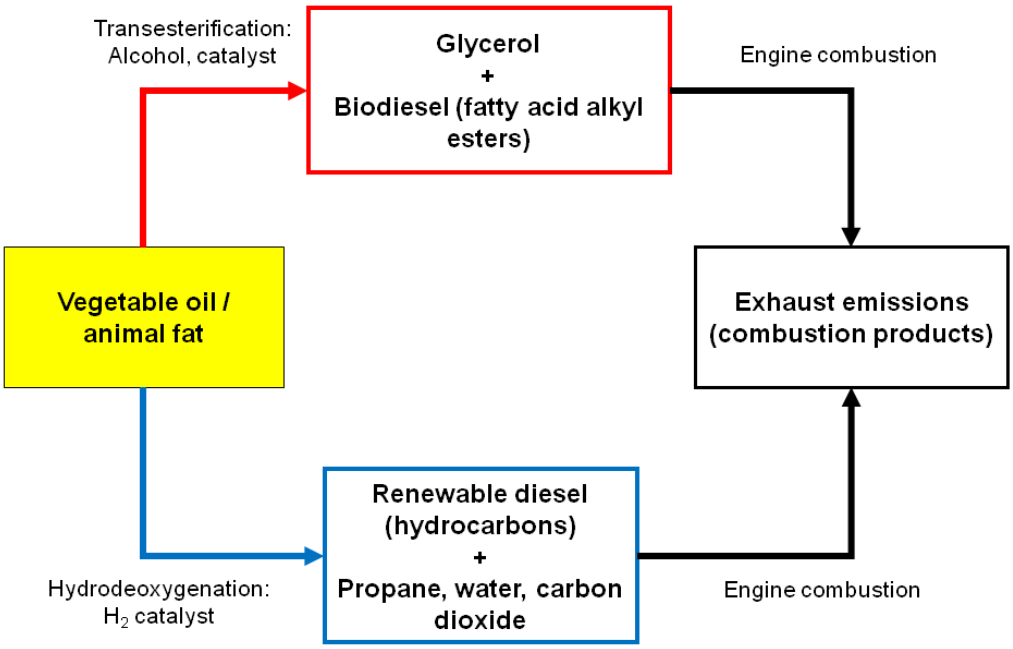

Fig. 15 – Flow chart for the transformation of lipid materials to Bio-Diesel and renewable Diesel [31]

General Properties of Diesel Fuels

The following table summarizes the general fuel properties defined according the corresponding standards for Diesel fuels:

Property	**(Fossil) Diesel EN590**	**FAME EN 14214**
Density at 15°C [kg/m^3]	820-845	860-900
Kinematic viscosity at 40°C [mm^2/s]	2,00-4,00	3,50-5,00
Flash Point [°C]	min. 55	min. 101
Lower heating value [MJ/kg]	43,05 (not specified)	37,9 (not specified)
Cetane Number	min. 51	min. 51

Distillation: Total evaporated amount [Vol%] Up to 250°C Up to 350°C Temperature 95% evaporated [°C]	 max. 65 min. 85 max. 360	N/A
Cetane Index	min. 46	N/A
Carbon residue [mass %]	max. 0,3	max. 0,3
Water content [mg/kg]	max. 200	max. 500
Sulfur content [mg/kg]	max. 10	max. 10
Ash content [mass %]	max. 0,01	max. 0,02
Total contamination [mg/kg]	max. 24	max. 24
Oxidation stability [g/m^3]	max. 25	N/A
Polyaromates [mass %]	max. 11	N/A
Cu-corrosion [corrosion category]	1	1
Lubricity HFRR [µm]	max. 460	max. 320
Filterability/CFPP [°C] 15.04.-30.09. 01.10.-15.11. 16.11.-28.02. 01.03.-14.04.	 max. 0 max. -10 max. -20 max. -10	N/A

Tab. 2 – Required fuel properties according to European/German standards [21, 29]

2.1.3. Kerosene and Aviation Fuels

Kerosene and the family of aviation fuels is a product derived directly from refinery processing of crude oil. The following image depicts the general composition of these fuels regarding the relative distribution of the different hydrocarbon classes:

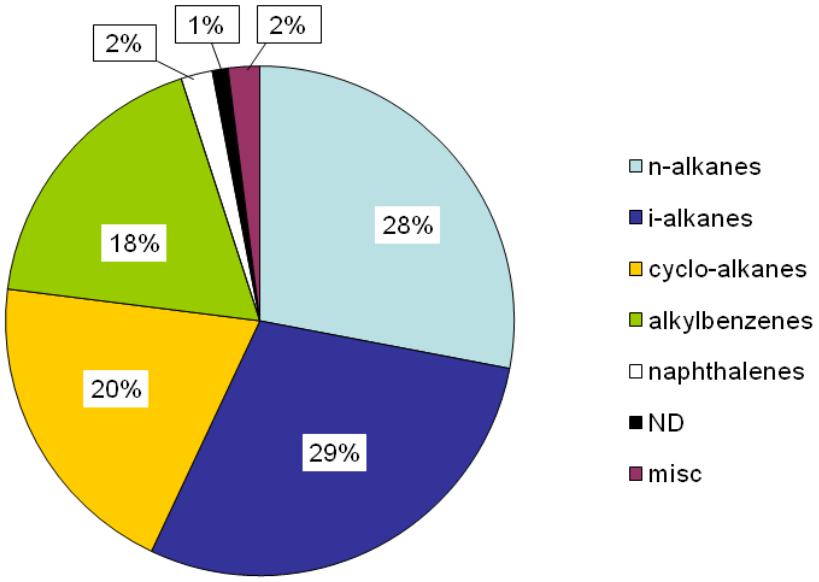

Fig. 16 – Hydrocarbon class distribution for a JET-A fuel [32]

Jet-A fuels are the commercial equivalent of the military JP-8 fuel differing only by trace amounts of additives (anti-corrosion, anti-static, anti-icing). As can be seen from the previous figure, alkanes and cycloalkanes are the predominant species in the fuel mixture, accounting almost 80% of the fuel. The near full saturation of the compounds results in high H/C ratios, which consequently implies a high energy release per unit weight. Cycloalkanes have slightly lower H/C ratios, but offer operational advantages such as lower freezing points and high volumetric energy densities. Aromatic compounds are the third largest class of compounds and are well known soot precursors. The composition of Kerosene varies, depending on the refinery process parameters, the crude oil provenience and even due to aging, the following table lists a mass spectrometer study performed by Guerét [33]:

Hydrocarbon Type	**Mass %**	**Identified components**	**Mass %**
Alkane	**78,0**		
C_8	1,1	n-octane	0,75
C_9	8,2	n-nonane	3,80
C_{10}	15,4	n-decane	4,82
C_{11}	13,6	n-undecane	4,80
C_{12}	13,7	n-dodecane	4,10
C_{13}	14,2	n-tridecane	3,10
C_{14}	7,2	n-tetradecane	1,40
C_{15}	2,1		
others	2,1		
Cycloalkane	**9,8**		
C_9	4,7	n-propylcyclohexane	1,00
C_{10}	2,5	n-butylcyclohexane	0,66
others	2,6		
Aromatic compounds	**12,2**		
C_8	0,6		
C_9	5,7	1,2,4-trimethylbenzene	2,20
C_{10}	4,5		
others	1,4		

Tab. 3 - Composition of Kerosene JET A-1 [33]

A generalized properties listing of JET A-1 (NATO Code F-35/F-34) and JP-8 (MIL-DTL-83133E) is shown in the following table:

Property	**JET A-1 /JP-8**
Approx. formula	$C_{11}H_{21}$
H/C ratio	1,91
Boiling range [°C]	205-300
Freeze point [°C]	-47
Critical temperature [°C]	410
Density at 15°C [kg/m^3]	775,0-840,0
Kinematic viscosity at 40°C [mm^2/s]	max. 8
Flash Point [°C]	min. 38
Specific Energy, Net Heat of Combustion [MJ/kg]	min. 42,80

Distillation: IBP [°C] 10% recovery [°C] 50% recovery [°C] 90% recovery [°C] FBP [°C] Distillation residue [vol%] Distillation Loss [vol%]	 N/A max. 205 N/A N/A N/A max. 300 1,5 1,5
Sulfur content [mass %]	max. 0,30
Total contamination particulates [mg/l]	max.1,0
Anti-oxidant, mandatory [mg/l]	17,0-24,0
Aromatics [vol %]	max. 25
Cu-corrosion [corrosion category]	1

Tab. 4 – Properties of and JET A-1, JP-8 fuels [32, 34]

2.1.4. Second-Generation Biofuels and the Fischer-Tropsch Process

As stated in the introductory section, second-generation biofuels are produced from cellulose, hemicellulose or lignin. Two main conversion routes exist:

- **Biochemical conversion route:** This process is based on enzymatic-hydrolysis of the lignocellulosic material or enzymatic break down of the cellulosic material into sugars. In the second step of the process, sugars are fermented to alcohol and distilled to ethanol.
- **Thermo-chemical conversion route:** Through gasification of the feedstock under high temperature a synthesis gas ($CO + H_2$) is obtained. This is then processed or reformed into different types of liquid or gaseous fuel (e.g. BTL-Diesel, Bio-SNG)

An overview of the different conversion routes and producible fuels is given in the following table:

Biofuel Type	**Specific Biofuel**	**Production Process**
Bioethanol	Cellulosic ethanol	Advanced enzymatic hydrolysis and fermentation
Synthetic fuels	Biomass-to-liquids (BTL) Fischer-Tropsch (FT) Diesel Biomethanol Heavier alcohols (Butanol and mixed) Dimethyl-ether (DME)	Gasification and synthesis
Methane	Bio-synthetic natural gas (SNG)	Gasification and synthesis
Bio-hydrogen	Hydrogen	Gasification and synthesis or biological processes

Tab. 5 – Classification of second-generation biofuels from lignocellulosic feedstocks [4, 6]

At present, no clear commercial or technical advantage between these two conversion paths has been shown. Both sets of technology remain unproven at a fully commercial scale, and are under continual development and evaluation and have significant technical and environmental barriers yet to overcome. Both processes can potentially convert 1 dry ton of biomass (~20 GJ/t) to around 6,5 GJ/t of energy carrier in the form of biofuels, giving an overall biomass to biofuel conversion efficiency of roughly 32,5% [6]. Overall efficiencies can be improved when surplus heat, power and co-product generation are included in the total system.

The Fischer-Tropsch Process

This process was developed in 1923 by Franz Fischer and Hans Tropsch. During World War II, 600000 t/year of liquid fuels were produced from coal in Germany. After WWII cheap crude oil made coal-to liquids or CTL-fuels uneconomic. Due to UN sanctions and with no available source of petroleum for fuel production, South Africa built three CTL SASOL plants in the 1980s using the FT process to convert coal to gasoline and Diesel. They are still operational. Shell Oil has been operating a commercial FT-Diesel plant called the "Shell Middle Distillate Synthesis" plant in Bintulu, Malaysia since 1993. Natural gas is used as a feedstock to produce primarily low-sulphur Diesel and food-grade wax. Currently the FT-process is used, as shown in the following figure, to create a range of liquid fuels suitable for aviation and marine applications, but primarily synthetic Diesel. The research and development activities of this technology have increased greatly in the last decade. An extensive overview of these activities can be found in a report by Sims et al. [6].

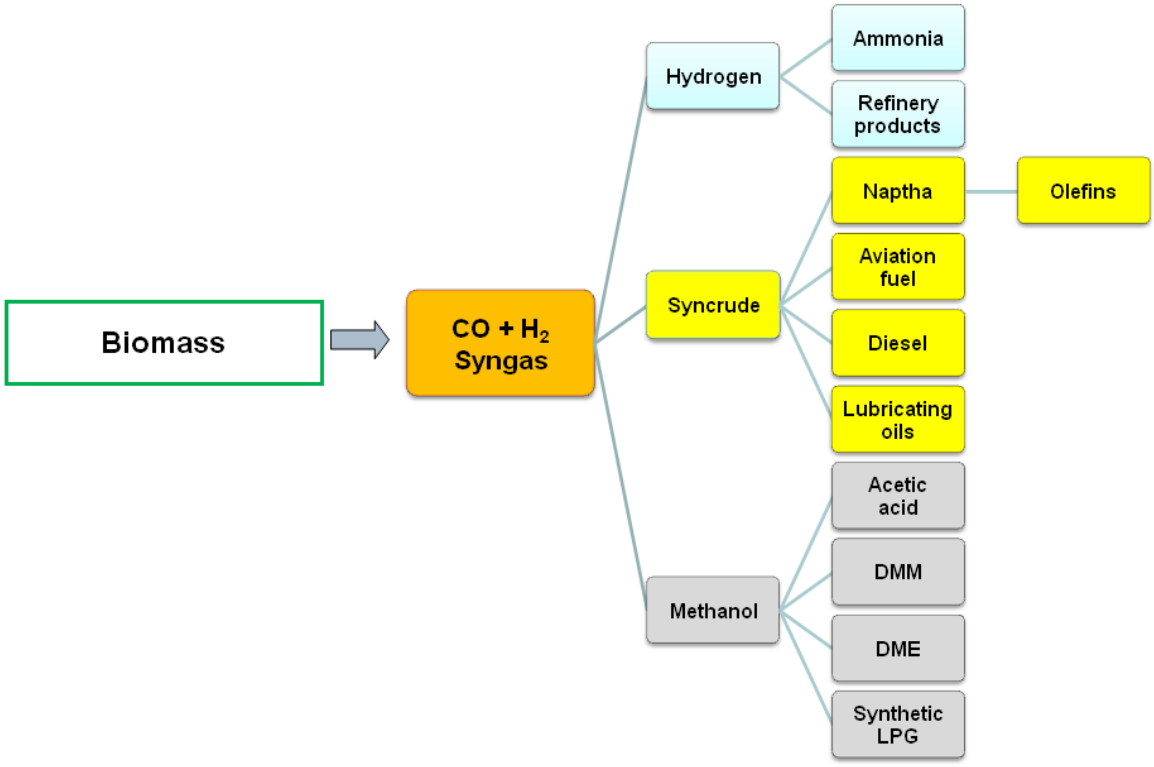

Fig. 17 – Example for fuels and chemicals obtainable with the Fischer-Tropsch process derived from biomass as a feedstock [6]

The Fischer-Tropsch process is a catalyzed chemical reaction in which carbon monoxide and hydrogen are produced from the gasification of a solid feedstock such as coal or woody biomass into a range of liquid hydrocarbons. Typical transition metal catalysts are based on iron and cobalt.

Eq. 10

$$(2n+1)H_2 + nCO \rightarrow C_nH_{(2n+2)} + nH_2O$$

The dry lignocellulosic biomass feedstock is initially subjected to a severe heat treatment in the presence of a controlled amount of air (or oxygen) so that gasification takes place to produce synthesis gas. The gasification occurs in a reactor at 700-1500 °C (typically around 850 °C). There are three main types of gasifiers: Fixed bed, fluidized bed and entrained flow. The syngas consists of a mix of mainly CO and H_2 with some CO_2, CH_4 and higher carbon compounds. The raw syngas is then cleaned before the catalysis in order to remove inhibitory substances that could inactivate the catalyst. Volatile tars as well as sulphur, nitrogen and chlorine compounds are removed. The FT-process is generally divided into two types of synthesis: The high temperature synthesis leads to the production of synthetic gasoline and chemical precursors and the low temperature synthesis leads to the production of waxy products that can be cracked in order to produce synthetic naphtha, Kerosene or Diesel fuel. The FT-process occurs in a reactor and four basic designs are currently in use and in study: Fixed-bed tubular, high-temperature circulating fluidized-bed, fixed fluidized bed SASOL advanced Synthol and the low-temperature slurry reactor. The following figures depict the thermo-chemical conversion processes to produce syngas from biomass feedstock and synthetic fuels from syngas:

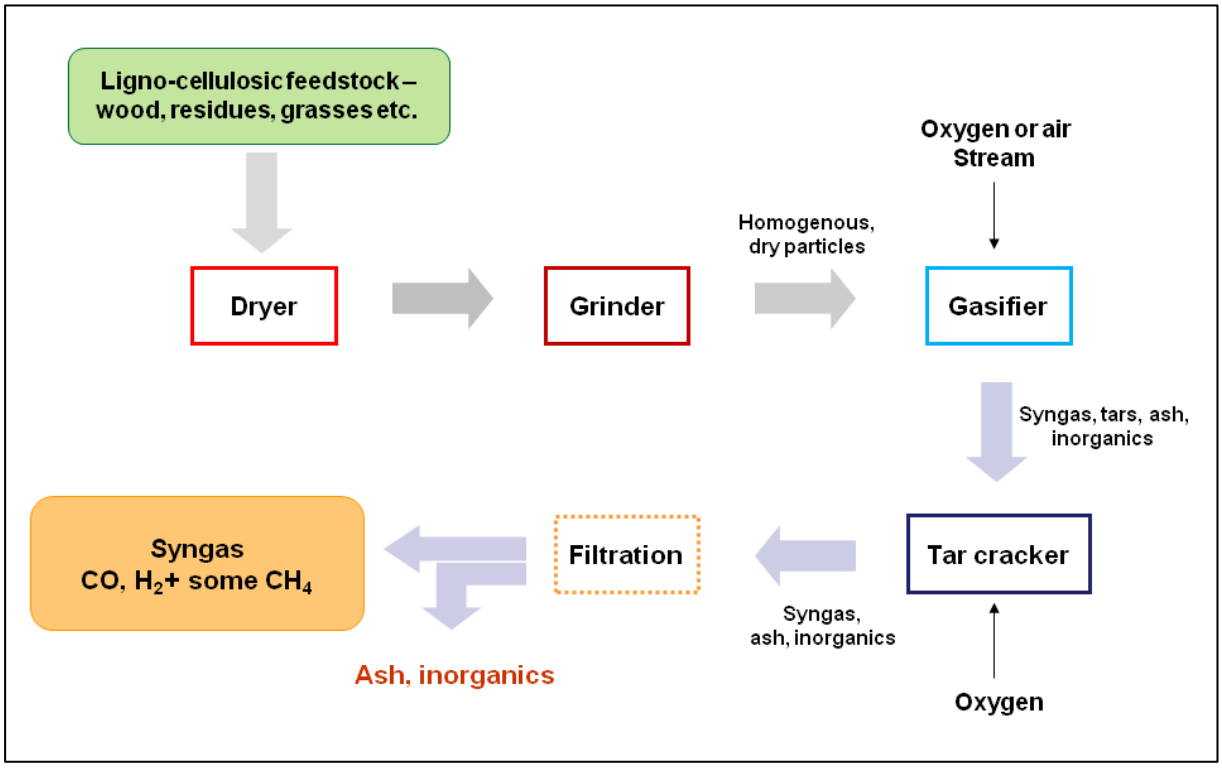

Fig. 18 – Thermo-chemical conversion process for the production of syngas [6]

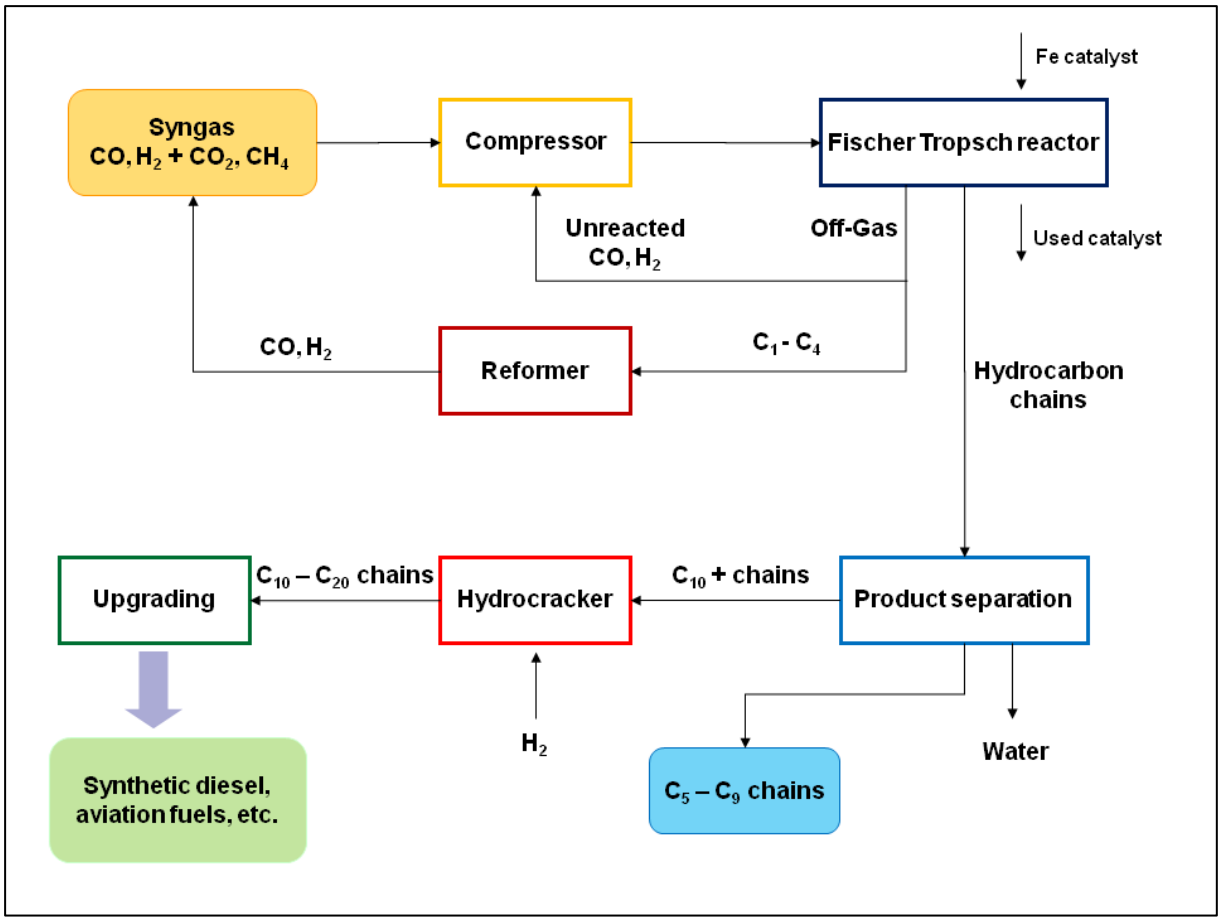

Fig. 19 – Fischer-Tropsch synthesis and conversion of syngas into synthetic fuels [6]

General Properties of Synthetic Diesel/GTL-Diesel

There is no detailed chemical analysis of FT-Diesel available in literature. No permission to perform one was provided by the producers/providers of the fuel sample for this study either. The only detail that is available is that there are no aromatic compounds present in the FT-fuel in contrast to the general composition of the mineral variant. The following table compares the general properties of fossil (mineral) Diesel and GTL-Diesel:

Property	Diesel EN 590	GTL-Diesel
Density at 15°C [kg/m^3]	835	778
Kinematic viscosity at 40°C [mm^2/s]	2,65	2,56
Flash Point [°C]	62	87
Lower heating value [MJ/kg]	43,05	44,3
Carbon residue [mass %]	< 0,01	< 0,01
Water content [mg/kg]	60	39
Sulfur content [mg/kg]	10,1	< 1
C mass fraction [% kg/kg]	85,2	83,6
H mass fraction [% kg/kg]	14,8	16,4
O mass fraction [% kg/kg]	0	0
H/C (molar)	2,07	2,34
Cetane index	52	79

Tab. 6 – Properties of fossil Diesel and GTL-Diesel [29]

General Properties of Synthetic Kerosene/GTL-Kerosene

The following table lists the fuel composition data provided by the fuel sample supplier:

Hydrocarbon Type	CAS Number	Proportion
Alkanes, C_{8-15}, branched and linear	172343-38-3	99-100%

Tab. 7 - Composition of GTL-Kerosene, provided by Shell Co. [35]

Some data found in literature concerning the general composition and physical properties of GTL-Kerosene is shown in the following table:

Hydrocarbon type	Identified components	Proportion
n-Alkanes	C_{9-15}	13,021%
Iso-alkanes	C_{8-16}	38,214%
Cyclo-alkanes	C_8	0,965%

Tab. 8 – Composition of Synthetic Jet-Fuel, similar to GTL-Kerosene, adapted from [36]

A comparison of the general properties of mineral Kerosene fuel from type JET A-1 and GTL-Kerosene is given in the following table:

Property	Kerosene JET A-1	GTL-Kerosene
Density at RT [kg/m^3]	775-825	736
Flash Point [K]	311	approx. 313
Initial Boiling Point [K]	N/A	approx. 423
Final Boiling Point [K]	573	approx. 473
Autoignition Temperature [K]	483	approx. 505

Tab. 9 - Properties of Kerosene JET A-1 and GTL-Kerosene [34, 35]

2.1.5. Surrogate Fuels, Selection Criteria and Determination Methods

Model or surrogate fuels are, regarding their composition, simplified fuels that are intended to represent and match a desired behavior and certain characteristics of a more complex fuel, such as conventional Diesel or Kerosene. The behavior of multi-component fuels is more complex than the behavior of single component fuels because species produced from one component can react with species from another component. Surrogate fuels allow numerical simulations to be conducted in a timely manner due to the reduced amount of chemical reactions and physical interactions of the species involved. Fuels derived from conventional petroleum sources are composed of hundreds of chemical compounds. The development of numerical models that represent all these components is prohibitive due to the sheer size of such a model which renders it impractical for current computational resources. Also fundamental data for most species, such as chemical kinetic rate constants, reaction paths, thermodynamic parameters, is not available. Generally, depending on the targeted characteristics, a surrogate fuel should not only properly reproduce combustion characteristics of the fuel, but also injection, vaporization and mixing behavior. For determining an appropriate component for a surrogate fuel, certain relevant chemical and physical characteristics should be fulfilled. Relevant chemical characteristics may include among others, ignition behavior, molecular structure, adiabatic flame temperature, C/H/O content and sooting propensity. Relevant physical characteristics may include volatility parameters, density, viscosity, surface tension and diffusion behavior.

Surrogate fuels can be used, besides for validating numerical models, as standardized fuels for further investigations. Conventional fossil fuels differ in their composition over time, complicating the reproducibility of experimental data. Standardized surrogate fuels allow direct comparison of data sets gained in different studies where different experimental devices or analysis techniques have been used.

Selection Criteria and Formulation Procedure

A surrogate or model fuel has to fulfill the following requirements:

- **Similarity:** The surrogate fuel is required to match the targeted physical and chemical properties of the original fuel.
- **Feasibility:** After the determination (or estimation) of the chemical composition and the different chemical classes contained in the original fuel, the candidates in the surrogate formula must have known detailed kinetic mechanisms.
- **Simplicity:** Quantity of components has to be reduced as much as possible in order to be computable.
- **Cost and availability:** The compounds have to be obtainable at a reasonable cost and be readily available.

The development of a surrogate fuel is a lengthy process. A generalized procedure for the selection of compounds for the formulation of a surrogate fuel can be defined as follows:

1. A chemical analysis is performed to identify the chemical composition of the fuel. This analysis can be conducted using gas chromatography and mass spectrometry (GCMS).
2. From this analysis, a list of representative fluids of the various chemical families is constructed including for example: branched or straight-chain alkanes, alkenes, aromatics, etc. Also the information on C/H ratio of the fluids found in the sample is gained. This ratio affects properties such as flame temperature, heat of reaction and flame speed.
3. Chemical kinetic models for each of the pure compounds in the surrogate fuel must be developed and validated by comparison to experimental data.
4. A testing procedure for identification of the best relative concentration of each component in the surrogate that reproduces the properties of the target fuel is performed. The chemical kinetic mechanisms of the individual components need to be combined. These must include important cross reactions between mechanisms.
5. The surrogate fuel model has to be reduced in size so that it can be used in multi-dimensional CFD models for simulating engine combustion.
6. Finally, the surrogate fuel model is validated by comparison with surrogate- and target fuel experiments in practical combustion devices of interest.

The following figure depicts the iterative formulation process of a surrogate fuel:

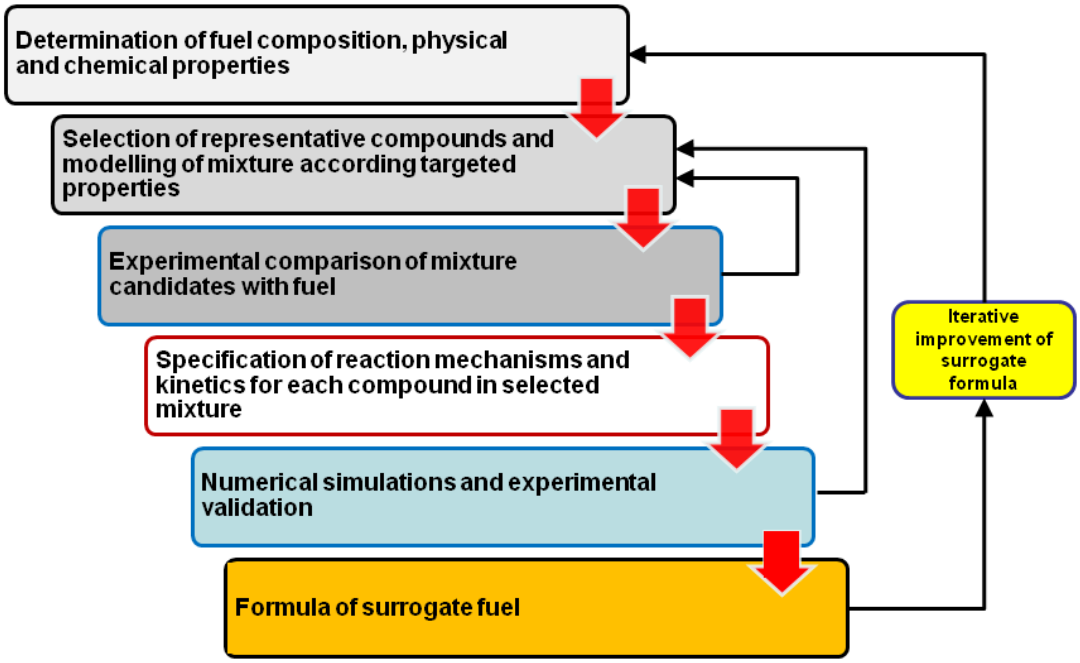

Fig. 20 – Selection procedure for surrogate fuel formulation

Additionally, as stated by Huber et al. [36, 37], physical property models need to be developed for surrogate fuel components and their mixtures. These include models for density, volatility, surface tension, viscosity, thermal conductivity and species transport of the components and their mixtures. Measurements of these properties are also needed for validation of the model. These properties are needed to predict properly the fuel spray break-up, the species transport that determines the reacting mixture temperature and the concentration fields of the species.

Huber [36] describes exemplarily this procedure for the formulation of a surrogate fuel that fulfills selected physical properties. Based on the aforementioned chemical analysis, a list of the possible candidate compounds for the surrogate fuel is obtained. For each chemical family at least a representative compound should be chosen. An important criterion for the selection is the availability of reliable experimental data concerning the physical properties of the compound. For each of the possible pure fluid constituents of the surrogate fuel, an equation of state, viscosity and thermal conductivity are needed. If this information is not available in literature, it must be developed from available experimental data or predictive methods. The equation of state is formulated in terms of the molar Helmholtz free energy as a function of density and temperature [38, 39]:

Eq. 11

$$a(\rho,T) = a^0(\rho,T) + a^r(\rho,T)$$

Where a is the molar Helmholtz energy, $a^0(\rho,T)$ is the ideal gas contribution to the molar Helmholtz energy, $a^r(\rho,T)$ is the real fluid molar Helmholtz energy that results from intermolecular forces. All thermodynamic properties can be calculated as derivatives of the Helmholtz energy.
To represent the properties of a mixture, mixture models are used that incorporate the pure fluid equations for both thermodynamic and transport properties. For the mixture model, according to Huber et al. [36-38, 40], the basic idea is to represent the molar Helmholtz

energy a of a mixture as the sum of an ideal contribution a^{id} and an excess contribution a^{excess}, according to:

Eq. 12

$$a = a^{id} + a^{excess}$$

Details on this model can be found in the previously mentioned references.

The fluids in the surrogate mixture and their compositions are found by a multi-property regression to determine the composition that minimizes the difference between predicted and experimental thermophysical property data for the sample of the target fuel. The process incorporates data, e.g., for density, speed of sound, viscosity, thermal conductivity, and volatility (i.e., the distillation curve). The cetane number of the mixture, estimated e.g. by a linear volume fraction mixing rule, can be used to predict roughly the ignition quality of the intended surrogate fuel. The following exemplary equation is the objective function with a weighted sum of the squared percentage differences between the experiment data and the predicted values estimated from the previous mentioned equations.

Eq. 13

$$F = \sum_{i=1}^{N_{dis}} W_{i,dis} F_{i,dis}^2 + \sum_{i=1}^{N_\rho} W_{i,\rho} F_{i,\rho}^2 + \sum_{i=1}^{N_\lambda} W_{i,\lambda} F_{i,\lambda}^2 + \sum_{i=1}^{N_\eta} W_{i,\eta} F_{i,\eta}^2 + W_{CN} F_{CN}^2$$

The objective function is denoted by F, the weights for each data point are denoted by W_i, the subscripts $dis, \rho, \lambda, \eta, CN$ refer to target properties (distillation, density, thermal conductivity, viscosity and cetane number). This equation can be extended to include other target properties if desired. The weighting factors for each type of property data are found by trial and error based on the desired results. The objective function components are defined as the percentage deviations between the calculated value and the experimental value for each type, as follows.

Eq. 14

$$F_{dis} = 100 \times (T_{calc} - T_{exp})/T_{exp}$$

Eq. 15

$$F_\rho = 100 \times (\rho_{calc} - \rho_{exp})/\rho_{exp}$$

Eq. 16

$$F_\lambda = 100 \times (\lambda_{calc} - \lambda_{exp})/\lambda_{exp}$$

Eq. 17

$$F_\eta = 100 \times (\eta_{calc} - \eta_{exp})/\eta_{exp}$$

Eq. 18

$$F_{CN} = 100 \times (CN_{calc} - CN_{exp})/CN_{exp}$$

Thus, the resultant surrogate mixture composition can be used to model the thermophysical properties of the target fuel.

Summary of surrogate fuels found in literature

The following tables are not intended to be exhaustive summaries of all surrogate fuels conceived and developed, rather its intention is to list surrogate fuels currently used and discussed in literature.

Denomination	Composition	Intended Use (Representation)
Lemaire et al. [41] (IDEA surrogate)	n-decane-70% 1-methylnaphthalene-30%	Representation of Sooting behavior of Diesel
Kook and Pickett [42, 43]	n-dodecane-77% m-xylene-23%	Combustion behavior Diesel (machine like conditions)
Natelson et al. Mix 2 [44]	n-decane-33% n-butylbenzene-33% n-butylcyclohexane-33%	Representation of Diesel
Douce et al. and Mathieu et al. [45, 46]	n- propylcyclohexane-39% n-butylbenzene-28% 2,2,4,4,6,8,8-heptamethylnonane-33%	Representation of sooting behavior of Diesel
Mati et al. [47]	n-hexadecane-23,5% iso-octane-19% n-propylcyclohexane-26,9% n-propylbenzene-22,9% 1-methylnaphthalene-7,7%	Representation of Diesel and validation of a kinetic model
Pera et al. (among others) [48]	n-heptane	Representation of Diesel, validation of kinetic model
Ra and Reitz [49]	Toluene-15% n-decane-14% n-dodecane-23% n-tetradecane-24% n-hexadecane-13% n-octadecane-11%	Representation of fossil Diesel for evaporation studies of single droplets and sprays
Eigenbrod et al. [50, 51]	n-tetradecane-50% 1-methylnaphthalene-50%	Representation of autoignition behavior of Diesel

Tab. 10 - Summary of Diesel Surrogate Fuels

Denomination	Composition	Intended Use (Representation)
Honnet et al. [52] (Aachen surrogate)	n-decane-80% 1,2,4-trimethylbenzene-20%	Representation of JP-8 (Kerosene)
Natelson et al. Mix 1 [44]	n-decane-50% n-butylbenzene-25% n-butylcyclohexane-25%	Representation of JP-8 with max. allowed aromatic content
Steil et al. [53]	n-decane-70% propylbenzene-30%	Representation of Kerosene
Huber et al. [48]	n- nonane 2,6-dimethyloctane 3-methyldecane n-tridecane n-tetradecane n-pentadecane n-hexadecane	Representation of Fischer-Tropsch-S8 fuel based on Advanced Distillation Curve (ADC) method
Vovelle et al. [48]	normal- and iso-alkanes 79% cyclo-alkanes 10% aromatics 11%	Representation of Kerosene
Kyne et al. [48]	n-decane -89% toluene-11%	Representation of Kerosene
Ranzi et al. [48]	n-dodecane-73,5% iso-octane-5,5% methyl-cyclohexane-10% toluene-10% benzene-1%	Representation of Kerosene

Violi et al. [32] Sur_1	m-xylene-15% iso-octane-10% methylcyclohexane-20% n-dodecane-30% n-tetradecane-20% tetralin-5%	Representation of JET A-1 and JP-8
Violi et al. [32] Sur_2	xylenes-8.5% n-octane-3,5% decalin-35% n-dodecane-40% n-hexadecane-20% tetralin-8% toluene-20%	Representation of JET A-1 and JP-8
Violi et al. [32] Sur_3	methylcyclohexane-10% toluene-10% benzene-1% isooctane-5,5% n-dodecane-73,5%	Representation of JET A-1 and JP-8
Schulz [54]	iso-octane-5,7% methylcyclohexane-5,1% m-xylene-4,5% cyclooctane-4,7% trimethylbenzol-4,4% n-decane-16,2% butylbenzene-4,6% tetralin-4,1% n-dodecane-21% MNL-3,9% n-tetradecane-15,6% n-hexadecane-10,2%	Representation of JET A-1 and JP-8
Eigenbrod et al. [20]	n-decane-60% 1,2,4-trimethylbenzene-40%	Representation of autoignition behavior of JET A-1

Tab. 11 - Summary of Kerosene Surrogate Fuels

Selection Procedure for Surrogate Fuels for GTL-Diesel and GTL-Kerosene

The selection procedure for the formulation of a surrogate fuel presented before is in principle directly applicable to the objectives of this study. The fuel sample provider has not given the permission to perform a chemical analysis of the fuel samples, therefore the selection procedure had to be changed and adapted. Many of the required inputs, such as the composition of the fuel have to be inferred or deducted from literature. As pointed out before, the basic information about the chemical composition of the GTL-fuels that is available is the absence of aromatic compounds. Other general information concerning the composition of GTL-fuels is based on the available information on their mineral (fossil) counterparts.
As stated by Pitz and Mueller [30] and described in sections 2.1.2 and 2.1.3, the primary chemical classes of the components in petroleum-based Diesel fuel are n-alkanes, iso-alkanes, cycloalkanes and aromatics. Although the composition of petroleum-based Diesel fuel is highly variable, there are some trends: The carbon numbers of the components range from approximately C_{10} to C_{22}. An average carbon number is 14 or 15. The iso-alkanes are usually lightly branched with one or two side methyl groups. The cycloalkanes typically have one ring with multiple alkyl side chains. There are some two-ring cycloalkanes with alkyl side chains as well. The aromatics are usually one ring with multiple side chains. The average carbon number of the aromatics is about C_{12}. This carbon number is lower than the other

chemical classes. There are also some two-ring aromatics with alkyl side chains. Similarly for mineral Kerosene the average carbon number is C_{10}.

The adapted selection procedure is as follows:

- An n-alkane is chosen as the base component for the surrogate fuel. Usually n-alkanes have higher CN than the target fuel; therefore the additive has to have a lower CN in order to decrease the CN of the surrogate mixture.
- The additive(s) must belong to a chemical family present in the target fuel.
- In order to be able to delay the ignition and thus reduce the CN of the mixture, the additive(s) must have higher volatility than the chosen n-alkane(s). For this the additive must possess a lower boiling temperature and higher vapor pressures.
- The formulation of the surrogate mixture is obtained experimentally.

The following tables summarize the general properties of the candidate n-alkanes and additives obtained by the selection procedure. The additives belong to the chemical families present in the target fuel, such as iso- and cyclo-alkanes.

Property	**n-decane**	**n-dodecane**	**n-tetradecane**	**n-hexadecane**
Formula	$C_{10}H_{22}$	$C_{12}H_{26}$	$C_{14}H_{30}$	$C_{16}H_{34}$
CAS-Nr.	124-18-5	112-40-3	629-59-4	544-76-3
Molecular Weight [g/mol]	142,29	170,34	198,4	226,45
Critical Temperature [K]	617,8	658,2	693,0	722
Critical Pressure [MPa]	2,12	1,82	1,44	1,4
Normal Boiling Point [K]	447,3	489,5	526,7	560
Liquid Density [kg/m^3]	730	748	763	773
Cetane Number	76-78	80-87,6	93-96,1	100
Antoine Constants (A/B/C)	4,07857 1501,268 -78,67	4,10549 1625,928 -92,839	4,13735 1739,623 -105,616	4,17312 1845,672 -117,054
Temperature Range [K]	367-449	399-490	428-527	463-560

Tab. 12 – Properties of n-alkanes [55-58]

Property	**2,5-Dimethyl-undecane**	**4-Propyl-decane**	**2,7-Dimethyl-4,5-Diethyl-octane**	**Bicyclohexyl**	**2,2,4,4,6,8,8-Heptamethyl-nonane**
Formula	$C_{13}H_{28}$	$C_{13}H_{28}$	$C_{14}H_{30}$	$C_{12}H_{22}$	C16H34
CAS-Nr.	17301-22-3	17312-61-2	500020-62-2	92-51-3	4390-04-9
Molecular Weight [g/mol]	186,36	184,36	198,39	166,31	226,44
Critical Temperature [K]	660,29	671,76	662,36	N/A	692
Critical Pressure [MPa]	1,75	1,753	1,673	N/A	1,57
Normal Boiling Point [K]	491,9	491,4	501,4	512	513,2
Liquid Density [kg/m^3]	755	757	760	887	793
Flash Point [K]	425	339	363	365	368
Cetane Number	58	39	39	47,4-53	15
Antoine Constants (A/B/C) Temperature Range [K]	9,098665 1605,1827 -103,53634 N/A	8,954022 1545,0333 -108,58657 N/A	9,217121 1693,7246 -100,73257 N/A	5,81921 1561,913 -101,351 424-577	6,01063 1715,365 -91,156 423-546

Tab. 13 – Properties of additives for Diesel surrogate fuels [55, 56, 58-60]

Property	Propylcyclohexane	Cyclooctane	1,3,5-Trimethyl-cyclohexane	2,2-Dimethyloctane
Formula	C_9H_{18}	C_8H_{16}	C_9H_{18}	$C_{10}H_{22}$
CAS-Nr.	1678-92-8	292-64-8	1839-63-0	15869-87-1
Molecular weight [g/mol]	126,24	112,21	126,24	142,28
Normal boiling point [K]	428	424,5	413,7	429
Critical Temperature [K]	N/A	647,2	N/A	N/A
Critical Pressure [MPa]	N/A	3,56	N/A	N/A
Liquid density [kg/m^3]	793	840	770	734
Flash Point [K]	308	303	292	313
Cetane Number	52	22	31	58
Antoine Constants (A/B/C) Temperature Range [K]	6,01632 1463,39 -64,985 321-459	5,98125 1434,67 -63,438 424-647	8,954022 1545,0333 -108,58657 N/A	6,03107 1439,6 -72,45 324-458

Tab. 14 - Properties of additives for kerosene model fuels [58, 61-63]

The vapor pressure behavior has been estimated using the Antoine equation:

Eq. 19

$$p = 10^{A-\frac{B}{C+T}}$$

Where p is the vapor pressure, T is temperature and A, B and C are component specific constants. The following figure depicts the vapor pressures of the candidate compounds.

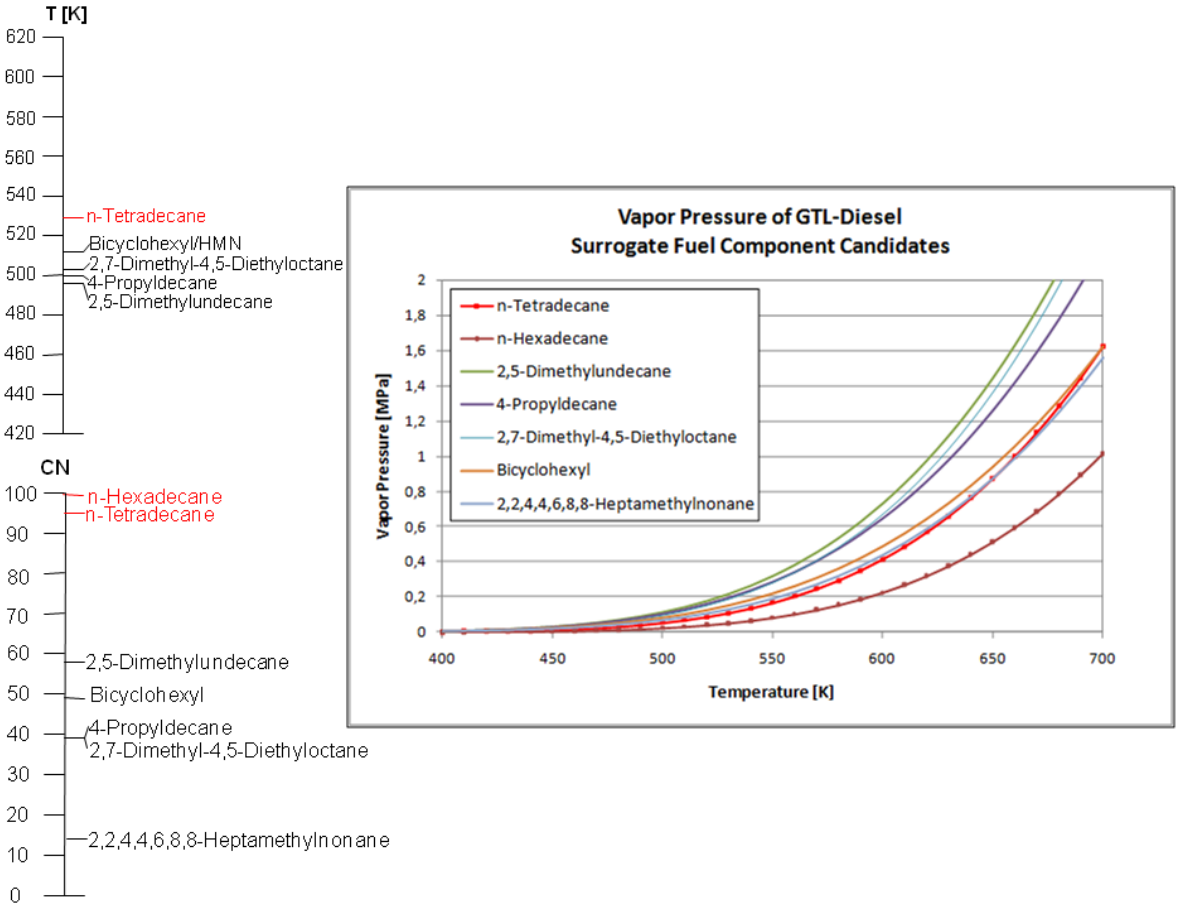

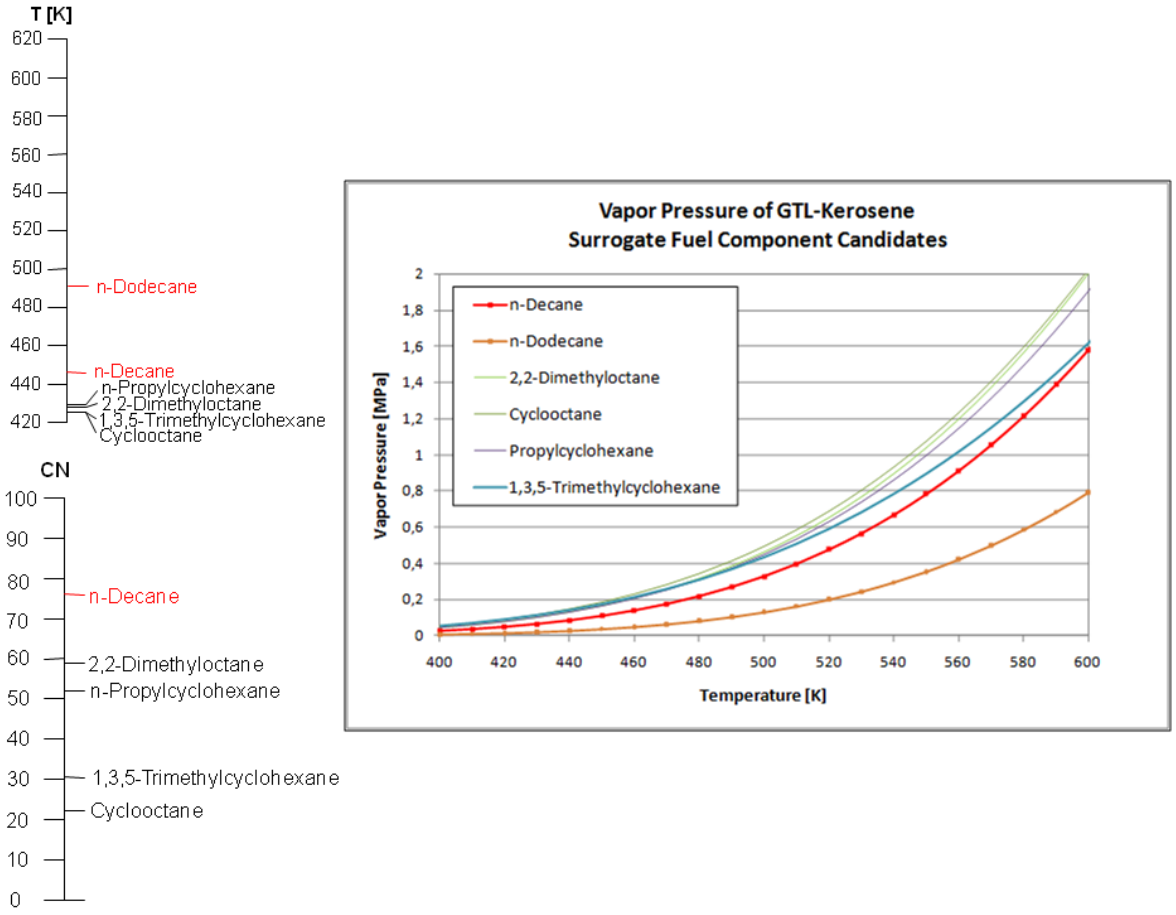

Fig. 21 –Vapor pressures, boiling temperatures and Cetane numbers of the candidate compounds for surrogate fuels

The compound specific constants for the Antoine equation are mainly valid for specified temperature ranges. Nonetheless it provides a general tendency of the evaporation behavior of a compound and therefore is applicable for selecting candidates for a surrogate fuel.

As can be seen from the previous diagram and the tabulated data, the selected candidate n-alkanes and additives (iso- and cycloalkanes) fulfill the requirements of the adapted selection procedure. The formulation of the surrogate fuel is obtained experimentally and the results of this work are presented in section 3.5.4 for GTL-Diesel and section 3.6.4 for GTL-Kerosene.

2.2. Single Droplet Autoignition Phenomenology

Liquid fuels are used in many technical devices, such as compression engines, gas turbines and aircraft engines, in form of sprays. In combustion science, sprays are often modeled as an ensemble of single droplets, in many cases, monodisperse and equidistant. In this chapter, general aspects of the autoignition of the primary unit of a spray, namely the single droplet, are reviewed.

2.2.1. Staged Ignition of a Single Fuel Droplet

The focus of combustion science is often rooted in studies between the interaction of fuel and oxidizer in the gas phase. However, many technical combustion processes and devices use

fuels starting as liquids which then react with a gaseous oxidizer. The study of these processes has to therefore include the analysis of the role of a phase change and a phase boundary. The general phenomena of single droplet combustion can be divided in three main phases [64]:

- **Heating Phase:** As soon as the droplet is exposed to hot ambient air, heat transfer from the gas phase causes the droplet surface to heat up. Much of the energy is conducted into the droplet until the entire droplet approaches boiling temperature. Within the droplet, heat conduction to the interior raises its centre temperature. Significant loss of droplet mass commences.

- **Fuel Evaporation Stage:** Fuel evaporates into the gas phase and a combustible mixture is formed, the square of the droplet diameter decreases in time (d^2-law). This law stems from the droplet temperature reaching a steady state where heat conduction to the droplet is balanced by evaporation of liquid at the droplet surface. This temporary balance leads to a constant evaporation rate.

- **Combustion Phase:** The mixture ignites and burns as a spherically symmetric laminar non-premixed flame. Ignition in the gas phase occurs after an induction time (ignition delay time). The flame leads to an augmented heating of the droplet, thus increasing the evaporation rate. The droplet diameter decreases in time by a different d^2-law.

Ignition is defined by [64] as the time-dependent process of starting with reactants and evolving in time towards a steadily burning flame.

Autoignition occurs when the temperature is high enough and when evaporation has locally sustained a combustible mixture for a time that allows a gas phase explosion to commence.

Autoignition Chemistry

A simplified and basic chemical model describes autoignition as a free-radical reaction comprising four basic steps [27]:

- **Initiation Step:** This step involves usually the reaction of the fuel with oxygen and the creation of radicals.
- **Propagation Step:** In this step radicals are converted into other type of radicals. In this case, usually peroxy radicals into hydroperoxides.
- **Branching Step:** This step involves the creation of an excess of radicals and the decomposition of hydroperoxides.
- **Termination Step:** In this step free radicals are converted into non radical products.

The balance of these four steps controls the autoignition of the fuel. A general schematic of such a free radical reaction network is as follows:

Eq. 20 - Initiation

$$RH + O_2 \xrightarrow{k_i} R^* + HO_2^*$$

Eq. 21 - Propagation

$$k_{p1}, k_{p2} \qquad \begin{cases} R^* + O_2 \rightarrow RO_2^* \\ RO_2^* + RH \rightarrow ROOH + R^* \end{cases}$$

Eq. 22 - Branching

$$ROOH \overset{k_b}{\rightarrow} RO^* + HO^*$$

Eq. 23 - Termination

$$k_t \qquad \begin{cases} 2R^* \rightarrow Products \\ 2RO_2^* \rightarrow Products \\ R^* + RO_2^* \rightarrow Products \end{cases}$$

Assuming that $\boldsymbol{X}$ is the sum of all free radicals in the system, the evolution equation for $\boldsymbol{X}$ yields:

Eq. 24

$$\frac{d\boldsymbol{X}}{dt} = r_i + k_b\boldsymbol{X} - k_t\boldsymbol{X}$$

Where r_i is the rate of initiation and k_b and k_t are the first order branching and termination rate constants. Furthermore it is assumed that the rate of initiation r_i is constant with time, which is true for early stages of the reaction, but may not hold true for long times. The propagation step is not included in this balance as it merely converts one radical into another thereby maintaining the same net $\boldsymbol{X}$. For the initial conditions $t = 0, \boldsymbol{X} = 0$ the previous equation has two solutions, depending on the rate constants k_b and k_t. If $k_t \geq k_b$, or the termination rate is faster than the branching rate, then the solution is:

Eq. 25

$$\boldsymbol{X} = \left(\frac{r_i}{k_t - k_b}\right)(1 - exp(k_t - k_b)t)$$

This solution converges to a steady state concentration of free radicals $\boldsymbol{X}^0 = r_i/(k_t - k_b)$. In the reversed case, where $k_b \geq k_t$, the solution is:

Eq. 26

$$\boldsymbol{X} = \left(\frac{r_i}{k_b - k_t}\right)(exp(k_b - k_t)t - 1)$$

No steady state is possible as $\boldsymbol{X}$ keeps building up exponentially with time. This leads to a rapid increase of pressure and temperature in the system. The following figure depicts this condition. As can be seen, the ignition delay time is defined in this context as the time where the growth of $\boldsymbol{X}$ takes off, or mathematically as the time at which the rate of radical growth, $d\boldsymbol{X}/dt$ reaches some critical threshold rate.

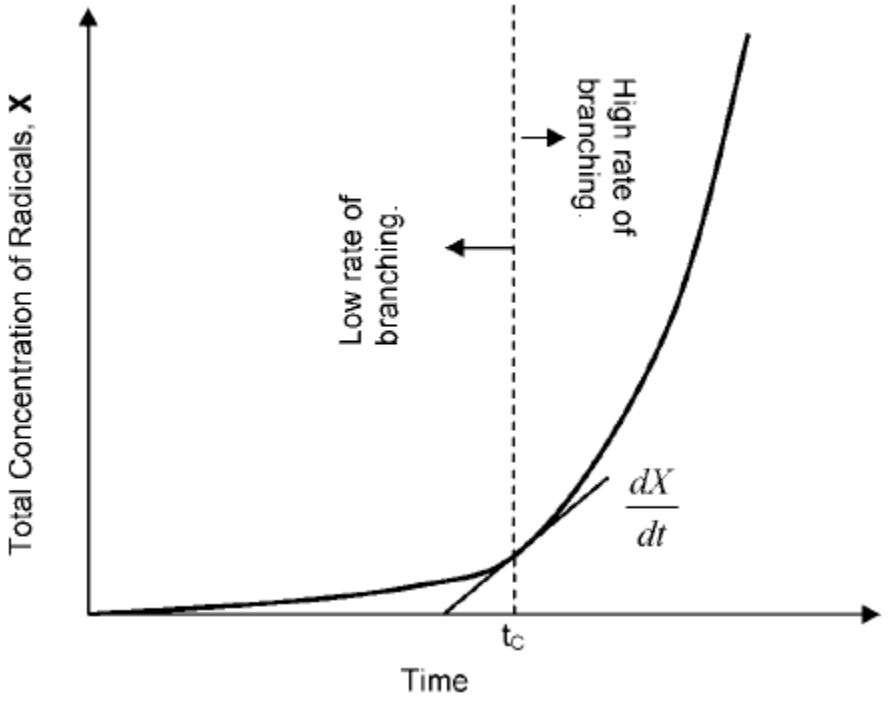

Fig. 22 – Qualitative growth of total free radicals as a function of time [27]

Cool Flames

The combustion phase described previously can show a staged behavior. This means a precursor flame occurring at lower temperatures, a so-called cool flame, can evolve and after reaching a ceiling temperature, a visible hot flame can appear. The cool flame phenomenon differs from the usual hot flame in the following: whereas in a usual flame molecules break down to small fragments and combine with oxygen producing carbon dioxide, in a cool flame, the fragments are relatively large and easily recombine with each other. Therefore, much less heat, light and carbon dioxide is released; the combustion process is often oscillatory and can sustain for a long time. A typical temperature increase upon ignition of a cool flame is a few tens °C whereas it is of the order of 1000 °C for a conventional flame.
According to Kolaitis and Founti [65], cool flames refer to the low-temperature (~500 – 800 K) oxidative chemical activity during which a hydrocarbon fuel is partially oxidized but not burnt. The dominant operating kinetic mechanisms during hydrocarbon oxidation change continuously depending on the temperature and pressure of the system. Cool flames manifest themselves in the region where transition between low-temperature and high-temperature oxidizing mechanisms occur, where both, thermal and kinetic feedback phenomena are important. A characteristic negative temperature (NTC) or zero temperature coefficient (ZTC) appears due to competition between chain-termination and chain-branching reactions. The NTC shows itself as a rising of the induction times with increasing temperature, whereas the ZTC is a region where the induction time is independent from the ambient temperature.

Ignition Delay Times

The ignition delay times of a fuel comprises a series of overlapping physical and chemical processes. The physical delay time is the time required for droplet formation, heating, vaporization, diffusion and mixing with air. The chemical delay is the time elapsed from the instant a combustible mixture has been formed until the appearance of a hot flame. It involves the kinetics of preflame reactions which result in the decomposition of high-molecular-weight

hydrocarbon species and the formation of critical concentrations of intermediate free-radical species or ignition precursors. It can be said, that the chemical processes start immediately after the introduction of fuel and air in a combustion chamber. They proceed initially at a very slow rate, where the mass of fuel vapor that undergoes chemical reaction is very small compared to the mass necessary to cause detectable pressure and temperature rise due to combustion. Therefore, the very early stages of the preignition processes are mainly dominated by the physical processes, the later stages by the chemical.
Autoignition is generally detected by measuring an (often) sudden increase in temperature, pressure, density, light emission or concentration of a tracer species, such as free radicals. Thus, the definition of the ignition delay time differs among the different authors in literature, mainly because their measuring techniques and their use of physical phenomena to indicate the end of these time periods vary. Consequently, the autoignition temperature of a fuel is not an absolute property of the substance and therefore all ignition data needs to be interpreted carefully considering the influence of the experimental apparatus and methods used.

A commonly used correlation, is an Arrhenius-type equation [66, 67]:

Eq. 27

$$\tau = \frac{A}{p^n} e^{\frac{E}{R^0 T}}$$

Where E is the global activation energy corresponding to all the physical and chemical processes occurring during the induction period, R^0 is the universal gas constant, A and n are empirical constants. Although each fuel is affected by pressure to a different extent, in literature authors tend to use one value for their correlations. Spadaccini and TeVelde [66] have found the best fits for their data with $n = 2$, other investigators [68-70] have found similar pressure dependencies, meaning $n > 1$. The activation energies from hydrocarbons range in the order 12-50 kcal/mol for liquid hydrocarbons in air, but comparison between different studies is difficult, as mentioned before. An expanded version of the Arrhenius correlation is used, when the equivalence ratio Φ is included in the measurements [8].

Eq. 28

$$\tau_{ign} = \frac{A}{\Phi p^n} e^{\frac{E}{R^0 T}}$$

In some studies [8] R^0 is included in the activation energy term, thus the equation takes the form:

Eq. 29

$$\tau_{ign} = \frac{A}{\Phi^m p^n} e^{\frac{E}{T}}$$

The ignition of a droplet of hydrocarbon fuel can occur in two stages, as seen and confirmed by Faeth et al. [71] in the 1960s. These two stages are characterized by two main chemical reaction mechanisms, denominated low and high temperature reactions. For certain hydrocarbon fuels, such as e.g. n-heptane, at a fixed pressure level, the transition from the low temperature reactions to the high temperature reactions shows a ZTC region.

Staged ignition is preceded by evaporation of the fuel droplet. For the purpose of estimating the amount of vapor formation prior the onset of the first stage of ignition, the ignition mass delay can be defined as [72]:

Eq. 30

$$m_{id} = 1 - \left(\frac{D_i}{D_0}\right)^3$$

where D_0 is the initial droplet diameter and D_i is the diameter at the onset of the first stage of ignition.

As stated by [64], during the ignition delay period, the radical-pool population is increasing at an exponential rate. Yet, the amount of fuel consumed, and hence the amount of energy liberated, is too small to be detected. Thus, important chemical reactions, such as chain branching and formation of radicals, take place during the induction time, whereas the temperature remains nearly constant. Finally, the radical pool becomes large enough to consume a significant fraction of the fuel and rapid ignition will take place. The precise definition of induction time depends on the criterion used, often determined by the measuring technique used, e.g. consumption of fuel, formation of CO, formation of OH, increase of pressure in a constant volume vessel, increase of temperature in an adiabatic vessel, etc. As mentioned before, due to the temperature dependence of the underlying elementary reactions, the ignition delay time depends strongly on the ambient temperature. This is reflected by the Arrhenius law.

2.2.2. Autoignition and General Combustion Behavior of Single Droplets in Microgravity

The main difference between the experimental conditions for autoignition studies in normal gravity and microgravity is the absence of natural convection and buoyancy in the latter one. The effect of natural convection on the autoignition of single fuel droplets has been studied in e.g. [72]. Natural convection is driven by density differences between the gas in the vicinity of the droplet and the surrounding ambient gas. The droplet acts as a heat sink, reducing the gas-phase temperature around the droplet. Also the fuel vapor, which is denser than air, sinks. After heating up, the evaporation rate increases, increasing convection. Convection promotes the heat inflow to the droplet and contributes to temperature rise at the droplet surface. This effect helps to shorten induction times in normal gravity. On the other hand, the temperature rise caused by the exothermal chemical reactions is slower under normal gravity due to the convectional flow around the droplet removing heat and chemical intermediates that are produced by the chemical reactions in the gas-phase. These two processes compete against each other, and the predominance of either one depends on the heating of the droplet and the time available for it. For instance, at low ambient temperatures the first process is dominant, because at the beginning there is little vaporization. As the temperature in the liquid phase rises, the rate of vaporization increases and the latter process becomes more dominant. In a two-stage ignition process, the ignition of the second stage often happens when the cool flame ignites underneath the droplet and due to its lower density rises, and as it passes the droplet initiates the hot flame ignition. The following schematic depicts the staged autoignition of a droplet under normal gravity conditions.

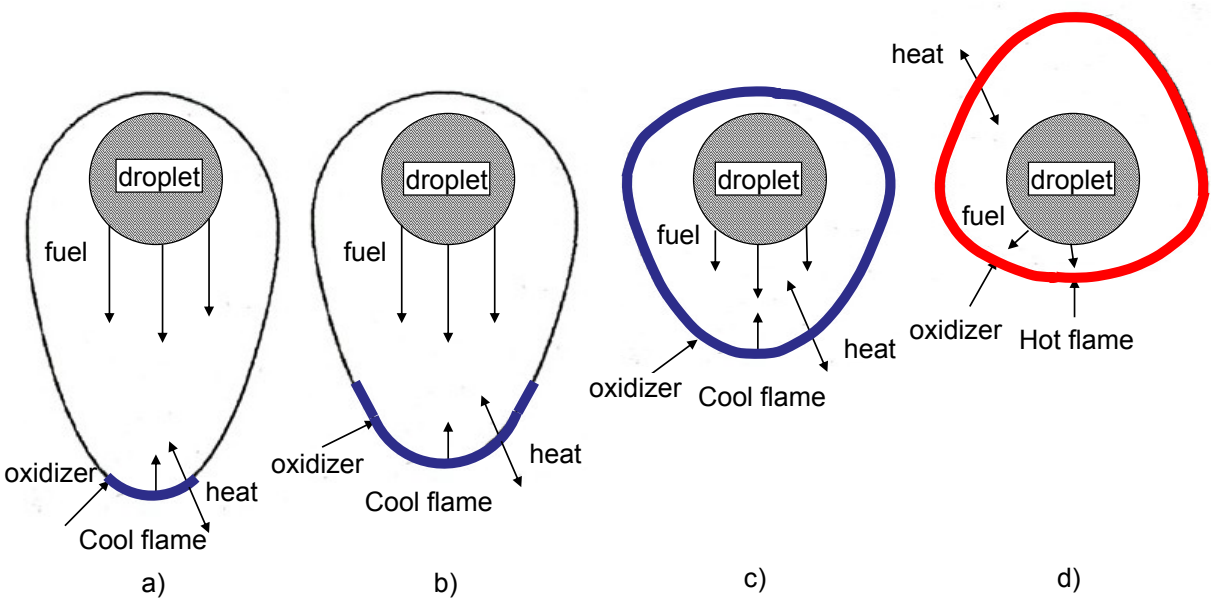

Fig. 23 – Schematic of the two-stage autoignition of a droplet under normal gravity conditions, a) Fuel vapor sinks and Cool flame ignites, b) Propagation of Cool flame, c) Cool flame wrapped around droplet, d) Hot flame ignites

In contrast to the previous figure, the following schematic shows the two-stage autoignition of a droplet under microgravity conditions. As can be seen, the basic geometry of the flame is assumed to be spherical. The cool flame ignites at a certain radius and moves towards the droplet. As mentioned before, the cool flame and hot flame reaction mechanisms compete against each other and depending on the ambient conditions, one of the mechanisms predominates. In conditions where both flames can appear, the hot flame appears shortly after the cool flame and becomes the dominating mechanism.

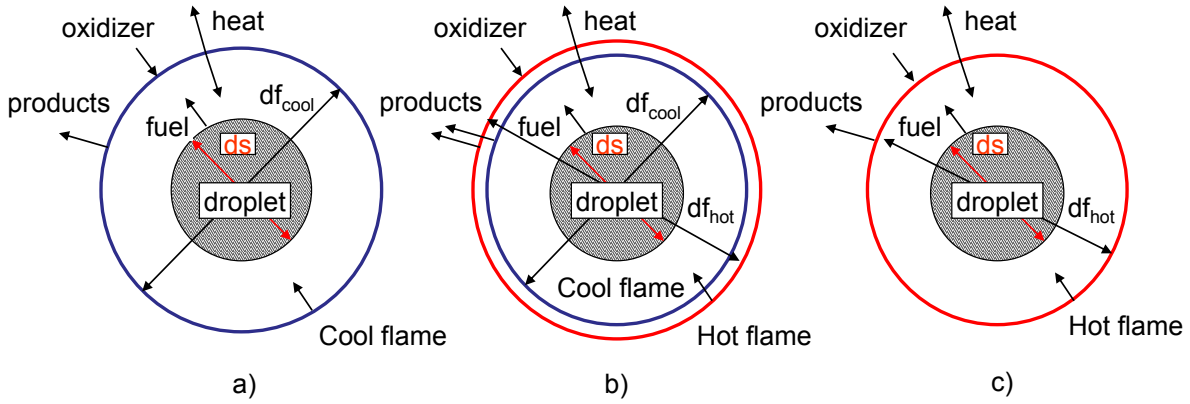

Fig. 24 – Schematic of the two-stage autoignition of a droplet under microgravity conditions, a) Cool flame ignition, b) Transition: Cool flame moves toward droplet and Hot Flame ignites, c) Hot flame

The following figure depicts the different appearance of a droplet burning under microgravity (non-buoyant) and normal gravity (buoyant) conditions. This figure depicts also the basic droplet combustion model, describing the gasification of the liquid fuel at the droplet surface and its subsequent outward transport to meet inwardly-diffusing oxidizing gas in a thin flame region. The classical d^2-law, derived by assuming spherical symmetry, quasi-steadiness and flame-sheet combustion, predicts the decrease of the square of the droplet diameter d_s^2

linearly with time, and the ratio of the flame diameter d_f to the droplet diameter d_f/d_s (or flame standoff ratio) is a constant. Numerous attempts [73, 74] have been made to verify this assumption. Normal gravity experiments show that d_s^2 indeed varies approximately linearly with time. Attempts to quantify the behavior of the flame size however, proved futile because it is meaningless to define a flame diameter when the flame is severely elongated by the presence of buoyant flow. Furthermore, since the intensity of buoyancy continuously changes because of the steadily decreasing droplet size, an unsteady effect is also introduced. Thus, µg experiments are needed to improve the understanding of droplet combustion.

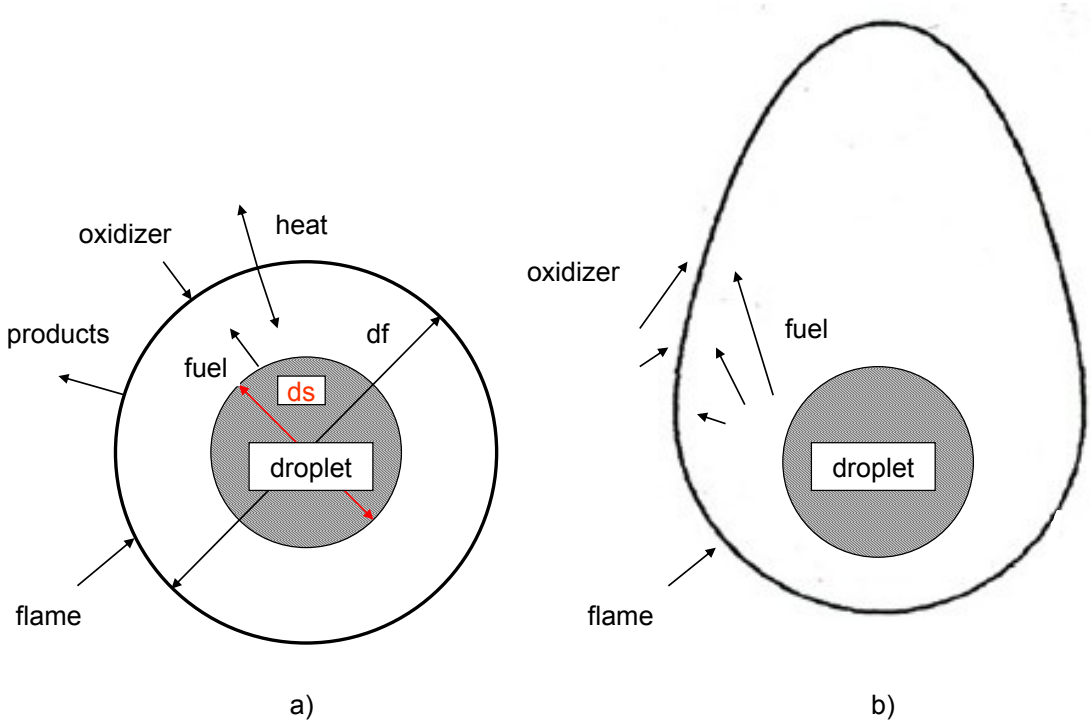

Fig. 25 – Schematic of a droplet burning under a) microgravity and b) normal gravity conditions [73, 74]

To minimize natural convection, as stated by [73], one must reduce buoyant transport relative to diffusive transport of the fuel vapor towards the flame. In the absence of forced convection, the non-dimensional Grashof number represents the ratio of these transport mechanisms:

Eq. 31

$$Gr = \frac{(\Delta\rho/\rho)gd_s^3}{D_g^2}$$

Where $\Delta\rho$ is the characteristic density change, ρ is the mean density, g is the local acceleration due to gravity, D is diffusivity, d the droplet diameter. The subscript s denotes the droplet surface, g the gas phase. Based on this definition, there are three parameters that can be adjusted in order to reduce the Grashof number of the system: the initial droplet diameter, the ambient pressure and the effective gravity. The use of very small fuel droplet diameters, similar to those found in practical spray combustors can minimize the asymmetry since the attendant smaller flame increases the predominance and importance of diffusive transport. The use of reduced ambient pressure increases the diffusivity, being another means of decreasing natural convection effects. The lowest pressure at which a droplet can be ignited and burned in air, does not provide a spherical concentric flame, as shown by Choi in [73]. Increasing the oxygen concentration enables a further reduction of the pressure, but inherent

changes in the chemical kinetics have to be taken into account. Through the use of drop towers and other microgravity facilities, the third means of reducing the Grashof number can be achieved. Besides, larger droplet sizes can be obtained and studied under microgravity conditions, providing a higher spatial resolution for diagnostic measurements.

Great model simplification results when spherical symmetry is assumed, since then the mathematical model becomes one–dimensional. The absence of natural convection in the experimental setup allows the droplets to be almost spherical, allowing a direct comparison of the experiments with a one-dimensional mathematical model.

More about the experimental hardware used for the microgravity autoignition experiments is reviewed in section 3.1 of this study.

3. Experimental Studies on the Autoignition of Fischer-Tropsch synthesized fuels and proposed surrogates

3.1. Microgravity and Drop Tower Experimental Hardware

A microgravity environment is a condition where the force of gravity is compensated in such a way that it has almost no measurable effect on an experimental system.
Microgravity can be attained by attenuation or during free fall. The first is achieved by being located at a large distance from a gravitational body thus reducing the gravitational pull, which is inherently impractical. The second means is currently achievable by using drop towers/shafts, flying parabolic trajectories on airplanes and sounding rockets or, on orbits in spacecrafts such as the International Space Station or the Space Shuttle.
The residual accelerations are for instance in the case of a drop tower in the order of 10^{-5} to 10^{-6} g_0 for experimental times up to 10 s. The residual accelerations are also known as microgravity quality or µg-quality. For parabolic flights the µg-quality is in the order of 10^{-2} - 10^{-4} g_0 for times up to 20 s for each parabola, for sounding rockets this time is in the order of several minutes with µg-quality in the order of 10^{-5} g_0. On orbiting systems such as the ISS the µg-quality is in the order of 10^{-4} - 10^{-6} g_0 with indefinite experimental times. The cost increases with the available experimental time, ranging from € 5000 for a drop experiment at ZARM up to € 50000/kg payload on the ISS.

In the context of combustion, the microgravity condition is mostly used and understood as the establishment of a buoyancy-free experimental environment. Buoyant or natural convection provides oxidizer to sustain and invigorate fires on Earth. In the absence of convection, the only means for providing a flame with oxidizer is diffusion, which is a slower process than convection. On Earth combustion processes and gravity are coupled. By minimizing the influence of buoyancy in a system with the aid of microgravity facilities, weak forces, effects and transport mechanisms in combustion experiments become visible and mathematical model simplifications can be applied and verified. Combustion research demands for a very high microgravity quality as the buoyancy driven temperature differences are large and the inertia of gases is low.

The experiments take place at the Drop Tower Facility at ZARM University of Bremen. The Bremen Drop Tower [75] is a large facility, unique in Europe. It is a ground-based short-term microgravity laboratory with its most prominent feature being the 146 m tall concrete shaft and the enclosed steel drop tube. This steel drop tube stands detached at a height of 13m without any connection to the concrete shaft itself on the 2 m thick roof of the deceleration chamber. The detachment of the drop tube from the concrete tower serves for quiescent conditions inside the tube even at stormy weather conditions. The installation delivers 4,74 s of near weightlessness up to three times a day. It offers also the possibility of doubling the microgravity time up to 9,3 s with the aid of a catapult system.
The microgravity laboratory system itself is a cylindrical capsule with a diameter of 800 mm with a possible length of 1,6 m or 2,4 m depending on the space required by the experimental apparatus. Inserted platforms, held in by aluminum profiles (stringers), form a modular drop capsule structure. The whole capsule is enclosed pressure tight with an aluminum cover after the integration of the experiment.
For the drop procedure, the drop capsule is pulled up by a winch to a height of 120 m. The 1700 m^3 volume of the tube and the deceleration chamber is then evacuated to eliminate the effect of air drag acting on the falling capsule.

A system of 18 pumps with a nominal capacity of 32000 m^3/h require about 1,5 h for the evacuation procedure. The drop is initiated at a residual pressure of 10 Pa. Residual accelerations of less than 10^{-5} g_0 are achieved during the free fall for a distance of 110 m. A deceleration unit, filled with polystyrene pellets, decelerates the drop capsule. The capsule experiences, during the brake phase, decelerations on the order of 20-50 g. For retrieval, the drop tube is refilled with preconditioned air within 20 min.
Monitoring of the experiment (telemetry data and live video signals) is enabled for all the phases of the drop procedure.

The basic dimensions and masses of the capsule used for this study are summarized in the following table [76]:

Max. Payload height [m]	1,730
Total area of experiment platform [m^2]	0,359
Stringer length [m]	2,310
Base structure incl. batteries and CCS [kg]	110
Top lid plate [kg]	36
Covering incl. clamping rings [kg]	54
4x Stringers [kg]	60
Nose cone and connection rod [kg]	6
4x experiment platforms [kg]	60,4
Capsule net weight [kg]	266
Max. Payload mass [kg]	234
Capsule gross weight [kg]	500

Tab. 15 - Dimensions and masses of a drop capsule, long version

The experiment environment conditions inside the drop capsule during the drop procedure are depicted in the following table:

Pressure	
Nominal capsule pressure [hPa]	1013
Pressure loss	$\Delta p < 1\%$ within 3h
Safety values [hPa]	$980 < p < 1300$
Temperature	
Nominal	RT
Accelerations	
Residual accelerations during drop	10^{-5} - 10^{-6} g_0
Deceleration, average	25 g
Deceleration, max value	50 g

Tab. 16 - Experiment environment conditions [76]

3.2. Experiment Setup and Diagnostics

In this section the experimental apparatus employed for the characterization of the autoignition behavior of the studied fuels is described. The main subsystems are:

- Pressure chamber and furnace
- Droplet suspender and fuel supply system
- Optics and laser diagnostics
- Experiment control and data acquisition and processing

The following caption depicts the integrated experimental setup for the drop tower experiments:

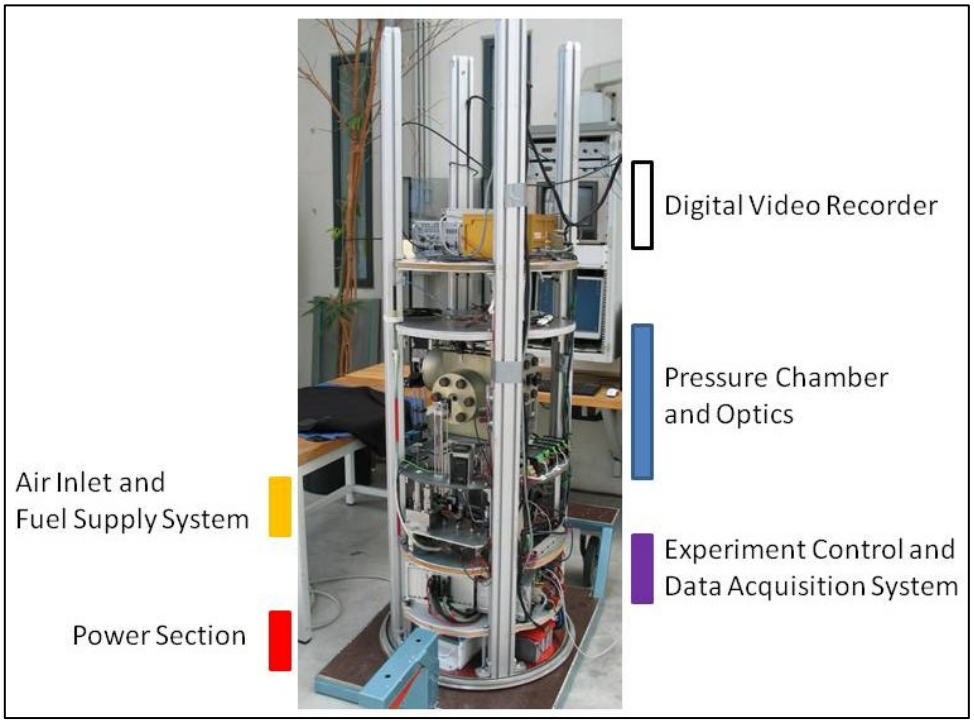

Fig. 26 - Experimental setup

3.2.1. Pressure Chamber and Furnace

In order to achieve a high-pressure and high-temperature environment for the study of single droplet ignition a pressure chamber is used. The chamber consists of two sections, as depicted in the following figure:

a) A hot (upper) section containing the electric furnace
b) A cold (lower) section containing the droplet suspender and fuel supply system

Each section possesses an optical axis, reinforced quartz windows, and two flanges. The furnace in the hot section is resistance heated with a wire driven by a pulsed electric current regulated by a temperature controller. The hot section is thermally insulated using porous ceramics. This configuration keeps the cold lower section at RT and the volume inside the furnace at the desired high temperature with a uniform distribution. This also ensures that the droplet generated in the cold section remains at RT prior its insertion into the furnace. The temperature inside the hot section of the chamber is measured with a type-K thermocouple.

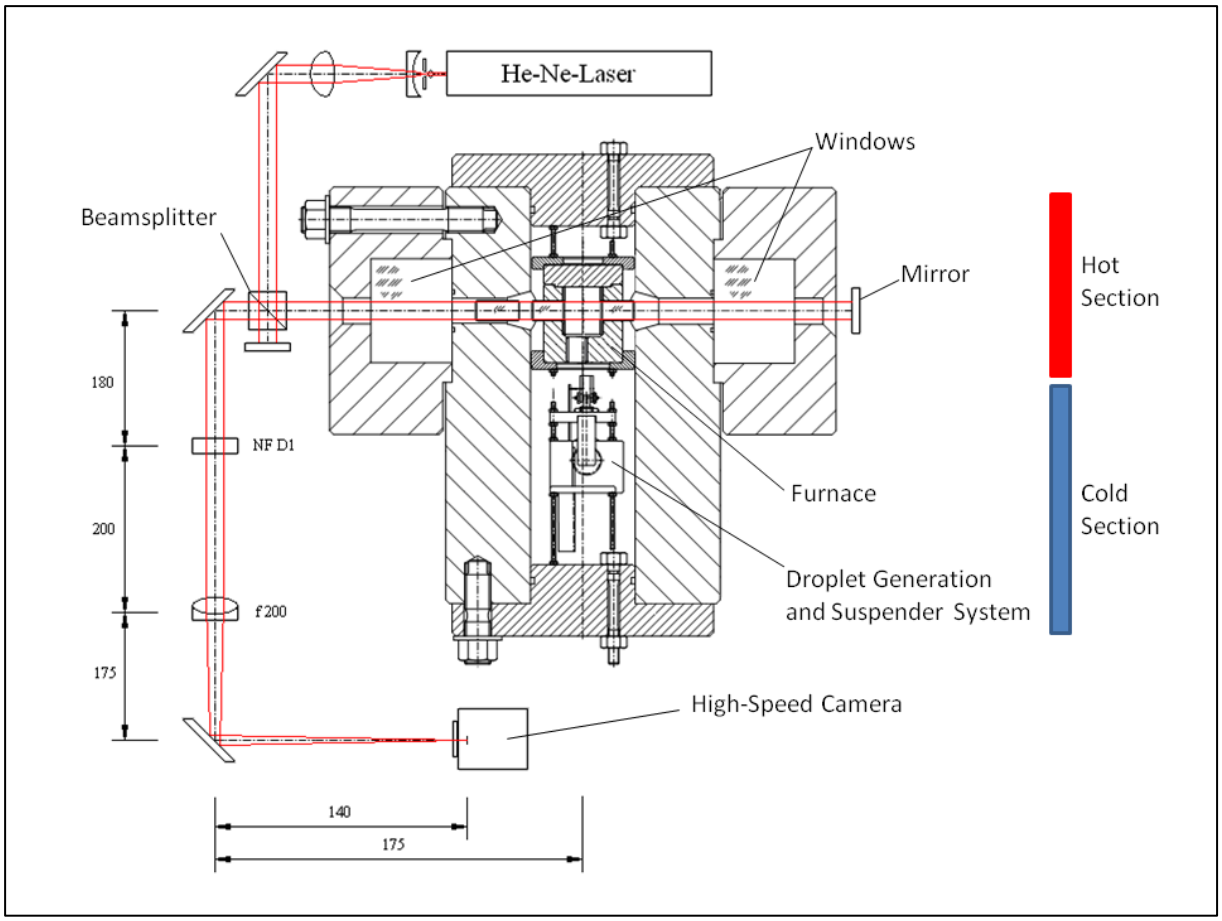

Fig. 27 Schematic of the pressure chamber and Michelson interferometer

The following table summarizes the main dimensions and technical data of the pressure chamber:

Operation parameters	
Max operation pressure	40 MPa
Max operation temperature	1100 K
Temperature operation range	500-1000 K
Pressure operation range	0,1-1,0 MPa
Dimensions	
Dimension of inner space in chamber	Ø80 mm x 260 mm
Dimension of inner space in furnace	Ø30 mm x 40 mm

Tab. 17 - Technical Data of the pressure chamber

Attached to the bottom flange are the main components of the fuel supply system, the ambient gas valves and exhaust. Also several feed-through-plugs for the electrical components inside the chamber are located here. For the experiments in this study air is used as ambient gas.

3.2.2. Droplet Generation and Fuel Supply System

The droplet is generated in the cold section of the pressure chamber. A fuel supply nozzle, retractable by means of solenoid, delivers the fuel on a horizontal sapphire filament, a suspender. The diameter of the filament is 0,125 mm and its length is 10 mm. The tip of the suspender is shaped as a sphere with a diameter of 0,3 mm holding the droplet in its position.

The size of the droplet is controlled visually with the aid of a video camera and a software tool ensuring a desired diameter of the droplet of 0,7 mm.
The insertion of the suspender into the furnace is achieved by means of a lift system. This device consists of rack and pinion gear driven by a step motor. The motor and the resulting motion behavior of the lift system are controlled by a SPS system. A constant acceleration and deceleration ramp is applied in order to maximize insertion speed while avoiding a detachment of the droplet from the suspender.

Insertion time	120 ms
Insertion distance	65 mm
Droplet diameter	0,7 mm
Suspender dimensions	Ø0,125 mm (filament),Ø0,3 mm (tip), 10 mm (length)
Suspender material	Sapphire Monofilament (transparent), Al_2O_3 CAS Nr. 1344-28-1 Density: 3,985 g/cm^3, Tensile strength: 250-400 MPa Compressive strength: 2100 MPa, Thermal conductivity (20°C): 35-40 W/mK, Melting point: 2323 K, Upper continuous temperature:2073-2223 K

Tab. 18 - Technical data of the droplet generation and fuel supply system

The main components of the fuel supply system, as shown in the following figure, are attached to the bottom flange of the pressure chamber. A linear step motor drives a small piston that pushes the fuel in the reservoir via a thin tube up to the fuel nozzle. This system enables a quick change of the studied fuels and a precise fuel droplet generation.

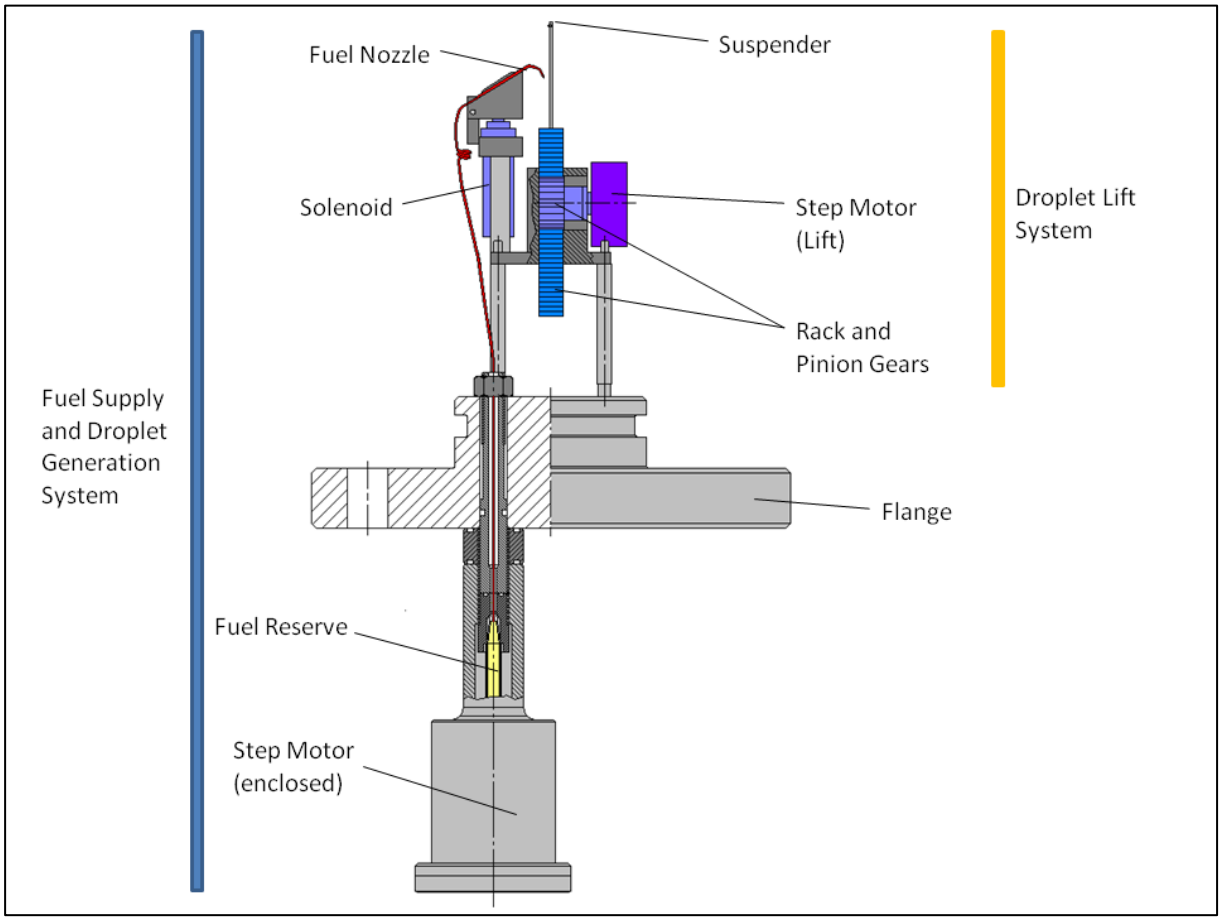

Fig. 28 - Schematic of the droplet generation and fuel supply system

3.2.3. Optics and Laser Diagnostics

The goal of the experiments of this study is the characterization of the ignition delay times of the different fuels analyzed. As stated in the theory background chapter, section 2.2, in the case of two stage ignition, a cool flame appears. Cool flames have very little light emission compared to hot flames. In order to detect the cool flame, the gas phase temperature is observed. The diagnostics used in this apparatus are based on a Michelson interferometer, which permits the observation of a two dimensional temperature field and also changes in the size of the fuel droplet. The time resolution is not limited inherently by the technique itself, just by the image acquisition device. The type of diagnostics implemented in this setup is suitable for obtaining information pertaining temporal changes in the interference fringes due to changes of the optical density caused by temperature changes from the exothermal chemical reactions, not for quantifying the temperature field observed.
The light source used is a He-Ne laser with a wavelength of 632,8 nm and 1,2 mW power. The laser beam is expanded to a parallel beam with a diameter of 15 mm, which is split into a reference and an object beam. The reference beam is sent through a series of lenses to the camera system. The object beam passes through the quartz windows and the furnace and is reflected back at the end of the other side of the optical axis of the hot section and guided to the camera. The beam splitter, the reference and object beam mirrors are attached directly to the flanges of the pressure chamber, which reduces the system's susceptibility to vibrations. A schematic of the Michelson interferometer used in this study is shown in section 3.2.1.
The camera used for the acquisition of the interferogramms is a Photron Fastcam MC-2™ digital high speed video system. It is based on light sensitive CMOS imaging sensors and has the following performance:

- Up to two remote camera heads (35 mm x 35 mm x 35 mm; 90 g; without lens) can be simultaneously used
- 512 x 512 pixel resolution
- 1000 f/s recording rate at full image resolution, for both camera heads and 8 s recording time
- up to 10000 f/s with reduced image resolution (512 x 96 pixel)
- Global electronic shutter from 20 ms to 6 μs
- Color (24 Bit) or monochrome (8 Bit)
- Cameras precisely synchronized to an external source
- Lens mount: C-mount
- Processor unit (H: 195 mm x W: 159 mm x D: 130 mm; 5 kg)
- Live Video during recording, NTSC, PAL
- Ethernet camera control
- Start, End, Center and Manual Trigger Modes
- Saved formats: JPEG, AVI, TIFF, BMP, RAW, RAWW, PNG, FTIF

The live video output can be transmitted to ground prior and during the drop. The high-speed data is stored onboard. The bandwidth of the transmitted data is a standard video link.

The following table summarizes the main technical data concerning the optics and laser diagnostics:

Light source	He-Ne laser 632,8 nm, 1,2 mW
Beam diameter	15 mm
Camera frame rate, resolution	Photron Fastcam MC-2™ 1000 f/s, 512 x 512 pixel
Shutter speed	1/8000 s

Tab. 19 - Technical data of the optics and laser diagnostics

The rate of temperature rise detectable by this Michelson-interferometer setup can be determined by the following relation [16]:

Eq. 32

$$\frac{dT}{dt} \geq \frac{a\lambda}{4\pi l} \cdot \frac{p_0}{(n_0 - 1)T_0} \cdot \frac{T^2}{p}$$

Where a is the minimum detectable phase shift, λ the wavelength of the laser light, l is the object size, n is the refractive index, p is pressure and T is temperature. The subscript "0" denotes the reference state. Exemplarily for the present configuration, $a = \frac{\pi}{4}$ per 1 ms (this value being the frame rate), the size of the heat release zone being at 1 mm, n_0 estimated at 1,000292, a typical analyzed temperature of 700 K where ignition is observed and a pressure 0,1 MPa, a temperature rise of 0,34 K/ms can be detected. At higher pressures the detectable temperature change decreases.

3.2.4. Experiment Control and Data Acquisition and Processing

The experiment control consists of two different main modules, a SPS unit and the Capsule Control System or CCS. The SPS unit controls the fuel droplet insertion mechanism. The overall control of the experimental apparatus, thus allowing autonomous operation during the drop procedure, is accomplished with the CCS. The CCS operates like a storage-programmable logic controller. Other tasks, including data handling and telemetry/ telecommand management are performed by this unit. The CCS triggers, according to a previously implemented routine, the SPS unit. In order to automate and control the drop capsule experiment, an "Experiment-VI" is developed. This VI or virtual instrument has been implemented on the National Instruments™ LabView programming platform.
Telemetry, control logs and specific experimental data, such as pressure and temperature developments, are stored on the CCS. Video data is stored directly on the camera control device and digital recorder. The following caption depicts the software interface for controlling the experiment.

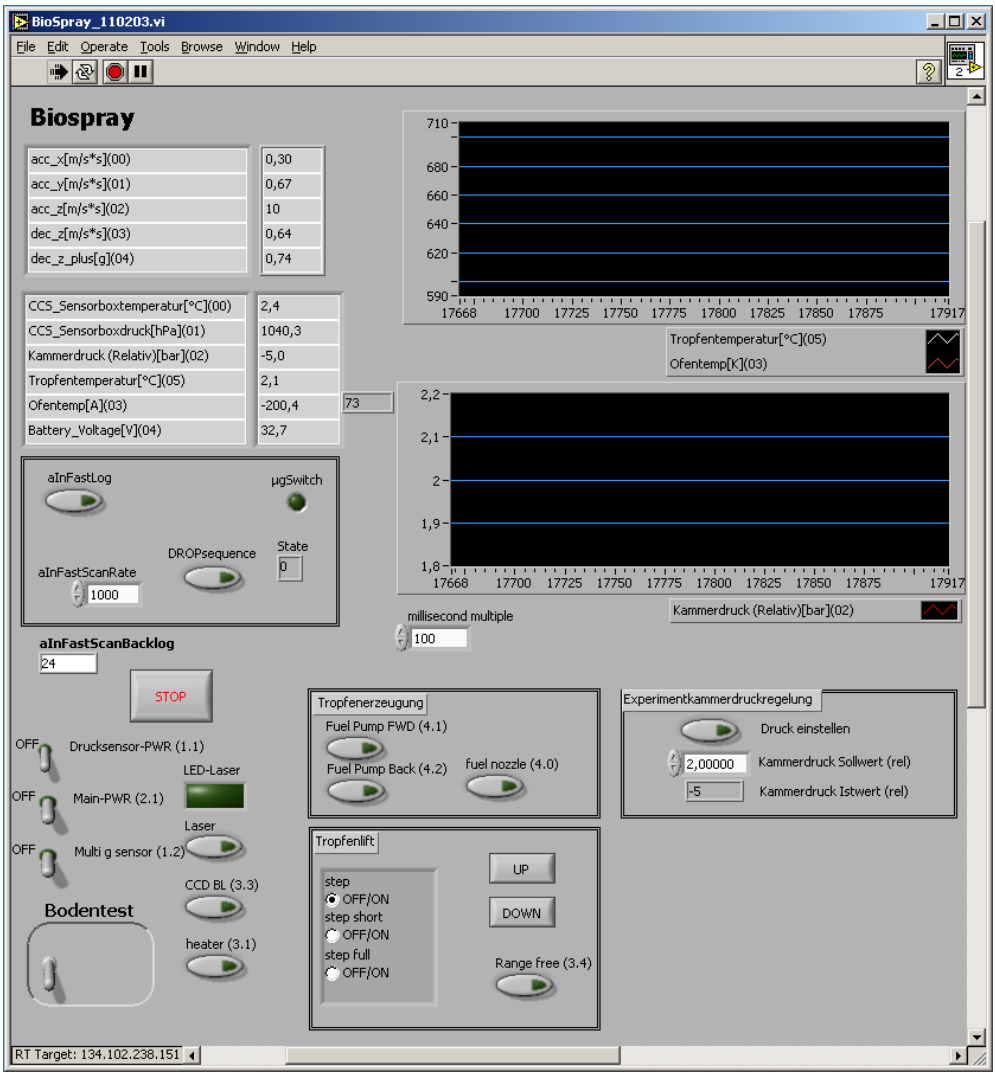

Fig. 29 – Screenshot of experiment control interface implemented in LabView

3.2.5. Procedures for Normal and Microgravity Experiments

A typical experiment run with this apparatus consists of the following steps:

- Setting and verification of the main experimental environment variables such as temperature and pressure
- Droplet generation, measurement and storage of an image of the measured droplet
- Droplet insertion, observation of the process
- Video and log data storage
- Flushing/purging of experimental pressure chamber with air

These steps are the same in both cases, normal and microgravity experiments. The repetition frequency varies largely; for normal-g experiments 80 to 100 experiments can be performed per day. In contrast, up to three microgravity experiments can be performed in the same time period.

3.3. Droplet Characterization and Determination of Ignition Delay Times

In this section the general procedures for evaluating the data obtained by the experiments are described. The pressure chamber shown in the previous section has been used in previous work [12, 14] performed at the Aerospace Combustion Engineering Group at ZARM and therefore allows the comparison of new and previously obtained data sets. The experiments in this study were mainly conducted at three pressure steps (0,3/0,5 and 1,0 MPa) in a temperature range of 550-950 K. The ambient gas was technical air with 21% O_2 and the droplet size was set to 0,7 mm. The following table summarizes the general experimental parameters in this study for the experiments described in the subsequent sections:

Pressure inside the pressure chamber	0,3/ 05/ 1,0 MPa
Furnace temperature range	550 – 950 K
Ambient gas	Technical air
Droplet diameter	0,7 mm

Tab. 20 - Summary of general experimental parameters

The droplet size is determined from images obtained by a camera during the droplet generation procedure. The image of the generated droplet is measured with the aid of a software tool as shown in the following image. The resolution of the image is 256x256 Pixel. Each droplet's diameter is verified by this way prior to its insertion into the furnace.

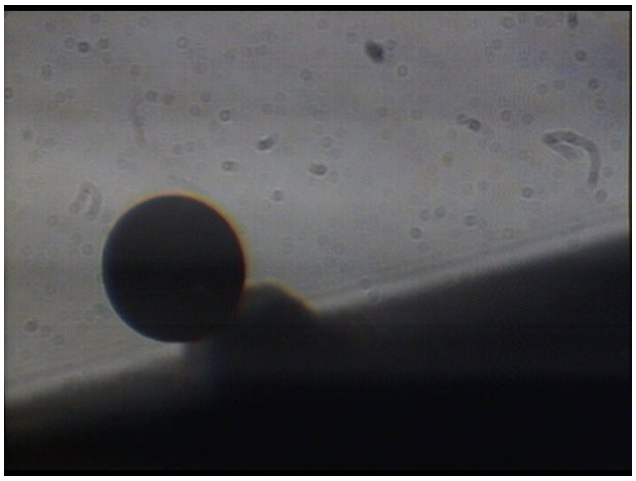

Fig. 30 Screenshot of the image acquired by the software tool for estimation of the droplet size prior insertion

From the recorded interferogramms the ignition delay times are determined. These manifest themselves as sudden changes in the size and number of fringes. Ignition delay or induction times are both used as synonyms in this study. The induction times in this work are defined as:

τ_1: First induction time: The time lapse from the insertion point to the appearance of the cool flame. The insertion point is defined as the instant when the suspender passes through the boundary of the ceramic insulation. From this instant the droplet is directly exposed to the hot ambient of the furnace.

τ_2: Second induction time: The time lapse from the appearance of the cool flame till the appearance of the hot flame, or $\tau_t - \tau_1$. It's only defined when both times are detected.

τ_C: Hot flame combustion duration: The time lapse from the appearance of the hot flame till the complete burnout of the droplet, or τ_{Lt}-τ_t. It's only defined when both events are detected.

τ_t: Total induction time: The time lapse from the insertion point till the appearance of the hot flame.

τ_{Lt}: Total droplet life time: The time lapse from the insertion point till the complete evaporation of the droplet in the case where no ignition takes place. In case of ignition it is defined as the time till the droplet is entirely burnt out.

The following caption depicts a series of false colored images extracted from the interferogramm-videos. These images show exemplarily the different phenomena and flame appearances obtained with this experimental apparatus.

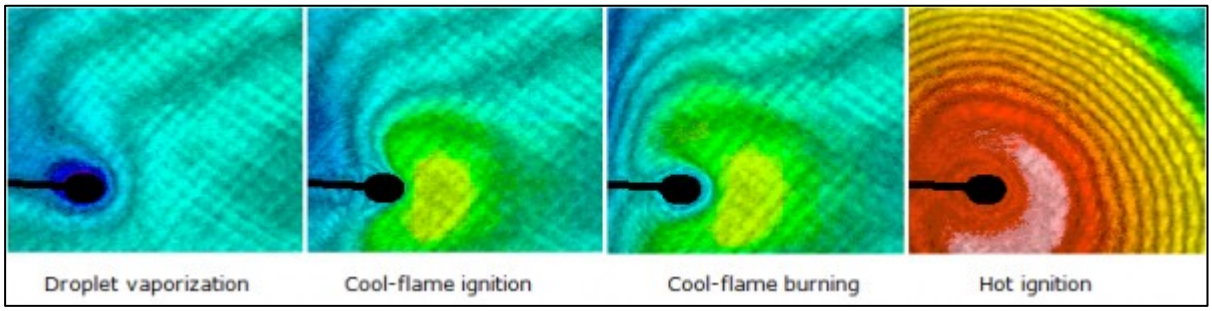

Fig. 31 - Interferogramm sequence of droplet ignition (false coloring)

The following diagram depicts the defined induction times in relation to the experiment timeline and shows qualitatively the temperature progression of a droplet during the insertion and ignition phases. The high speed camera starts beforehand triggered by a signal from the CCS. One second after this signal the SPS initiates the insertion procedure, which needs 40 ms till reaching the outer side of the ceramic insulation, 22 ms more till reaching the inner side of the insulation and 44 ms till reaching the ignition position inside the furnace. As previously defined, the induction times are defined in reference to the insertion point, which is the moment when the suspender passes the ceramic insulation. The trigger signal from the CCS and the drop sequence are simultaneous. The 1000 ms (1 s) pause between the trigger signal and the lift start are needed for microgravity experiments. This is done in order to compensate disturbances during the transition from normal-g to microgravity.

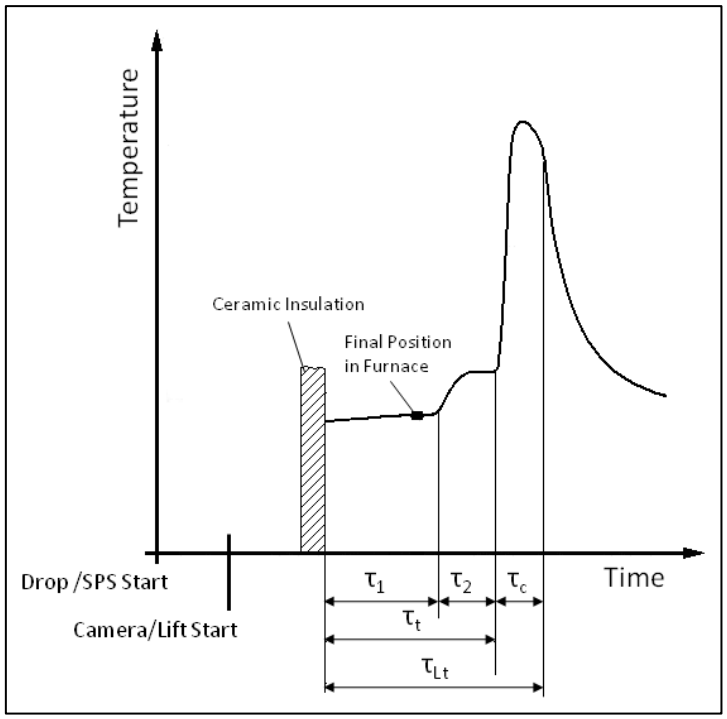

Fig. 32 - Experiment timeline and induction times

3.4. Experimental Error Estimation

This section deals with the different sources of error present in the experimental setup and measurement procedures. These errors have to be identified and minimized as much as possible. General errors present in any experimental setup are:

- Design, mechanical production and assembling errors of the experimental hardware
- Calibration errors in sensors
- Electrical interference, electronic noise, offsets
- Software implementation and usage errors
- Operational/operator errors

Errors that are innate to this setup are:

- Errors in the measurement of ambient parameters (pressure, temperature)
- Errors in droplet size estimation and droplet geometry
- Errors caused by mechanical deviations by stepping motor, vibrations.
- Purity and composition fluctuations or degradation of fuels employed
- Variation of residual gravitational acceleration or µg-quality
- Errors in video analysis

The ambient temperature inside the furnace is measured by a thermocouple and controlled by an OMRON C5W electrical circuit. According to the manufacturer the error caused by the electrical circuit is less than 0,5%. Previous studies that have employed the same experimental apparatus [12, 14] estimate an error caused by radiant heat flux from the furnace wall to be 11 K for an ambient temperature of 1000 K and 5 K for 700 K, but consider it to be overestimated by their calculations and therefore negligible.
The ambient pressure in the furnace is monitored by a pressure sensor from type STW-A09 [81]. The error is expected to be less than 0,002 MPa.

The droplet size is measured according to section 3.2.5 after droplet generation before insertion into the furnace. Images of this process are stored and the error of measurement is in the order of ±1 pixel, which is equivalent to ±0,005 mm.

The drop-lift mechanism and the insertion process show for the insertion time duration an error around ±0,5 ms.

The purities of the pure compounds used are higher than 99%. The fuels used are kept in glass flasks at RT and protected from light in order to minimize degradation of the components and variations in the composition.

The µg-experiments are conducted at a residual ambient pressure in the drop tube of 10 to 20 Pa, which is equivalent to 10-15x10^{-6} g_0. The effect on the measurements is negligible.
The videos of interferogramms and backlight imaging acquired during the experiments are the base for the determination of the induction times and droplet regression rates. These videos are acquired at a frame rate of 1000 f/s, which on the other hand means that the time resolution is set at 1 ms. The analysis is performed for the most part manually which can introduce evaluation errors to the data. For rapid processes such as the detection of hot flames, the time evaluation error is in the order of 1 frame or 1 ms, for slower processes such as cool flames at low temperatures (~580-620 K) the error is in the order of 5 to 10 frames or 5-10 ms. At higher temperatures this process speeds up and the error decreases.

3.5. Experimental Characterization of the Autoignition Behavior of GTL-Diesel and Determination of a suitable Surrogate Fuel

In this chapter the experimental results concerning the autoignition behavior of GTL-Diesel are presented. The experiments were conducted on the apparatus described previously, in normal and microgravity conditions. These results are the base for the development of a suitable surrogate fuel for numerical autoignition simulations.

3.5.1. Normal Gravity Autoignition Experiments

The experimental parameters for these experiments are summarized in the following table:

Ambient Pressure **Measurement Step Size**	0,1 – 1,0 MPa 0,1 MPa
Ambient Temperature **Measurement Step Size**	550 – 950 K 10 K (mostly)
Droplet Diameter	0,7 mm

Tab. 21 – Experiment parameters for normal gravity autoignition experiments

Influence of Ambient Temperature on the Ignition Delay Times

These experimental results show the influence of the ambient temperature on the ignition delay times for the pressure levels between 0,1-1,0 MPa. As can be seen in the following figures, the influence of temperature is very pronounced. For the τ_1-diagramm, the detection

of cool flames ends at 710 K. In the following diagrams, error bars have been omitted for the sake of clarity.

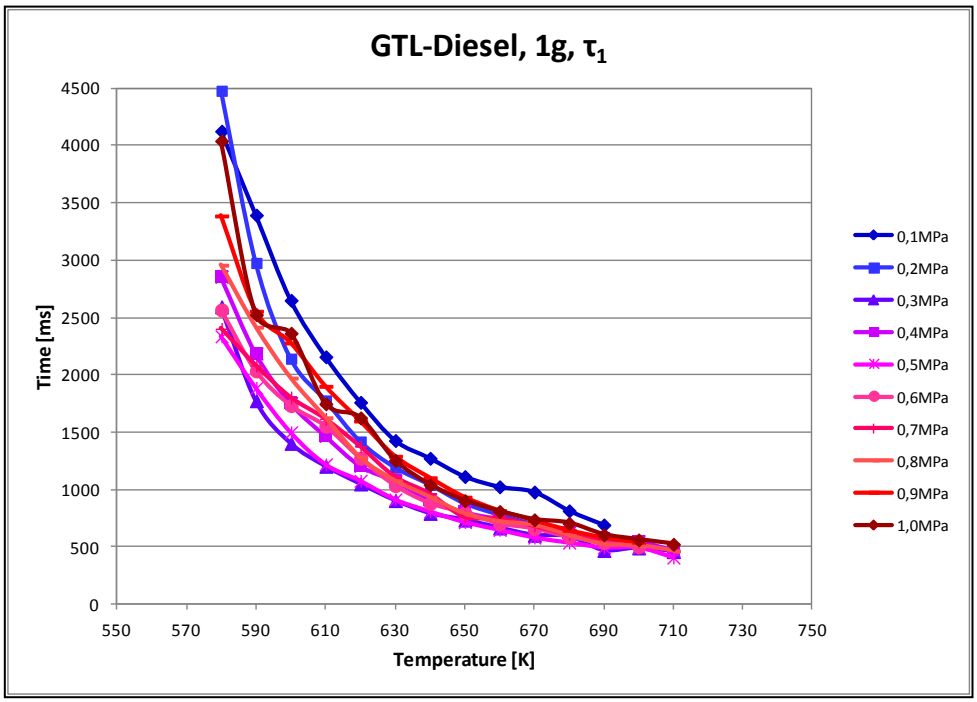

Fig. 33 - Comparison of the first ignition delay times for GTL-Diesel under 1g for the ambient pressures analyzed

For the τ_t-diagram, at low pressures (0,1-0,2 MPa) the first hot flames are detected at higher temperatures, for 0,1 MPa at 850 K, for 0,2 MPa at 690 K. For higher pressures, hot flames appear below 600 K. The total ignition delay times for these pressure levels are located in a band roughly 180 ms wide.

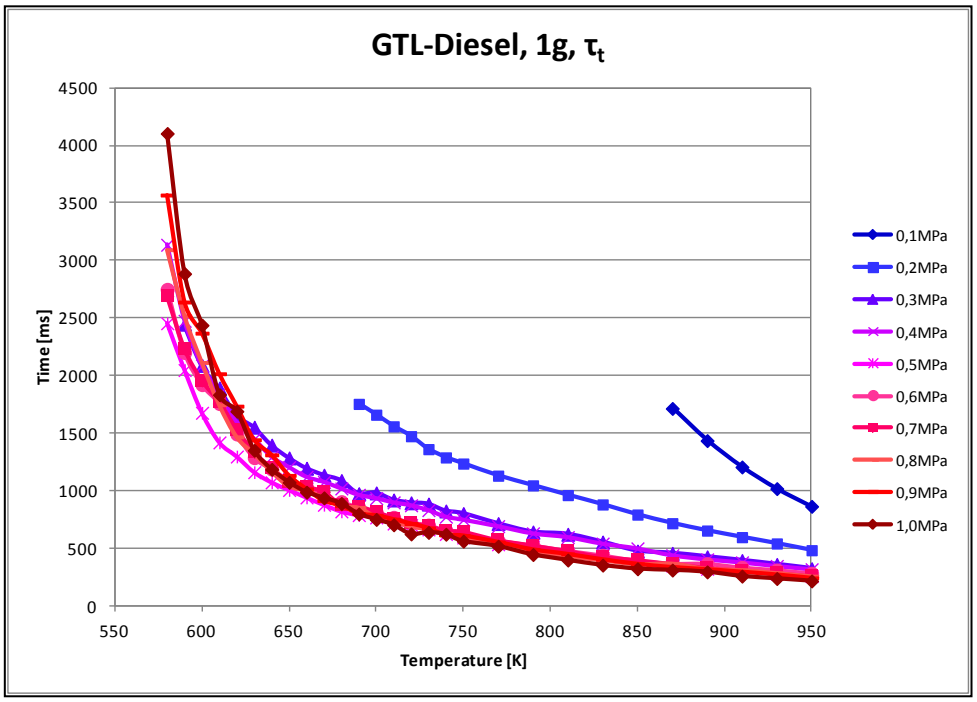

Fig. 34 - Comparison of the total ignition delay times for GTL-Diesel under 1g for the ambient pressures analyzed

The experimental data shown in the τ_{Lt}-diagram has a similar behavior as the previous diagram. For higher pressures (>0,3 MPa) the curves are located in band, roughly 100 ms wide.

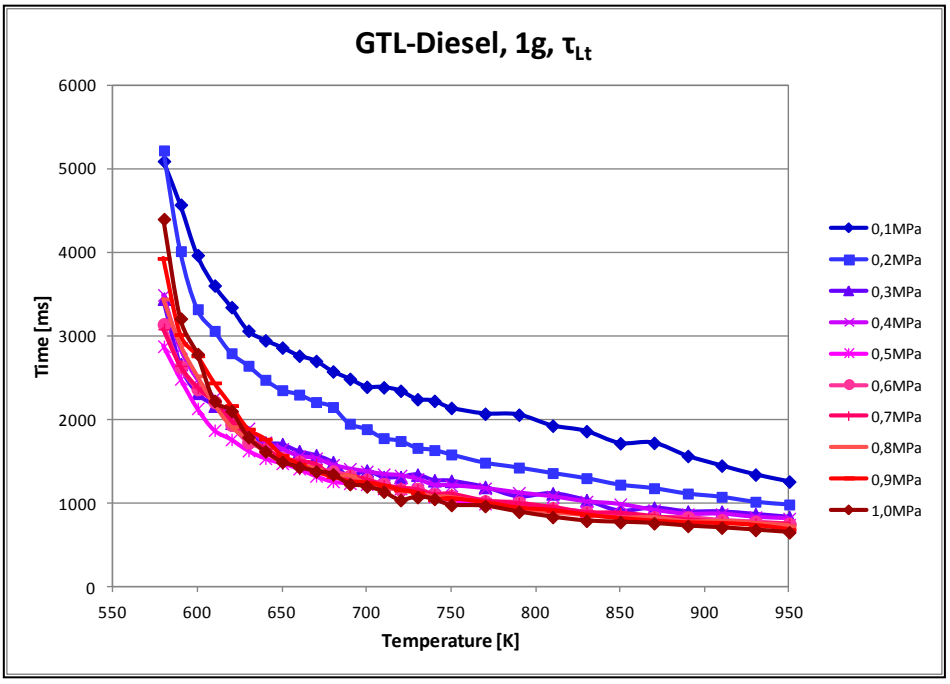

Fig. 35 - Comparison of the droplet lifetimes for GTL-Diesel under 1g for the ambient pressures analyzed

The τ_2-diagram shows that at 0,1 MPa no two-stage ignition is observed. For 0,2 MPa a short two-stage region at 690-700 K is detected. For data > 0,4 MPa the curves show a slight increase with rising ambient temperature, only the 0,3 MPa data shows a retrograde behavior. The τ_c-diagram shows for pressures > 0,3 MPa low temperature dependency, meaning that the combustion time of the hot flame is roughly constant within a 400-500 ms range.

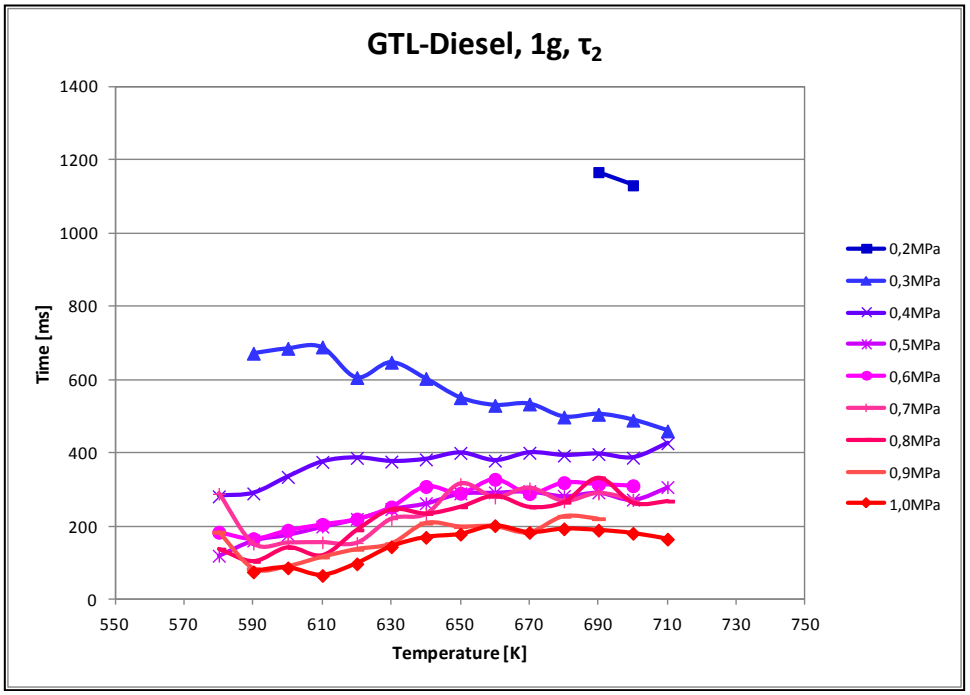

Fig. 36 - Comparison of τ_2 for GTL-Diesel under 1g for the ambient pressures analyzed

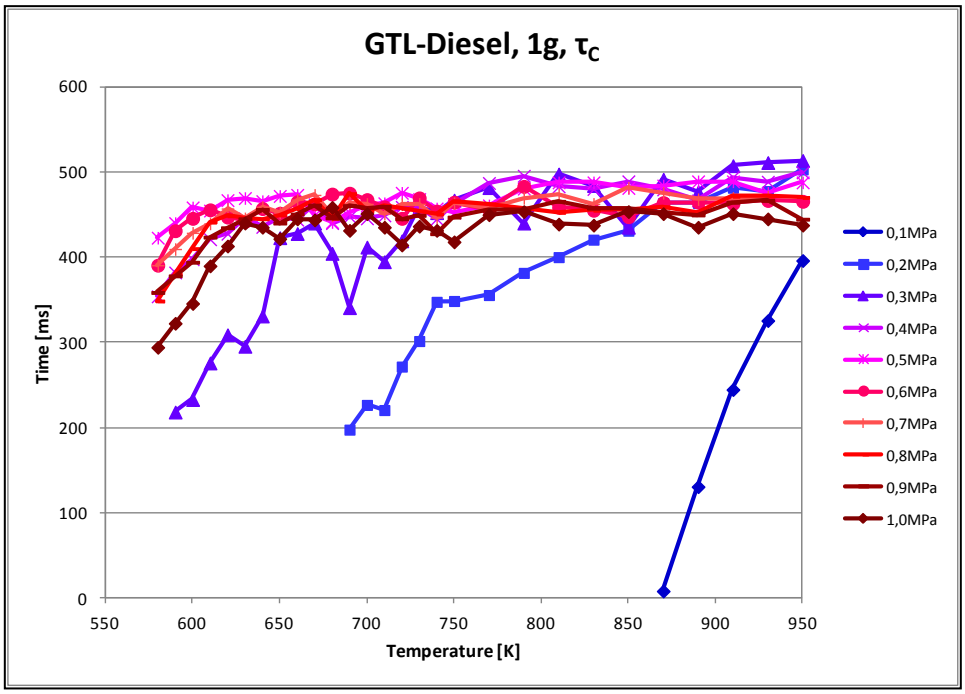

Fig. 37 - Comparison of τ_c for GTL-Diesel under 1g for the ambient pressures analyzed

The following diagrams depict experimental results for selected pressure levels. Exemplarily data for 0,3 MPa, 0,5 MPa and 1,0 MPa is shown. Two different axis settings, linear and logarithmic with the abscissa as 1/T (used widely in literature) are used. As can be seen, τ_1 (denoted in the figures as t1) never exceeds the ceiling temperature of about 710 K. Above this temperature only a hot flame is observed. For 0,3 MPa, at 585 K the first detection of a hot flame occurs, below this temperature only cool flames are observed, at slightly above 550 K being the first observation. For 0,5 MPa both, cool and hot flames, are detected, meaning no cool flame single stage temperature range is observed. The cool flame ceases to appear at 710 K. Similarly, for 1,0 MPa cool and hot flames are detected at about 562 K. The cool flame ceases to appear at 710 K.

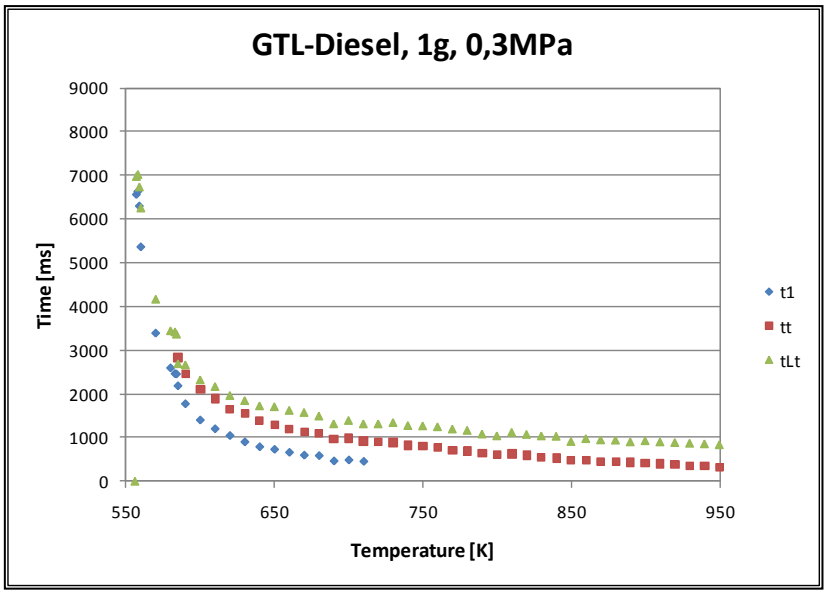

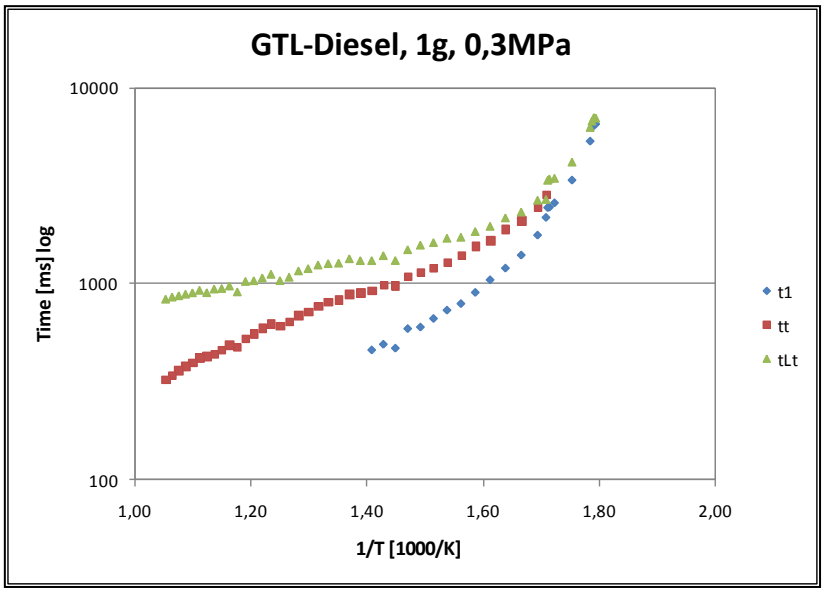

Fig. 38 – Experimental data on the ignition delay times of GTL-Diesel (0,3 MPa, 1g)

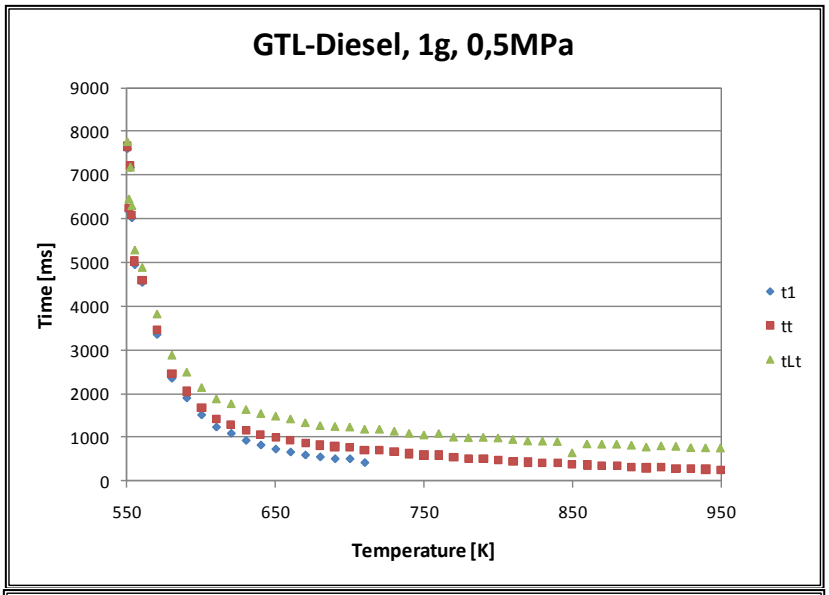

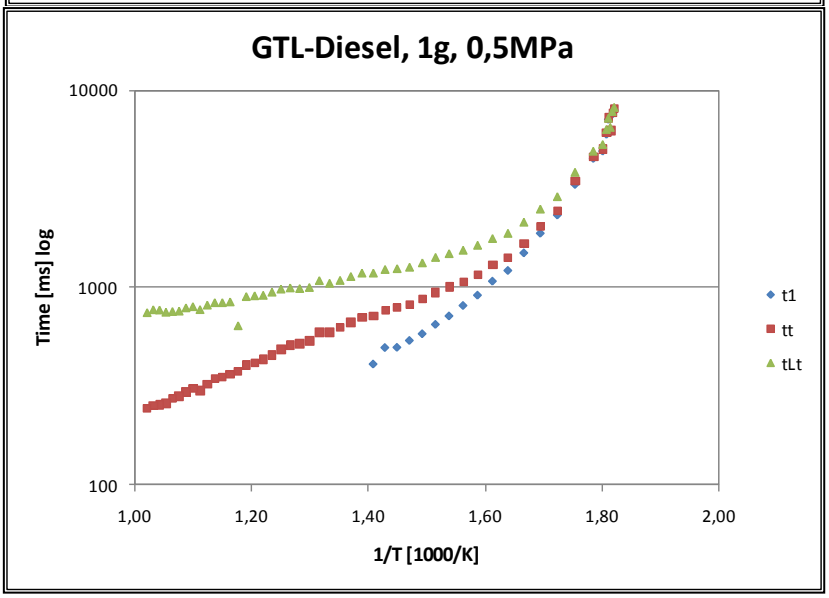

Fig. 39 – Experimental data on the ignition delay times of GTL-Diesel (0,5 MPa, 1g)

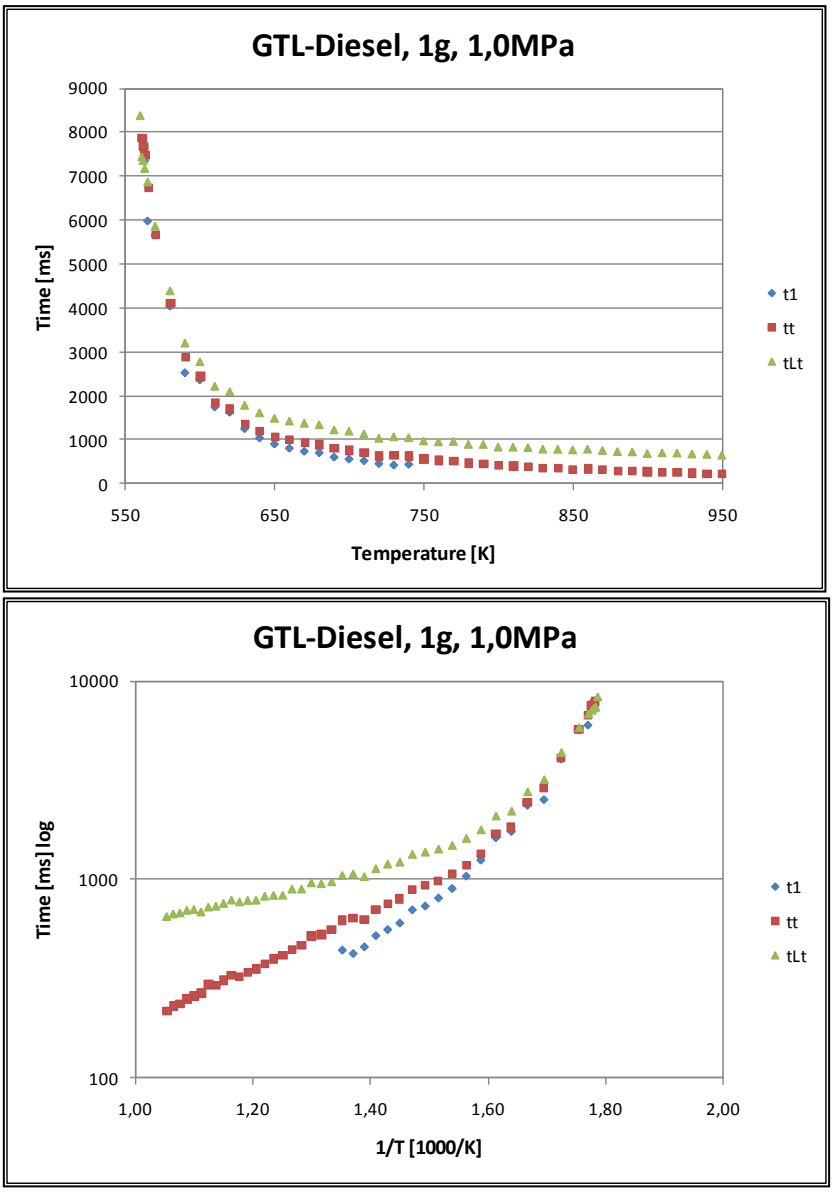

Fig. 40 – Experimental data on the ignition delay times of GTL-Diesel (1,0 MPa, 1g)

Each data point shown is an average of four experiments. The data points show little scattering and error bars have been omitted for clarity.

As presented before in section 2.2.1 exponential regression fits, also known as the Arrhenius equation, are used commonly in literature to correlate experimental data to the main experimental parameters, such as pressure and temperature. The following figure depicts exemplarily fitting curves for experimental data presented previously for the total ignition time τ_t of GTL-Diesel for 0,3 MPa. The red curve is a single term exponential fit; the blue curve is a two-term exponential fit of the type:

Eq. 33

$$\tau = ae^{-bT} + ce^{-dT}$$

The two-term exponential fit offers better results as indicated by the R-square values summarized in the following tables. These tables show also the obtained coefficients. This stems from the fact that the two main reactions paths, leading to either a cool flame or a hot flame, are competitive processes that exist simultaneously. Their manifestations depend on the ambient parameters temperature and pressure. This is reflected by the two terms in this

exponential fit. Nonetheless, it has to be taken into consideration that the Arrhenius equation and this two-term exponential equation are purely mathematical fits and not equations derived from a physical deduction process.

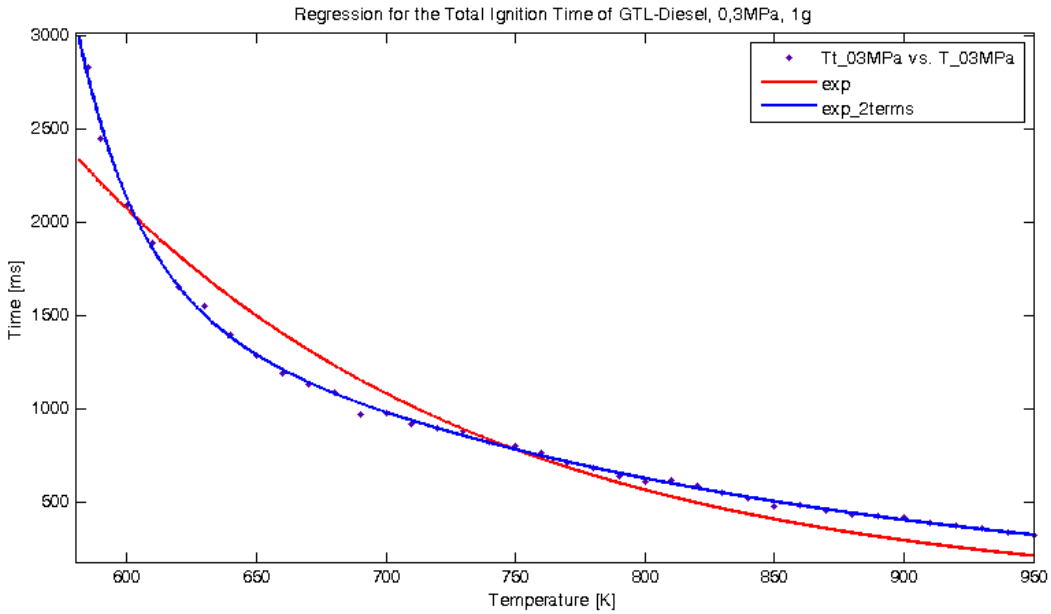

Fig. 41 – Regression for the Total Ignition Time of GTL-Diesel, 0,3 MPa, 1g

Regressions for τ_t at 0,3 MPa, 1g					
Equation Type	**Coefficient**		**SSE**	**R^2**	**Adjusted-R^2**
Exponential	a	1,007e5	8,166e5	0,9394	0,9377
	b	-0,006474			
Exponential 2 Terms	a	4,351e13	2,285e4	0,9983	0,9982
	b	-0,04162			
	c	2,077e4			
	d	-0,004371			

Regressions for τ_t at 0,5 MPa, 1g					
Equation Type	**Coefficient**		**SSE**	**R^2**	**Adjusted-R^2**
Exponential	a	1,377e10	1,227e7	0,9443	0,9431
	b	-0,02639			
Exponential 2 Terms	a	3,644e18	1,903e6	0,9914	0,9908
	b	-0,06203			
	c	2,947e4			
	d	-0,005147			

Regressions for τ_t at 1,0 MPa, 1g					
Equation Type	**Coefficient**		**SSE**	**R^2**	**Adjusted-R^2**
Exponential	a	1,142e10	6,479e6	0,968	0,9672
	b	-0,02537			
Exponential 2 Terms	a	1,33e15	8,692e4	0,9996	0,9995
	b	-0,04647			
	c	3,413e4			
	d	-0,005451			

Tab. 22 – Coefficients of the regressions for τ_t and evaluation of the quality of the fits

Regressions for τ_1 at 0,3 MPa, 1g					
Equation Type	**Coefficient**		**SSE**	**R^2**	**Adjusted-R^2**
Exponential	a	1,579e12	3,91e6	0,962	0,9605
	b	-0,0347			
Exponential 2 Terms	a	3,657e18	5,354e5	0,9948	0,9941
	b	-0,0614			
	c	1,118e5			
	d	-0,007708			

Regressions for τ_1 at 0,5 MPa, 1g					
Equation Type	**Coefficient**		**SSE**	**R^2**	**Adjusted-R^2**
Exponential	a	2,855e11	5,05e6	0,9661	0,9644
	b	-0,03188			
Exponential 2 Terms	a	4,246e20	1,833e6	0,9877	0,9857
	b	-0,07101			
	c	3,184e6			
	d	-0,01293			

Regressions for τ_t at 1,0 MPa, 1g					
Equation Type	**Coefficient**		**SSE**	**R^2**	**Adjusted-R^2**
Exponential	a	3,447e10	3,155e6	0,9726	0,9711
	b	-0,02739			
Exponential 2 Terms	a	3,014e17	7,68e5	0,9933	0,9921
	b	-0,05641			
	c	8,729e5			
	d	-0,01051			

Tab. 23 - Coefficients of the regressions for τ_1 and evaluation of the quality of the fits

The following figures show the behavior of two derived induction times, namely the second induction time τ_2 and the hot flame combustion time τ_c. In the case of the experiments conducted at 0,5 MPa and 1,0 MPa τ_2 increases as the ambient temperature rises reaching (for limited temperature ranges, in the case of 0,5 MPa 650-720 K and for 1,0 MPa 650-740 K) a plateau. This plateau decreases with increasing pressure. This is not the case for 0,3 MPa, where a retrograde behavior is observed.

For τ_c a similar phenomenon occurs. For all pressure levels an increasing of τ_c with rising ambient temperature is observed, reaching a plateau. For these three pressure levels the plateau is located between 400-500 ms. An explanation for this comes from the hot flame temperature. The hot flame has a higher temperature than the ambience (~2000 K) which isolates the droplet and gas phase beneath the reaction zone from the ambient influence. The similarity in the plateau times stems from the amount of fuel available, meaning the droplet diameter being the main parameter driving τ_c.

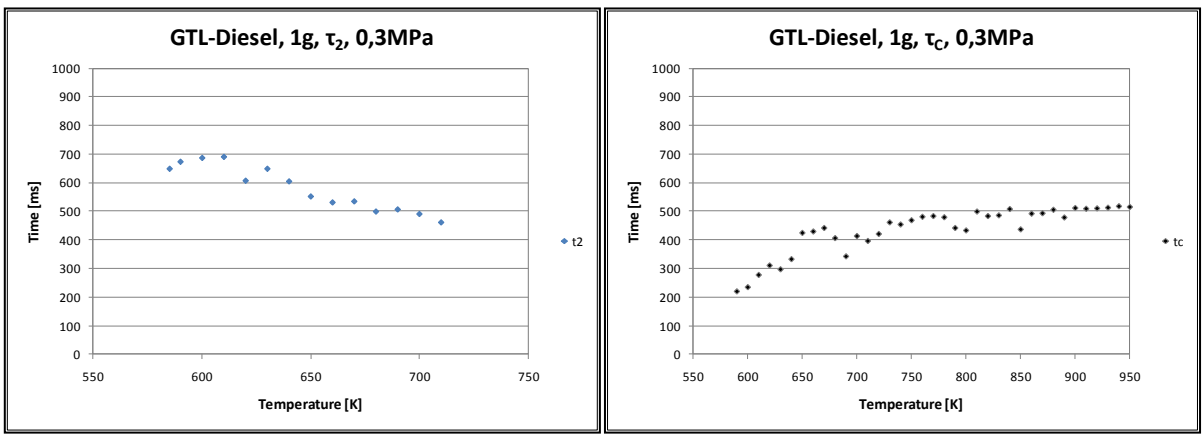

Fig. 42 – Second ignition delay times and hot combustion duration for GTL-Diesel (0,3 MPa, 1g)

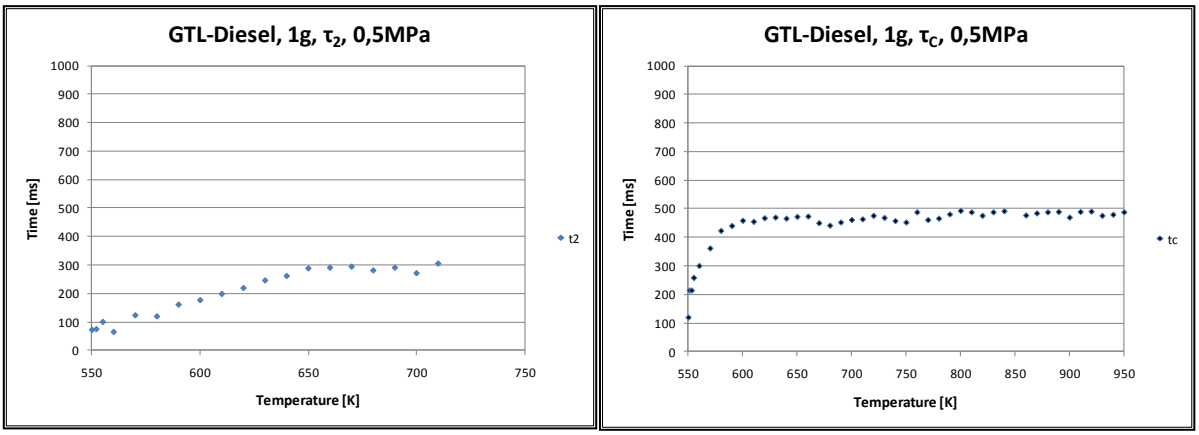

Fig. 43 – Second ignition delay times and hot combustion duration for GTL-Diesel (0,5 MPa, 1g)

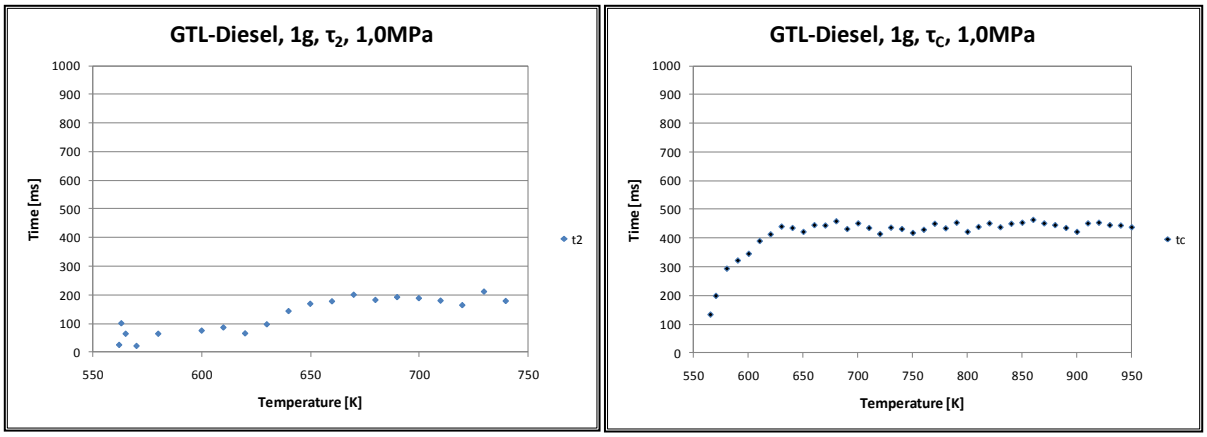

Fig. 44 – Second ignition delay times and hot combustion duration for GTL-Diesel (1,0 MPa, 1g)

Influence of Ambient Pressure on the Ignition Delay Times

The following figures compare the previously presented data and show the influence of pressure on the ignition delay times. (Some temperature steps have been omitted for presentation reasons.) As a general observation, it can be seen that low temperature curves show for each ignition delay time a large pressure dependency. This suggests that the low temperature reaction path that leads to a cool flame is strongly pressure dependent. On the other hand, high temperature curves show with increasing temperature small pressure dependency. This stems also form the phenomenology of the high temperature reactions which lead to a hot flame, being weakly dependent on ambient pressure.
As stated previously, both reaction mechanisms exist simultaneously. The predominance of either is to different extents temperature and pressure dependent. In the case of the diagram depicting τ_1, in the lower temperature regime (580-620 K), the low temperature reactions are highly pressure dependent, beyond 620 K the influence of pressure weakens, expressed in the almost horizontal curves at 700-710 K. For τ_t a similar behavior is observed. At higher pressures and higher temperatures the influence of the ambient pressure on τ_t becomes less accentuated. On the other side, there is pressure dependency for the first detection of a hot flame. With decreasing pressure, the first detection is shifted to higher temperatures. For the droplet lifetimes, at lower pressures (0,1-0,3 MPa) the lifetimes are highly pressure dependent. For higher pressures the influence weakens as well as in the previous cases.

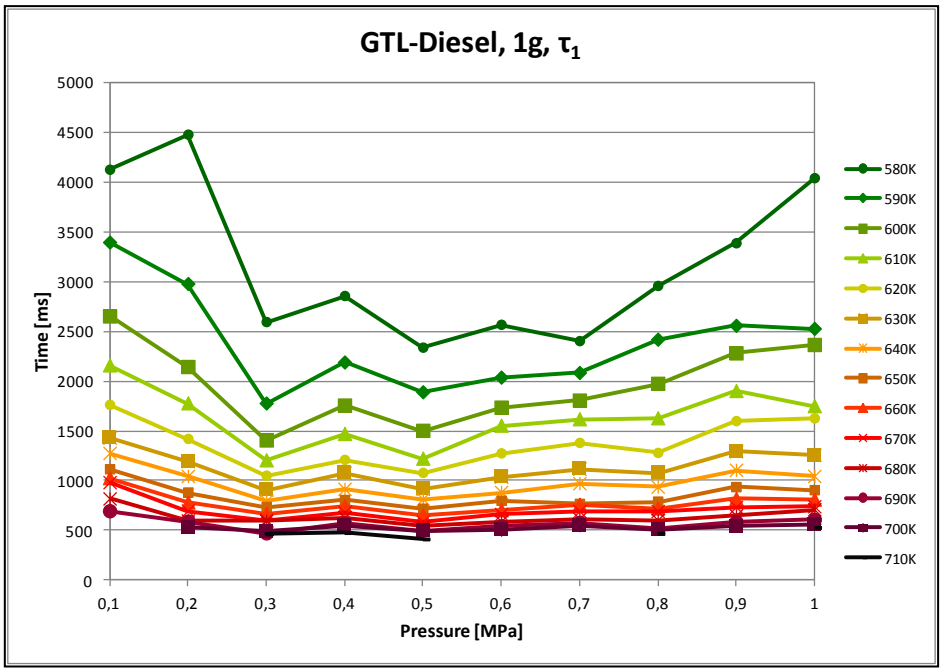

Fig. 45 - Experimental data on the first ignition delay times of GTL-Diesel and the influence of ambient pressure

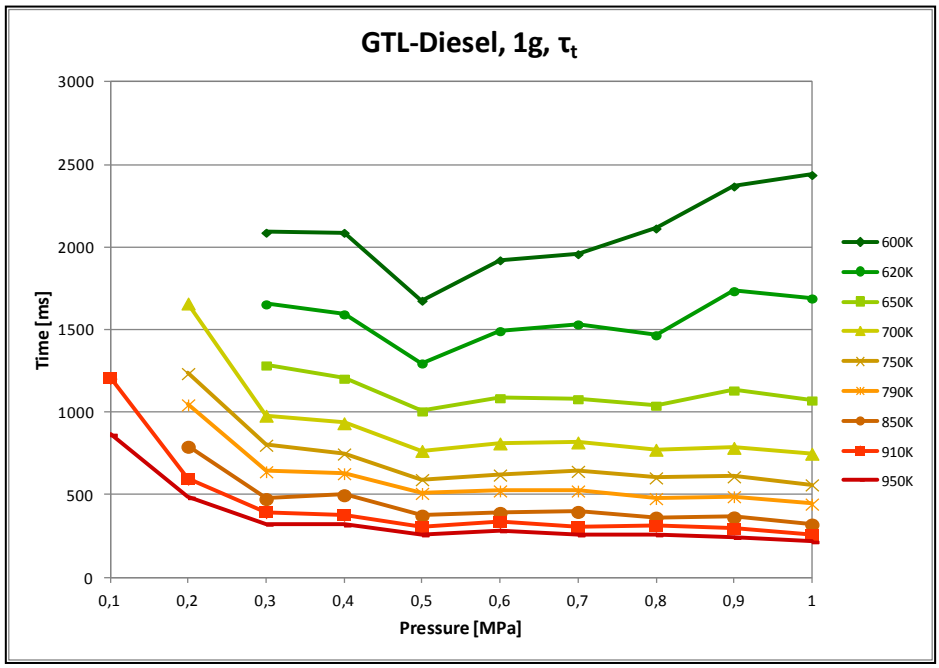

Fig. 46 - Experimental data on the total ignition delay times of GTL-Diesel and the influence of ambient pressure

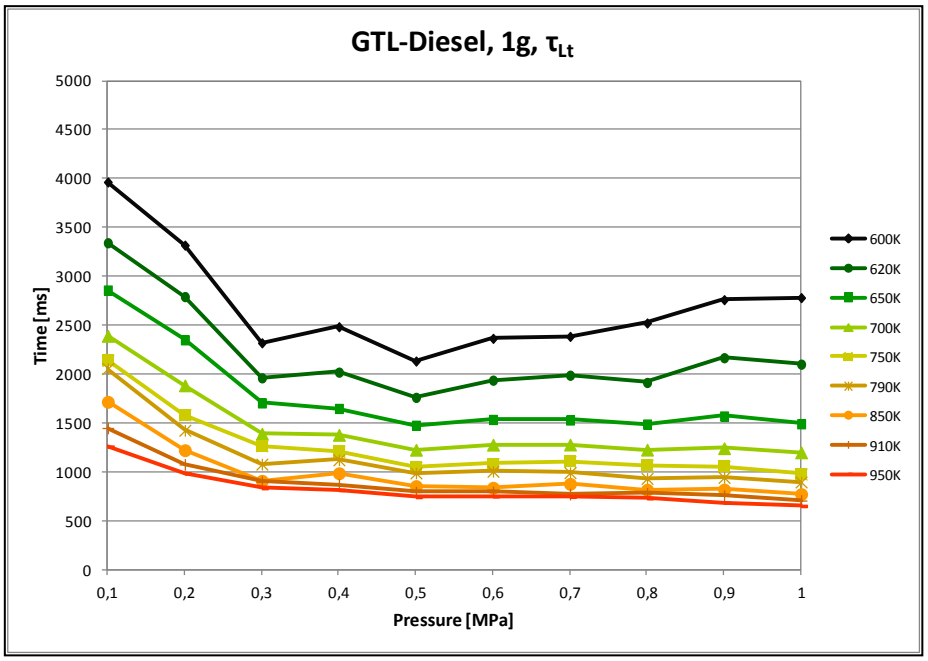

Fig. 47 - Experimental data on the droplet lifetimes of GTL-Diesel and the influence of ambient pressure

Summary of the Autoignition Experiments for GTL-Diesel conducted under Normal Gravity Conditions and Classification of the Ignition-Types observed

In this subsection, the experimental data presented previously on the autoignition of GTL-Diesel at normal gravity is summarized and single-term exponential fits of the Arrhenius-type such as

Eq. 34

$$\tau = A \cdot p^n \cdot e^{\frac{E}{T}}$$

and two-term exponential fits, as e.g.

Eq. 35

$$\tau = A_1 \cdot p^n \cdot e^{\frac{E_1}{T}} + A_2 \cdot p^m \cdot e^{\frac{E_2}{T}}$$

where *A,n* and m are empirical values determined by the regression, E is the global activation energy of the fuel, are shown. No data on these values is available for GTL-Diesel, and thus has to be determined by the regression. *T* and *p* are ambient temperature and pressure respectively. These regressions are shown for τ_1, τ_t, and τ_{Lt} in the following figures. For comparison and visualization purposes, figures showing linear interpolations have been added in order to present the raw experimental data. The values obtained from the regressions and the quality of the fits is listed in the table succeeding the previously mentioned figures. As expected and based on the values obtained for the quality of the fits, two-term exponential fits offer better results,. The two-term exponential regression reflects the two main ignition processes involved.

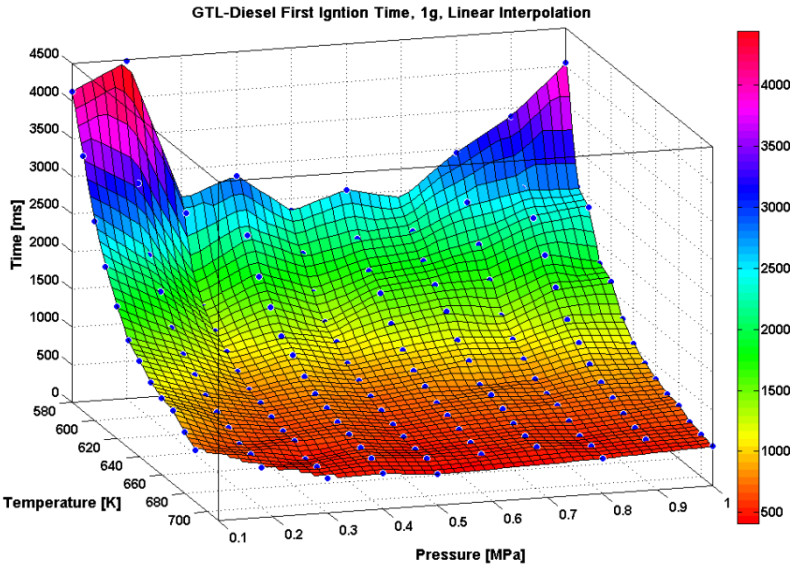

Fig. 48 – Experimental data on the first ignition time for GTL-Diesel under 1g

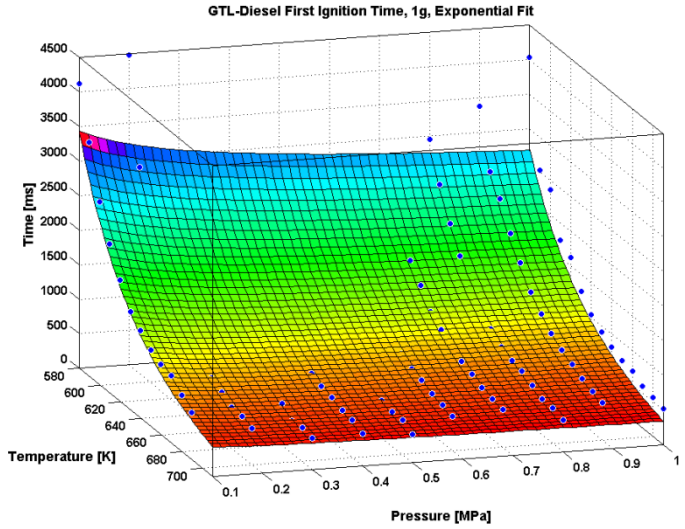

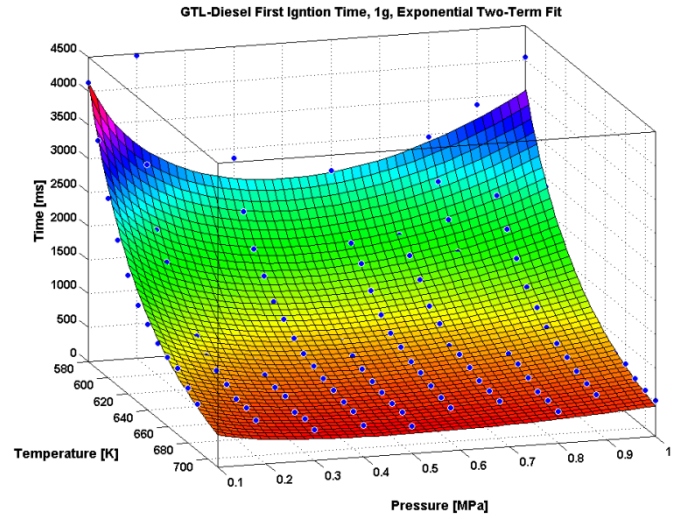

Fig. 49 - Exponential fits on the experimental data for the first ignition time of GTL-Diesel at normal gravity conditions

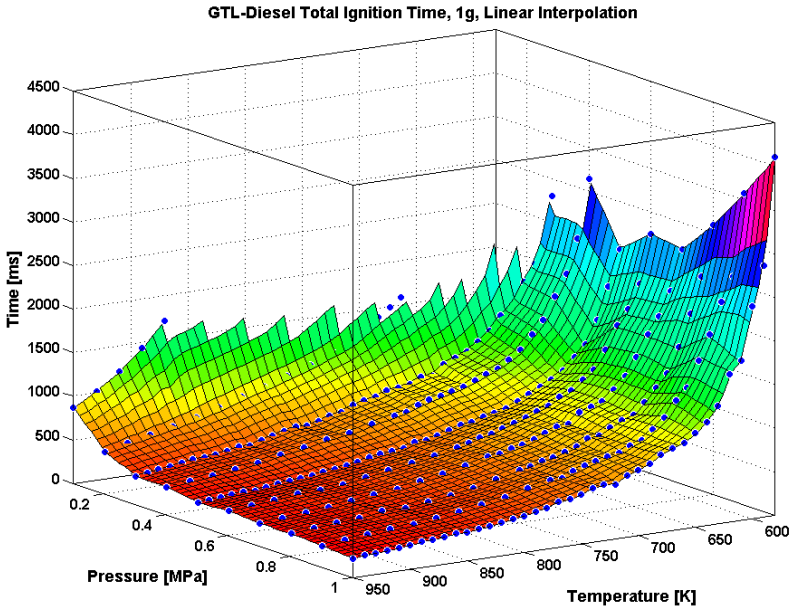

Fig. 50 – Experimental data on the total ignition time of GTL-Diesel under 1g

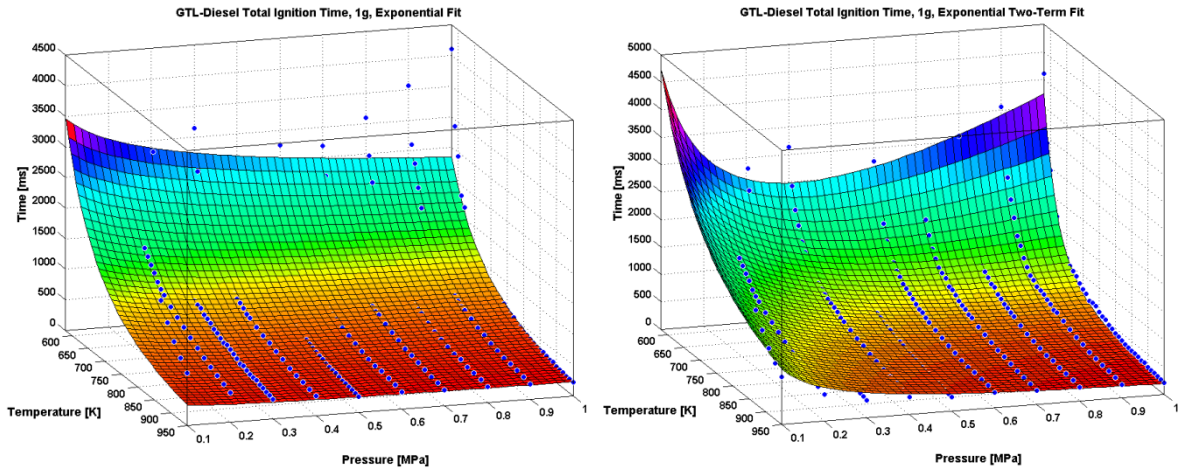

Fig. 51 - Exponential fits on the experimental data for the total ignition time of GTL-Diesel at normal gravity conditions

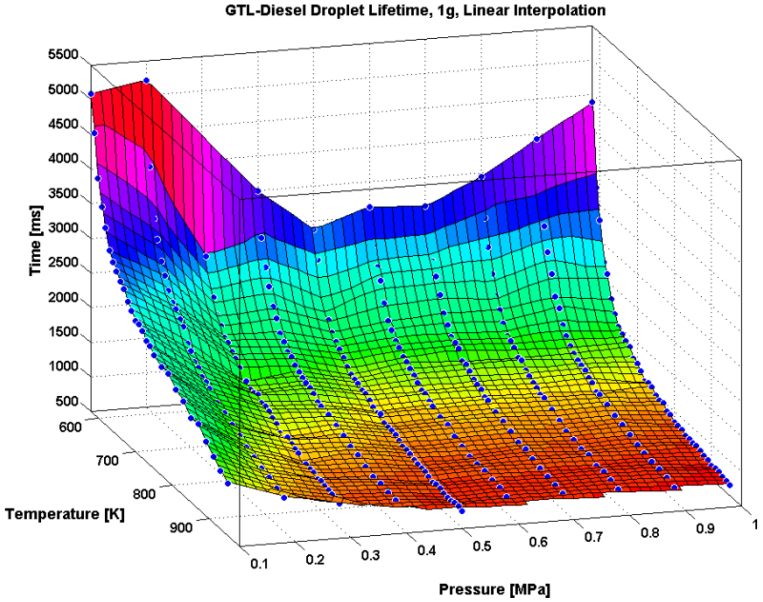

Fig. 52 – Experimental data on the droplet lifetime of GTL-Diesel under 1g (linear interpolation)

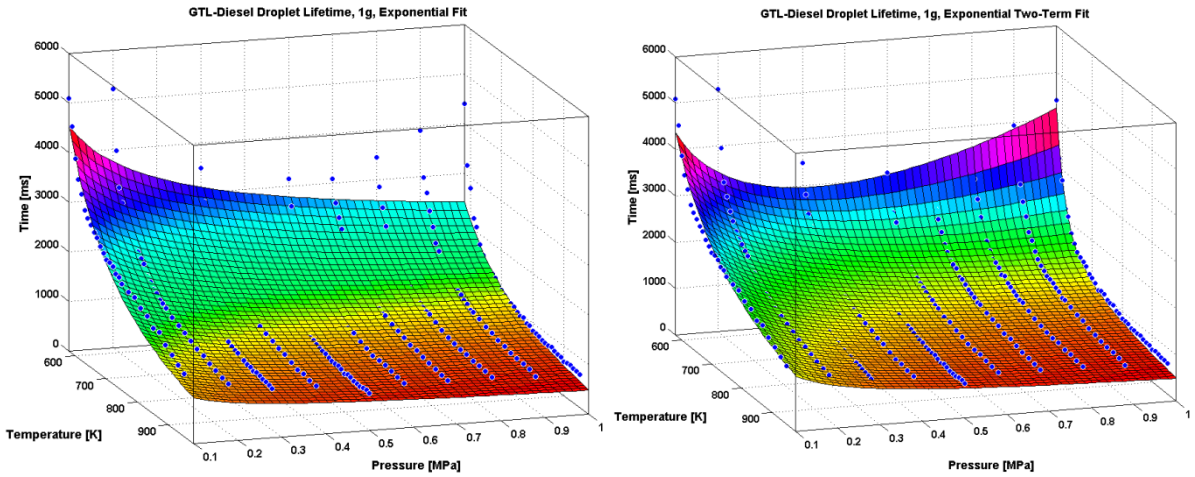

Fig. 53 – Exponential fits on the experimental data for the droplet lifetime of GTL-Diesel at normal gravity conditions

Regressions for τ_1, 1g					
Equation Type	**Coefficient**		**SSE**	**R^2**	**Adjusted-R^2**
Exponential	A	0,03245	1,139e7	0,881	0,8792
	E	6570			
	n	-0,1059			
Exponential 2 Terms	A_1	0,01274	4,483e6	0,9532	0,9514
	A_2	0,03139			
	E_1	6818			
	E_2	6393			
	m	2,478			
	n	-0,4066			

Regressions for τ_t, 1g					
Equation Type	**Coefficient**		**SSE**	**R^2**	**Adjusted-R^2**
Exponential	A	4,513	1,33e7	0,8738	0,8728
	E	3660			
	n	-0,09665			
Exponential 2 Terms	A_1	0,0006388	3,269e6	0,9724	0,9719
	A_2	17,9			
	E_1	8882			
	E_2	2261			
	m	-0,7167			
	n	1,419			

Regressions for τ_{Lt}, 1g					
Equation Type	**Coefficient**		**SSE**	**R^2**	**Adjusted-R^2**
Exponential	A	47,34	2,449e7	0,876	0,8752
	E	2283			
	n	-0,2706			
Exponential 2 Terms	A_1	2,778e-7	1,005e7	0,9491	0,9483
	A_2	77			
	E_1	1,328e4			
	E_2	1824			
	m	-0,3837			
	n	1,912			

Tab. 24 - Coefficients of the regressions for the induction delay times of GTL-Diesel at normal gravity conditions and evaluation of the quality of the fits

The following characteristic map summarizes the different ignition types encountered on the experiments performed. The line labeled “T cool begin” is the measurable cool flame lower limit, or the lowest temperature at which a cool flame is detected with the experimental apparatus employed in this study. “T cool begin ex.” is an extrapolation of the “T cool begin”

line. Consequentially the line labeled “T cool end” shows the highest temperature at which a cool flame is detected for each pressure step. The line denoted as “T hot begin” shows the first appearance of a hot flame. For 0,1 MPa only single-stage ignitions are detected. At T > 560 K a cool flame is detected. In the range of 690-870 K no ignition is observed. For T > 870 K hot flames are observed. At all pressures, below 550 K no ignitions are observed. For pressure levels between 0,2-0,5 MPa a two-stage ignition regime is preceded by a cool-flame single stage region at lower temperatures. Note that for experiments at ambient pressures of 0,5 MPa and higher, no cool flame single-stage regime is observed. As has been mentioned before, no cool flame is detected above 710 K and a single-stage hot flame regime exists above this temperature for all pressure levels, except for pressures lower than 0,2 MPa.

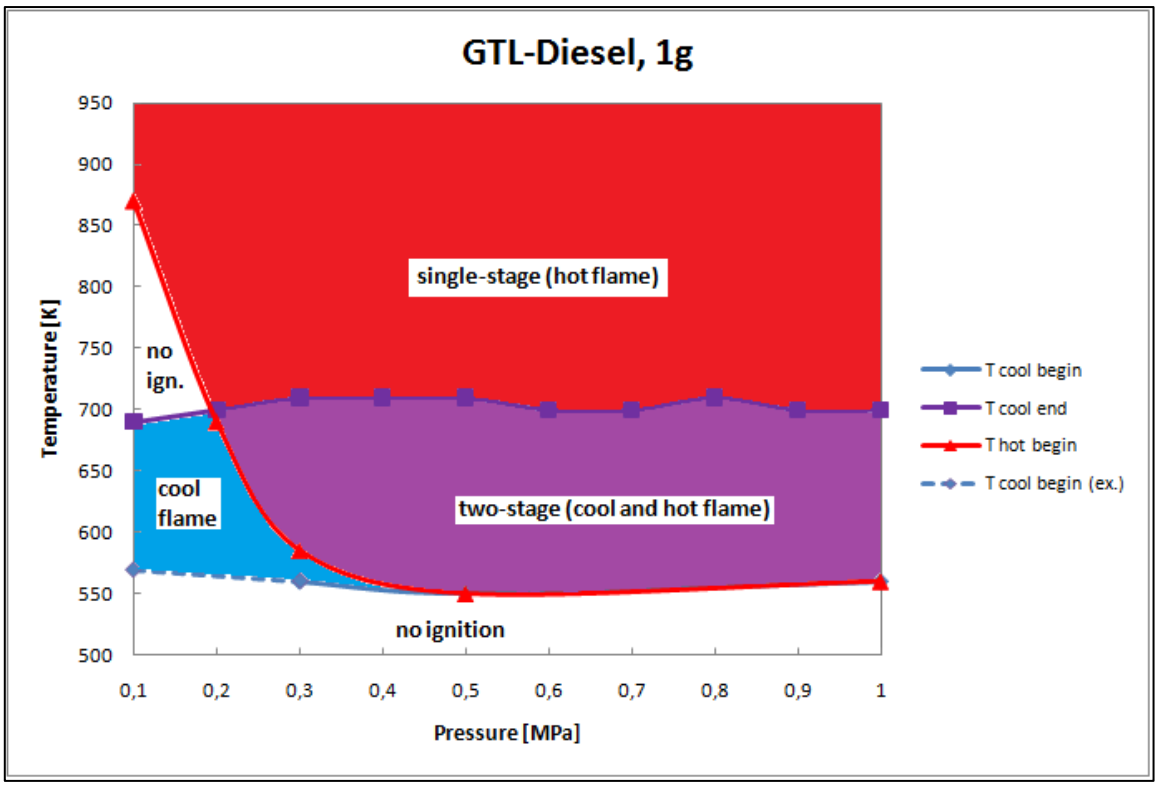

Fig. 54 – Characteristic map of ignition types for GTL-Diesel droplets at normal gravity condition

3.5.2. Microgravity Autoignition Experiments

Experiments on the autoignition of GTL-Diesel under microgravity conditions are presented in this section. The experiments were conducted for three pressure levels (0,3/0,5 and 1,0 MPa) in the temperature range between 550-800 K. Due to time and cost constraints and drop tower availability, in general two experiments for each data point were performed. This should serve as an explanation for the larger scattering in the data points obtained. The influence of ambient temperature and pressure on the ignition delay times is described in the following subsections. The following diagrams show the induction times for the three previously mentioned pressure levels. Two-term (Arrhenius-type) exponential regression fits are shown as well. The respective values of the coefficients of the regression fits are listed at the end of the subsequent section.

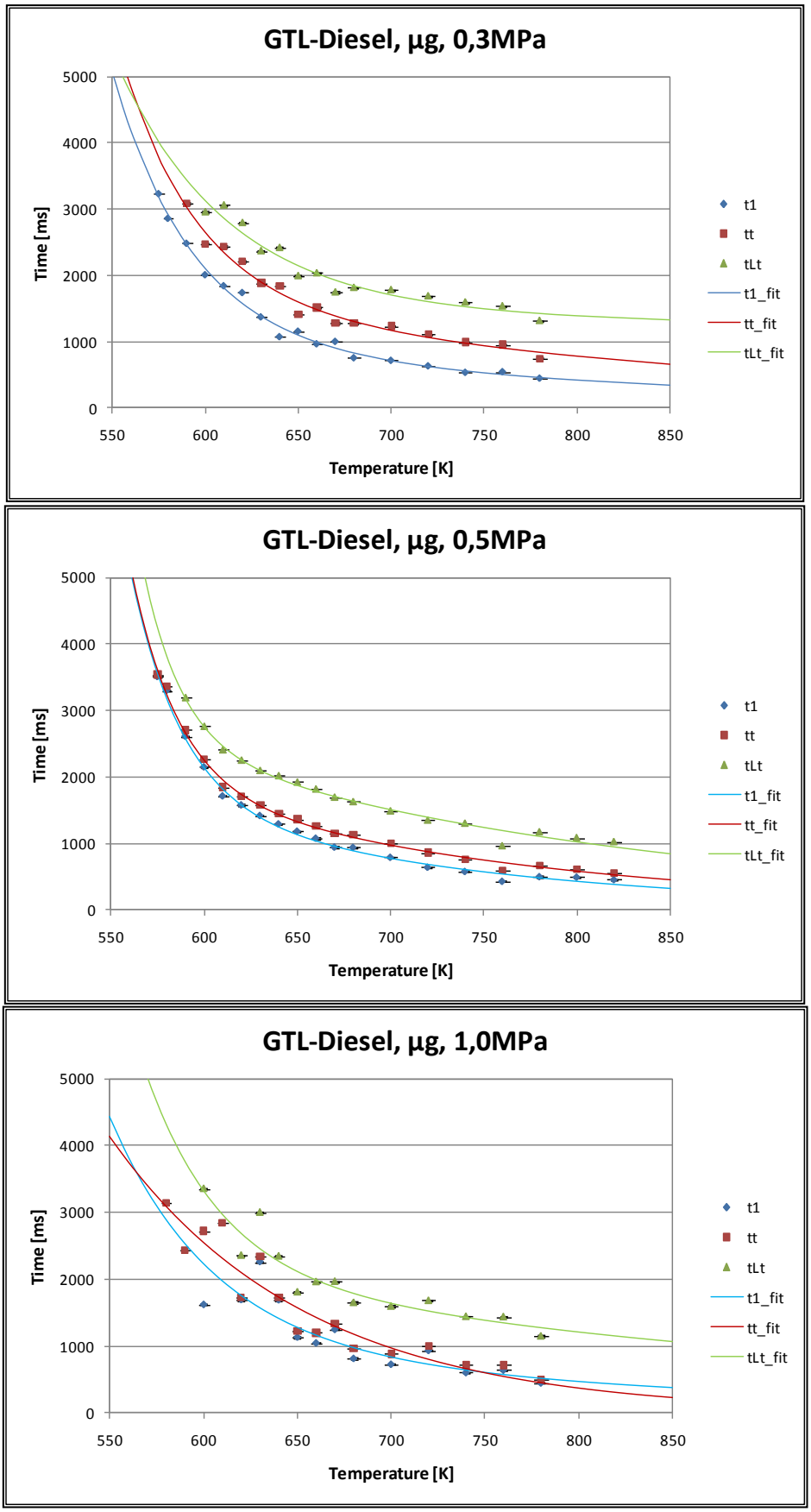

Fig. 55 – Experimental data and regression fits of the ignition delay times of GTL-Diesel in µg

Influence of Ambient Temperature on the Ignition Delay Times

The following diagrams show the behavior of τ_1, τ_t and τ_{Lt} for GTL-Diesel under microgravity conditions. The diagrams show, for the three pressure levels analyzed, similar progressions, meaning that the measured ignition delay times show relatively small differences between each pressure level at a given temperature. These differences are the smallest for τ_1 averaging 70 ms, for τ_t 270 ms and for τ_{Lt} 300 ms.
The diagram for the second induction times show the difference in the extent, for each pressure level, of the temperature range where both, cool and hot flames, are detectable. For 0,3 MPa this region ranges from 590 to780 K, for 0,5 MPa 575 to 820 K and for 1,0 MPa 620 to 780 K. As can be seen with increasing pressure the second ignition time decreases. The second induction times for 0,3 MPa show great scattering in the range between 600-670 K. These data points are based on single experiments, thus no averaging can be performed.
The diagram for the hot flame combustion times shows for 0,5 MPa the largest temperature range (590-820 K) where hot flames are detected. The hot flame combustion time shows for a fixed pressure level relatively small temperature dependence. Up to 670 K, with increasing pressure, τ_C tends to increase. Beyond 670 K the 1,0 MPa data still has the largest times, but the 0,3 MPa surpass the 0,5 MPa data.

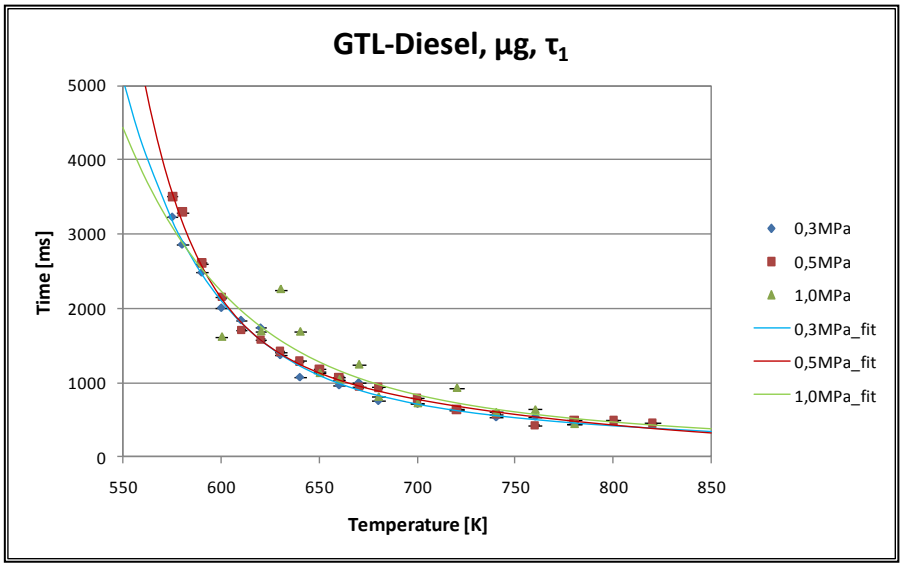

Fig. 56 – First ignition delay times for GTL-Diesel under µg

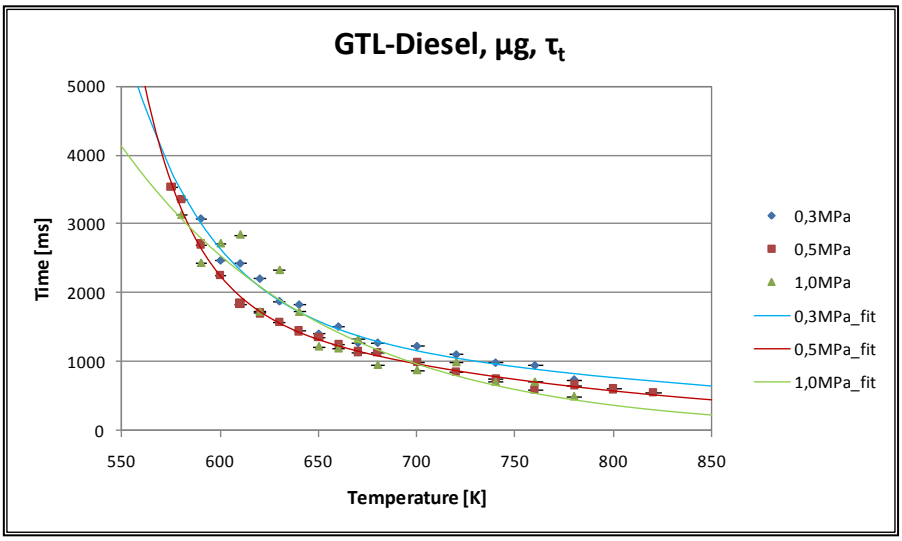

Fig. 57 – Total ignition times for GTL-Diesel under µg

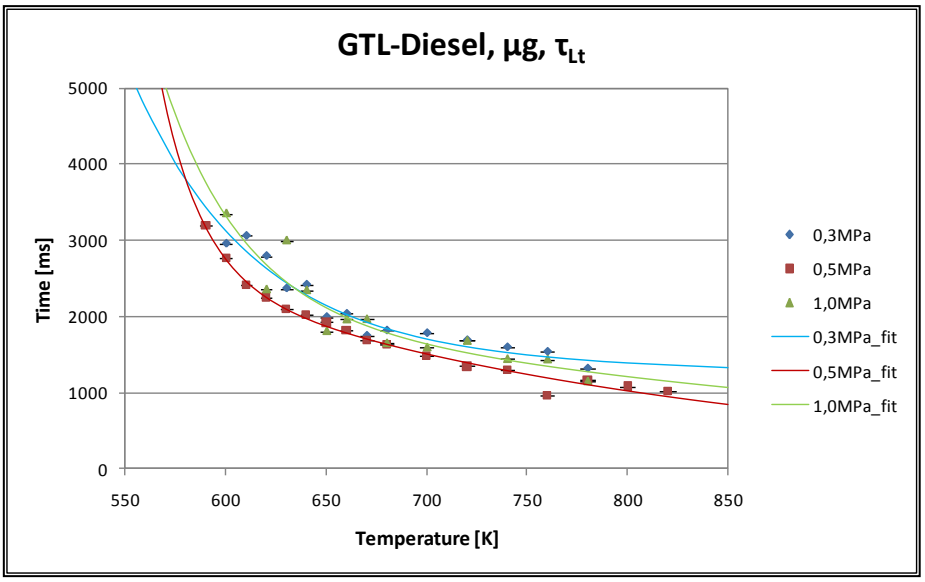

Fig. 58 – Droplet lifetimes for GTL-Diesel under µg

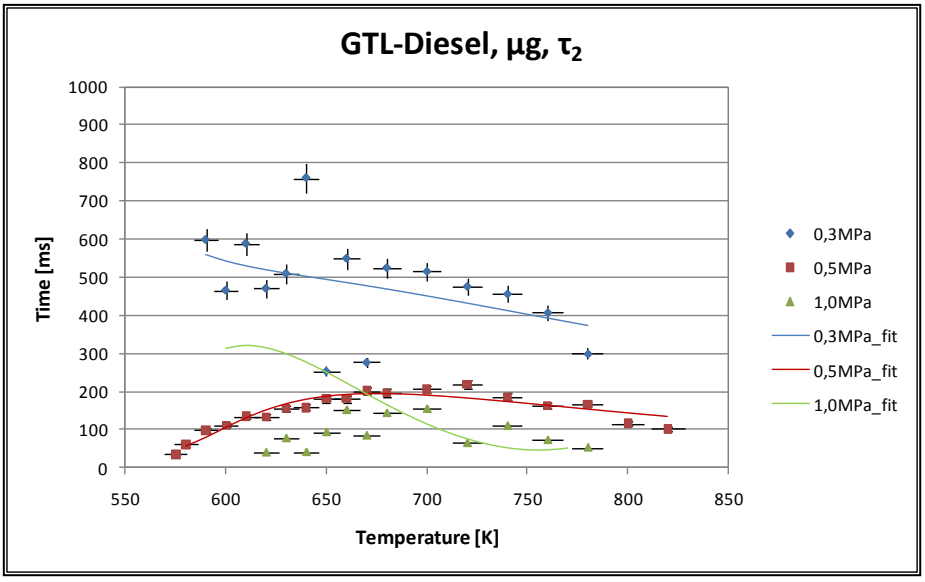

Fig. 59 - Second ignition times for GTL-Diesel under µg

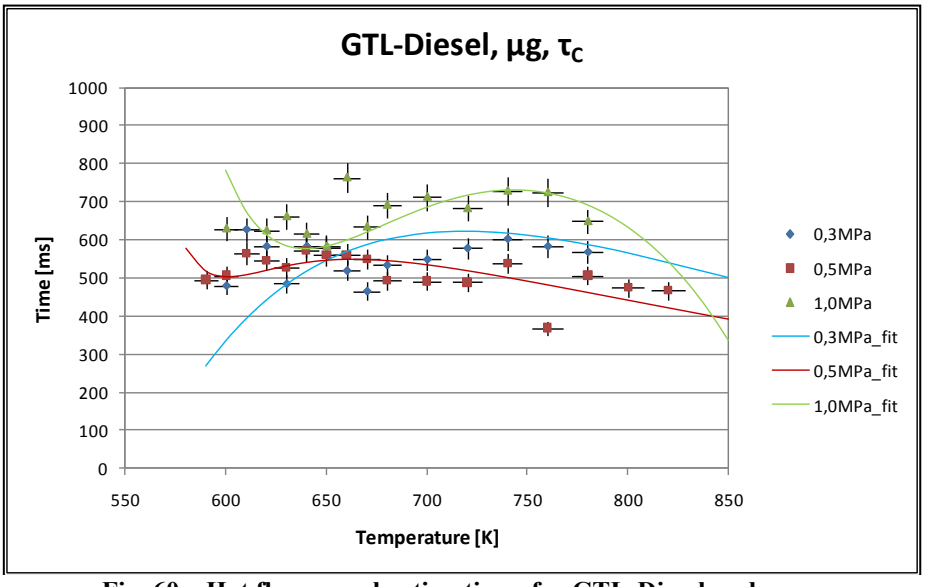

Fig. 60 – Hot flame combustion times for GTL-Diesel under µg

The following tables list the values of the regressions fits. As can be seen, two-term exponential fits have better R^2 values.

Regressions for τ_l at 0,3 MPa, µg			**Regression for τ_t at 0,3 MPa, µg**		
Equation Type	**Coefficient**		**Equation Type**	**Coefficient**	
Exponential	a	4,031e6	Exponential	a	2,967e5
	b	-0,01253		b	-0,007919
	R^2	0,9692		**R^2**	0,9388
Exponential 2 Terms	a	1,704e9	Exponential 2 Terms	a	3,733e9
	b	-0,02355		b	-0,02497
	c	8017		c	1,085e4
	d	-0,003713		d	-0,003312
	R^2	0,9925		**R^2**	0,9797

Regressions for τ_l at 0,5 MPa, µg			**Regression for τ_t at 0,5 MPa, µg**		
Equation Type	**Coefficient**		**Equation Type**	**Coefficient**	
Exponential	a	5,155e6	Exponential	a	1,227e6
	b	-0,01283		b	-0,01036
	R^2	0,9508		**R^2**	0,935
Exponential 2 Terms	a	2,731e12	Exponential 2 Terms	a	2,084e13
	b	-0,03654		b	-0,04028
	c	3.845e4		c	3,352e4
	d	-0,005604		d	-0,005077
	R^2	0,9961		**R^2**	0,9962

Regressions for τ_l at 1,0 MPa, µg			**Regression for τ_t at 1,0 MPa, µg**		
Equation Type	**Coefficient**		**Equation Type**	**Coefficient**	
Exponential	a	2,067e5	Exponential	a	8,392e5
	b	-0,007753		b	-0,009663
	R^2	0,7428		**R^2**	0,9012
Exponential 2 Terms	a	7,981e7	Exponential 2 Terms	a	1,324e6
	b	-0,01831		b	-0,01043
	c	7226		c	0,001999
	d	-0,003504		d	0,01472
	R^2	0,8622		**R^2**	0,9045

Tab. 25 – Coefficients of the regressions for τ_l and τ_t and evaluation of the quality of the fits

Influence of ambient pressure on the ignition delay times

The following diagrams show the influence of the ambient pressure on the autoignition behavior of GTL-Diesel under microgravity conditions. The general behavior for the ignition delay times is characterized by a weak dependence on pressure. For τ_l and temperature up to 600 K, an increase in pressure shows an increase in the first ignition delay time. For higher temperatures, this tendency gets weaker exemplified by the almost horizontal curves seen in the diagram. The τ_t-diagram shows for all temperatures the general tendency that for higher pressures a decrease of the total ignition times is observed. A similar behavior is seen on the τ_{Lt}-diagram for 0,3 and 0,5 MPa. For 1,0 MPa the droplet lifetimes are larger than the data points at lower pressures. This behavior is less pronounced at higher temperatures, flattening at 780 K. Some temperature lines show crossings with other lower temperature lines, as in the case of the 630 K line in the τ_l-diagram. The reason for this lies in the larger scattering of the experimental data obtained.

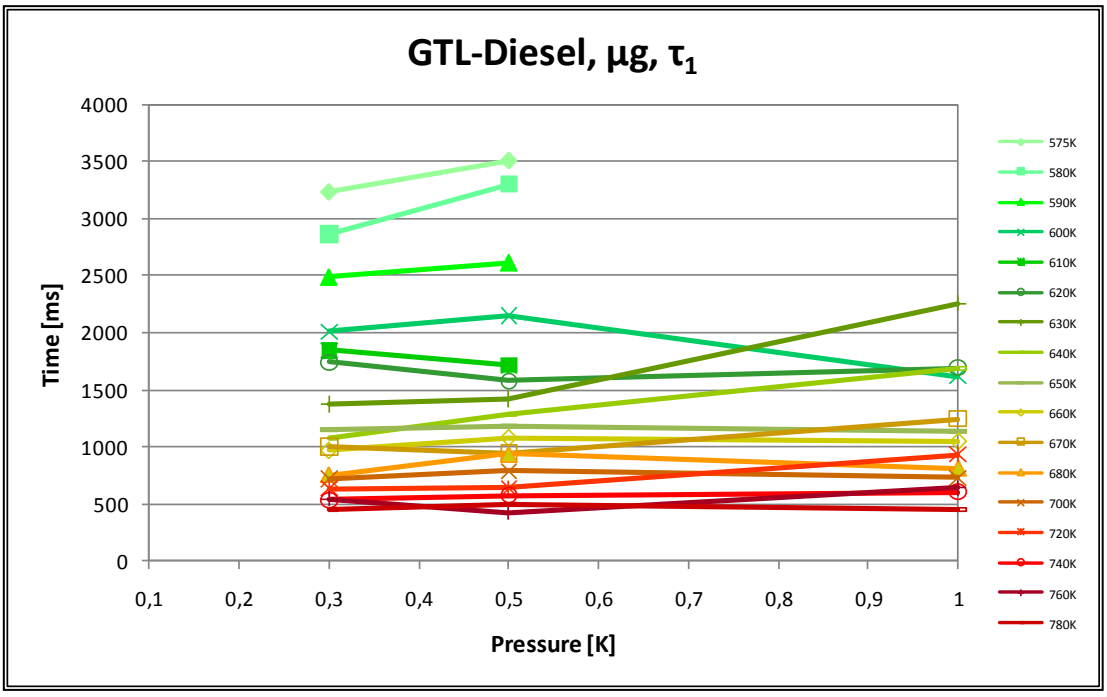

Fig. 61 – Experimental data on τ_1 of GTL-Diesel in µg and the influence of ambient pressure

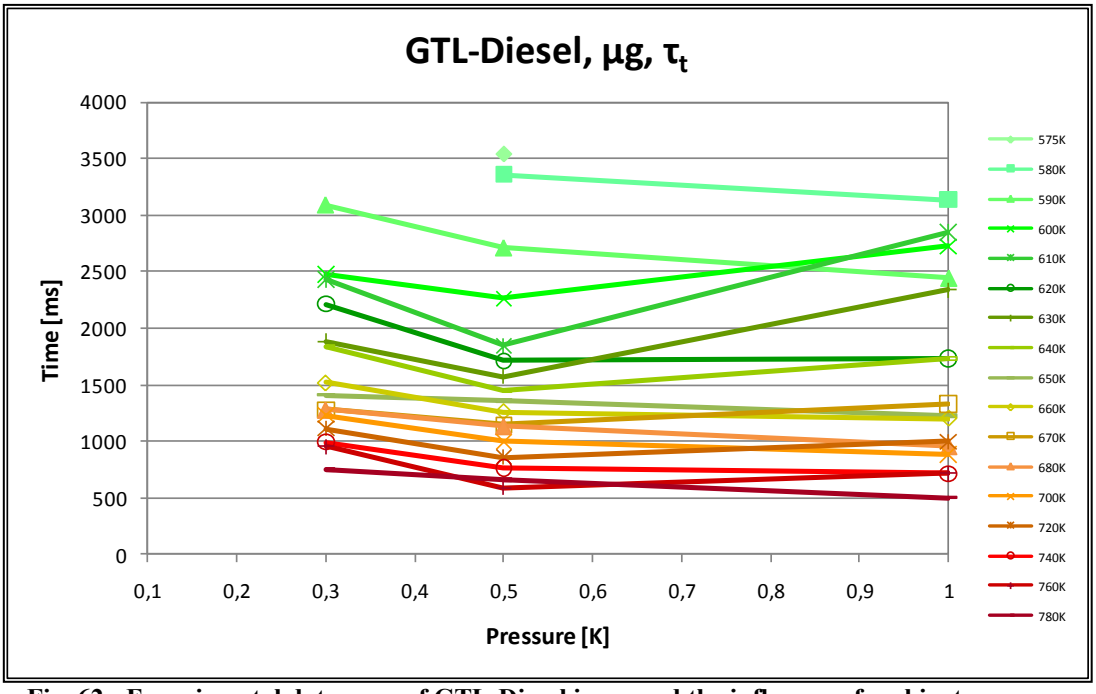

Fig. 62 - Experimental data on τ_t of GTL-Diesel in µg and the influence of ambient pressure

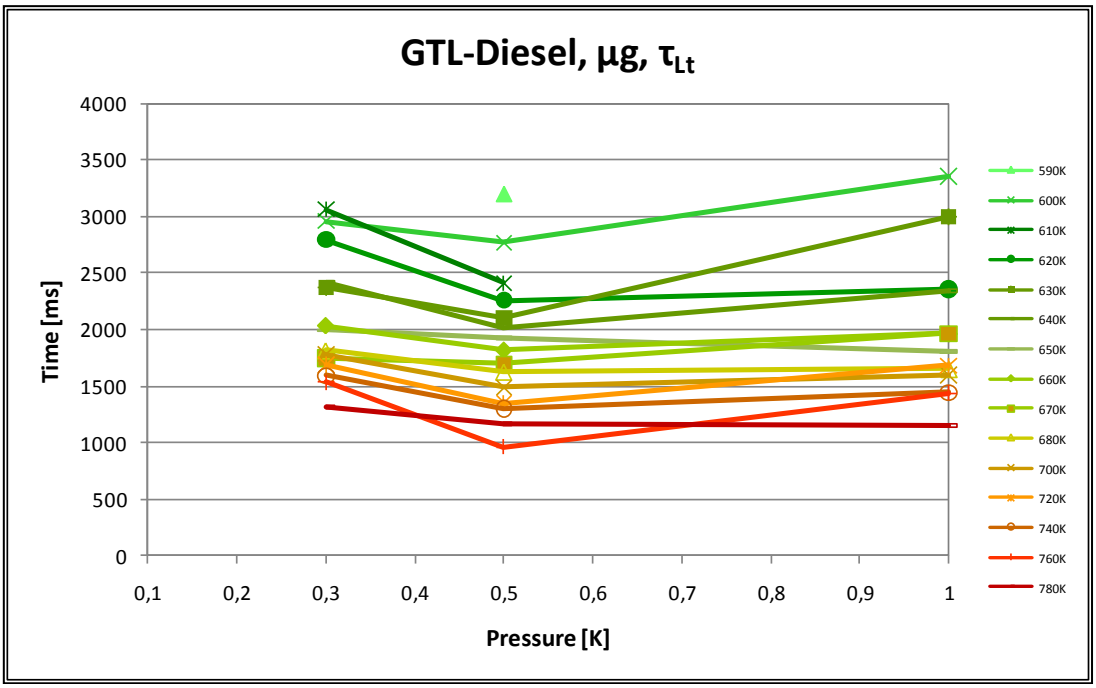

Fig. 63 - Experimental data on τ_{Lt} of GTL-Diesel in µg and the influence of ambient pressure

Classification of the Ignition-Types observed

The following "ambient pressure"-"ambient temperature" characteristic map summarizes the results previously presented and shows a classification of the experimental data according their ignition types. The "T cool begin" curve delineates the measurable cool flame lower limit, "T cool end" the cool flame upper limit. "T hot begin" shows the hot flame lower limit. As presented before, only data for 0,3/0,5 and 1,0 MPa is available. The lines marked with "ex." in the diagram legend denote extrapolations of the lines obtained experimentally. The experiments concentrated on acquiring data of the two-stage region where both cool and hot flames appear. Only one data point at 0,5 MPa denotes the highest temperature at which cool flames are detected. The extrapolation of this line is intended only for illustration purposes.
Below 570 K no ignition is observed. Three single-stage ignitions are observed, a cool flame only region between 0,1-0,5 MPa and 570-620 K, a "low temperature" hot flame region where no preceding cool flame is observed in the temperature range of 575-600 K and pressures between 0,5-1,0 MPa and a "high temperature" hot flame region expected to be at temperature above 780 K for all pressures. The region framed by the single-stages is the two-stage ignition region where both, cool and hot flames, are observed.

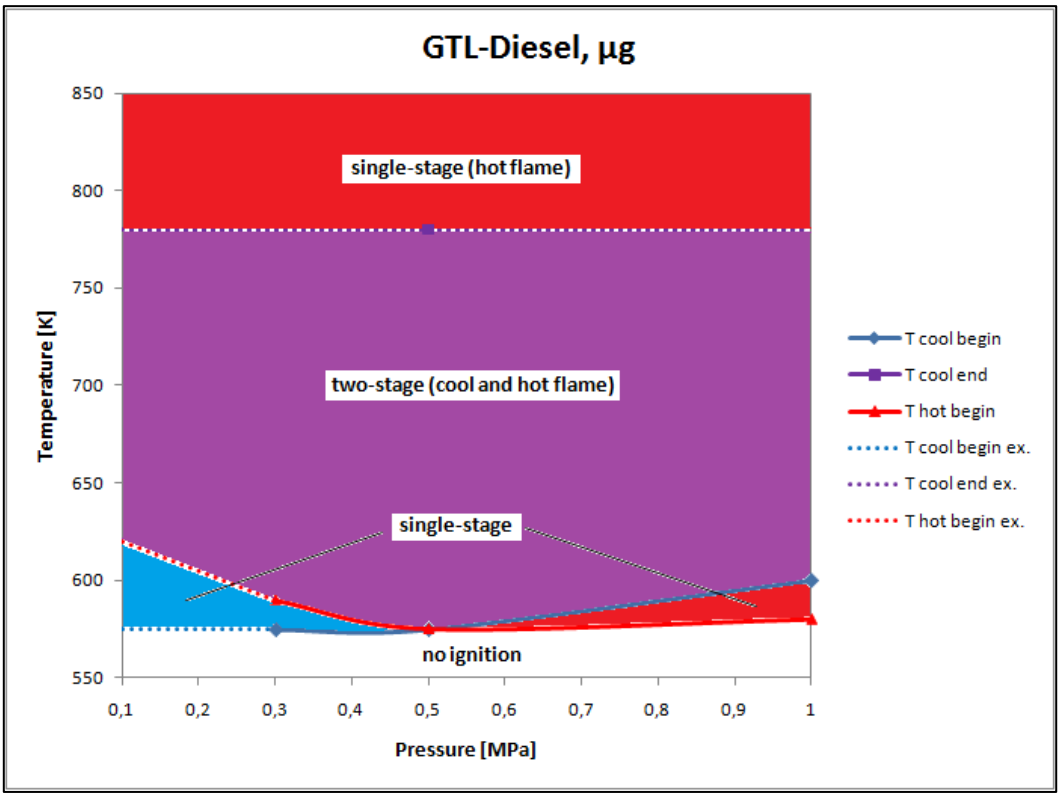

Fig. 64 – Characteristic map of ignition types for GTL-Diesel droplets at microgravity conditions

3.5.3. Comparison of Normal-g and Microgravity Experiments

An expected discrepancy concerning the experimental results obtained during the µg and normal-g experiments, due to the absence of natural or buoyant convection which affects the transport of oxidizer, is presented in this section. The diagrams shown here are intended to illustrate the resulting differences and the influence of the gravity environment on the autoignition of single fuel droplets of GTL-Diesel.

The adjacent diagrams depict the difference in the autoignition behavior of the cool flame. The cool flame appears at lower ambient temperatures in normal-g conditions. Under µg the cool flames appear at higher temperatures and the first induction time shows higher values.

For the total ignition delay times a similar behavior is observed, the first hot flame detection occurs at higher temperatures for the µg data and the τ_t values are higher. For increasing pressures the difference between the µg and normal-g measured values decreases.

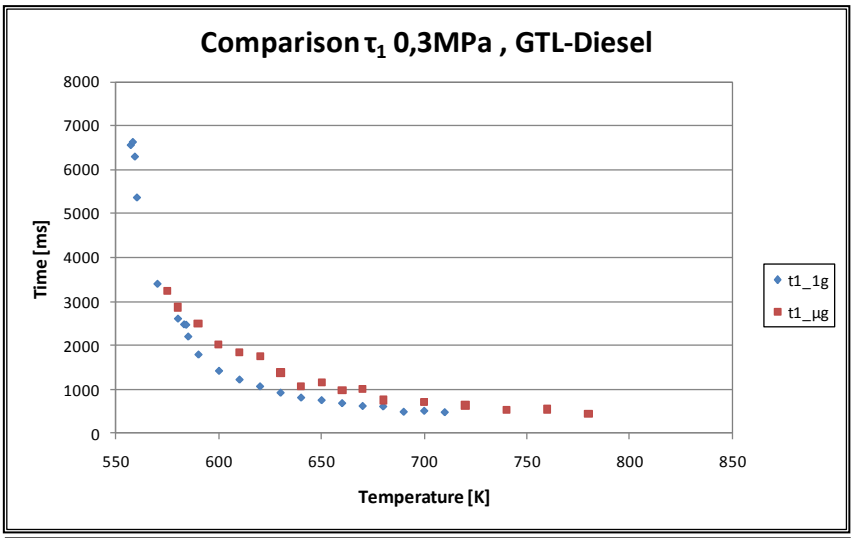
Comparison τ1 0,3MPa , GTL-Diesel
Time [ms]
Temperature [K]
t1_1g
t1_µg

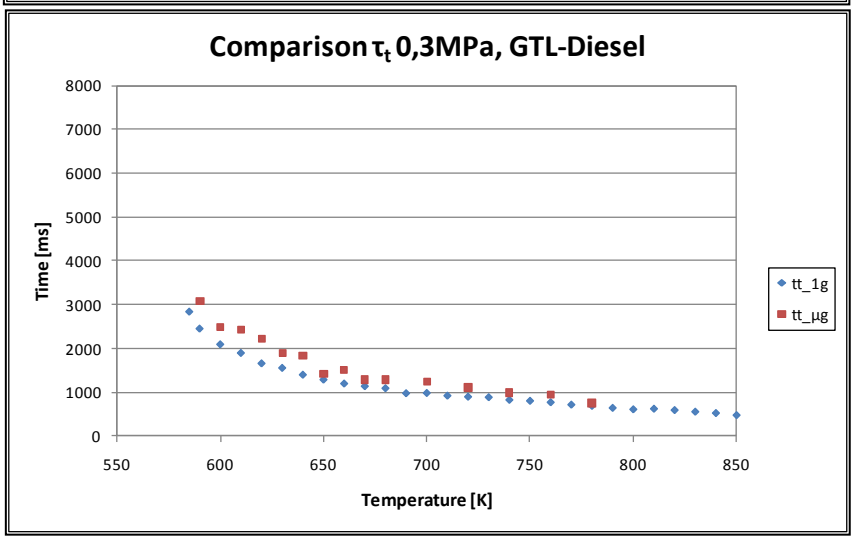
Comparison τt 0,3MPa, GTL-Diesel
Time [ms]
Temperature [K]
tt_1g
tt_µg

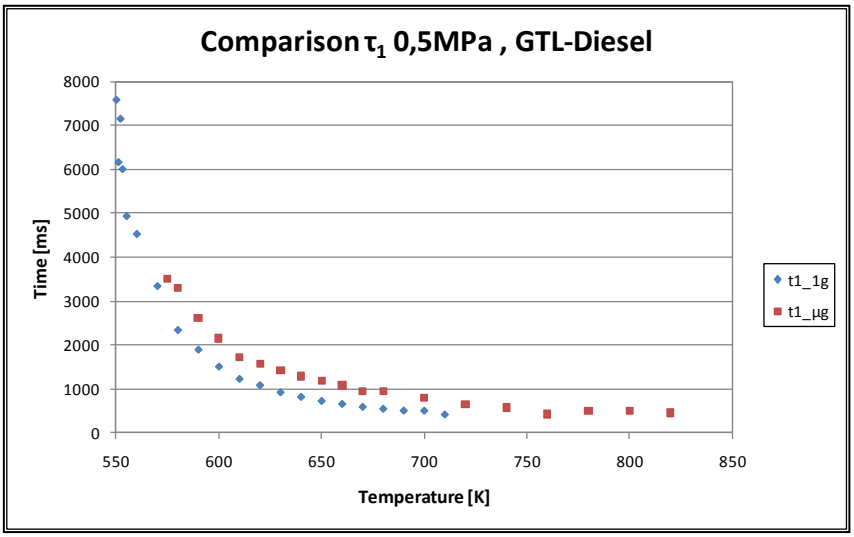
Comparison τ1 0,5MPa , GTL-Diesel
Time [ms]
Temperature [K]
t1_1g
t1_µg

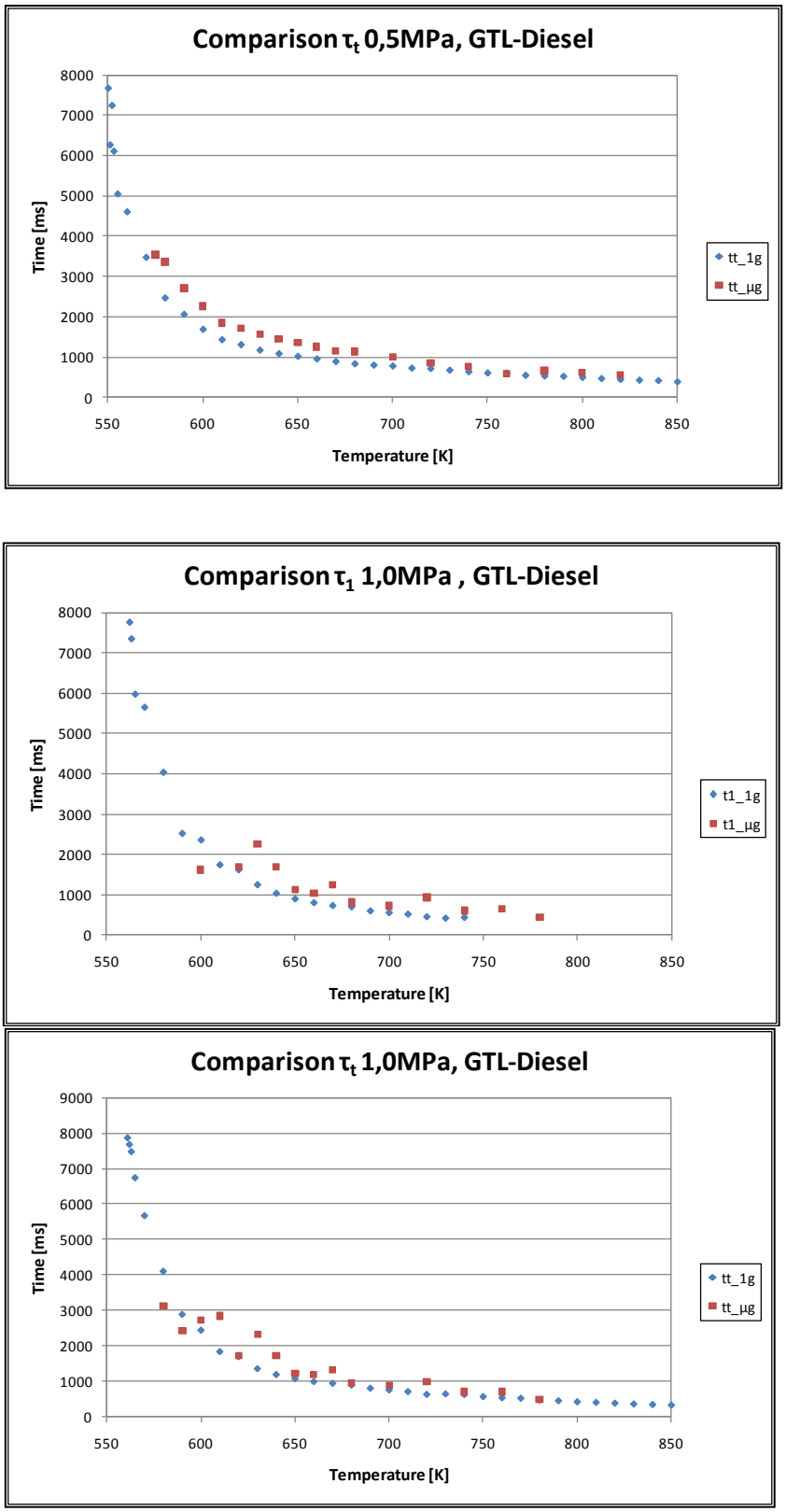

Fig. 65 – Comparison of the first and total induction times for GTL-Diesel for microgravity and normal-g conditions

The droplet lifetimes of GTL-Diesel under microgravity and normal gravity show a very similar behavior like the previous ignition delay times.

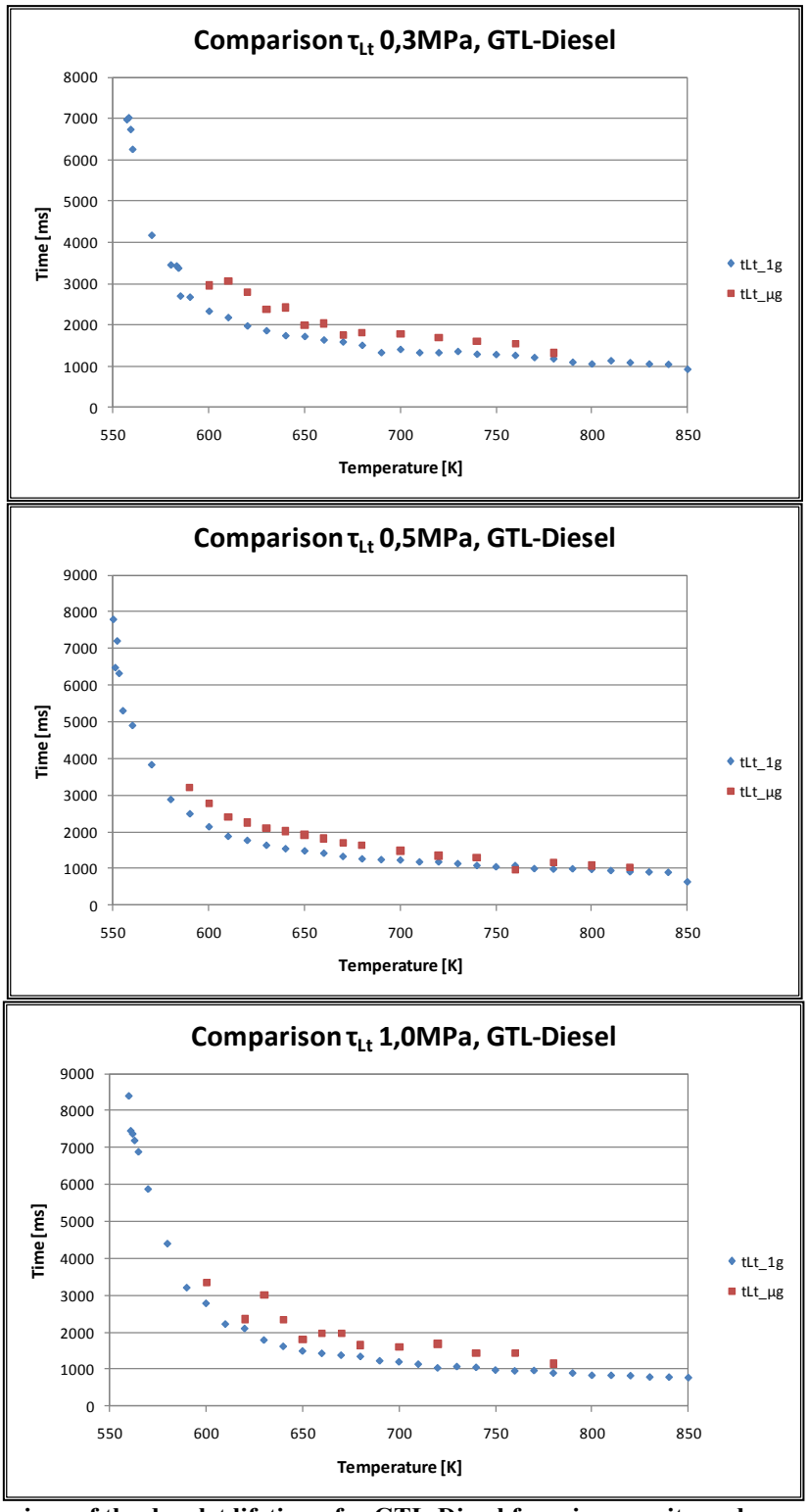

Fig. 66 – Comparison of the droplet lifetimes for GTL-Diesel for microgravity and normal-g conditions

For τ_2 and τ_C the influence of the gravity environment is shown in the following diagrams. For τ_2 the values under µg conditions are generally lower than the normal-g, meaning that the cool flames have shorter combustion periods under µg.
For τ_C the behavior is different. The experimental results for normal-g, tend to converge to a constant value at about 450 ms. For µg the values show plateaus at temperatures >650 K, but have higher values than the normal-g counterparts, meaning that the hot flame combustion time is generally longer under µg for GTL-Diesel.

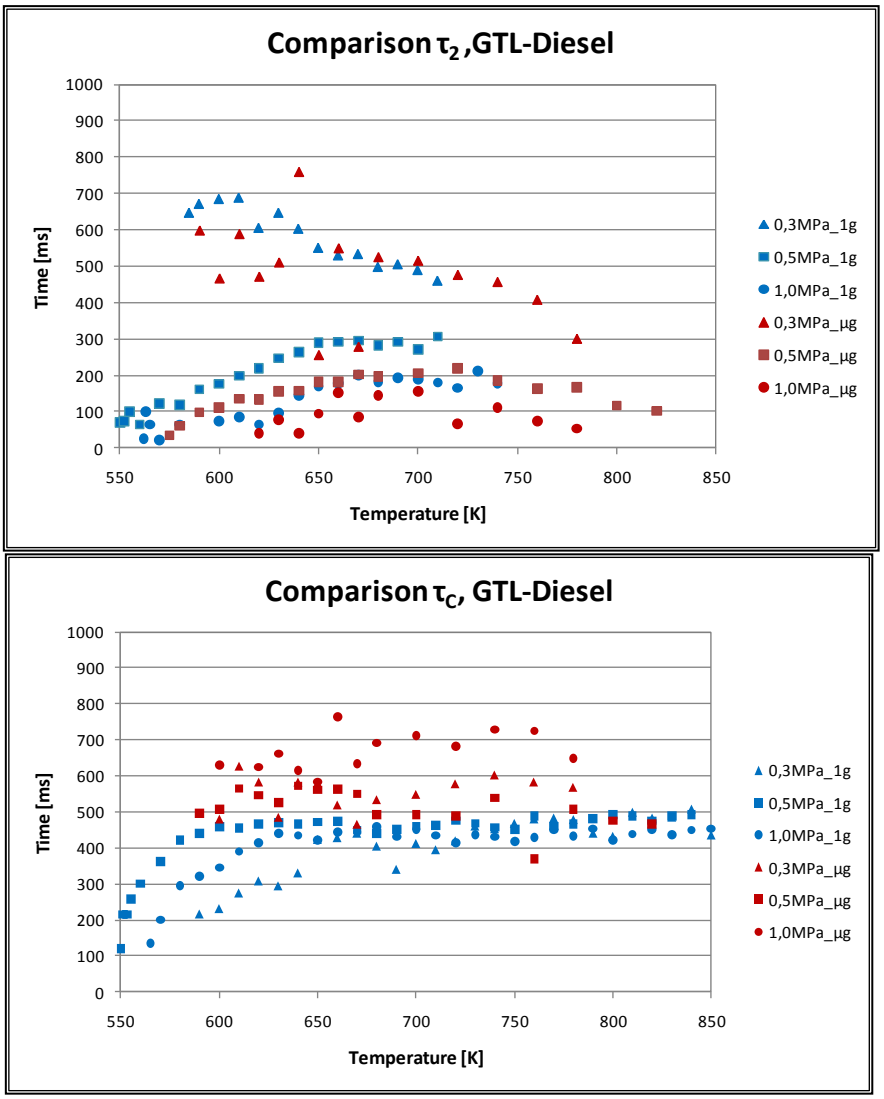

Fig. 67 – Comparison of the second ignition delay and hot flame combustion times for GTL-Diesel for microgravity and normal-g conditions

3.5.4. Determination of a suitable Surrogate Fuel for GTL-Diesel

The approach used in this study for the selection of the components for the surrogate fuel formulation differs from the general procedure described in section 2.1.5. This stems from the circumstance that for this study no permission was given by the fuel manufacturer for a detailed chemical analysis of the fuel samples provided. The only information provided, concerning the composition of the fuels, is that no aromatic compound is present in the Fischer-Tropsch fuels.

The basic approach for the determination of a suitable model fuel for GTL-Diesel is as follows:

- Selection of a base component from a known major component of the analyzed fuel, usually an aliphatic compound such as an n-alkane.
- Selection of an additive or series of additives to approach the required behavior (e.g. autoignition behavior in different pressure and temperature regimes). The nature of

this additive can be aliphatic (cyclic or acyclic) or aromatic. (Although preferably aromatic compounds are avoided.)

As stated at the beginning of this section, only data obtained with normal-g experiments is used for the selection and determination of the model fuel for GTL-Diesel.

Selection of an n-alkane

The following diagrams depict the comparison of the experimental results for the characterization of the ignition delay times obtained for GTL-Diesel and the autoignition behavior of n-alkanes as candidates for the base component of the surrogate fuel. The n-alkanes selected are n-decane, n-dodecane, n-tetradecane and n-hexadecane and the experimental data shown is for three pressure levels (0,3/0,5 and 1,0 MPa) at normal-g conditions. The data is shown also in logarithmic scaling, which allows for a better visual separation and clarity of the data points at higher temperatures and lower ignition times.

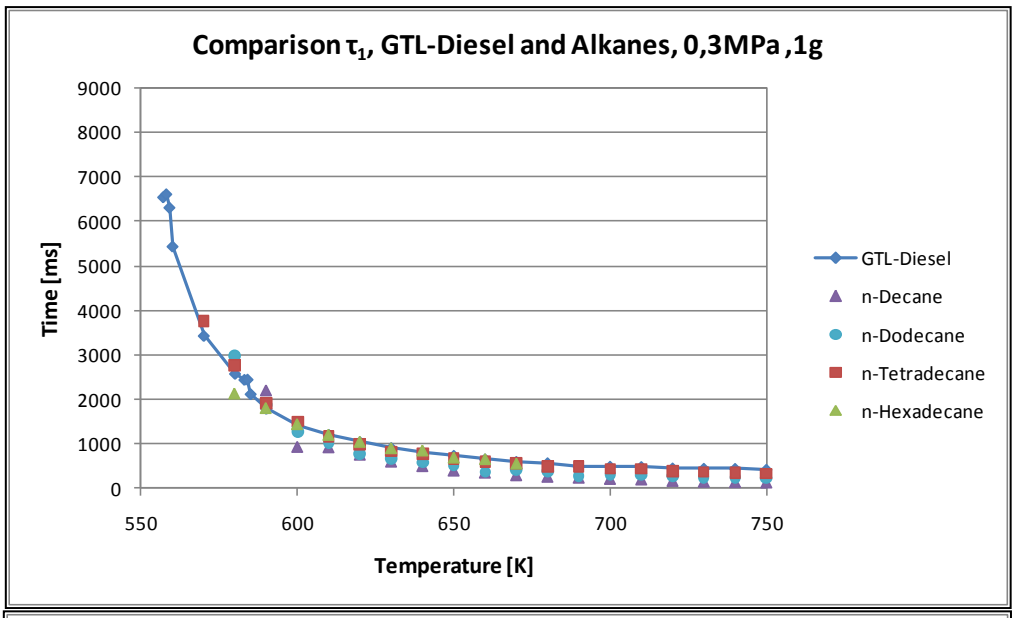

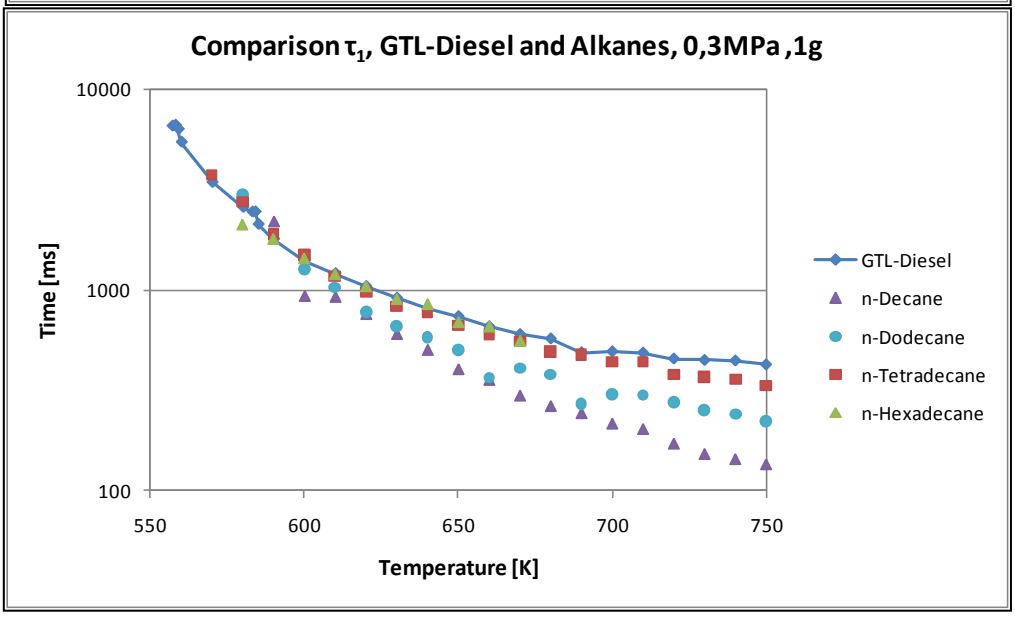

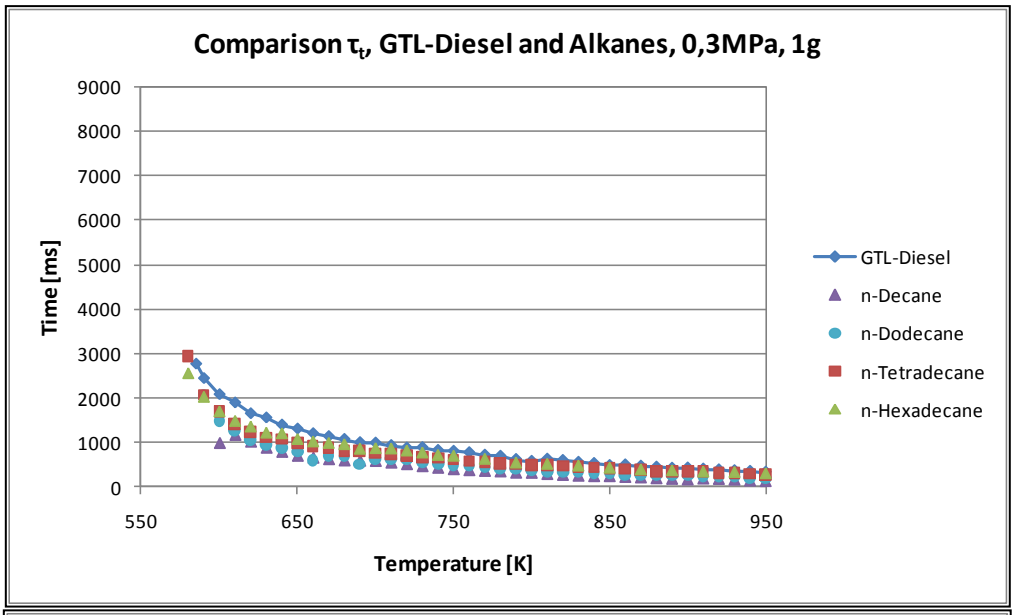
Comparison τt, GTL-Diesel and Alkanes, 0,3MPa, 1g
Time [ms]
9000
8000
7000
6000
5000
4000
3000
2000
1000
0
550
650
750
850
950
Temperature [K]
GTL-Diesel
n-Decane
n-Dodecane
n-Tetradecane
n-Hexadecane

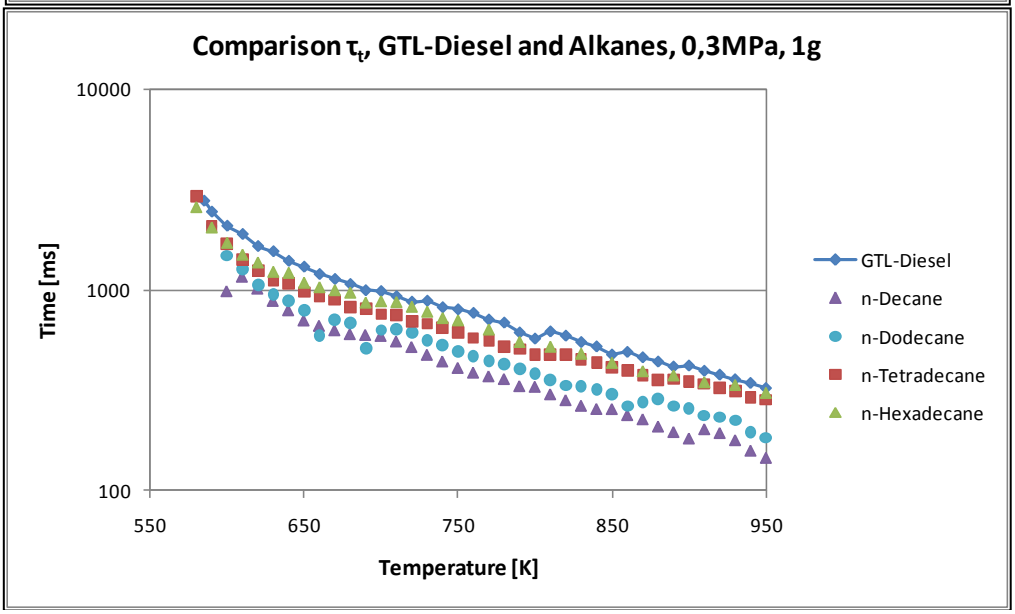
Comparison τt, GTL-Diesel and Alkanes, 0,3MPa, 1g
Time [ms]
10000
1000
100
550
650
750
850
950
Temperature [K]
GTL-Diesel
n-Decane
n-Dodecane
n-Tetradecane
n-Hexadecane

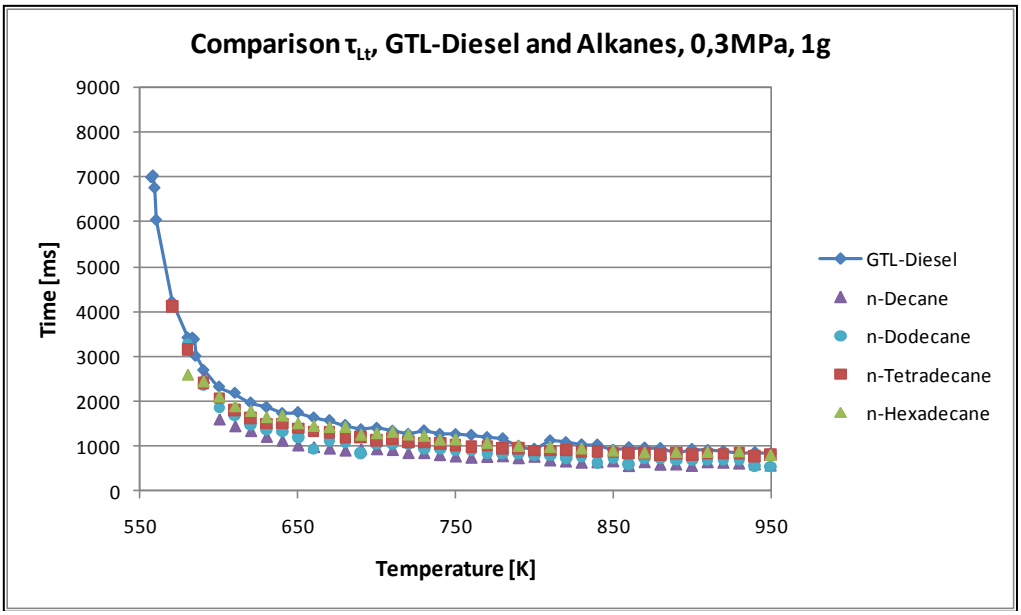
Comparison τLt, GTL-Diesel and Alkanes, 0,3MPa, 1g
Time [ms]
9000
8000
7000
6000
5000
4000
3000
2000
1000
0
550
650
750
850
950
Temperature [K]
GTL-Diesel
n-Decane
n-Dodecane
n-Tetradecane
n-Hexadecane

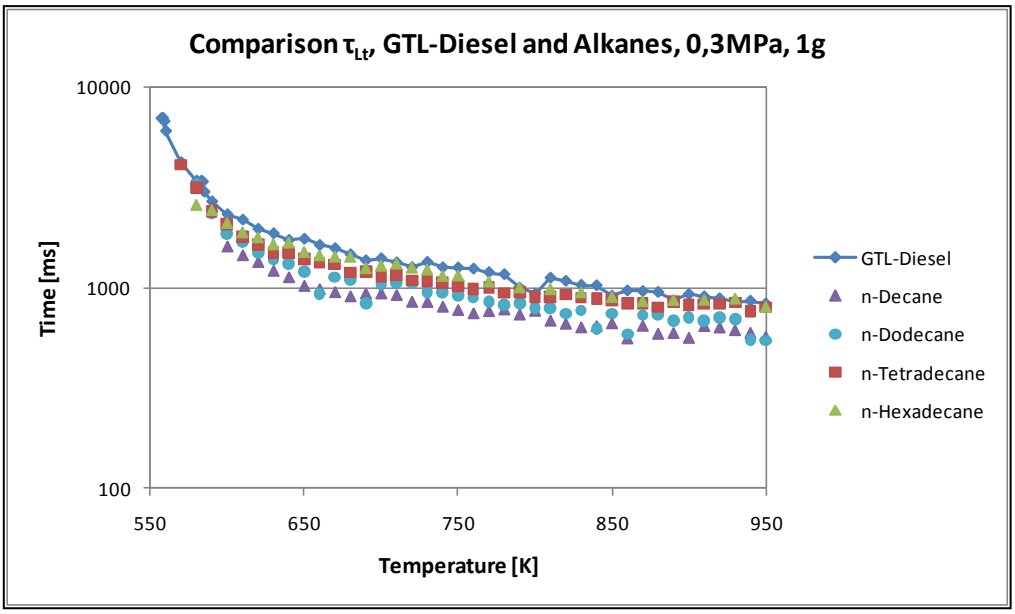

Fig. 68 – Comparison of the ignition delay times of GTL-Diesel with selected alkanes (0,3 MPa, 1g)

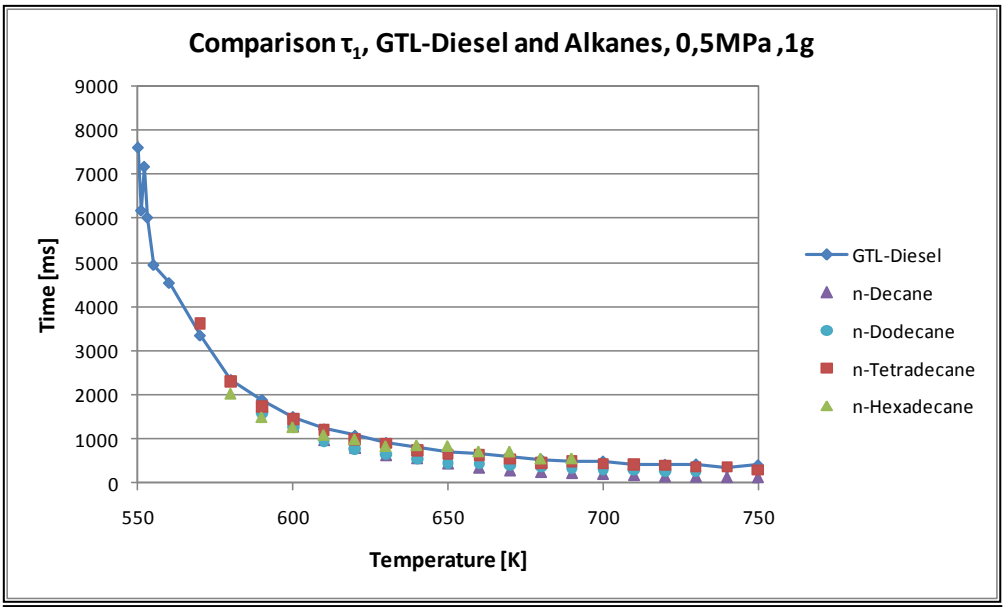

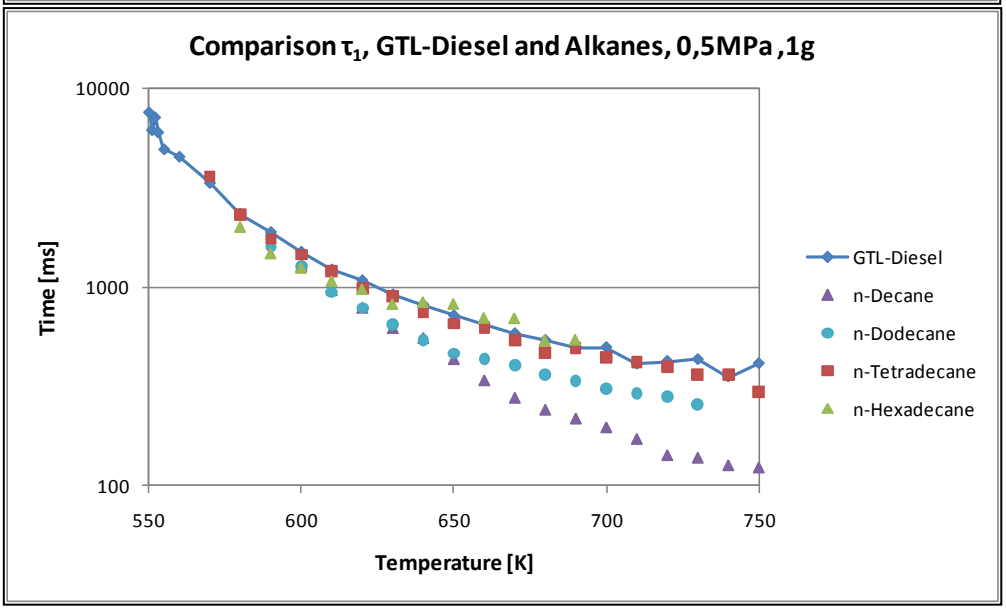

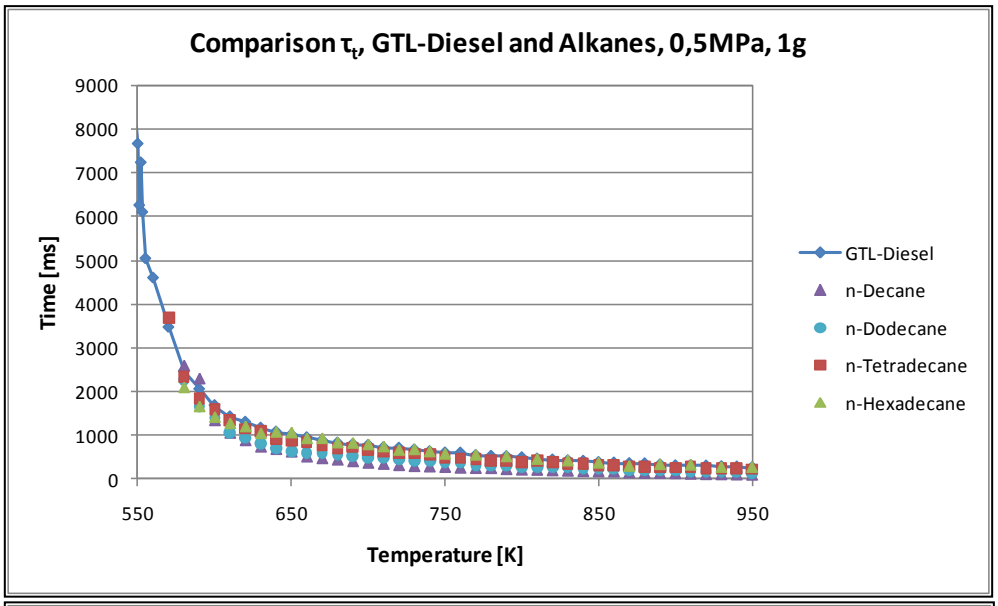
Comparison τt, GTL-Diesel and Alkanes, 0,5MPa, 1g
Time [ms]
9000
8000
7000
6000
5000
4000
3000
2000
1000
0
550
650
750
850
950
Temperature [K]
GTL-Diesel
n-Decane
n-Dodecane
n-Tetradecane
n-Hexadecane

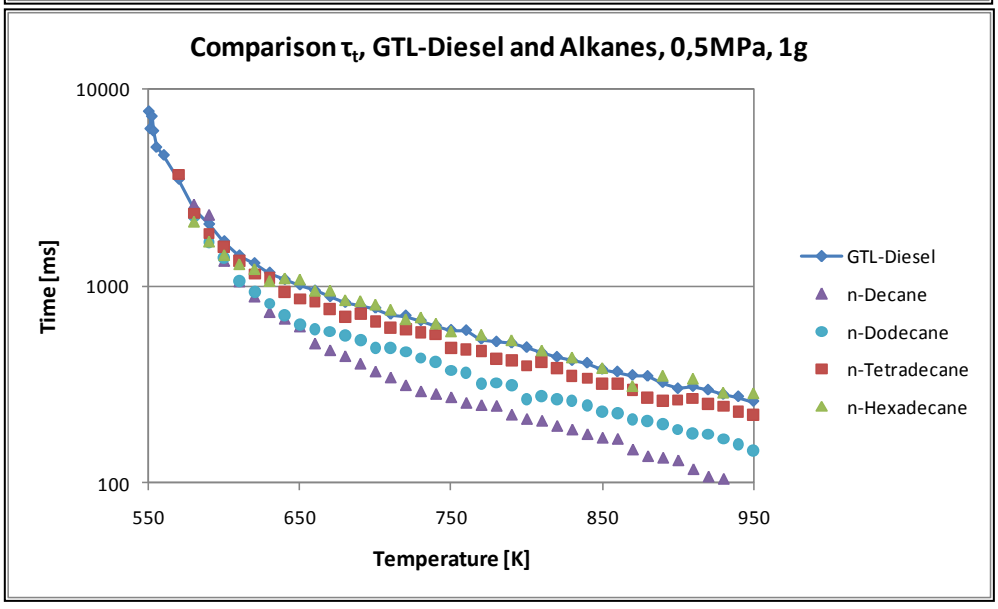
Comparison τt, GTL-Diesel and Alkanes, 0,5MPa, 1g
Time [ms]
10000
1000
100
550
650
750
850
950
Temperature [K]
GTL-Diesel
n-Decane
n-Dodecane
n-Tetradecane
n-Hexadecane

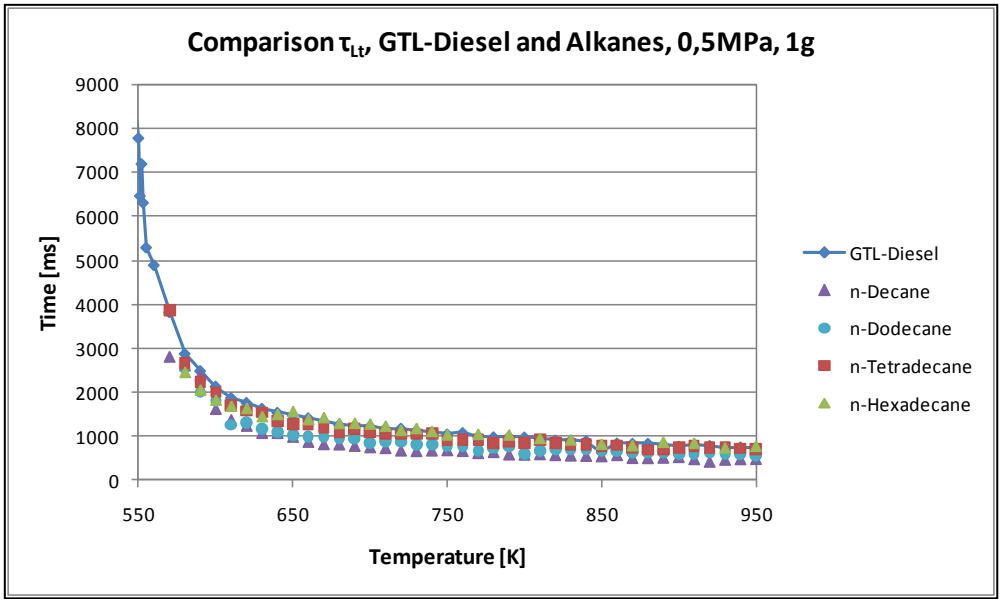
Comparison τLt, GTL-Diesel and Alkanes, 0,5MPa, 1g
Time [ms]
9000
8000
7000
6000
5000
4000
3000
2000
1000
0
550
650
750
850
950
Temperature [K]
GTL-Diesel
n-Decane
n-Dodecane
n-Tetradecane
n-Hexadecane

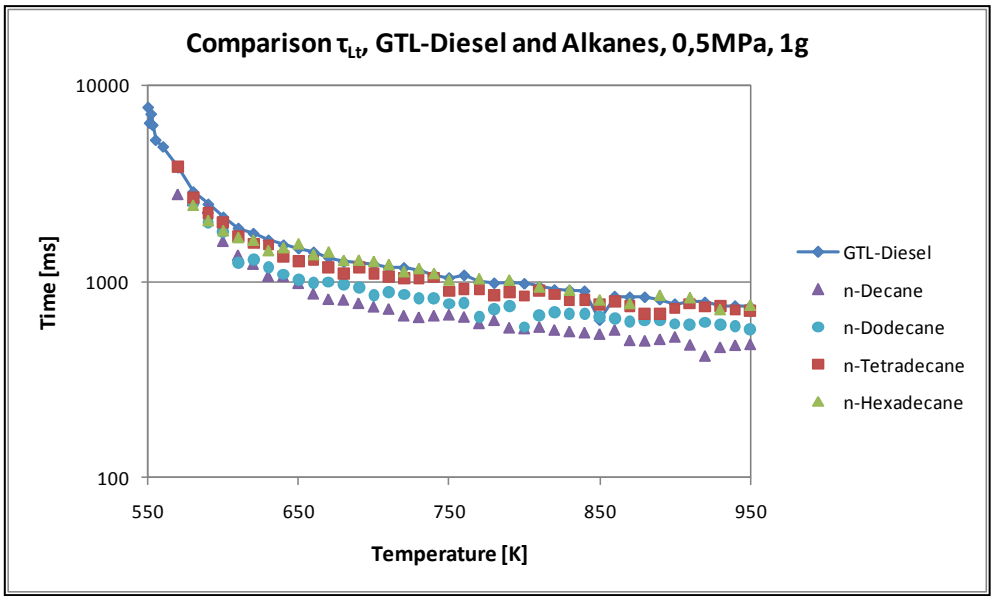

Fig. 69 - Comparison of the ignition delay times of GTL-Diesel with selected alkanes (0,5 MPa, 1g)

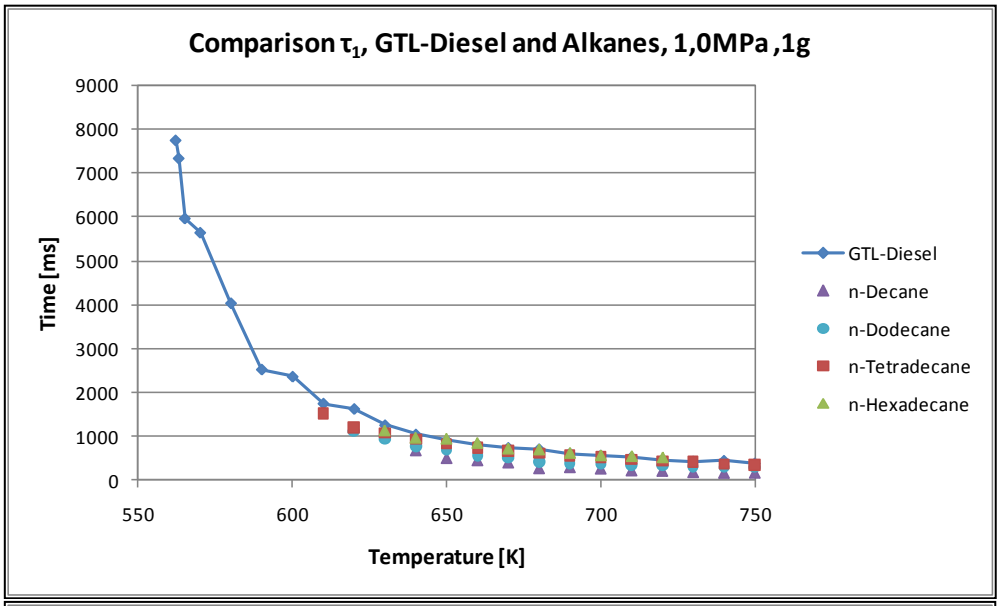

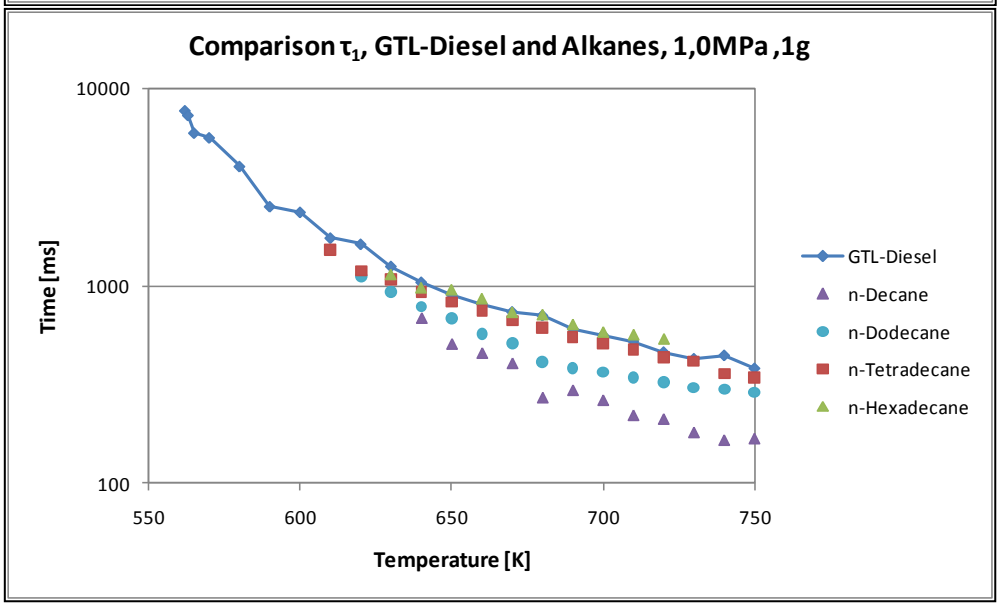

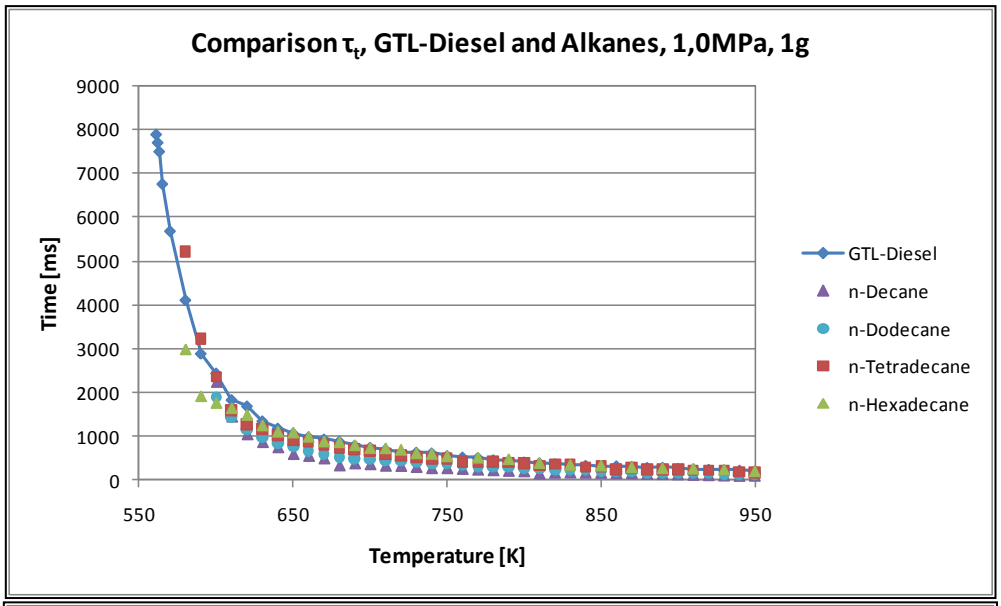
Comparison τt, GTL-Diesel and Alkanes, 1,0MPa, 1g
Time [ms]
9000
8000
7000
6000
5000
4000
3000
2000
1000
0
550
650
750
850
950
Temperature [K]
GTL-Diesel
n-Decane
n-Dodecane
n-Tetradecane
n-Hexadecane

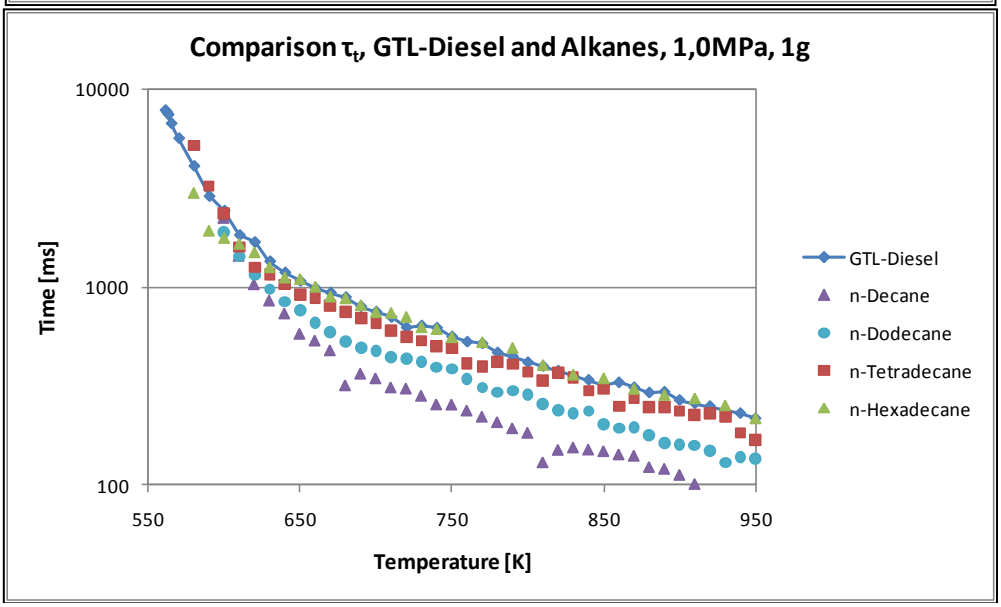
Comparison τt, GTL-Diesel and Alkanes, 1,0MPa, 1g
Time [ms]
10000
1000
100
550
650
750
850
950
Temperature [K]
GTL-Diesel
n-Decane
n-Dodecane
n-Tetradecane
n-Hexadecane

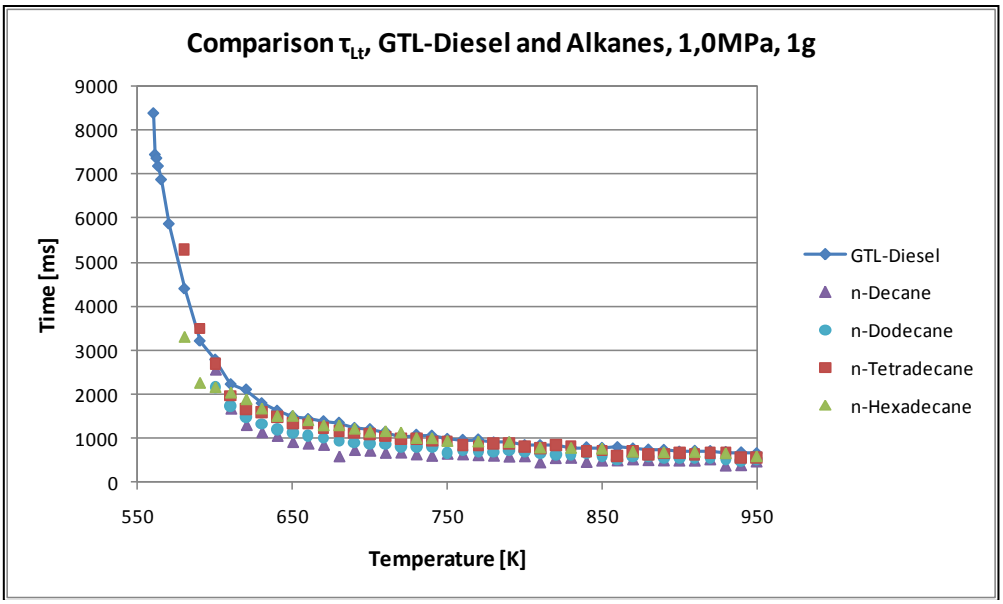
Comparison τLt, GTL-Diesel and Alkanes, 1,0MPa, 1g
Time [ms]
9000
8000
7000
6000
5000
4000
3000
2000
1000
0
550
650
750
850
950
Temperature [K]
GTL-Diesel
n-Decane
n-Dodecane
n-Tetradecane
n-Hexadecane

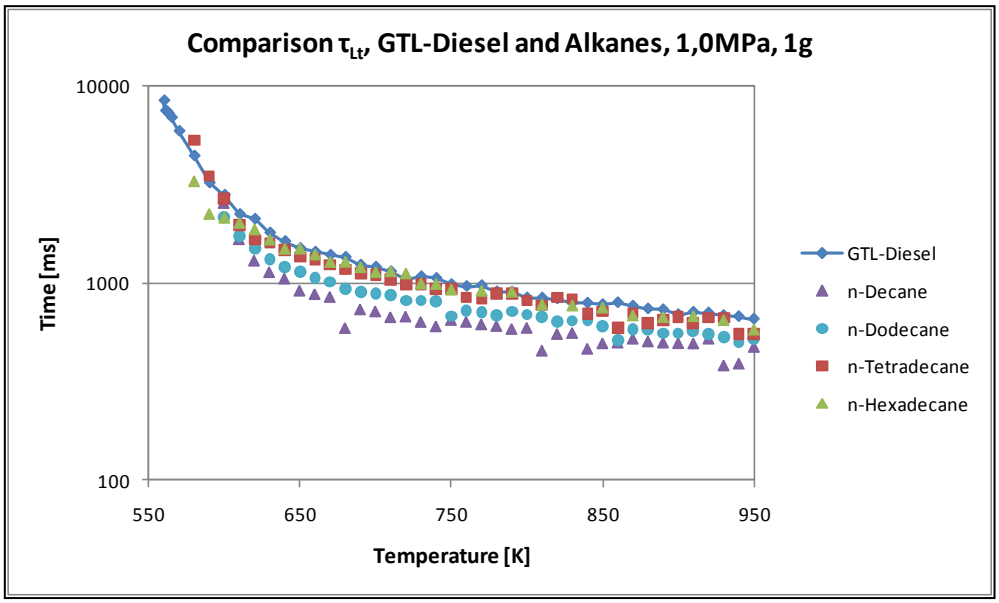

Fig. 70 - Comparison of the ignition delay times of GTL-Diesel with selected alkanes (1,0 MPa, 1g)

As can be seen from the previous diagrams, the ignition delay times have the lowest values for n-Decane. For increasing molecule chain lengths the ignition delay times increase with n-Hexadecane having the largest values. n-Tetradecane and n-Hexadecane show good correspondence to the measured GTL-Diesel data. The following table compares the measured data values of each ignition delay time and shows the average (first value) and squared (second value) deviations using the GTL-Diesel data as a reference.

	n-Tetradecane			**n-Hexadecane**		
Pressure	τ_1	τ_t	τ_{Lt}	τ_1	τ_t	τ_{Lt}
0,3MPa	0,07/0,01	0,50/0,27	0,13/0,02	0,02/0,005	0,43/0,19	0,07/0,01
0,5MPa	0,06/0,01	0,13/0,02	0,08/0,01	0,02/0,02	0,01/0,01	0,01/0,01
1,0MPa	0,11/0,02	0,12/0,02	0,08/0,01	0,03/0,01	0,03/0,01	0,07/0,01
Average	0,08/0,01	0,25/0,10	0,10/0,01	0,02/0,03	0,16/0,07	0,05/0,01
Total average	0,14/0,04			0,08/0,04		

Tab. 26– Comparison of the deviation of the ignition delay times for n-Tetradecane and n-Hexadecane compared to GTL-Diesel

From this analysis n-Hexadecane shows the best agreement to GTL-Diesel. Nonetheless, the following has to be taken into consideration: n-Tetradecane shows a better agreement for the extent of the temperature range of the cool flame detection, e.g., at 0,3 MPa the extent of τ_1 is for GTL-Diesel from 557 to 750 K. n-Tetradecane shows a larger temperature range (570-760 K) than n-Hexadecane (580-670 K). Similar behavior is observed for the other pressures analyzed. Also a reduced semi-empirical chemical kinetic mechanism is available for n-Tetradecane, which makes it at this stage a more interesting candidate for a surrogate fuel component. Although n-Hexadecane shows a better fit of the overall autoignition behavior in relation to GTL-Diesel, n-Tetradecane has been chosen due to its better cool flame behavior and the imminent availability of a chemical kinetic mechanism.

Selection of an additive

Based on the adapted selection process described in the previous section and in section 2.1.5, autoignition experiments in normal-g are conducted for the following mixtures:

- n-Tetradecane 50% - n-Hexadecane 50%
- n-Tetradecane 50% - Bicyclohexyl-50%
- n-Tetradecane 75% - Bicyclohexyl-25%
- n-Tetradecane 50% - 2,2,4,4,6,8,8-Heptamethylnonane-50%
- n-Tetradecane 75% - 2,2,4,4,6,8,8-Heptamethylnonane-25%
- n-Tetradecane 50% - Bicyclohexyl-25%-2,2,4,4,6,8,8-Heptamethylnonane-25%

The mixture fractions are given in vol% and in this study two main mixture fractions are shown, namely 75 vol% - 25 vol% and 50 vol% - 50 vol%. The experimental parameters are analogous to the settings described in previous sections. The experimental data shown here is for 0,3 MPa ambient pressure.

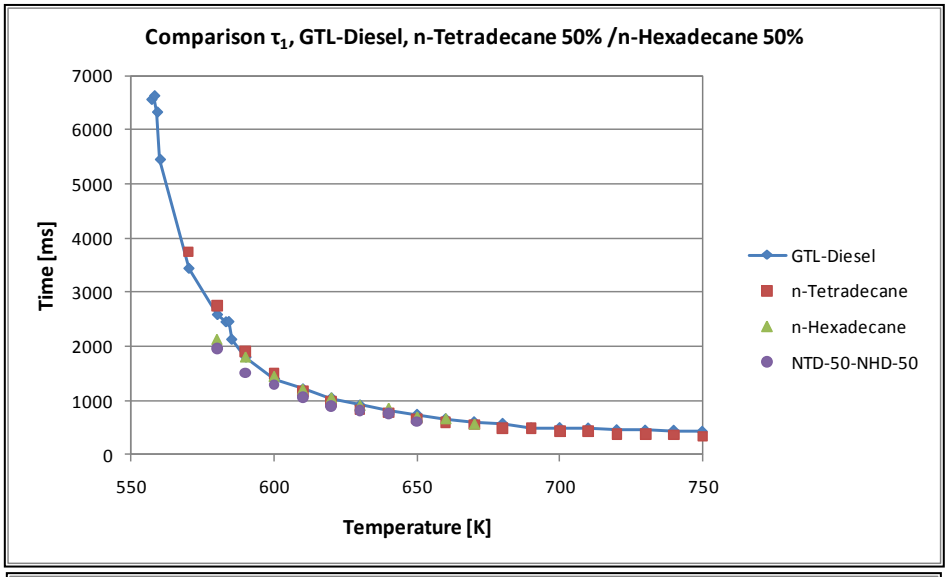

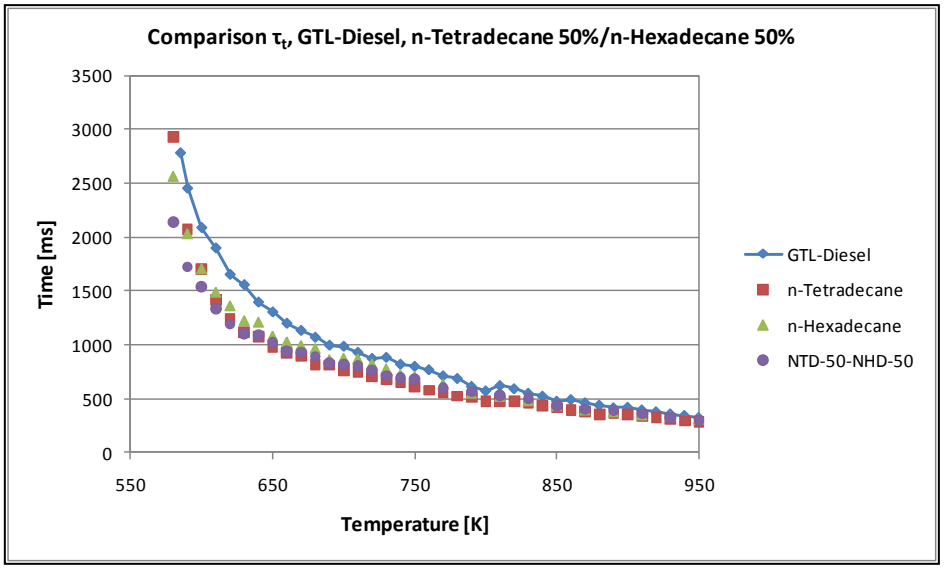

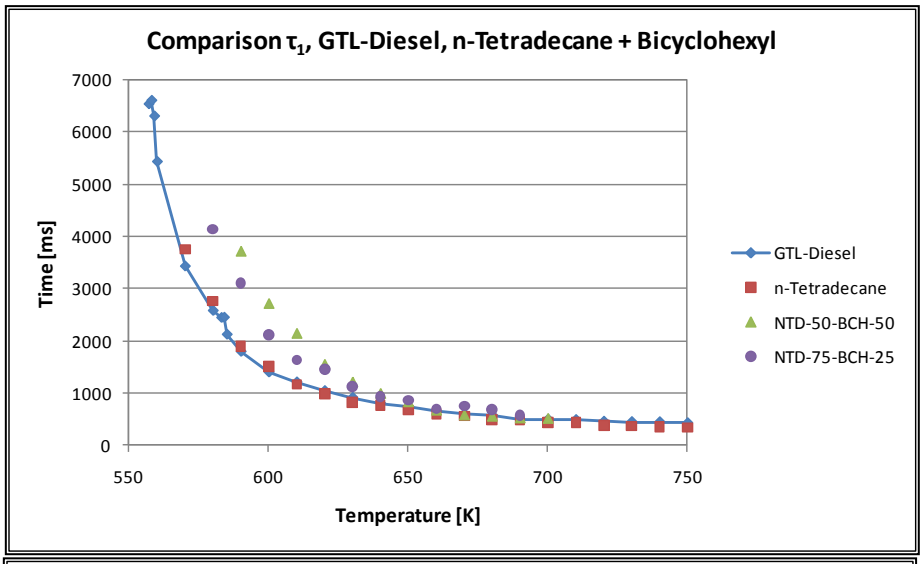
Comparison τ_1, GTL-Diesel, n-Tetradecane + Bicyclohexyl
Time [ms]
7000
6000
5000
4000
3000
2000
1000
0
550
600
650
700
750
Temperature [K]
GTL-Diesel
n-Tetradecane
NTD-50-BCH-50
NTD-75-BCH-25

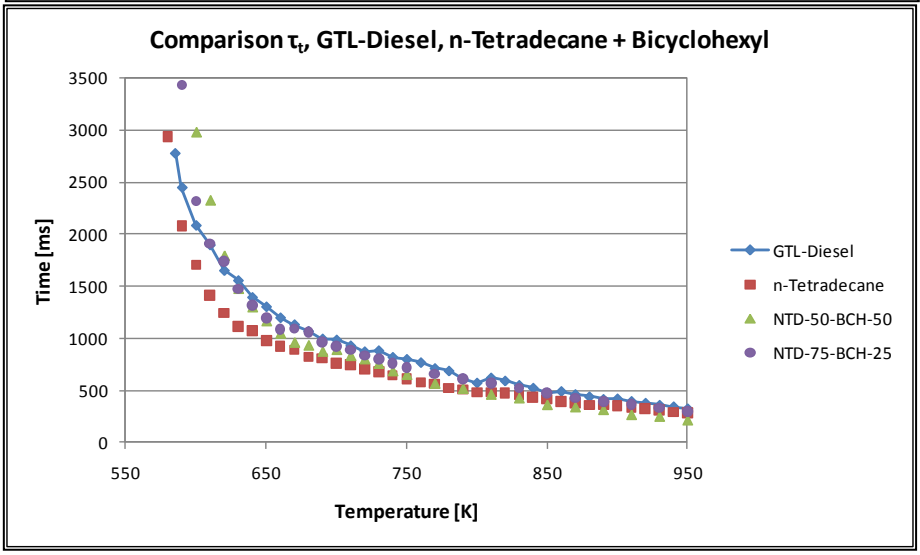
Comparison τ_t, GTL-Diesel, n-Tetradecane + Bicyclohexyl
Time [ms]
3500
3000
2500
2000
1500
1000
500
0
550
650
750
850
950
Temperature [K]
GTL-Diesel
n-Tetradecane
NTD-50-BCH-50
NTD-75-BCH-25

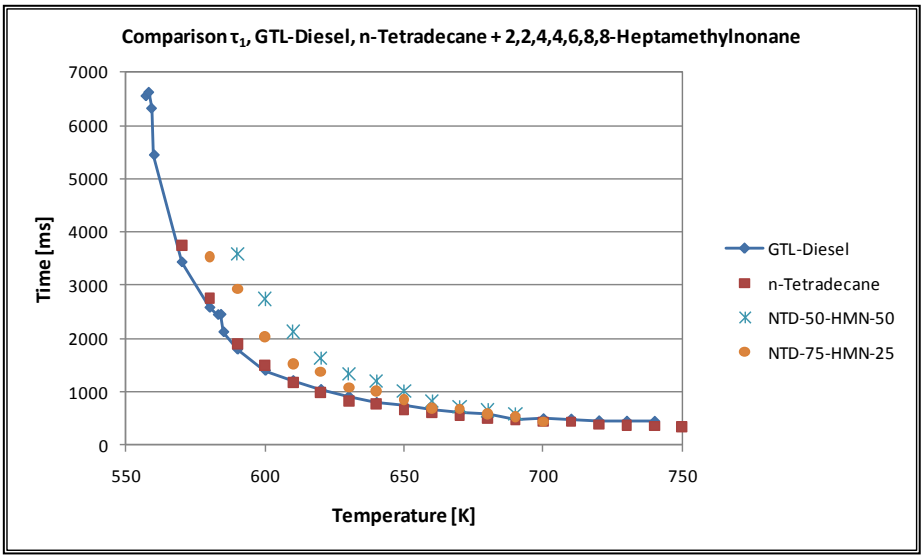
Comparison τ_1, GTL-Diesel, n-Tetradecane + 2,2,4,4,6,8,8-Heptamethylnonane
Time [ms]
7000
6000
5000
4000
3000
2000
1000
0
550
600
650
700
750
Temperature [K]
GTL-Diesel
n-Tetradecane
NTD-50-HMN-50
NTD-75-HMN-25

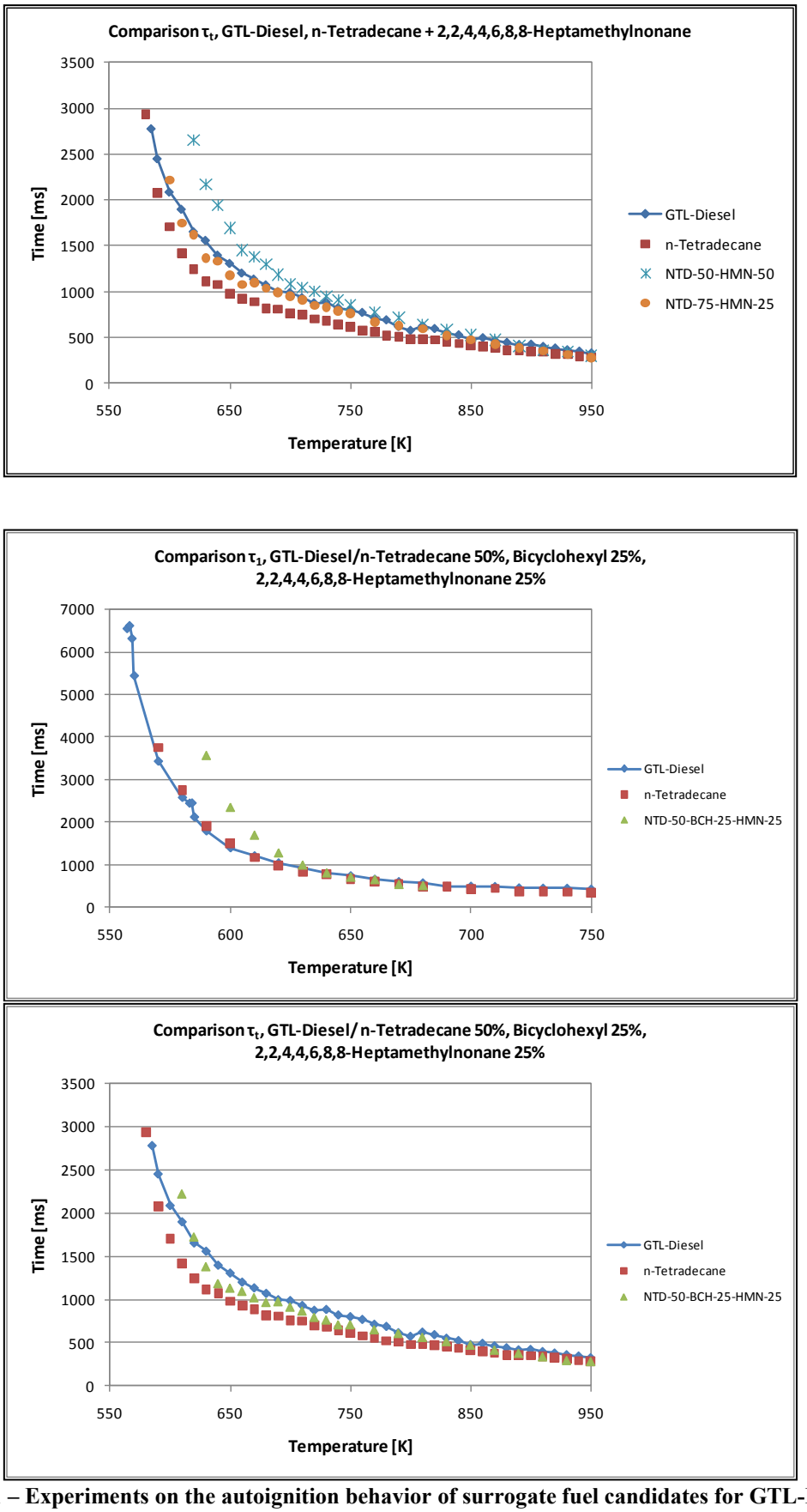

Fig. 71 – Experiments on the autoignition behavior of surrogate fuel candidates for GTL-Diesel under normal-g for 0,3 MPa

Surrogate fuel candidate	τ_l	τ_t	τ_{Lt}	Average
n-Tetradecane 50% - n-Hexadecane 50%	0,14	0,17	0,14	0,15
n-Tetradecane 50% - Bicyclohexyl-50%	0,32	0,10	0,05	0,16
n-Tetradecane 75% - Bicyclohexyl-25%	0,32	0,03	0,05	0,13
n-Tetradecane 50% - 2,2,4,4,6,8,8-Heptamethylnonane-50%	0,49	0,14	0,14	0,26
n-Tetradecane 75% - 2,2,4,4,6,8,8-Heptamethylnonane-25%	0,22	0,05	0,05	0,11
n-Tetradecane 50% - Bicyclohexyl-25% - 2,2,4,4,6,8,8-Heptamethylnonane-25%	0,20	0,09	0,005	0,10

Tab. 27 - Comparison of the deviation of the ignition delay times for the surrogate fuel candidates compared to GTL-Diesel

From the previous diagrams the following observations can be made:

- The mixture of n-Tetradecane and n-Hexadecane shows an improvement in matching the GTL-Diesel total ignition times. On the other hand, the temperature range of τ_l is shortened compared to GTL-Diesel (and pure n-Tetradecane). Thus, the addition of n-Hexadecane inhibits the appearance of cool flames at higher temperatures.
- The addition of bicyclohexyl retards the appearance of cool flames and shortens the detectable temperature range. The total ignition times and droplet lifetimes are substantially improved, as can be seen in the average deviations shown in the previous table, with a mixture of n-Tetradecane 75% - Bicyclohexyl-25% having the best results for this additive.
- The addition of iso-cetane or 2,2,4,4,6,8,8-Heptamethylnonane induces a similar behavior like the previous additive. The average values are best for a mixture composed of n-Tetradecane 75% - 2,2,4,4,6,8,8-Heptamethylnonane-25%.
- The best matching behavior is given a by the ternary mixture composed of n-Tetradecane-50% - Bicyclohexyl-25% -2,2,4,4,6,8,8-Heptamethylnonane-25%. This mixture contains three of the chemical compound types present in GTL-Diesel, namely n-alkanes, iso-alkanes and cycloalkanes, thus being a more apt representative composition-wise than the binary mixtures.

From these observations, the binary mixture composed of n-Tetradecane 75% - 2,2,4,4,6,8,8-Heptamethylnonane-25% has been chosen as the surrogate fuel. Although the ternary mixture shows slightly better average values, the binary mixture has the advantage of requiring only two chemical reaction mechanisms and showing a sufficiently good representation of the autoignition behavior of GTL-Diesel.

Validation of the selected surrogate fuel candidate in microgravity

The selected blend, n-Tetradecane 75% - 2,2,4,4,6,8,8-Heptamethylnonane-25%, is validated in µg and the results are compared with µg-data on n-Tetradecane and GTL-Diesel for 0,3/0,5 and 1,0 MPa. The total average deviation of the surrogate mixture is 0,064 compared to 0,074 reached by n-Tetradecane, showing that the developed surrogate fuel is a good representative for the autoignition behavior of GTL-Diesel.

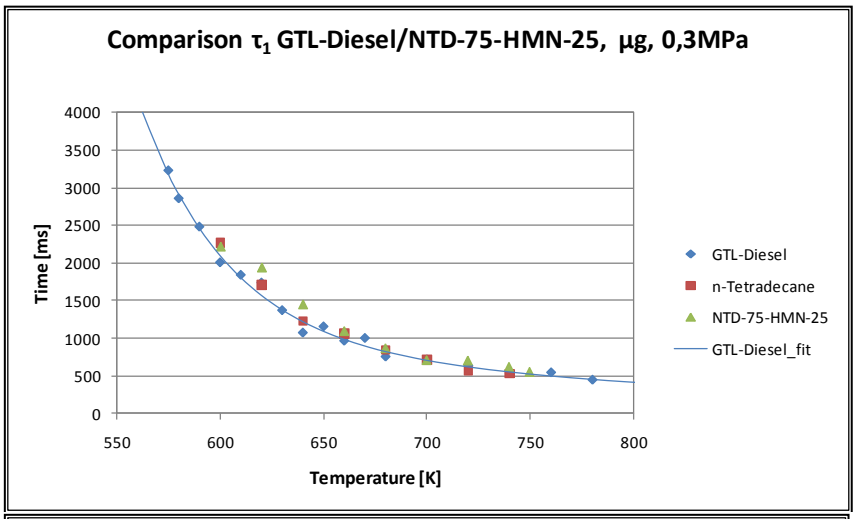

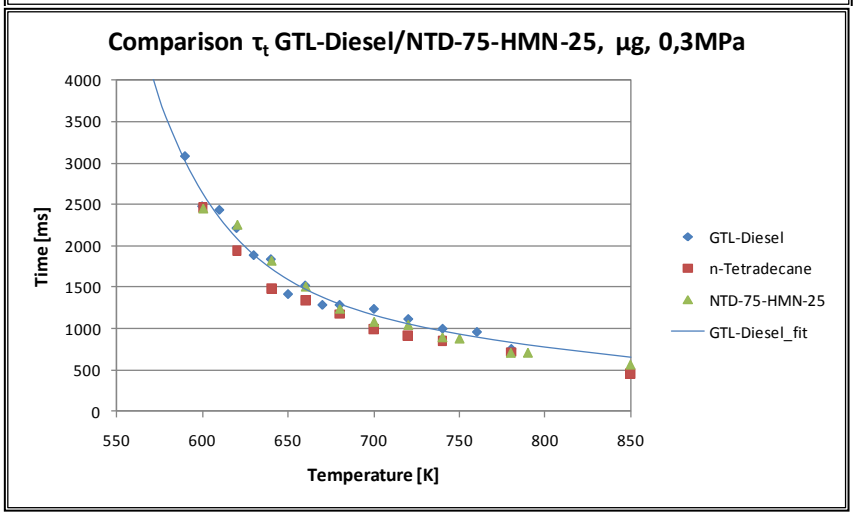

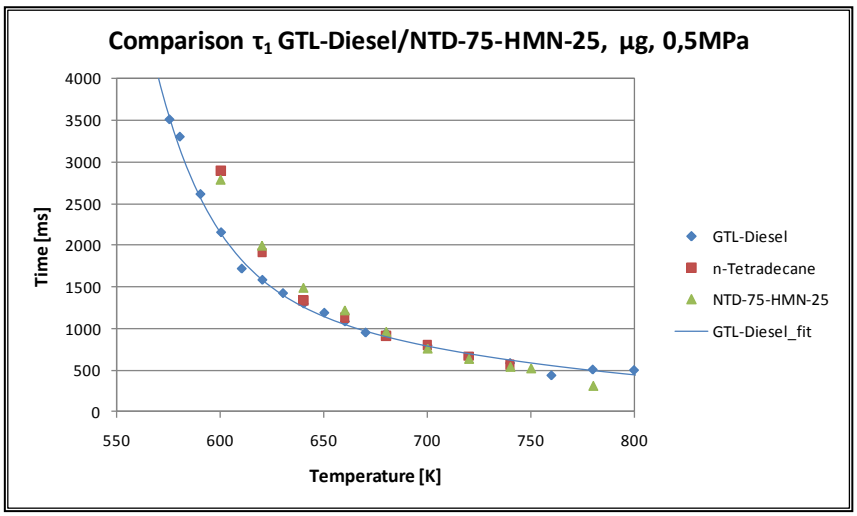

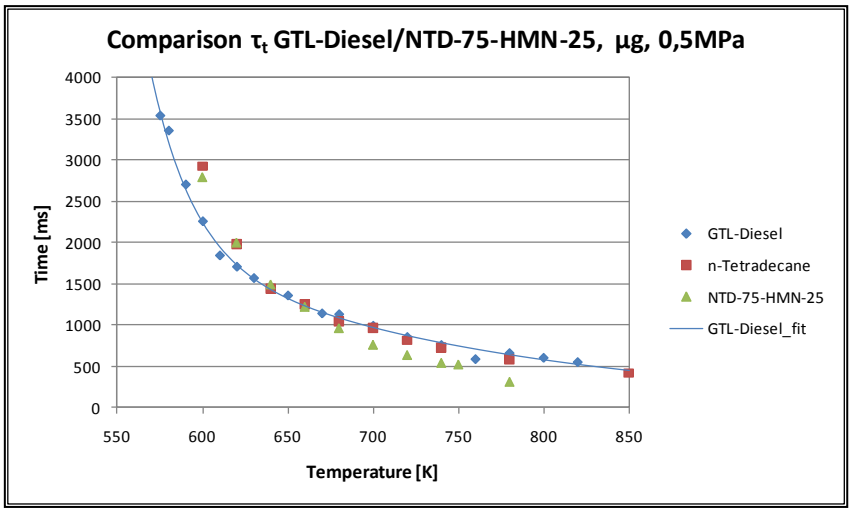

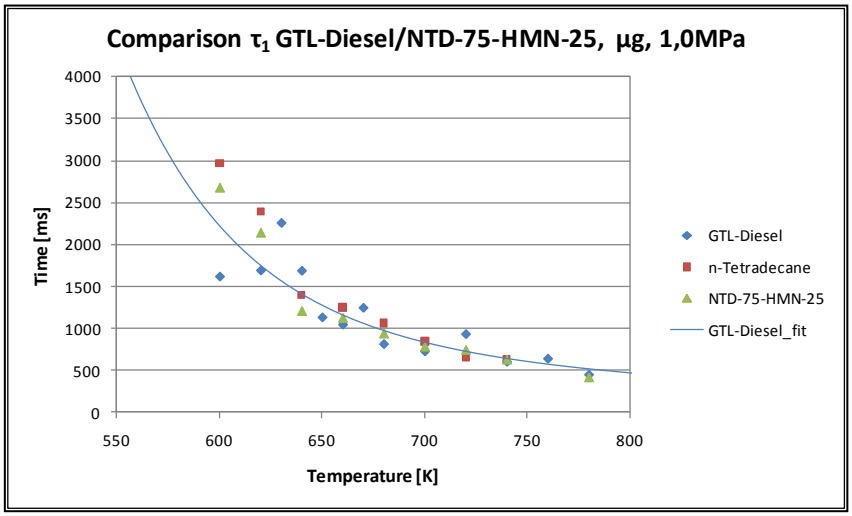

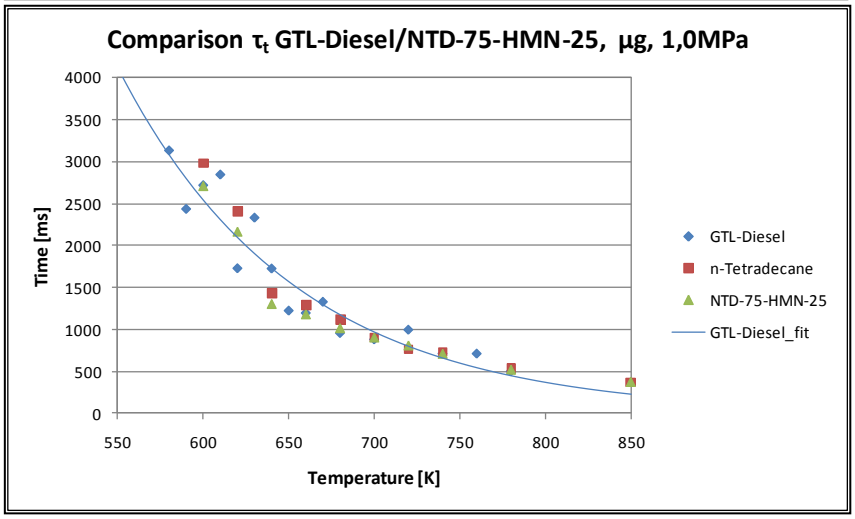

Fig. 72 – Comparison of the ignition delay times of GTL-Diesel, the surrogate fuel candidate and n-tetradecane under µg for the pressure levels analyzed

Experiments at 0,3 MPa	τ_1	τ_t	τ_{Lt}
n-Tetradecane 75%- 2,2,4,4,6,8,8-Heptamethylnonane-25%	0,14	0,04	0,07
n-Tetradecane	0,07	0,12	0,10
Experiments at 0,5 MPa	τ_1	τ_t	τ_{Lt}
n-Tetradecane 75%- 2,2,4,4,6,8,8-Heptamethylnonane-25%	0,04	0,06	0,07
n-Tetradecane	0,08	0,01	0,03
Experiments at 1,0 MPa	τ_1	τ_t	τ_{Lt}
n-Tetradecane 75%- 2,2,4,4,6,8,8-Heptamethylnonane-25%	0,08	0,01	0,07
n-Tetradecane	0,19	0,04	0,03

Tab. 28 - Comparison of the deviation of the ignition delay times for the surrogate fuel candidate and n-Tetradecane compared to GTL-Diesel in µg

3.5.5. Evaporation Experiments

The evaporation behavior of a liquid fuel and the processes that are related to it are of great importance for the autoignition phenomenon. As described in section 2.2 the physical ignition delay is directly dominated by the evaporation process. This was also taken into consideration for the formulation procedure of the surrogate fuel as described in section 2.1.5. Nonetheless, as the detailed composition of GTL-Diesel is not known and as a reference for numerical simulations, experiments on the evaporation of single droplets of this fuel have been conducted. Evaporation experiments of the obtained surrogate fuel and the base-alkane n-Tetradecane have been performed as well. These experiments are conducted in the same facility as the autoignition experiments with N_2 as ambient gas. The main goal is to measure the regression of the diameter of the droplet for given temperatures and ambient pressure conditions. This is done using a backlight/shadowgraph configuration of the experiment, were the interferometer optics are replaced by a laser diode as a light source, and some lenses to magnify the image of the observed contour of the droplet. The images are recorded with the same high-speed camera employed for the autoignition experiments. The following table summarizes the experiment parameters:

Ambient Pressure	0,3/0,5/1,0MPa
Ambient Temperature **Measurement Step Size**	550 – 950 K 50 K
Initial Droplet Diameter	0,7 mm
Ambient Gas	N_2

Tab. 29 – Experiment parameters for normal gravity evaporation experiments

Evaporation Experiments of GTL-Diesel

Normal gravity and microgravity evaporation experiments have been conducted for GTL-Diesel. The regression of the droplet diameter through time for set ambient temperatures and pressures is presented in the following diagrams. For comparability the axis are normed to t/d_o^2 (x-axis), d/d_o^2 (y-axis) with d_o being initial droplet diameter, d the measured diameter in [mm] and t the time in [s]. The following diagrams show the experimental results for GTL-Diesel in microgravity and normal gravity conditions.

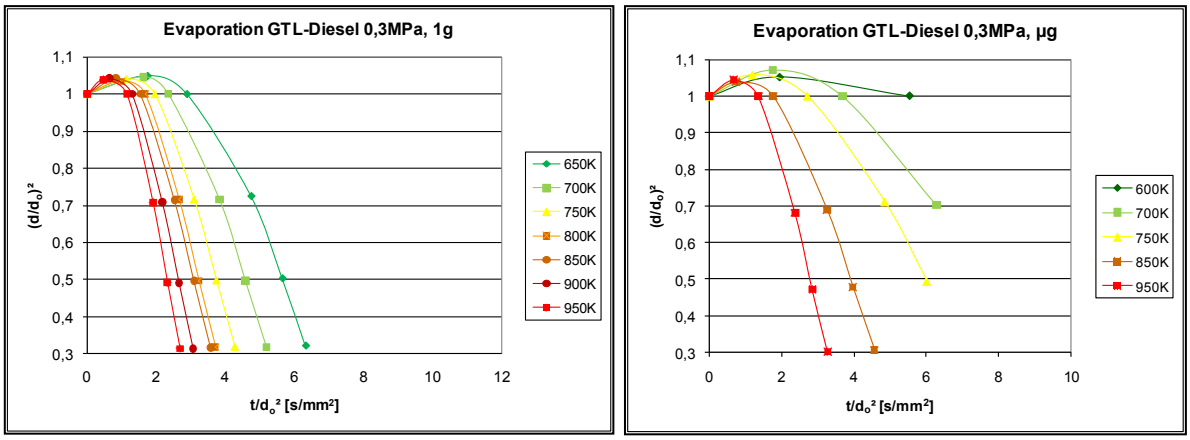

Fig. 73 – Droplet diameter regression for GTL-Diesel for 0,3 MPa, 1g and µg

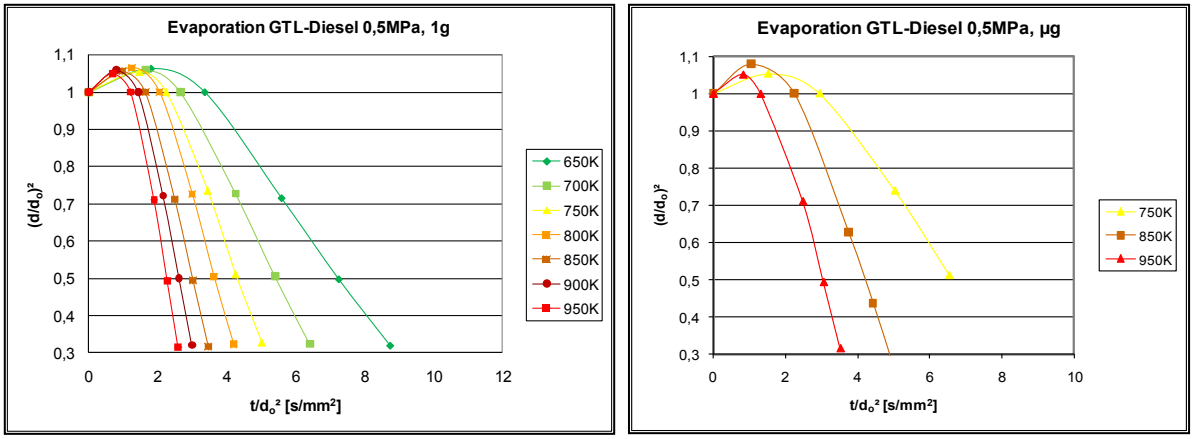

Fig. 74 - Droplet diameter regression for GTL-Diesel for 0,5 MPa, 1g and µg

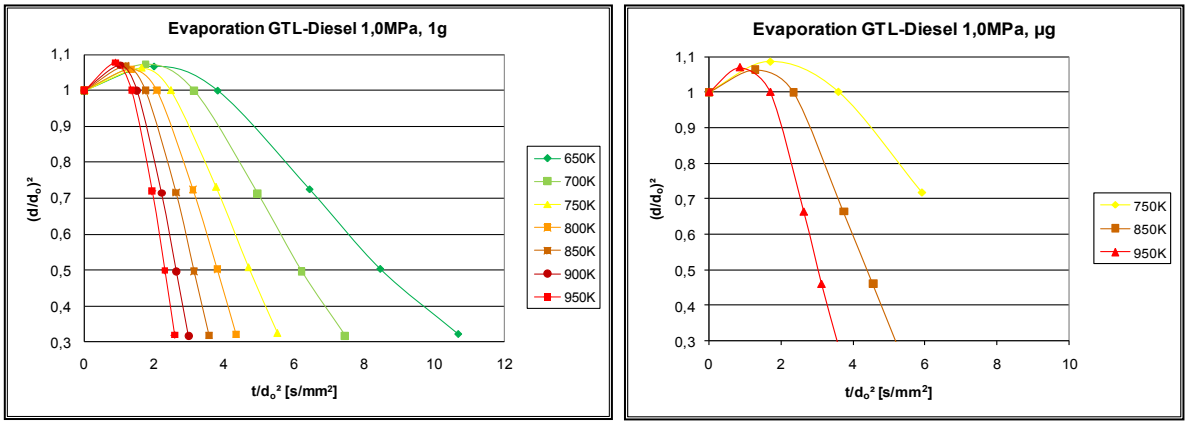

Fig. 75 - Droplet diameter regression for GTL-Diesel for 1,0 MPa, 1g and µg

From these diagrams the evaporation rate is extracted. It is defined, as shown in the following diagram and according to [77], as the negative slope of the obtained curves for the regression of the droplet diameter. The obtained evaporation rates are listed in the adjacent table.

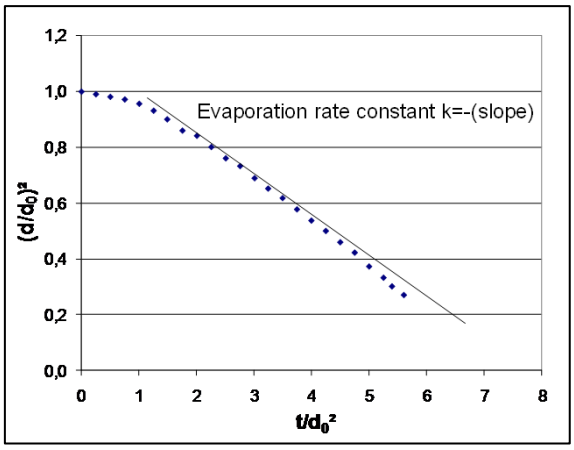

Fig. 76 – Definition of the evaporation rate constant k [77]

	Evaporation Rate, 1g		
Temperature	**0,3 MPa**	**0,5 MPa**	**1,0 MPa**
650K	0,1935	0,1274	0,0996
700K	0,2377	0,1814	0,1596
750K	0,2928	0,2445	0,2226
800K	0,3344	0,3173	0,2988
850K	0,3347	0,3758	0,3760
900K	0,3877	0,4356	0,4631
950K	0,4458	0,4970	0,5532
	Evaporation Rate, µg		
700K	0,1142	N/A	N/A
750K	0,1507	0,1351	0,1220
850K	0,2464	0,2657	0,2459
950K	0,3628	0,3061	0,3744

Tab. 30 – Evaporation rates for GTL-Diesel, 1g and µg

As can be seen, at the beginning of the vaporization process a swelling effect of the droplet is observed, as the liquid density decreases with increasing temperature. Also, as expected, the evaporation rate increases with rising ambient temperature. The pressure dependence shows an interesting behavior. For 650 K< T <800 K the evaporation rate decreases with increasing pressure. At temperatures higher than 800 K an increase of the evaporation rate is observed for increasing ambient pressure.
The µg data shows smaller evaporation rates than the 1g counterparts, indicating that the absence of natural convection affects the transport of vapor from the droplet, which is then accomplished only by diffusion. The evaporation rates increase with increasing temperature; a decrease of the rates is also observed for 750 K for increasing pressures. For 850 K the rates remain relatively constant for 0,3 and 1,0 MPa, a slight increase is observed for 0,5 MPa. For 950 K the behavior is similar, only the rate for 0,5 MPa drops off.

The following diagrams show a comparison of the experimental data in both gravity conditions on the evaporation behavior of GTL-Diesel, n-Tetradecane and the surrogate mixture n-Tetradecane-75 vol%-2,2,4,4,6,8,8-Heptamethylnonane-25 vol%. For the surrogate mixture there is no microgravity data available.

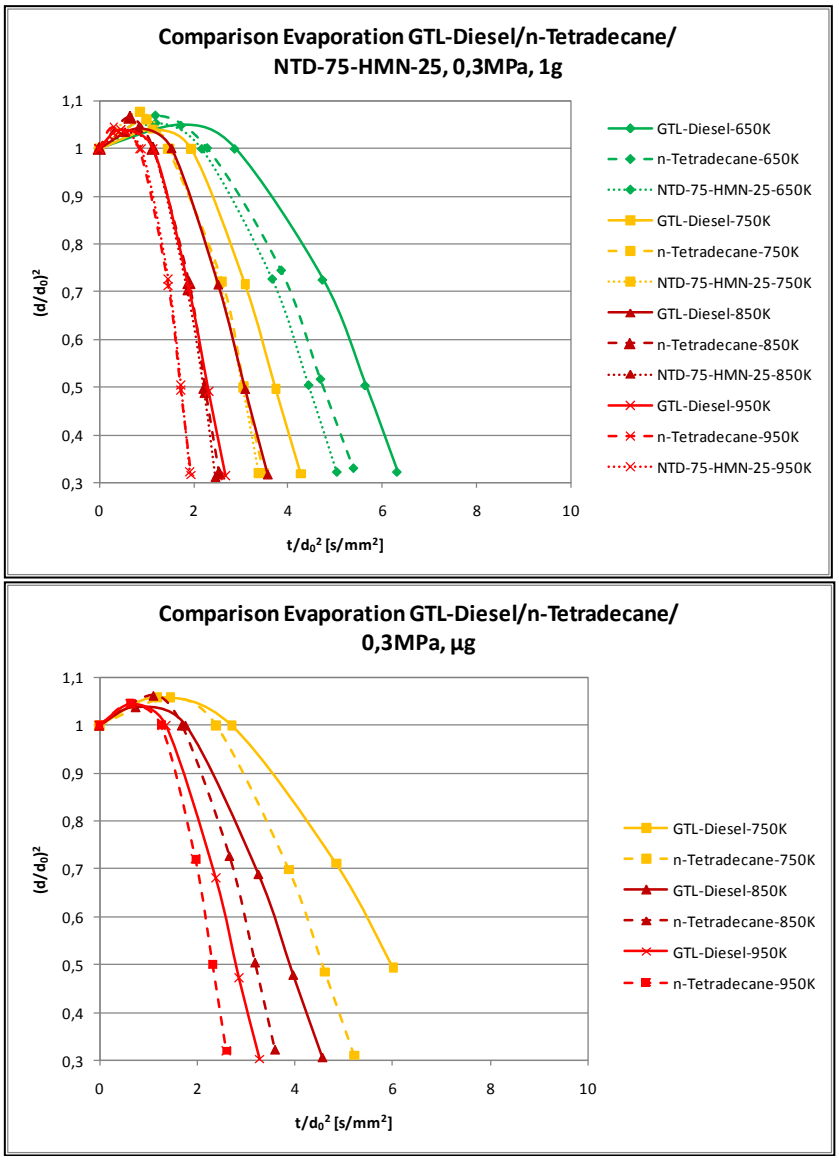

Fig. 77 - Comparison evaporation of GTL-Diesel, n-Tetradecane and NTD-75-HMN-25, 0,3 MPa, 1g and µg

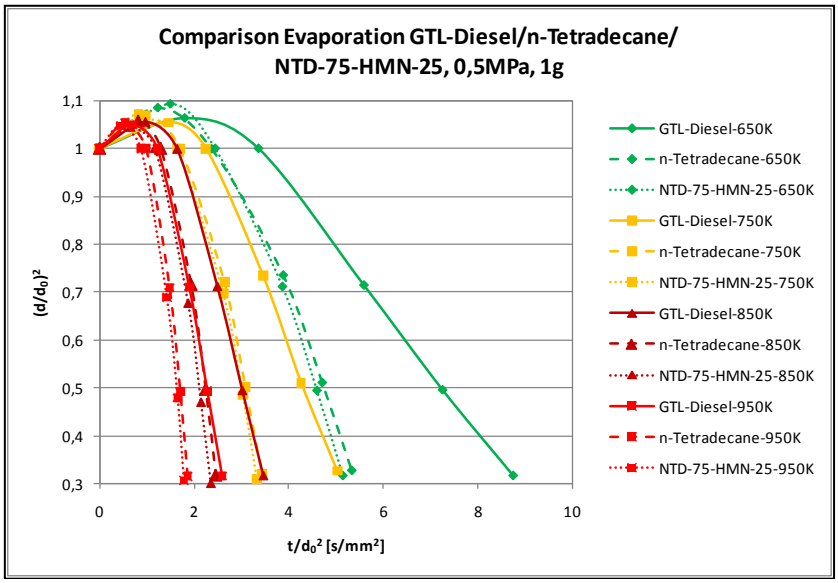

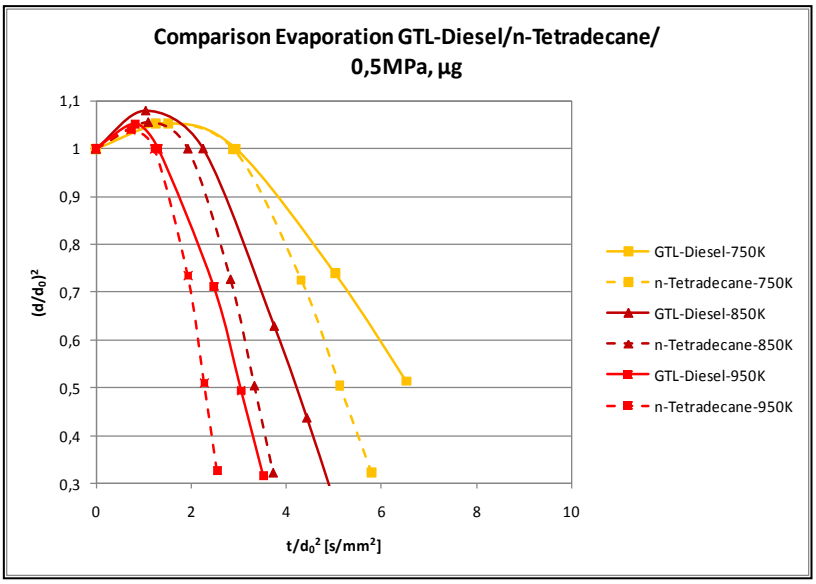

Fig. 78 - Comparison evaporation of GTL-Diesel, n-Tetradecane and NTD-75-HMN-25, 0,5 MPa, 1g and µg

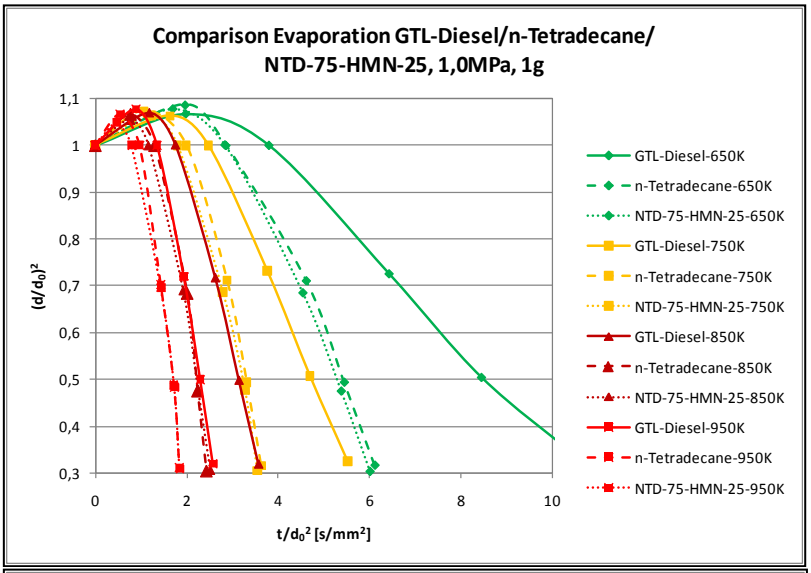

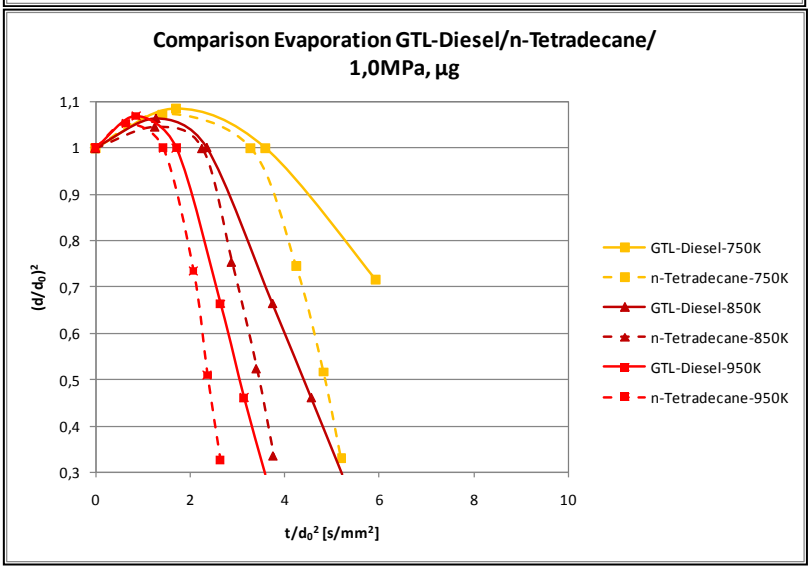

Fig. 79 - Comparison evaporation of GTL-Diesel, n-Tetradecane and NTD-75-HMN-25, 1,0 MPa, 1g and µg

The overall evaporation rate of GTL-Diesel is smaller than for n-Tetradecane and the surrogate mixture. The swelling phase of GTL-Diesel droplets lasts longer and after this phase the rates show roughly similar values as the other two fuels. The surrogate mixture shows a very similar behavior compared to n-Tetradecane, but nonetheless the evaporation rates are always slightly higher for the mixture, as shown in the following tables.
A similar behavior is observed for the µg experiments, only with smaller values for the evaporation rates for both fuels.

	Evaporation Rate, 1g		
Temperature	**0,3 MPa**	**0,5 MPa**	**1,0 MPa**
600K	0,1650	0,1598	0,1324
650K	0,2149	0,2257	0,2074
700K	0,2909	0,3162	0,2872
750K	0,3288	0,3856	0,4126
800K	0,4309	0,4951	0,4948
850K	0,4801	0,5721	0,5920
900K	0,5313	0,6691	0,6849
950K	0,5149	0,7620	0,7579
	Evaporation Rate, µg		
750K	0,2424	0,2316	0,3425
850K	0,3511	0,3762	0,4382
950K	0,5047	0,5028	0,5534

Tab. 31 – Evaporation rates for n-Tetradecane, 1g and µg

	Evaporation Rate, 1g		
Temperature	**0,3 MPa**	**0,5 MPa**	**1,0 MPa**
600K	0,1734	0,1716	0,1432
650K	0,2344	0,2503	0,2170
700K	0,2952	0,3163	0,2904
750K	0,3525	0,3975	0,3873
800K	0,4718	0,4612	0,4482
850K	0,5077	0,5780	0,5061
900K	0,5588	0,6152	0,6993
950K	0,6457	0,7358	0,6137

Tab. 32 - Evaporation rates for NTD-75-HMN-25, 1g

3.6. Experimental Characterization of the Autoignition Behavior of GTL-Kerosene and Determination of a suitable Surrogate Fuel

In this chapter the experimental results concerning the characterization of the autoignition behavior of GTL-Kerosene are presented. Based on these results, a surrogate fuel is derived.

The characterization has been performed using normal gravity and microgravity experiments. The experiments conducted under microgravity conditions enable the simplification of having an almost spherical, axis-symmetrical geometry. The data obtained is used for validation of the numerical models as explained in Chapter 4, “Calculations and Modeling”. On the other hand, the experiments conducted on normal-g are used for the creation of the surrogate fuels. Ideally all experiments should be conducted under µg conditions, but the amount of experiments required for the characterization of a suitable model is prohibitive.

3.6.1. Normal Gravity Autoignition Experiments

The experimental parameters are analogous to the parameters listed in section 3.5.1.

Influence of Ambient Temperature on the Ignition Delay Times

The following diagrams depict the influence of the ambient temperature on the autoignition behavior in normal gravity conditions of GTL-kerosene for pressure levels between 0,1 and 1,0 MPa in a temperature range from 550–950 K. As expected, the induction delay times show a pronounced dependence on the ambient temperature. As seen previously in the diagrams for GTL-Diesel no strict consecutiveness of the curves is observed. This means, that no clear separation between each experimental curve for different pressures is observed and crossovers occur. This is owed to the complex composition of the two fuels, having on the one hand side, components with different boiling behaviors and on the other, the chemical processes that lead to the ignition of the mixtures.

As can be seen from the τ_1-diagram, the first cool flames are observed at temperatures as low as 580 K for 0,6 MPa and as high as 790 K for 0,8 MPa. In the case of the τ_t-diagram, no hot flames are observed for 0,1 MPa. Except for the data for 0,2 and 0,3 MPa, the total ignition times lie for temperatures above 650 K in a range roughly 150 ms wide approaching asymptotically a total ignition time of roughly 120 ms. The τ_{Lt}-diagram diagram shows a similar behavior as the previous diagram. Except for the 0,1 and 0,2 MPa curves, the droplet lifetimes above 650 K lie in a 180 ms wide band approaching asymptotically a droplet lifetime of 500 ms. From the τ_2- and τ_c-diagrams the following information can be extracted: The τ_2-diagram shows that no two-stage ignition (cool and hot flame) is observed for 0,1 and 0,2 MPa. The τ_c-diagram shows as previously noted that no hot flame is observed for 0,1 MPa. All curves have the tendency to reach a plateau between 350 and 400 ms for the hot flame combustion time.

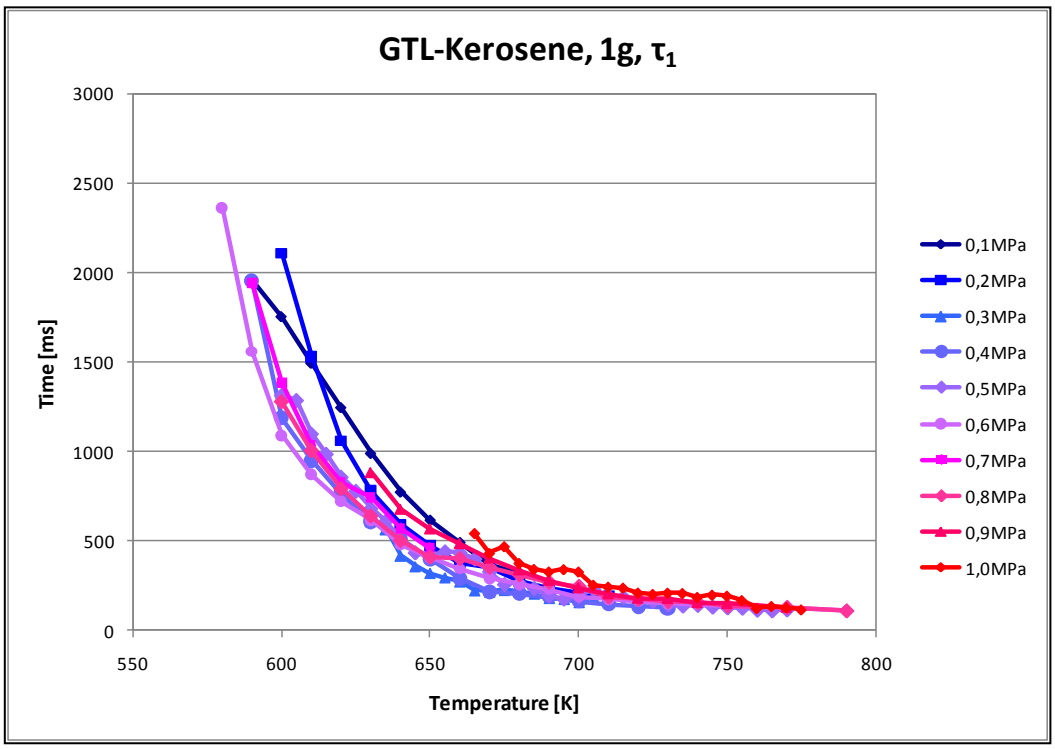

Fig. 80 – Comparison of the first ignition delay times for GTL-Kerosene at 1g for the ambient pressures analyzed

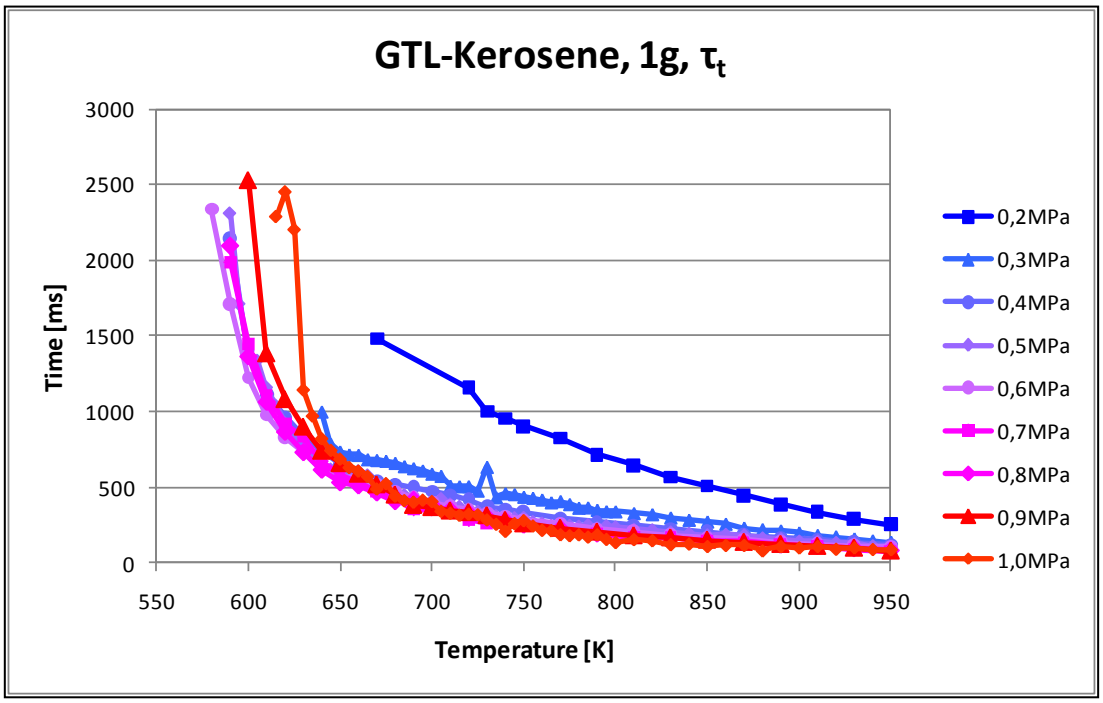

Fig. 81 – Comparison of the total ignition delay times for GTL-Kerosene under 1g for the ambient pressures analyzed

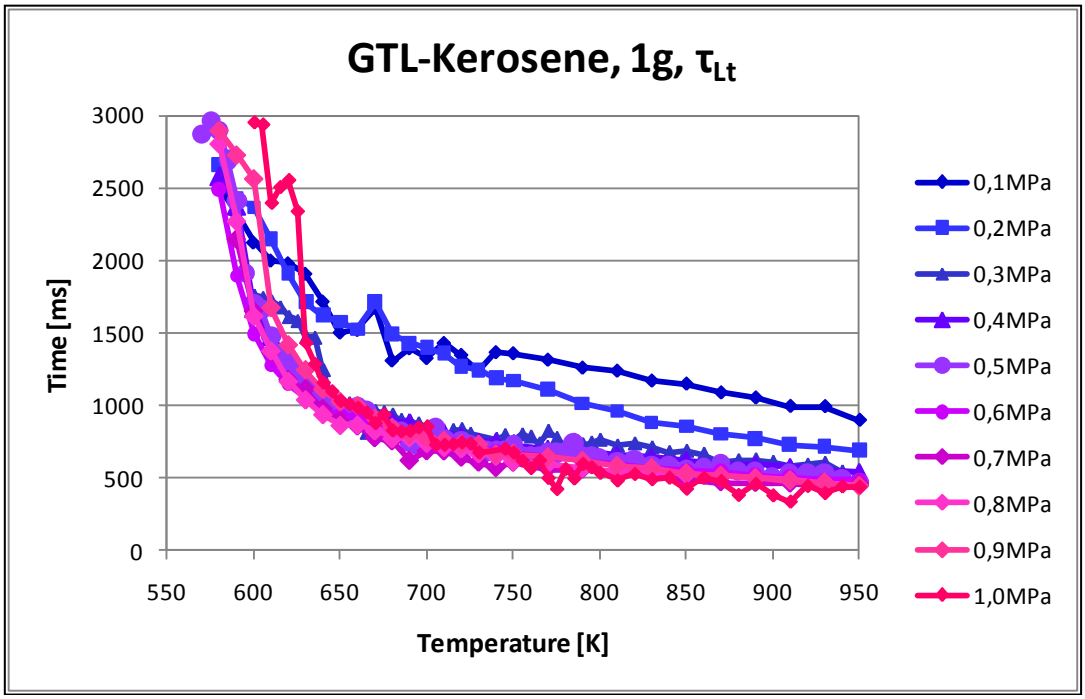

Fig. 82 – Comparison of the droplet lifetimes for GTL-Kerosene under 1g for the ambient pressures analyzed

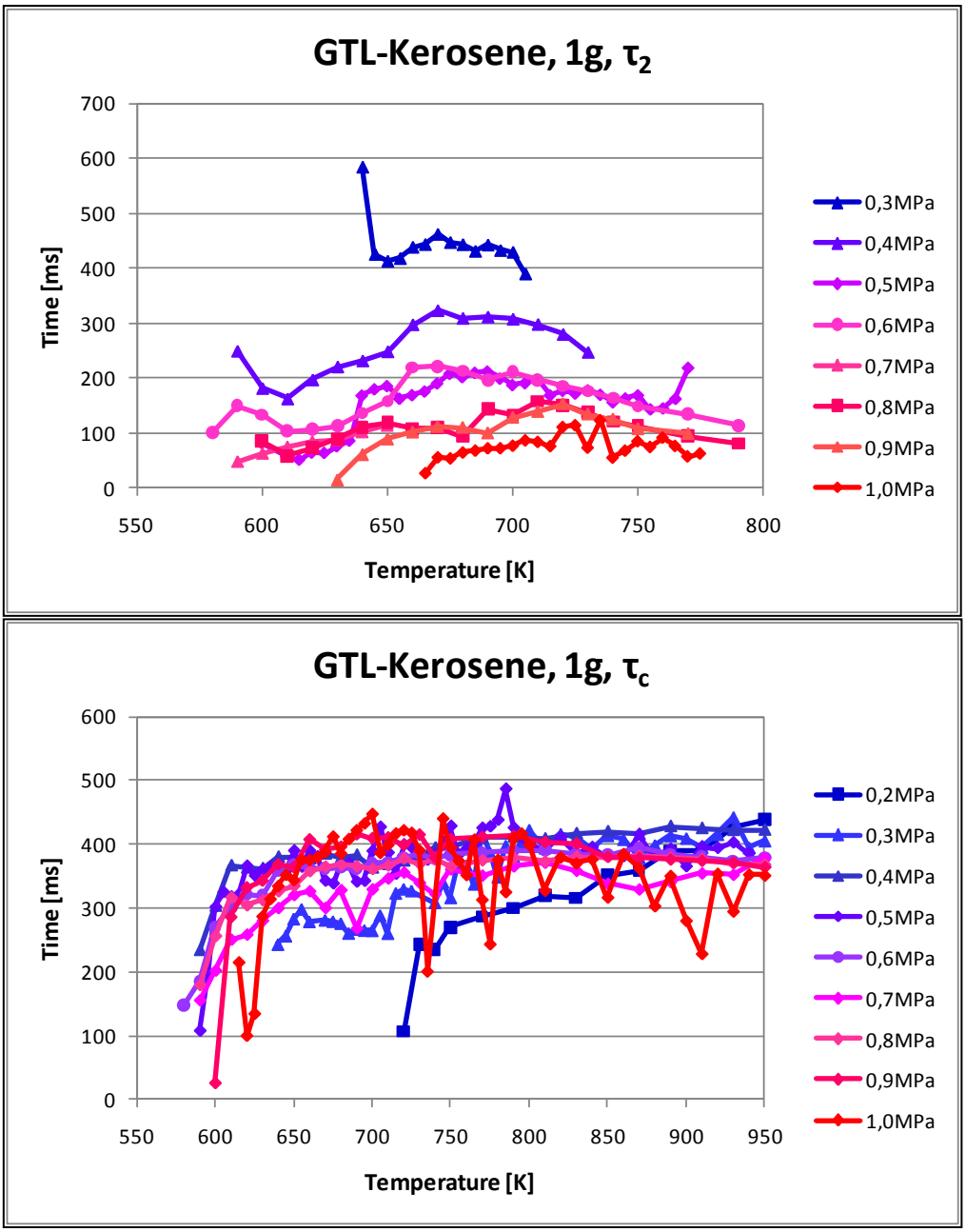

Fig. 83 – Comparison of τ_2 and τ_c for GTL-Kerosene under 1g for the ambient pressures analyzed

From the previous data, three pressure levels (0,3/0,5/1,0 MPa) and their corresponding data sets have been selected. As presented in section 3.5.1 the selected data is shown in two different axis settings. In all three pressure levels a ZTC is observed. For 0,3 MPa the ZTC is seen in a temperature range between 710-730 K, for 0,5 MPa between 640-670 K and for 1,0 MPa this is detected between 670-720 K. All three data sets show the presence of cool flames and two-stage ignition behavior. Characteristic data concerning the initial appearances of cool and hot flames has been summarized in the following table. The values shown are averaged measurements. The droplet lifetimes for the three data sets approach asymptotically at high temperatures a value of around 500 ms.

Pressure	Flame type	T initial [K]	τ_l initial [ms]	T final [K]	τ_l final [ms]
0,3 MPa	cool	630	612,75	705	183,75
0,5 MPa	cool	600	1316,50	770	119,00
1,0 MPa	cool	665	545,88	775	118,75
Pressure	**Flame type**	**T initial [K]**	**τ_t initial [ms]**	**τ_t at 950K [ms]**	
0,3 MPa	hot	640	1002,25	136,25	
0,5 MPa	hot	590	2306,75	102,75	
1,0 MPa	hot	615	2290,25	88,75	

Fig. 84 - Initial and final detections of cool and hot flames for GTL-kerosene under normal-g

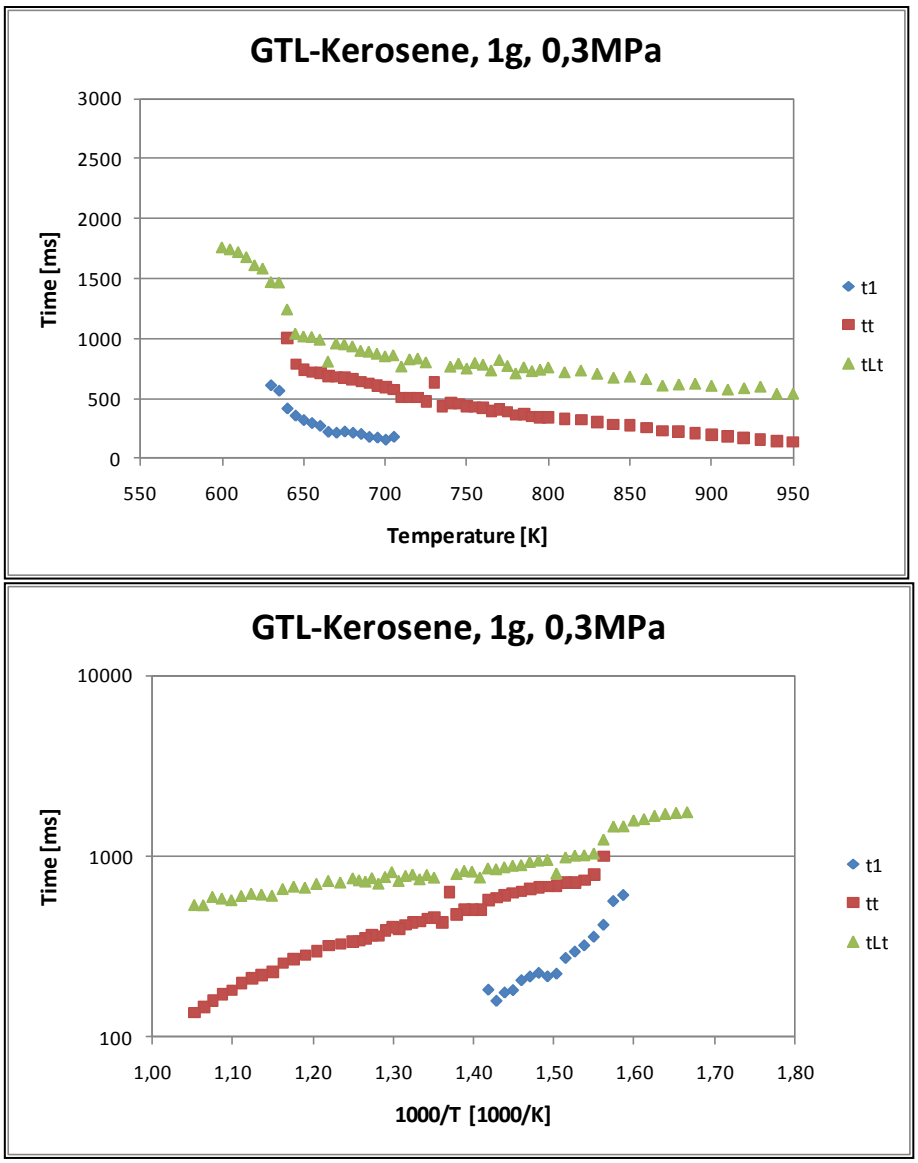

Fig. 85 – Experimental data on the ignition delay times for GTL-Kerosene (0.3 MPa, 1g)

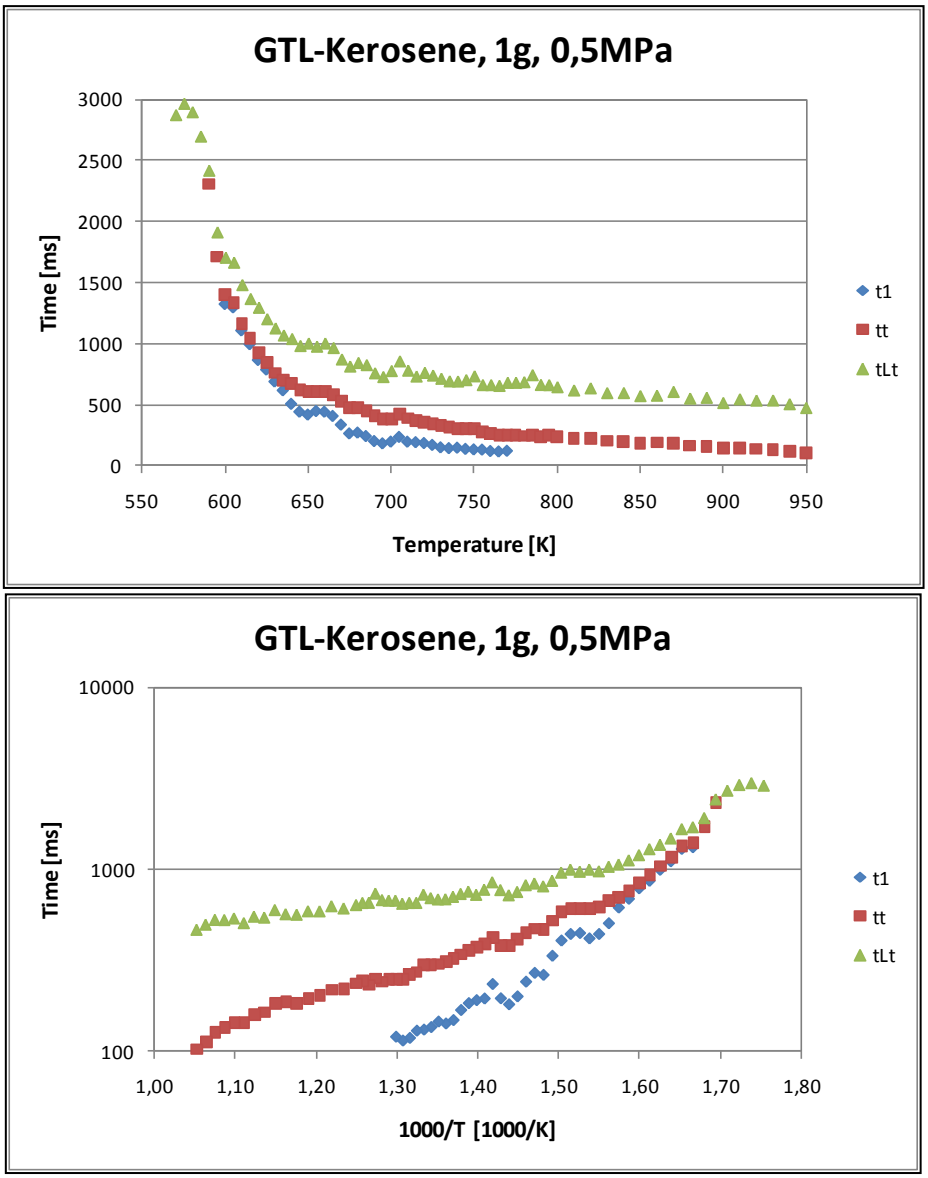

Fig. 86 – Experimental data on the ignition delay times for GTL-Kerosene (0,5 MPa, 1g)

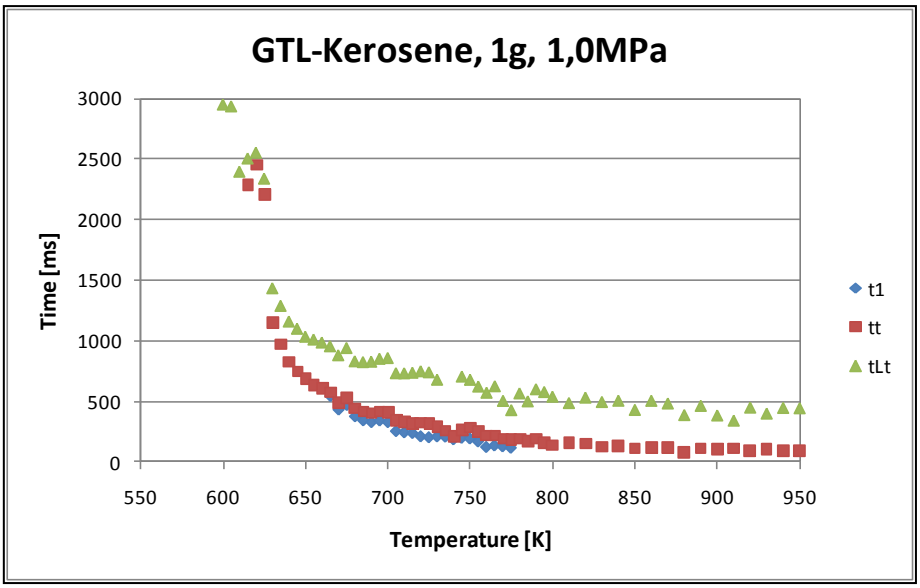

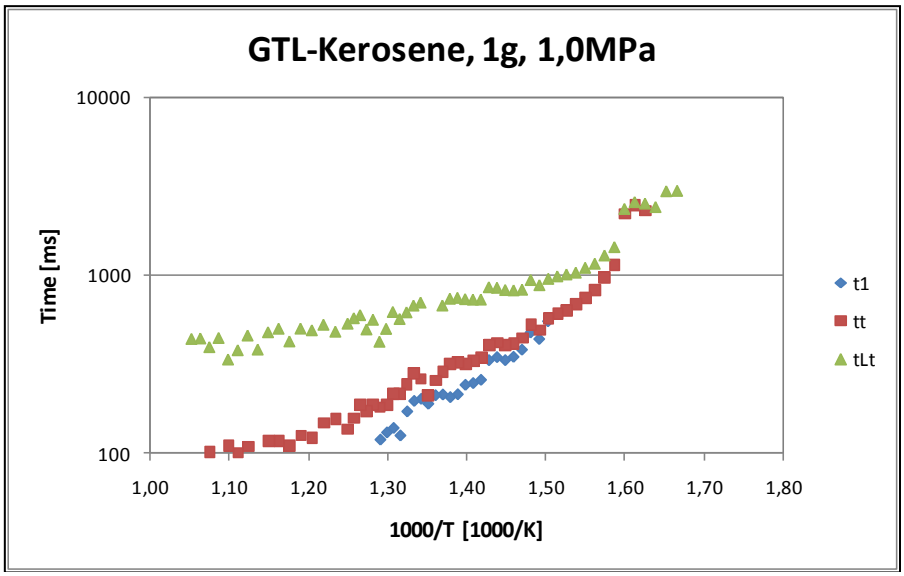

Fig. 87 – Experimental data on the ignition delay times for GTL-Kerosene (1,0 MPa, 1g)

The previous presented data has been fitted with exponential Arrhenius-type single-term and two-term functions. The obtained coefficients and the quality of the fits are summarized in the following table. It has to be noted that the first ignition time is best fitted with a single-term exponential function. Two-term functions do not show for this data better fitting qualities. In the case of the total ignition time, two-term exponential functions show an improvement of the quality of the fits, as can be seen in the R^2 values.

Regressions for τ_1 at 0,3 MPa, 1g					
Equation Type	**Coefficient**		**SSE**	**R^2**	**Adjusted-R^2**
Exponential	a	2,518e8	2,511e4	0,911	0,9046
	b	-0,02066			
Regressions for τ_1 at 0,5 MPa, 1g					
Equation Type	**Coefficient**		**SSE**	**R^2**	**Adjusted-R^2**
Exponential	a	1,484e8	9,447e4	0,9766	0,9759
	b	-0,01941			
Regressions for τ_1 at 1,0 MPa, 1g					
Equation Type	**Coefficient**		**SSE**	**R^2**	**Adjusted-R^2**
Exponential	a	3,309e6	1,417e4	0,9521	0,9499
	b	-0,01325			

Tab. 33 – Coefficients of the regressions for τ_1 and evaluation of quality of the fits

Regressions for τ_t, at 0,3 MPa, 1g					
Equation Type	**Coefficient**		**SSE**	**R^2**	**Adjusted-R^2**
Exponential	a	3,043e4	6,623e4	0,9646	0,9639
	b	-0,005636			
Exponential 2 Terms	a	2,053e4	5,403e4	0,9712	0,9692
	b	-0,00513			
	c	8,978e16			
	d	-0,05349			
Regressions for τ_t, at 0,5 MPa, 1g					
Equation Type	**Coefficient**		**SSE**	**R^2**	**Adjusted-R^2**
Exponential	a	4,033e6	1,161e6	0,8844	0,8823
	b	-0,01323			
Exponential 2 Terms	a	1,026e18	6,992e4	0,993	0,9927
	b	-0,058			
	c	2,478e4			
	d	-0,005855			

Regressions for τ_t, at 1,0 MPa, 1g					
Equation Type	**Coefficient**		**SSE**	**R^2**	**Adjusted-R^2**
Exponential	a	1,746e10	1,763e6	0,8764	0,874
	b	-0,0258			
Exponential 2 Terms	a	1,868e18	6,571e5	0,9539	0,9511
	b	-0,056			
	c	2,515e4			
	d	-0,006201			

Tab. 34 - Coefficients of the regressions for τ_t and evaluation of quality of the fits

The second induction time and the hot flame combustion duration show an interesting behavior. The second induction delay shows pronounced pressure dependence and almost no temperature sensitivity. The value of τ_2 decreases with increasing pressure but remains relatively constant for the studied temperature range. Only the temperature where it first occurs changes depending on the pressure level. For τ_C a weak pressure and temperature dependence is observed, suggesting its stronger dependence on other parameters such as the initial droplet diameter. As in τ_2, for τ_C its first detection changes with the pressure level. The data obtained for τ_2 and τ_C is shown in the following diagrams:

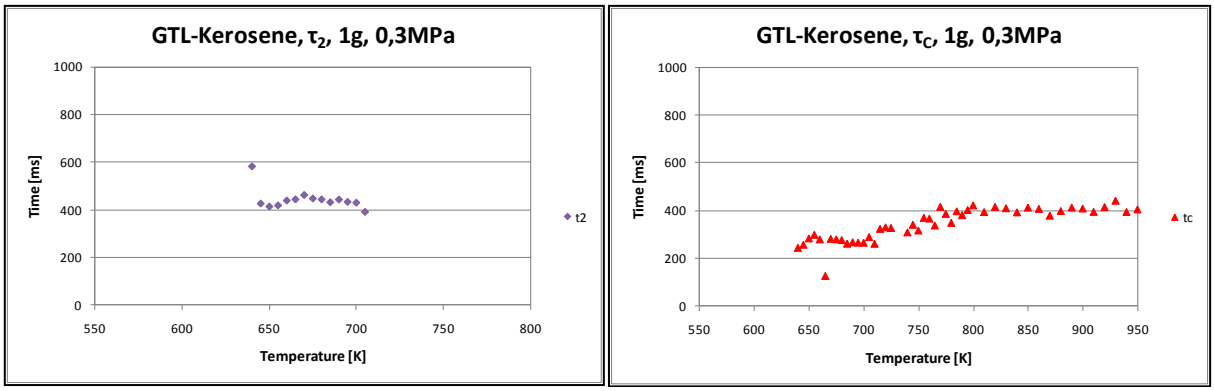

Fig. 88 - Second ignition delay times and hot flame combustion duration for GTL-Kerosene for 0,3 MPa

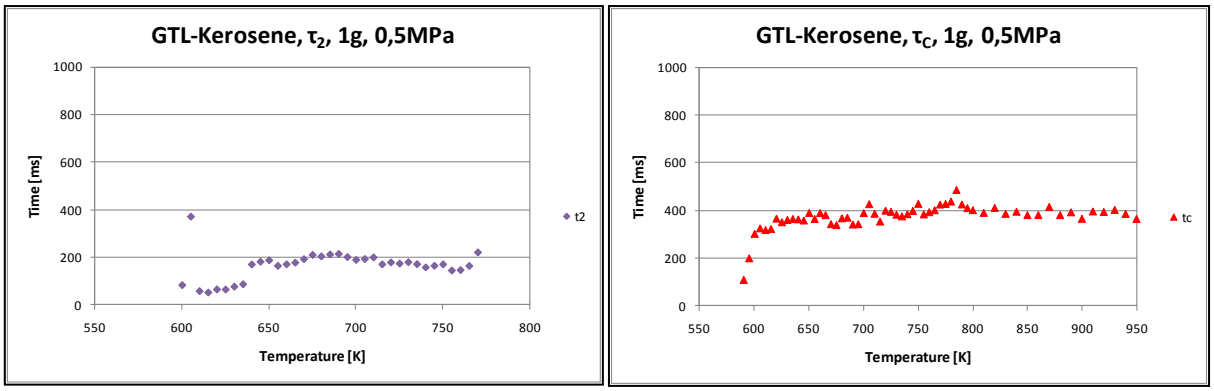

Fig. 89 - Second ignition delay times and hot flame combustion duration for GTL-Kerosene for 0,5 MPa

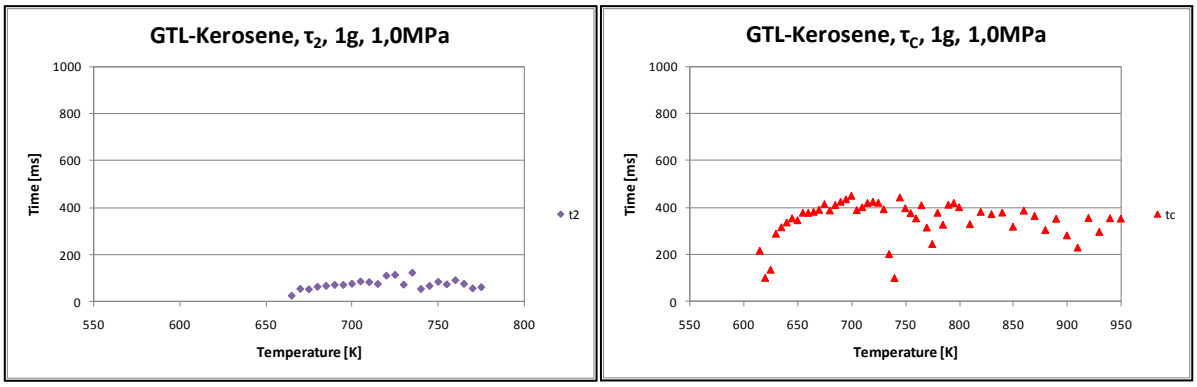

Fig. 90 - Second ignition delay times and hot flame combustion duration for GTL-Kerosene for 1,0 MPa

Influence of Ambient Pressure on the Ignition Delay Times

The following figures compare the previously presented data and show the influence of pressure on the autoignition behavior of GTL-Kerosene. Similarly to the observations made in the studies concerning GTL-Diesel, a general behavior can be observed: Low temperature curves (T<650 K) show for each ignition delay time (τ_1, τ_t, τ_{Lt}) a high pressure dependency. This suggests, as noted in previous sections, the low temperature reaction path that leads to a cool flame is strongly pressure dependent. The high temperature reaction path is weakly pressure dependent as shown by the almost horizontal curves for higher temperatures.

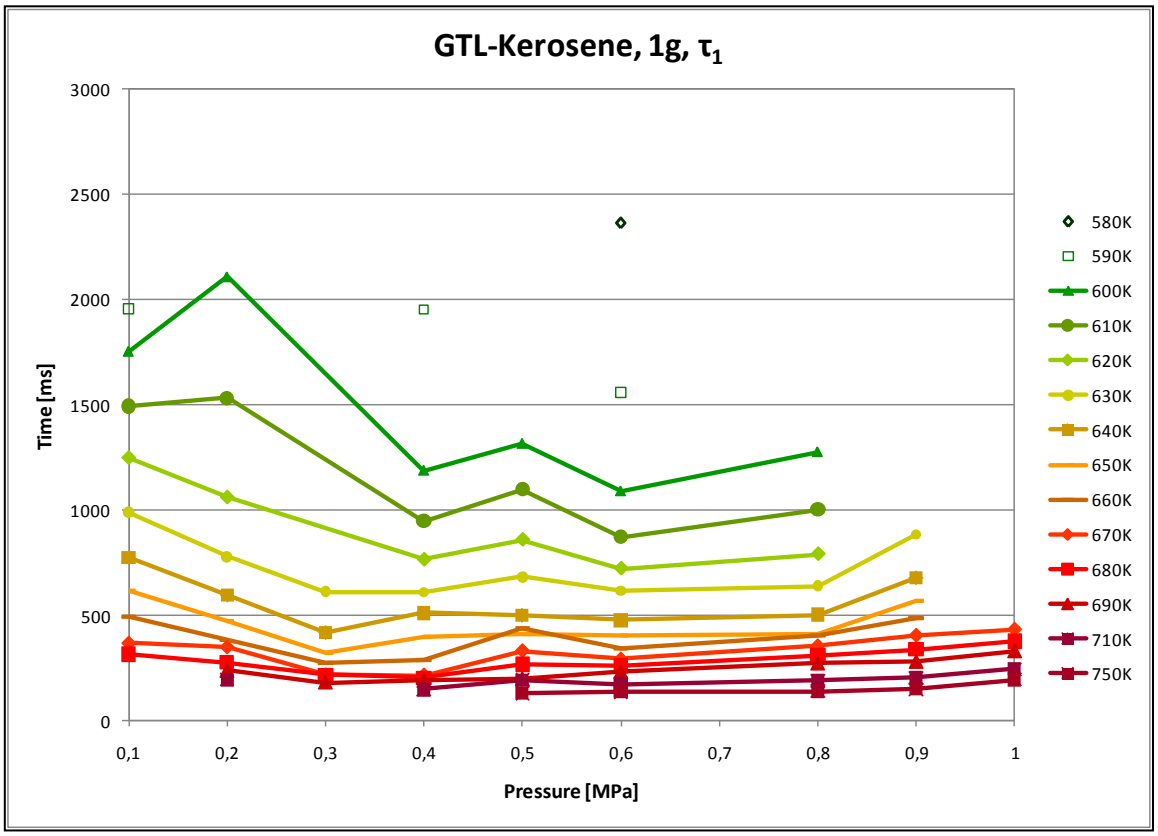

Fig. 91 – Experimental data on the first ignition delay times of GTL-Kerosene and the influence of ambient pressure

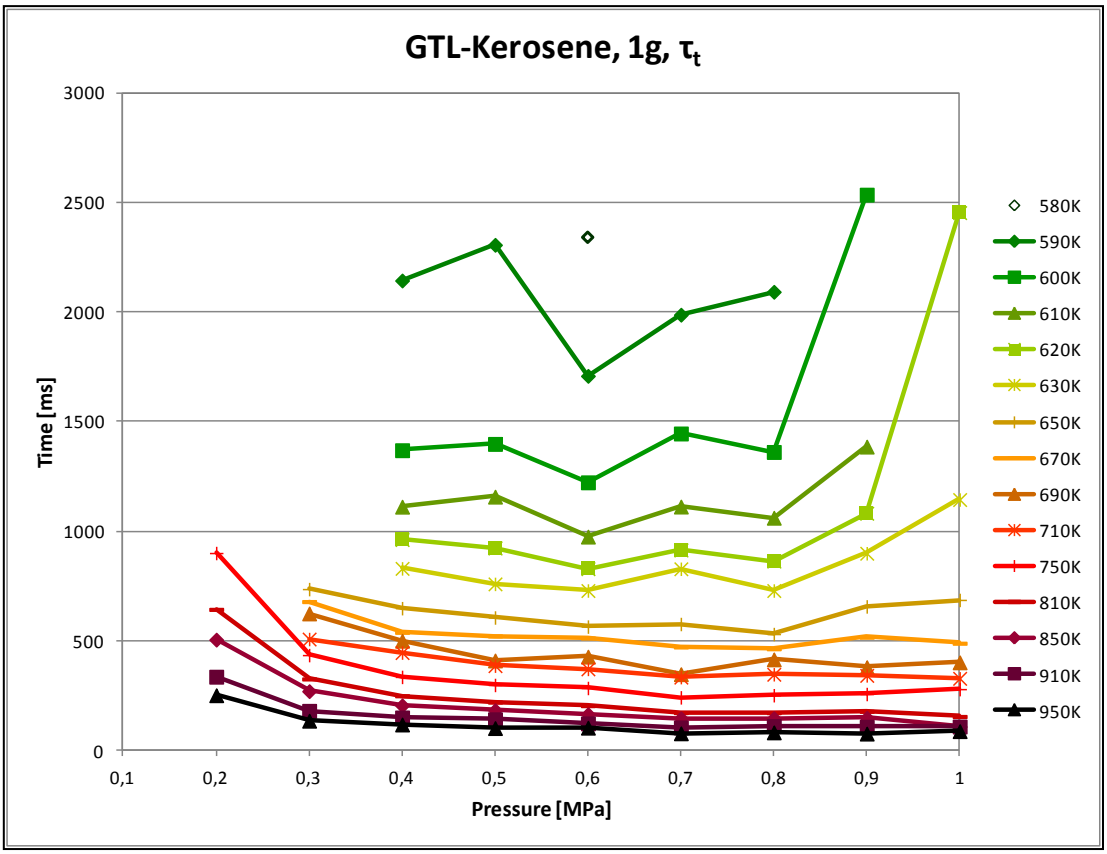

Fig. 92 - Experimental data on the total ignition delay times of GTL-Kerosene and the influence of ambient pressure

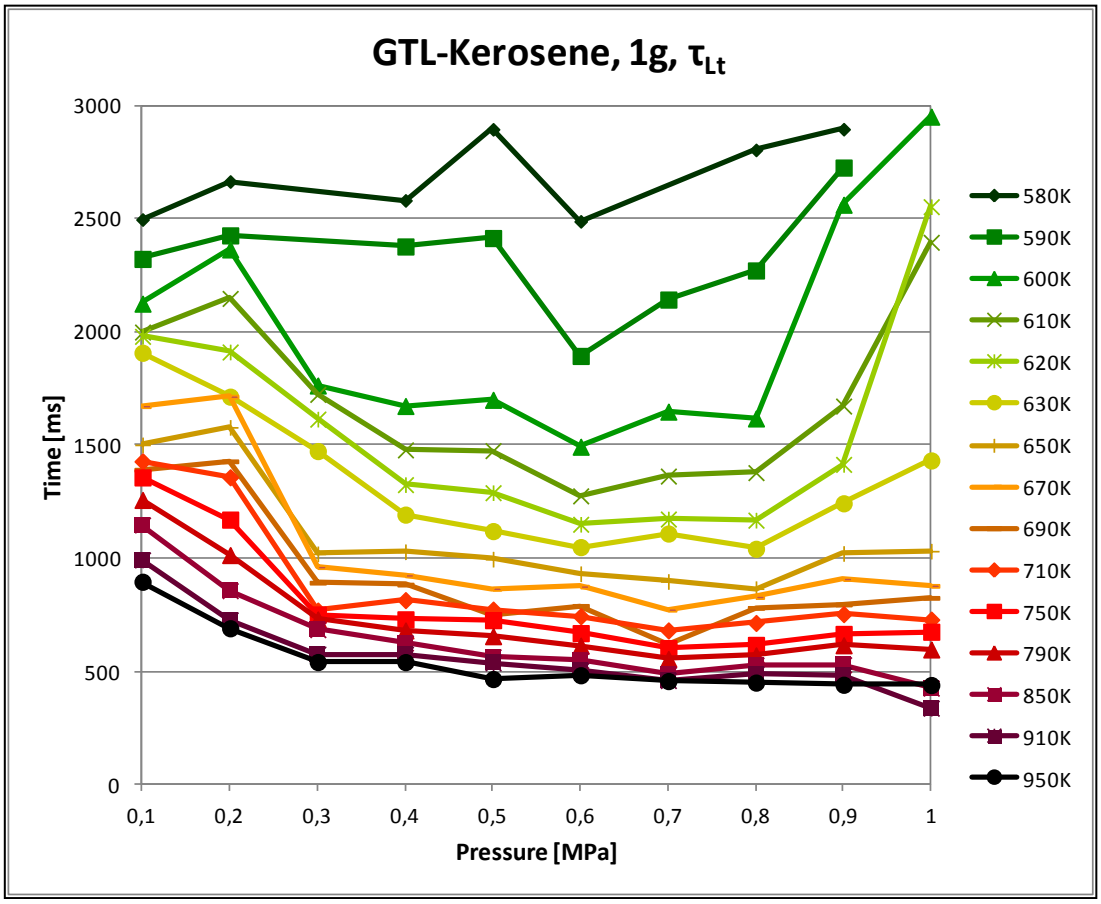

Fig. 93 - Experimental data on the total ignition delay times of GTL-Kerosene and the influence of ambient pressure

Summary of the Autoignition Experiments for GTL-Kerosene conducted under Normal Gravity Conditions and Classification of the Ignition-Types observed

This section summarizes the data on the autoignition of GTL-Kerosene under normal gravity and shows regressions for τ_1, τ_t and τ_{Lt}. Analogous to the fits obtained in the section on the influence of temperature on the autoignition times of GTL-Kerosene, two-term exponential fits show better results concerning the quality of the regressions as expressed by the R^2 values.

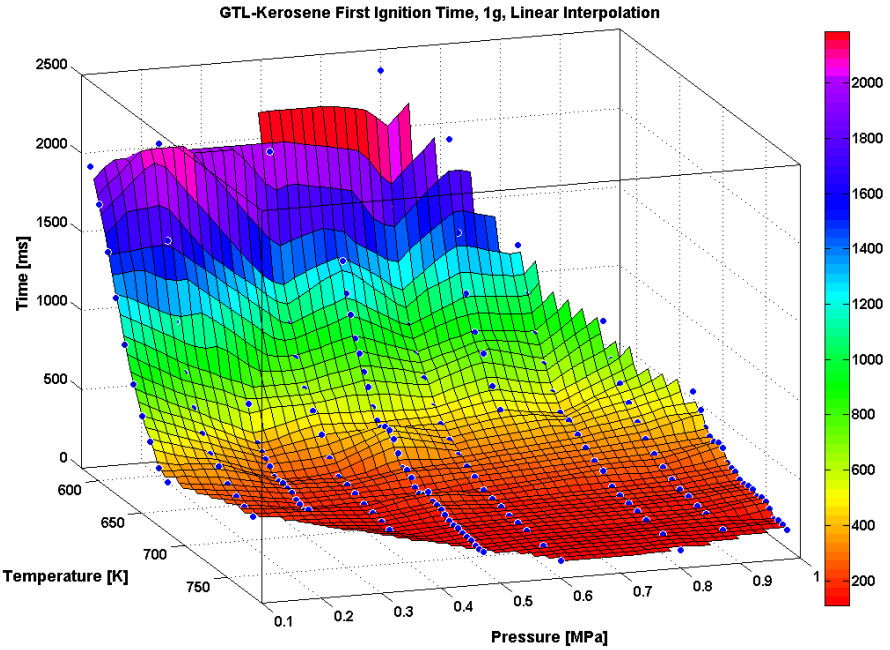

Fig. 94 – Experimental data on the first ignition time for GTL-Kerosene under 1g

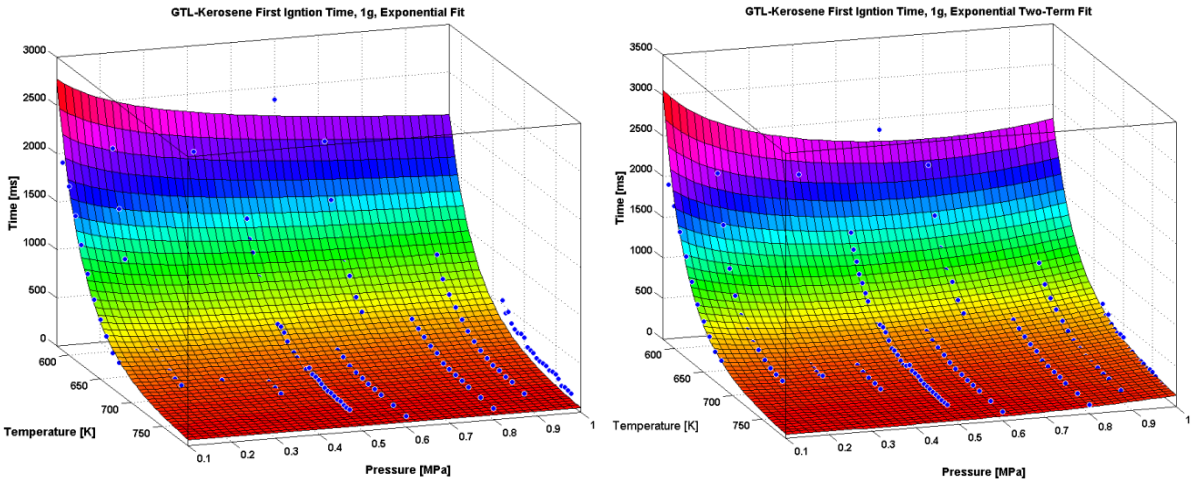

Fig. 95 – Exponential fits on the experimental data for the first ignition time of GTL-Kerosene under 1g

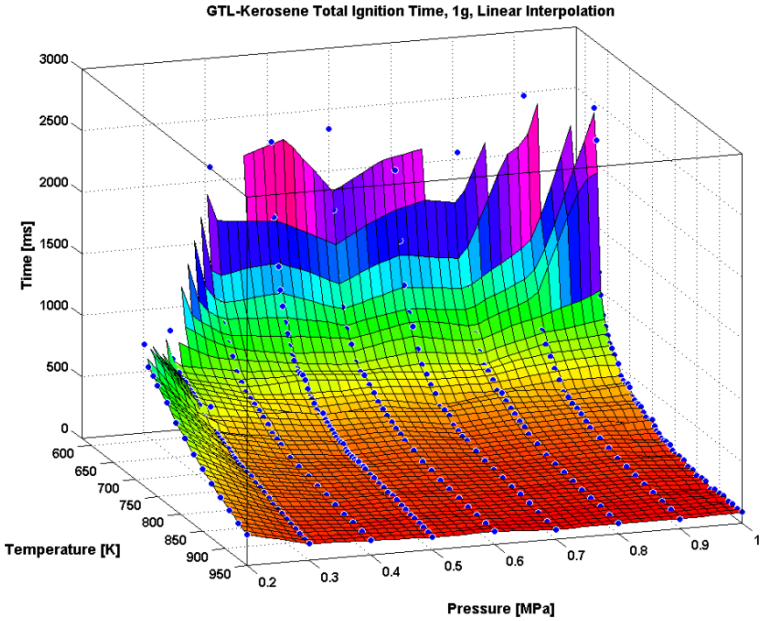

Fig. 96 - Experimental data on the total ignition time for GTL-Kerosene under 1g

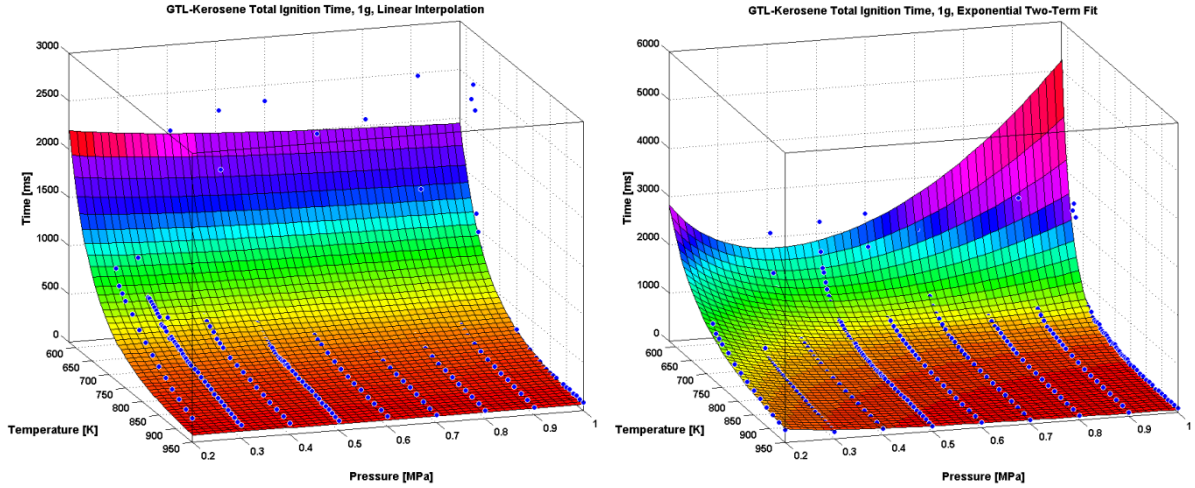

Fig. 97 – Exponential fits on the experimental data for the total ignition time for GTL-Kerosene under 1g

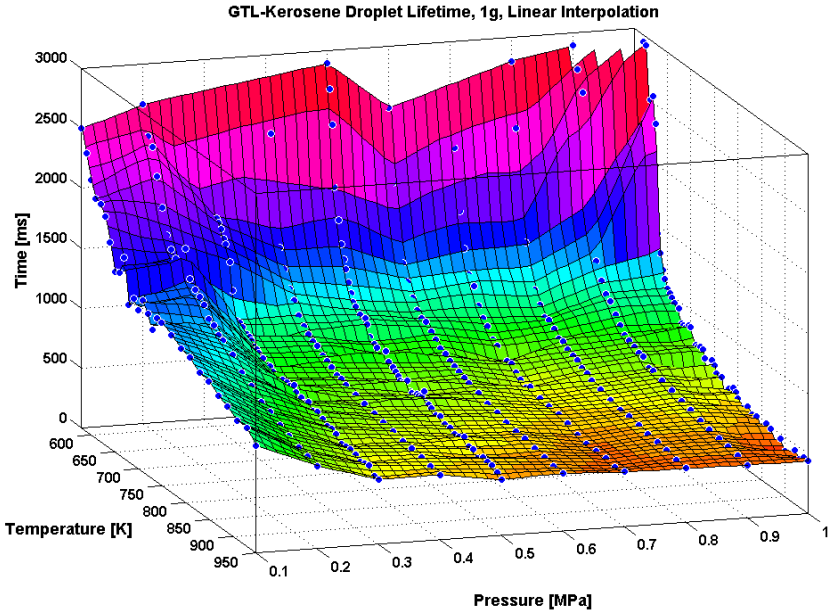

Fig. 98 – Experimental data on the droplet lifetime for GTL-Kerosene under 1g

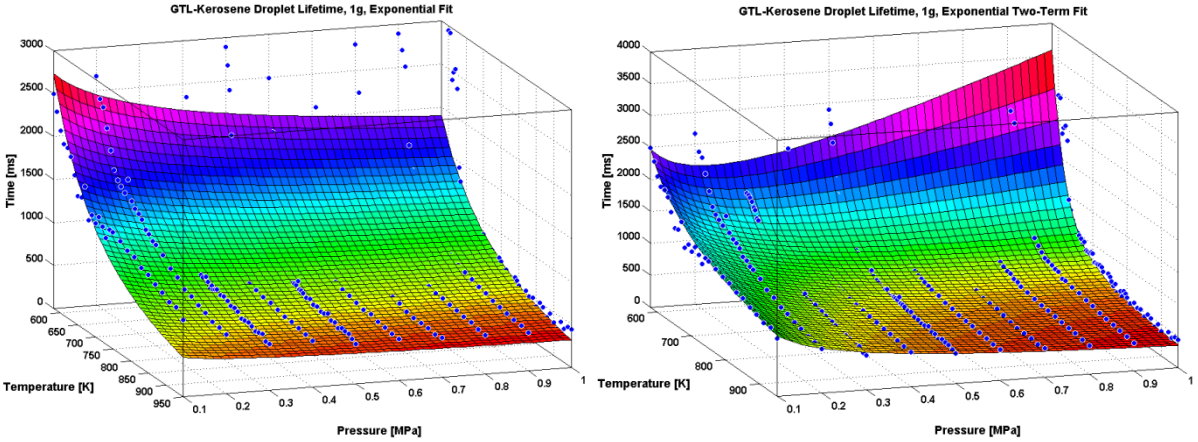

Fig. 99 – Exponential fits on the experimental data for the droplet lifetime of GTL-Kerosene under 1g

Regressions for τ_1, 1g					
Equation Type	**Coefficient**		**SSE**	**R^2**	**Adjusted-R^2**
Exponential	A	0,001115	1,87e6	0,9437	0,943
	E	8368			
	n	-0,1299			
Exponential 2 Terms	A_1	-0,002793	1,222e6	0,9632	0,9621
	A_2	3,164			
	E_1	9138			
	E_2	2803			
	m	3,258			
	n	-0,1985			

Regressions for τ_t, 1g					
Equation Type	**Coefficient**		**SSE**	**R^2**	**Adjusted-R^2**
Exponential	A	0,1739	9,012e6	0,8402	0,8391
	E	5482			
	n	0,08856			
Exponential 2 Terms	A_1	1,401	4,958e6	0,9144	0,913
	A_2	3407			
	E_1	1,172e4			
	E_2	7,957e-6			
	m	2,55			
	n	-1,063			

Regressions for τ_{Lt}, 1g					
Equation Type	**Coefficient**		**SSE**	**R^2**	**Adjusted-R^2**
Exponential	A	17,39	2,679e7	0,769	0,7677
	E	2741			
	n	-0,151			
Exponential 2 Terms	A_1	92,6	1,011e7	0,9053	0,904
	A_2	0,0001175			
	E_1	1259			
	E_2	9848			
	m	1,018			
	n	-0,4324			

Tab. 35 – Coefficients of the regressions for the induction delay times of GTL-Kerosene at normal gravity conditions and evaluation of the quality of the fits

The following characteristic map summarizes the different ignition-types encountered in this study for GTL-Kerosene. The lowest temperature (for given ambient pressure) at which cool flames are detected by the experimental apparatus used in this study is denoted by the curve marked as “T cool begin”. Similarly, the highest temperature at which a cool flame is observed is described by the “T cool end” curve. “T hot begin” describes the lowest

temperature at which a hot flame is observed. The resulting segments in this diagram denote the ignition types encountered. For 0,1 MPa no hot flame was observed in the temperature range analyzed. Thus, the curve marked as "T hot begin ex." is an extrapolation of the "T hot begin" curve. Below 580 K no ignition is observed over the experimental pressure range. A single-stage cool flame region is observed between 0,1-0,3 MPa, at temperatures roughly between 600-700 K. Between pressures slightly above 0,2 MPa and 1,0 MPa, and in the range of 580-790 K, a two-stage cool and hot flame ignition region is observed. For temperatures above this range, a single-stage hot flame region is detected. Special consideration has to be given for two regions where single-stage hot flame ignition is observed. The first one lies between 0,4-0,6 MPa between 580-590 K, the second between 0,7-1,0 MPa and 590-660 K. The temperatures where these regions appear are fairly low. These two regions are preceded by the "no ignition" region at lower temperatures and succeeded at higher temperatures by a "two-stage (cool and hot flame)" region.

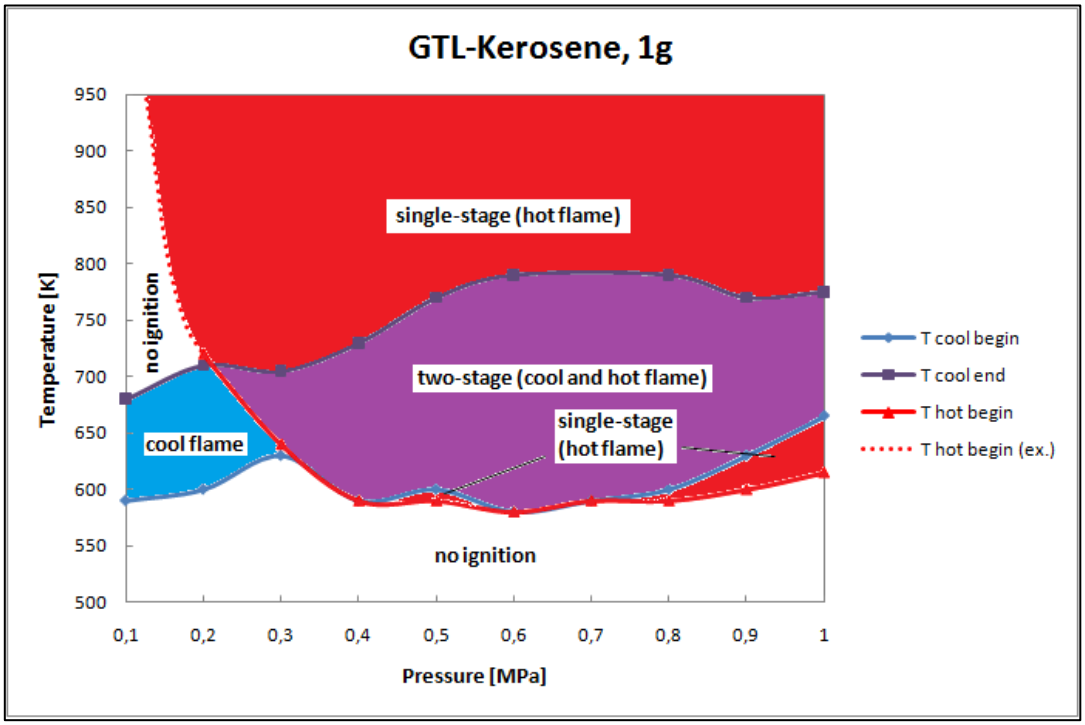

Fig. 100 – Characteristic map of ignition types for GTL-Kerosene droplets at normal gravity condition

3.6.2. Microgravity Autoignition Experiments

The results of the experiments on the autoignition of GTL-Kerosene under microgravity conditions are presented in this section. The following diagrams depict the autoignition behavior in microgravity of GTL-Kerosene for three pressure levels (0,3/0,5 and 1,0 MPa) in a temperature range from 550–800 K. The values of τ_l, τ_t and τ_{Lt} with respective Arrhenius-type exponential fits are plotted over the specified temperature range. Experiments in microgravity were conducted mainly in a temperature regime where two-stage-ignition is clearly established and its extent can be assessed.

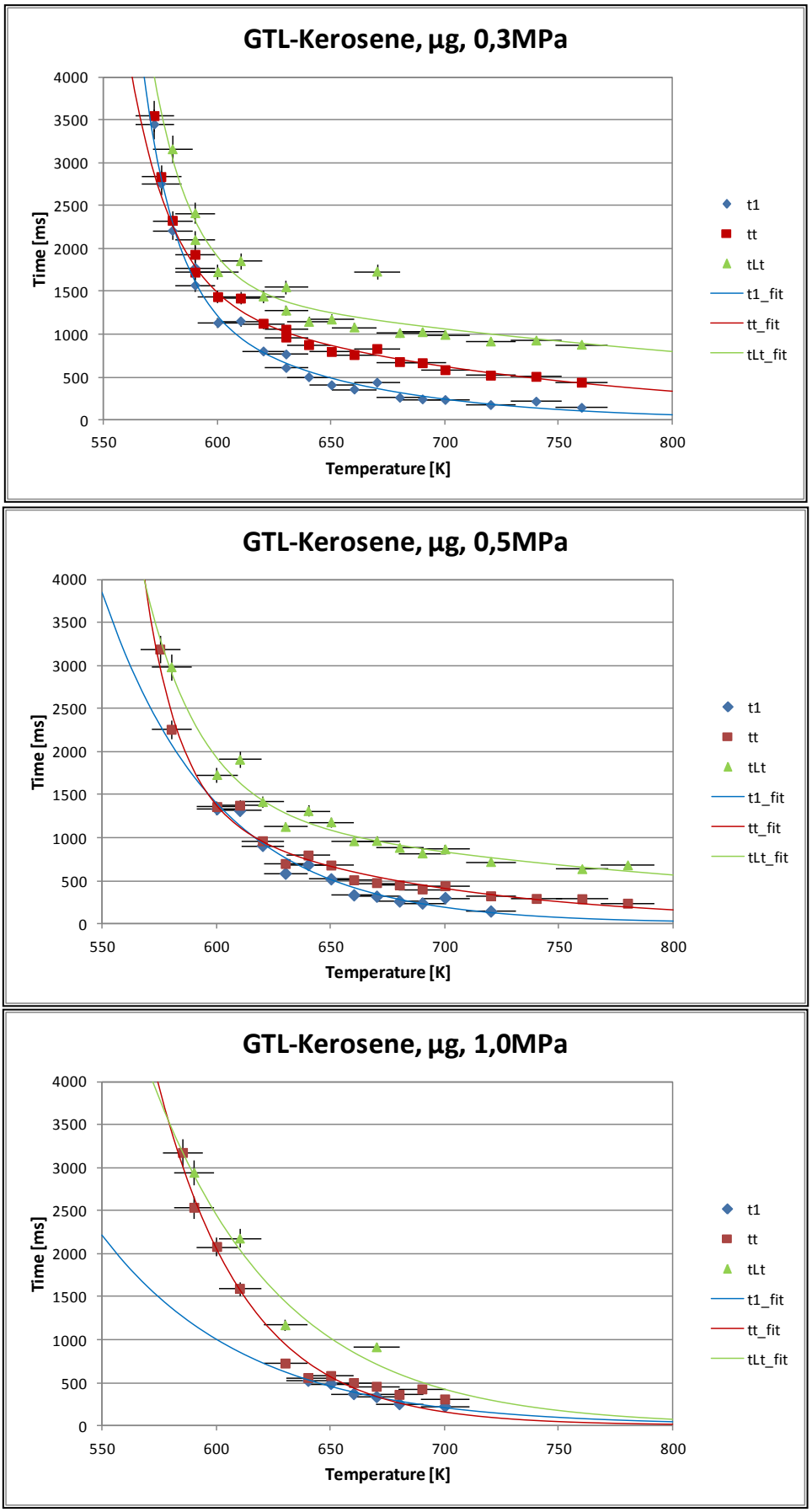

Fig. 101 - Experimental data and regression fits of the ignition delay times of GTL-Kerosene in µg

Influence of Ambient Temperature on the Ignition Delay Times

The diagrams show in general, for the three pressure levels analyzed, similar progressions, meaning that the measured ignition delay times show relatively small differences between each pressure level at a given temperature. These differences are the smallest for τ_1 and increase for τ_t. The diagram for the second induction times show the difference in the extent, for each pressure level, of the temperature range where both, cool and hot flames, are detectable. For 0,3 MPa this region ranges from 570 to760 K, for 0,5 MPa 600 to 720 K and for 1,0 MPa 640 to 700 K. As can be seen, with increasing pressure the second ignition time decreases. The diagram for the hot flame combustion times shows for 0,3 MPa a rather erratic behavior, but for 0,5 and 1,0 MPa the data shows a tendency to flatten at around 400 ms.

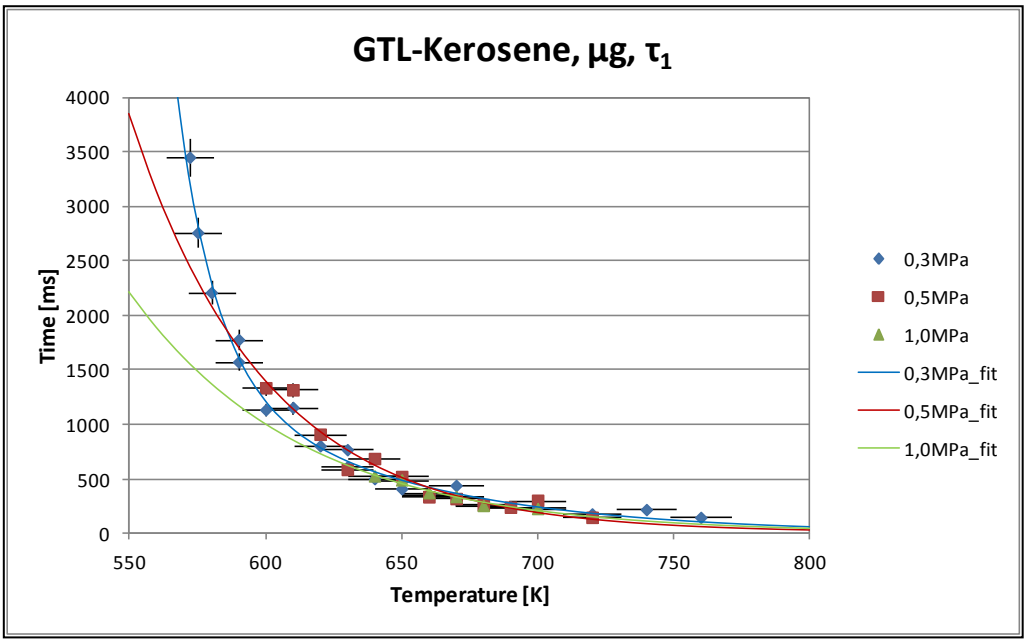

Fig. 102 – First ignition delay times for GTL-Kerosene under µg

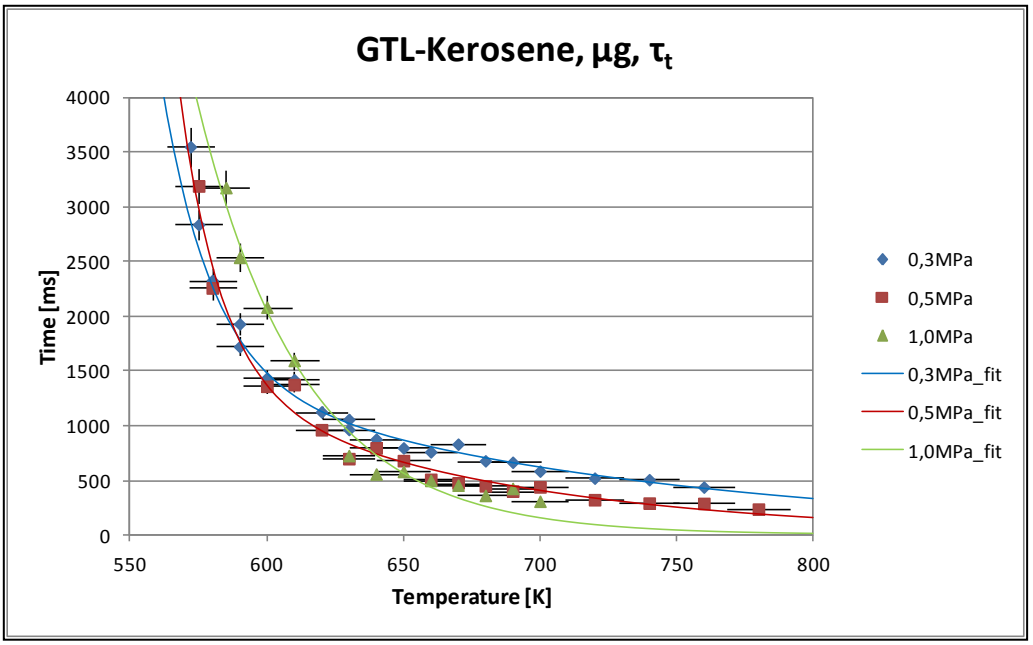

Fig. 103 – Total ignition times for GTL-Kerosene under µg

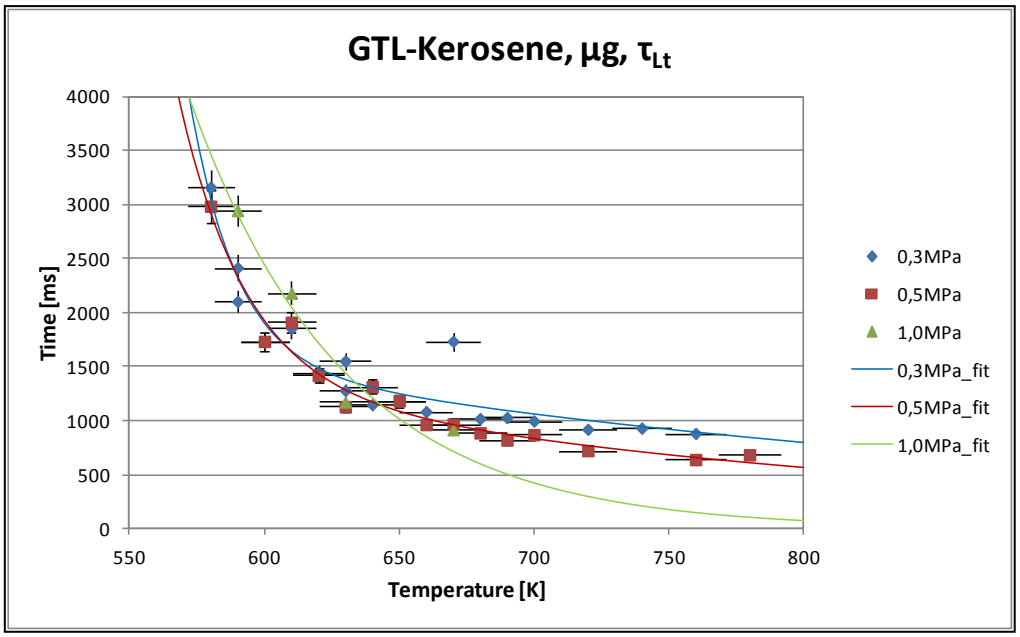

Fig. 104 – Droplet lifetimes for GTL-Kerosene under µg

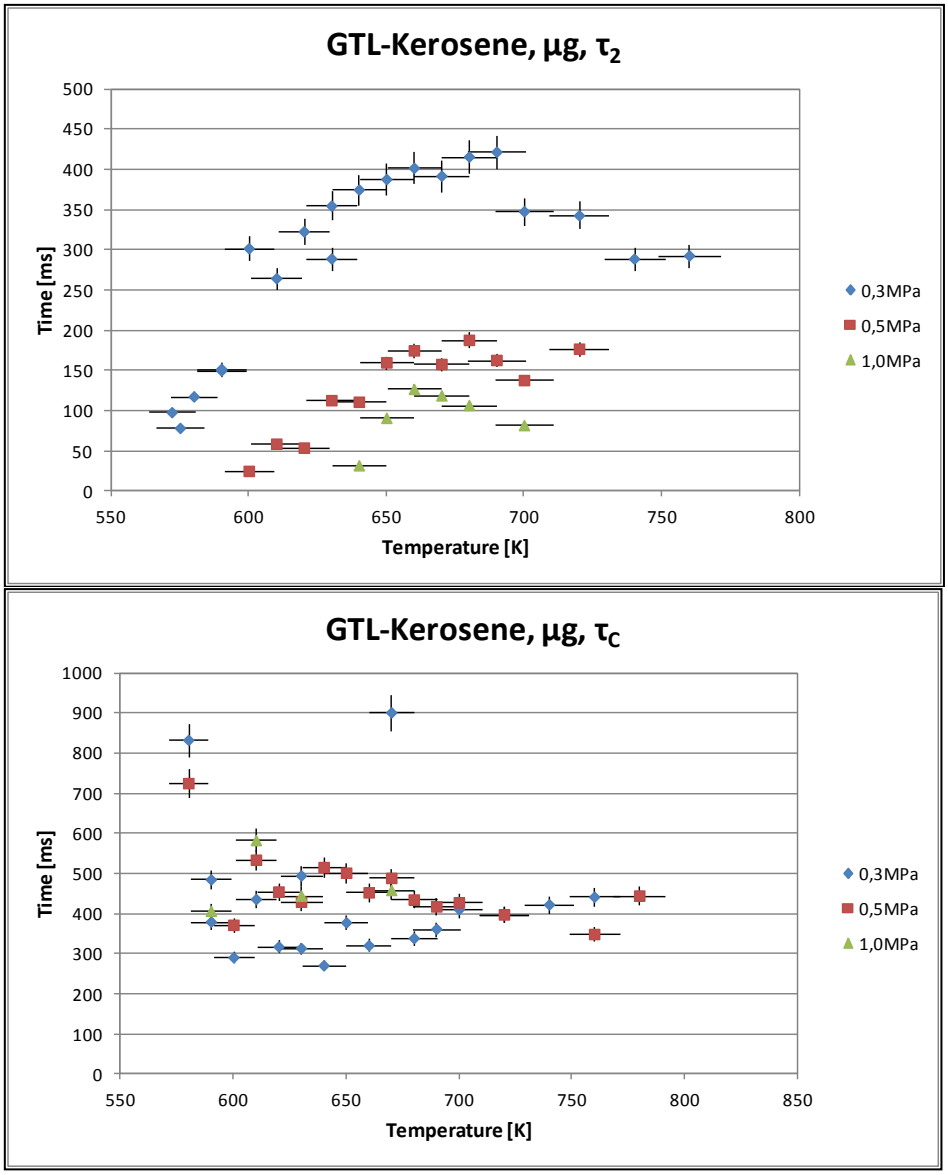

Fig. 105 – Second ignition and hot flame combustion times for GTL-Kerosene under µg

The experimental data shown previously is fitted with exponential (Arrhenius-type) functions. Two-term fits show generally better R^2 values. In some cases the two-term exponential fits were omitted, because the fitting algorithm reduced the two-term to a single-term.

Regressions for τ_l at 0,3 MPa, µg			**Regression for τ_t at 0,3 MPa, µg**		
Equation Type	**Coefficient**		**Equation Type**	**Coefficient**	
Exponential	a	2,046e10	Exponential	a	1,206e6
	b	-0,02749		b	-0,01104
	R^2	0,9642		**R^2**	0,9249
Exponential 2 Terms	a	3,551e20	Exponential 2 Terms	a	5,931e16
	b	-0,06952		b	-0,0547
	c	3,213e6		c	4,997e4
	d	-0,01354		d	-0,006279
	R^2	0,9899		**R^2**	0,9872

Regressions for τ_l at 0,5 MPa, µg			**Regression for τ_t at 0,5 MPa, µg**		
Equation Type	**Coefficient**		**Equation Type**	**Coefficient**	
Exponential	a	2,598e8	Exponential	a	2,748e8
	b	-0,02022		b	-0,02001
	R^2	0,95		**R^2**	0,935
Exponential 2 Terms	a	9,592e8	Exponential 2 Terms	a	4,185e19
	b	-0,02239		b	-0,06563
	c	0,002198		c	3,09e5
	d	0,01474		d	-0,009477
	R^2	0,954		**R^2**	0,9813

Regressions for τ_l at 1,0 MPa, µg			**Regression for τ_t at 1,0 MPa, µg**		
Equation Type	**Coefficient**		**Equation Type**	**Coefficient**	
Exponential	a	1,342e7	Exponential	a	1,137e10
	b	-0,01581		b	-0,02587
	R^2	0,9622		**R^2**	0,9771
Exponential 2 Terms	a		Exponential 2 Terms	a	3,007e11
	b			b	-0,03146
	c			c	0,02817
	d			d	0,01321
	R^2			**R^2**	0,9916

Tab. 36 – Coefficients of the regressions for τ_l and τ_t and evaluation of the quality of the fits

Influence of Ambient Pressure on the Ignition Delay Times

The following diagrams show the influence of the ambient pressure on the autoignition behavior of GTL-Kerosene under microgravity conditions. The general behavior for the ignition delay times is characterized by a weak dependence on pressure. For τ_l the amount of data is scarce, but the general tendency can be inferred. The τ_t-diagram shows that as a general behavior, that data for 0,3 MPa have larger ignition delay times and experience a decrease at 0,5 MPa and stay at the same level for 1,0 MPa. A similar behavior is seen on the τ_{Lt}-diagram for 0,3 and 0,5 MPa. Some increase can be observed for data points at 1,0 MPa.

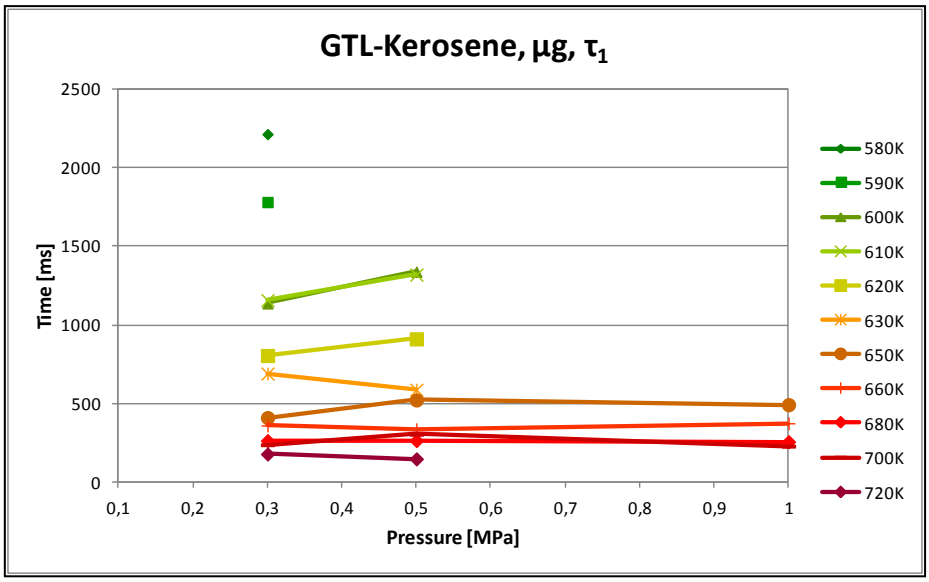

Fig. 106 – Experimental data on τ_1 of GTL-Kerosene in µg and the influence of ambient pressure

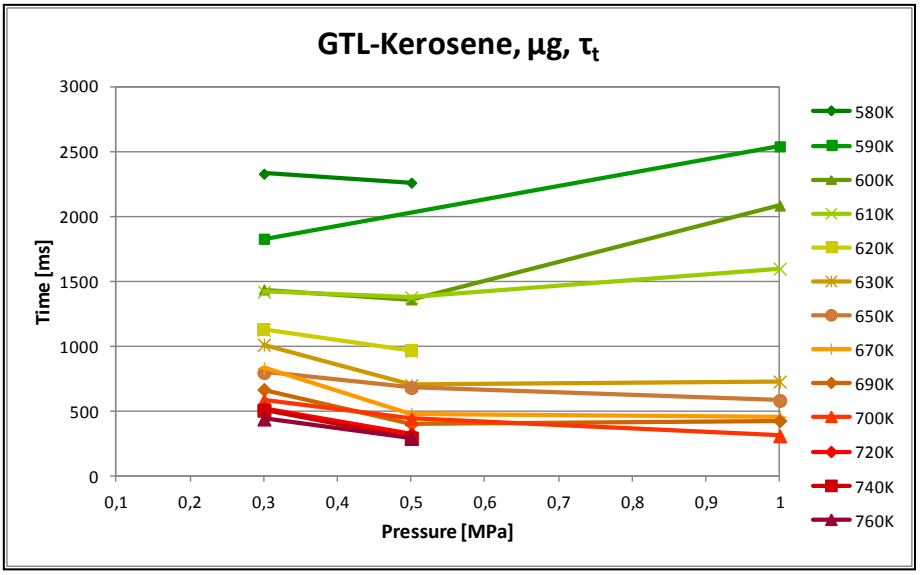

Fig. 107 – Experimental data on τ_t of GTL-Kerosene in µg and the influence of ambient pressure

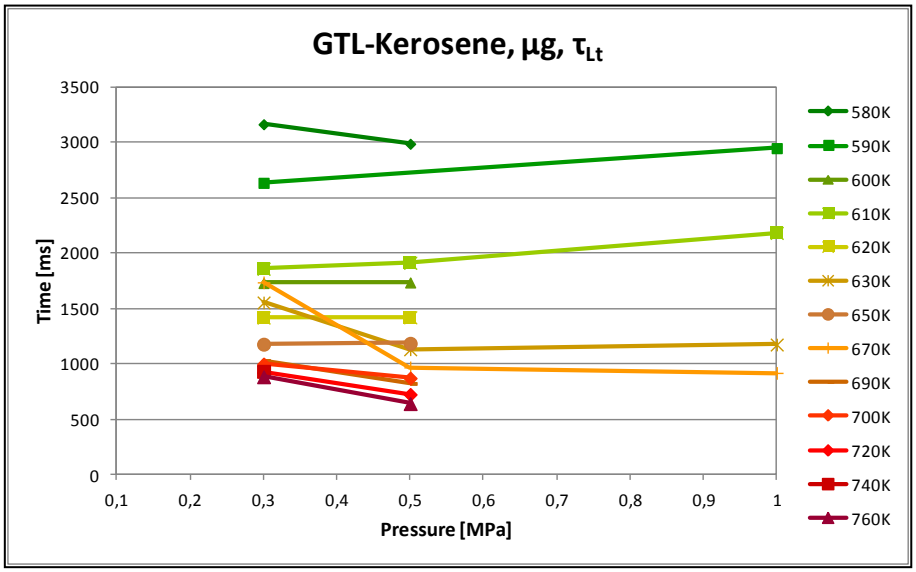

Fig. 108 - Experimental data on τ_{Lt} of GTL-Kerosene in µg and the influence of ambient pressure

Classification of the Ignition-Types observed

The initial and final temperatures for the detection of cool and hot flames are summarized in the following table. For 0,3 MPa the initial temperatures are not available, the value shown is the lowest temperature that was set for the experimental run (*). For 0,5 and 1,0 MPa the first appearance of a hot flame precedes the cool flame.

Pressure	Flame type	T initial [K]	τ_l initial [ms]	T final [K]	τ_l final [ms]	τ_t initial [ms]
0,3MPa	cool	572*	3451,76	N/A	N/A	
	hot	572*				3549,80
0,5MPa	cool	600	1338	720	150	
	hot	575				3191,96
1,0MPa	cool	640	530	N/A	N/A	
	hot	585				3177,25

Tab. 37 - Initial and final detections of cool and hot flames for GTL-kerosene under µg

The following characteristic map shows the different ignition-types encountered in this study for GTL-Kerosene under microgravity conditions. Analogous to section 3.5.2, experiments were conducted for three pressure levels and the different demarcation lines are extrapolated for illustration purposes. Below 572 K no ignition is observed. In the range of 572-640 K, a single-stage hot flame region is observed. At lower pressures (0,1-0,3 MPa) a single-stage cool flame region is expected. Above the "T cool begin" line, the two-stage ignition region exists. The measurements in this study concentrate on this region. For 0,5 MPa and 720 K the "high temperature" single-stage flame region begins.

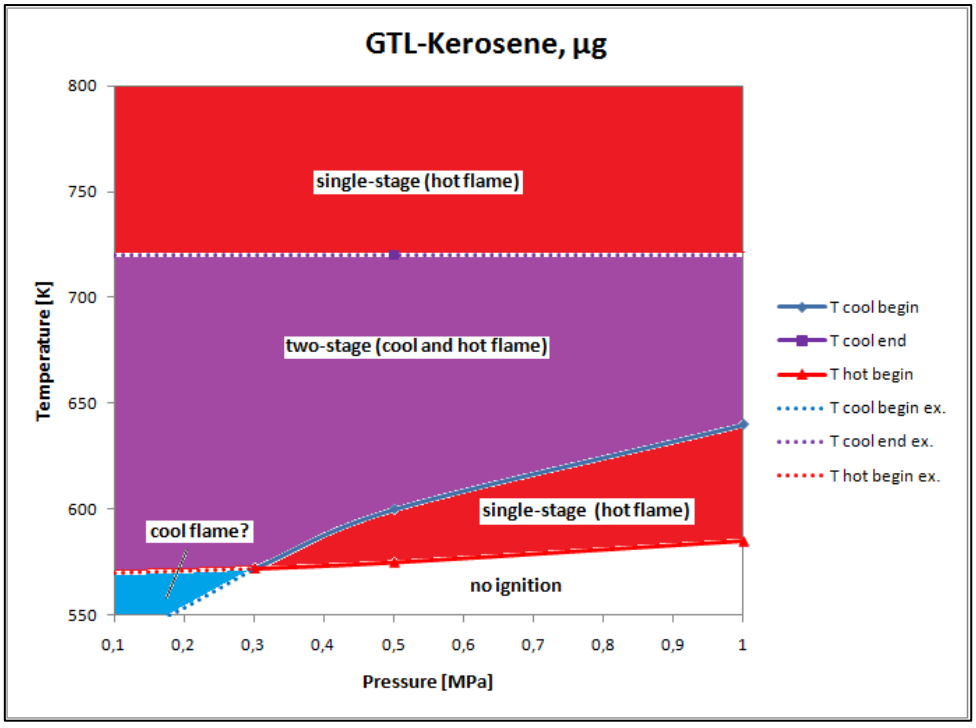

Fig. 109 – Characteristic map of ignition types for GTL-Kerosene droplets at microgravity conditions

3.6.3. Comparison of Normal-g and Microgravity Experiments

As seen in the previous sections there is as expected a discrepancy pertaining to the experimental results obtained during the µg and normal-g experiments, which is mainly due to the fact that the absence of natural or buoyant convection affects the transport of oxidizer and consequentially the ignition delay times. The diagrams in this section are shown to illustrate the resulting differences and the influence of the gravity environment on the ignition of single fuel droplets of GTL-Kerosene.

The following diagrams depict the difference in the autoignition behavior of the cool flame and its first detection, namely the first induction time. The cool flame appears at lower ambient temperatures in microgravity and the first induction times are higher. This behavior decreases with higher pressures. The extent of the temperature range where cool flames are observed at 0,3 MPa is much larger for the microgravity data than the normal-g. For 0,5 MPa this behavior is switched: For normal-g data cool flames are detected throughout a larger temperature range compared to µg data. For 1,0 MPa there are no measurements beyond 700 K at microgravity conditions, so the extent of the cool flame detection cannot be assessed.

The autoignition behavior of the hot flame for the two gravity environments has similarities to the behavior observed for the cool flame. The hot flame is detected at lower ambient temperatures and the value of the induction time is much higher than the one observed for normal-g conditions. The behavior is less pronounced for 0,5 MPa but is still observable at 1,0 MPa.

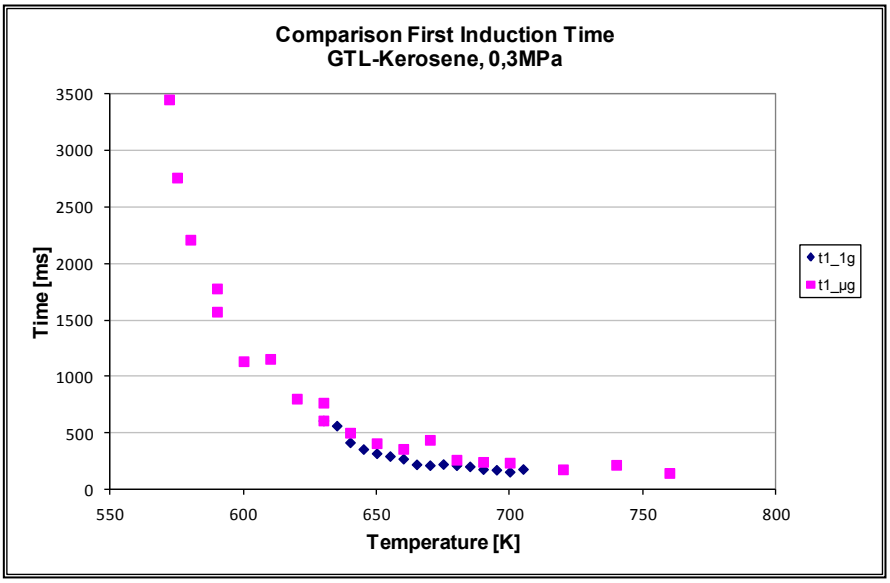

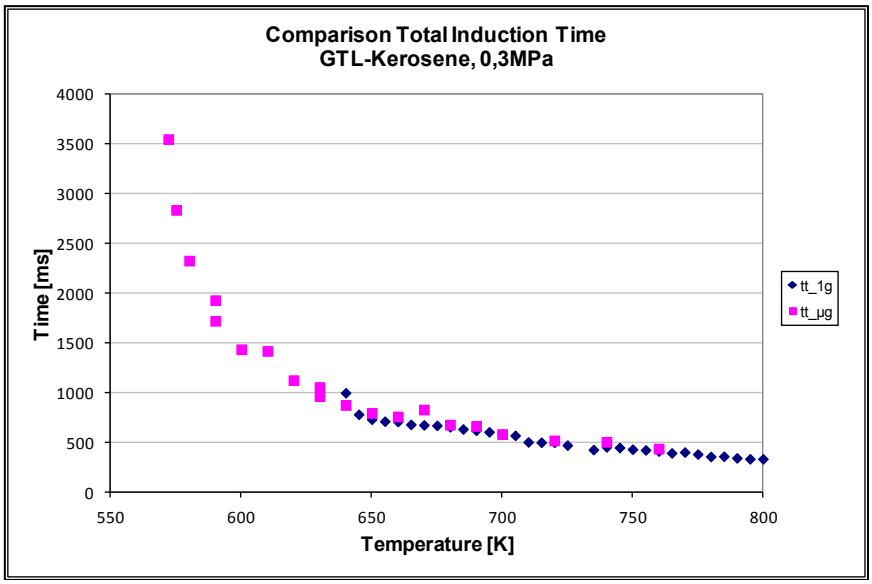
Comparison Total Induction Time
GTL-Kerosene, 0,3MPa
Time [ms]
Temperature [K]
tt_1g
tt_µg

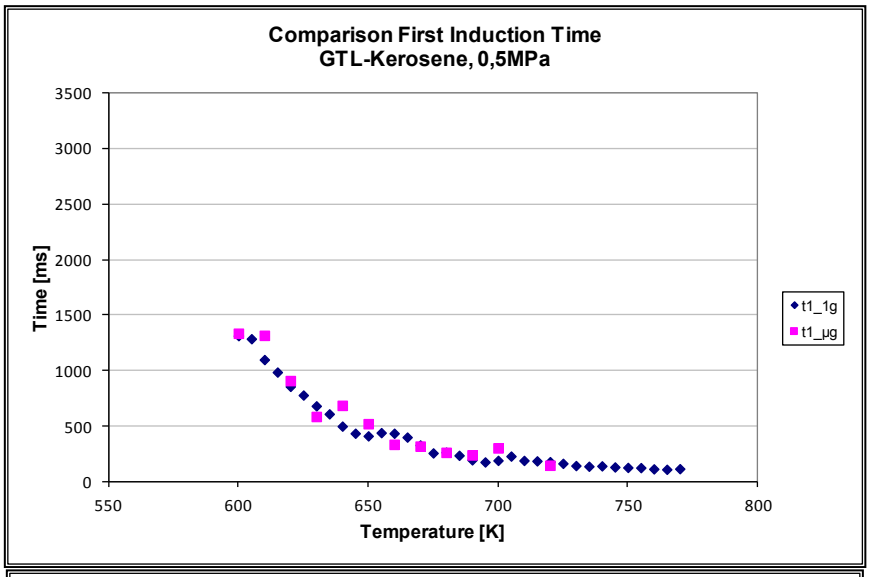
Comparison First Induction Time
GTL-Kerosene, 0,5MPa
Time [ms]
Temperature [K]
t1_1g
t1_µg

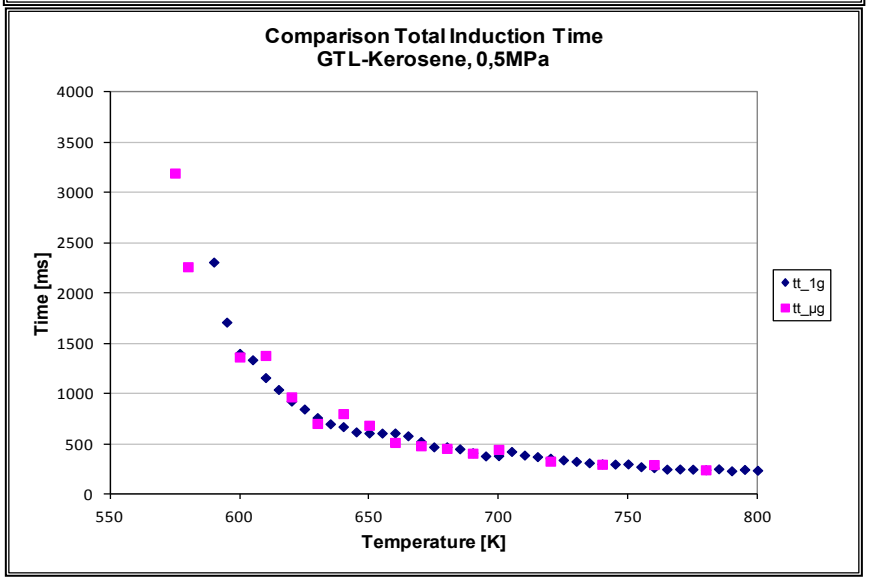
Comparison Total Induction Time
GTL-Kerosene, 0,5MPa
Time [ms]
Temperature [K]
tt_1g
tt_µg

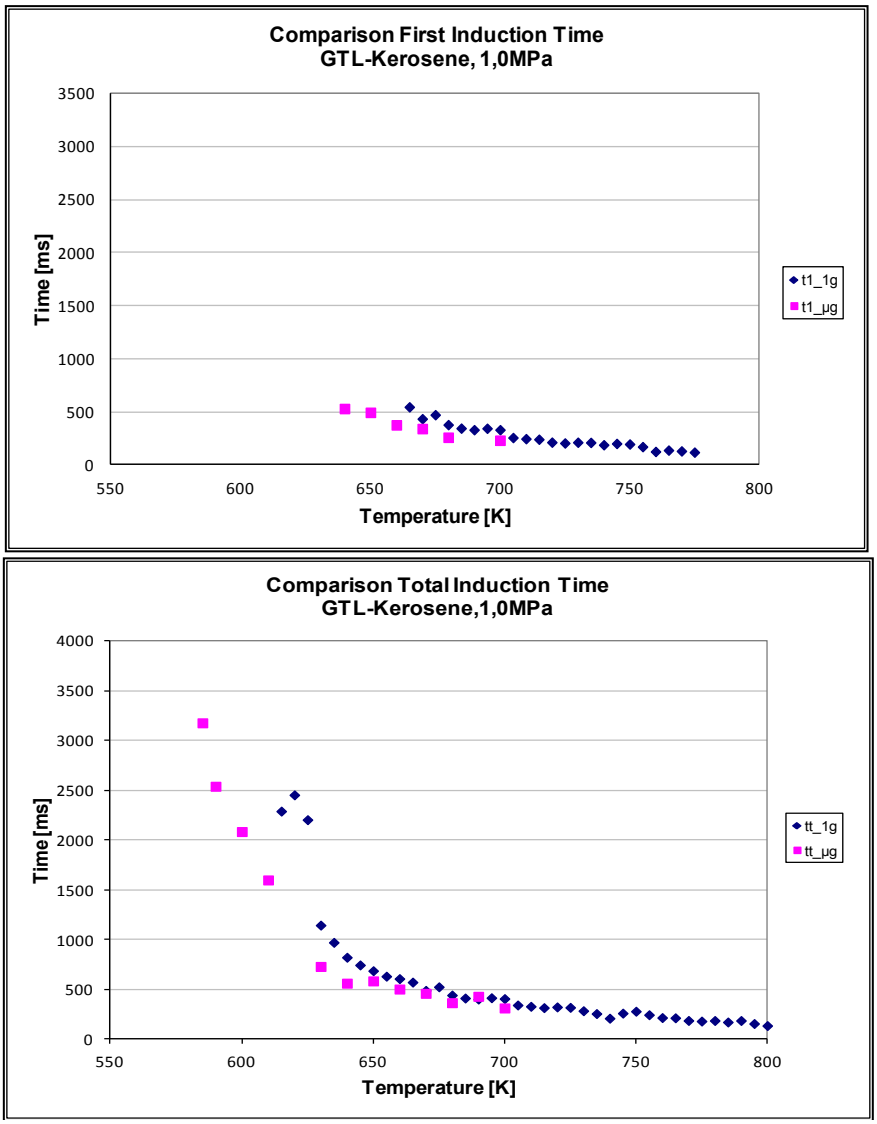

Fig. 110 - Comparison of first and total induction times for GTL-Kerosene for normal-g and microgravity conditions

For the droplet lifetimes of GTL-Kerosene under microgravity and normal gravity conditions the behavior is very similar. For 0,3 MPa, ignitions are detected at lower temperatures in the case of the microgravity data than in normal-g. From 600 K on, there is both data for normal-g and microgravity and the differences are very subtle, but still the µg data has slightly longer droplet lifetimes. For 0,5 MPa, between 600 and 670 K, the µg data shows slightly higher values, for higher temperatures the values are almost coincident. For 1,0 MPa the available µg data is scarce; nonetheless the general trend for both data sets is very similar.

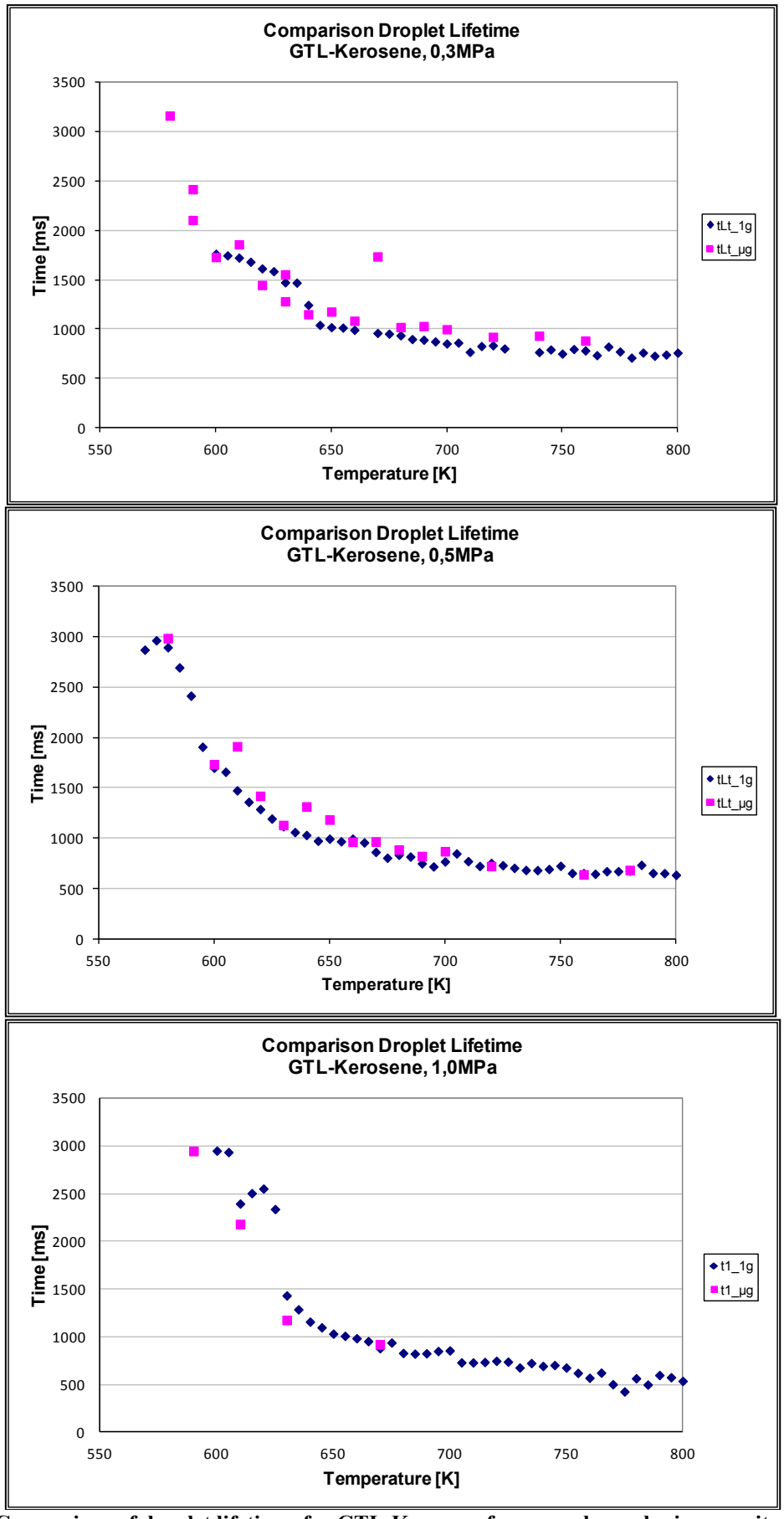

Fig. 111 - Comparison of droplet lifetimes for GTL-Kerosene for normal-g and microgravity conditions

For t_2 and t_C the influence of the gravity environment is shown in the following diagrams. As stated in the previous section pertaining to the results of the normal-g experiments, t_2 shows a tendency to approach a constant value which decreases with rising pressure level. For the microgravity experiments the values for t_2 tend to converge also to the constant value of the normal-g counterparts.

For t_C a similar behavior is observed. The experimental results for both data sets, microgravity and normal-g, tend to converge to a constant value at about 400 ms. Differences are observed in the lower temperature regime at about 550-650 K. The values for normal-g data start at about 100 ms (for 0,5 and 1,0 MPa) and increase till reaching the previously stated value of about 400 ms. The microgravity experiments start at high values in the lower temperature regime at, e.g. about 740 ms for 0,5 MPa decreasing with increasing temperature to 400 ms.

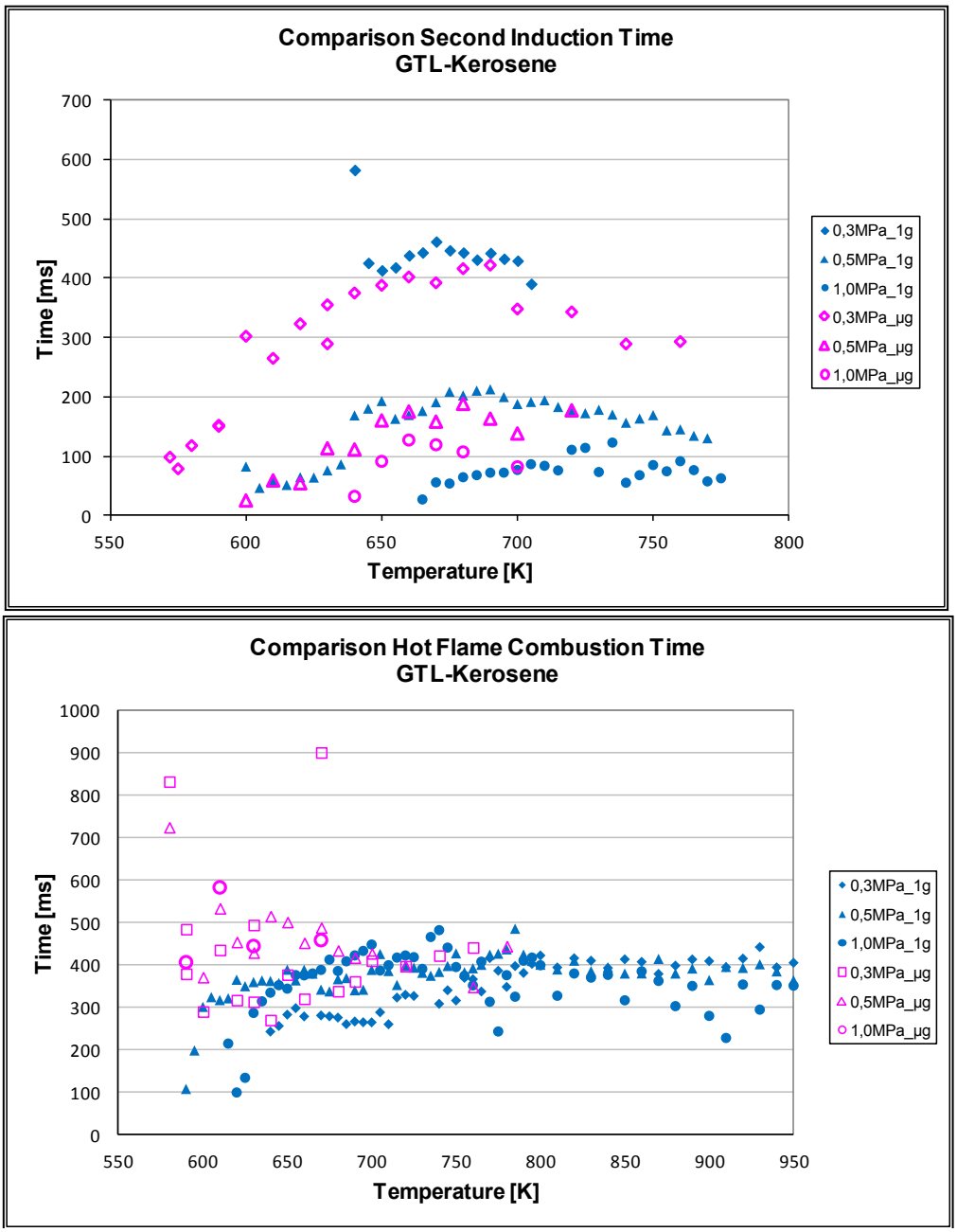

Fig. 112 - Comparison of second induction and the hot combustion times for GTL-Kerosene for microgravity and normal-g conditions

3.6.4. Determination of a suitable Surrogate Fuel for GTL-Kerosene

The basic approach for the determination of a suitable model fuel for GTL-Kerosene is analogous to section 3.5.4 and is as follows:

- Selection of a base component from a known major component of the analyzed fuel, usually an aliphatic compound such as an n-alkane.
- Selection of an additive or series of additives to approach the required behavior. The nature of this additive can be aliphatic (cyclic or acyclic).

In the case of GTL-fuels, as stated by the manufacturer [35] aromatic compounds are absent, therefore no aromatic compounds are included in the selection procedure.

Selection of an n-alkane

As potential candidates for the base component for the model fuel, based on the data provided by [33], n-Decane and n-Dodecane have been selected. Only data obtained with normal-g experiments is used for the selection and determination of the model fuel for GTL-Kerosene.

The following diagrams depict the comparison of the experimental results for the characterization of the ignition delay times obtained for GTL-Kerosene and the two candidates for the base component, n-Decane and n-Dodecane. For illustration purposes, n-Tetradecane and n-Hexadecane are included and shown in comparison.

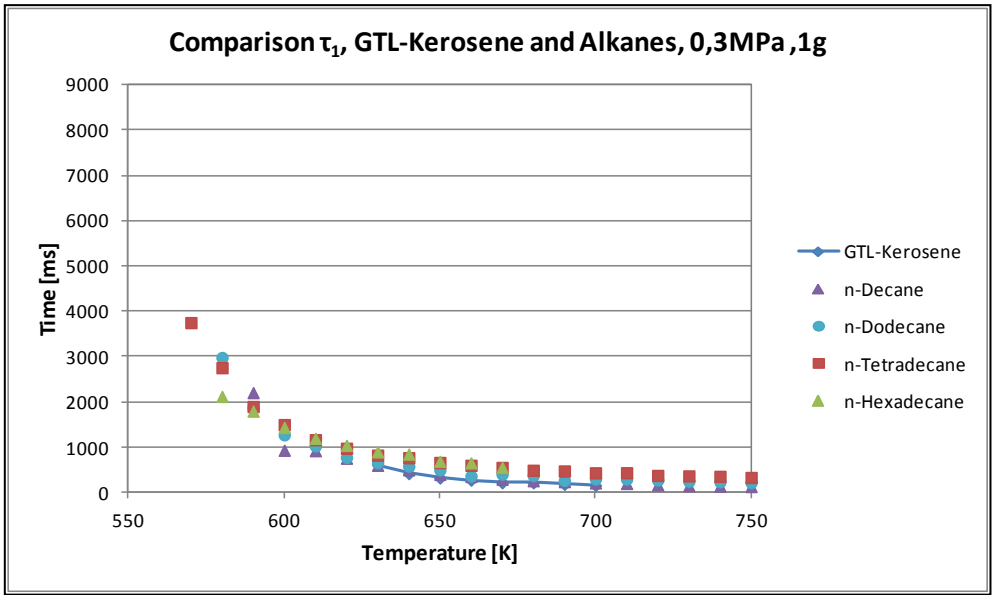

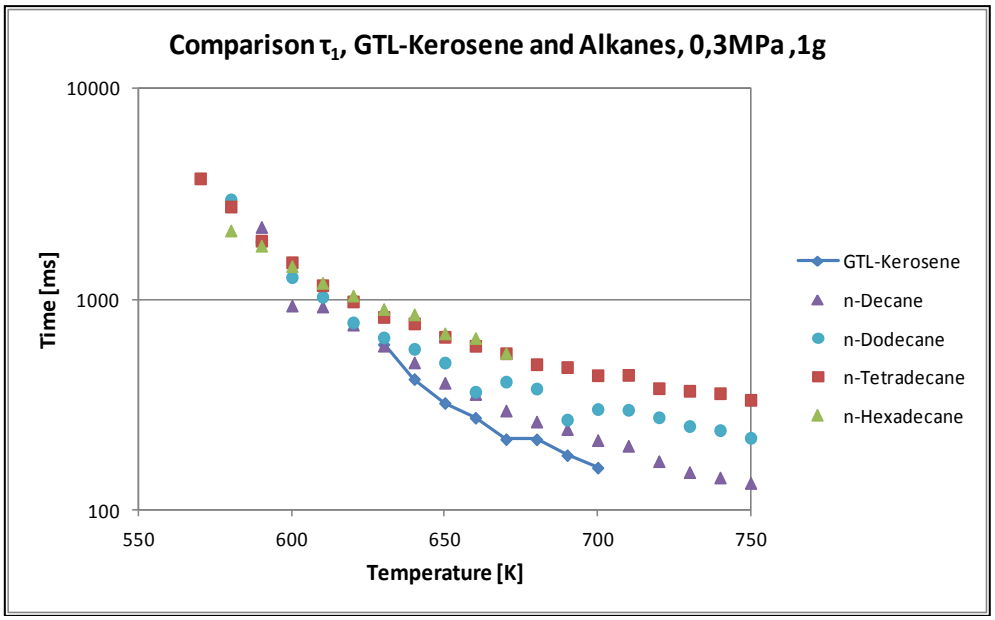
Comparison τ1, GTL-Kerosene and Alkanes, 0,3MPa ,1g
10000
1000
100
Time [ms]
550
600
650
700
750
Temperature [K]
GTL-Kerosene
n-Decane
n-Dodecane
n-Tetradecane
n-Hexadecane

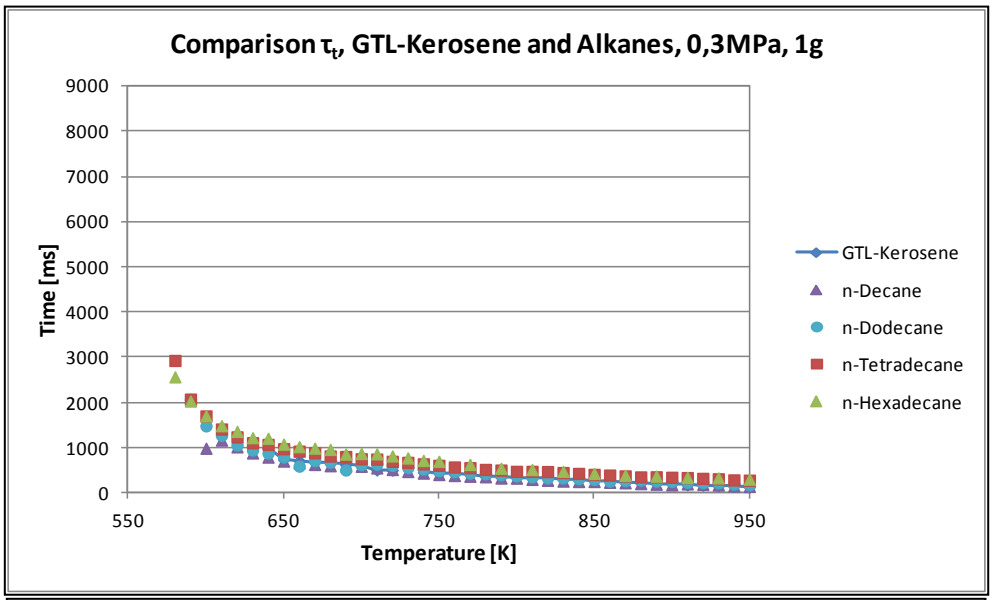
Comparison τt, GTL-Kerosene and Alkanes, 0,3MPa, 1g
9000
8000
7000
6000
5000
4000
3000
2000
1000
0
Time [ms]
550
650
750
850
950
Temperature [K]
GTL-Kerosene
n-Decane
n-Dodecane
n-Tetradecane
n-Hexadecane

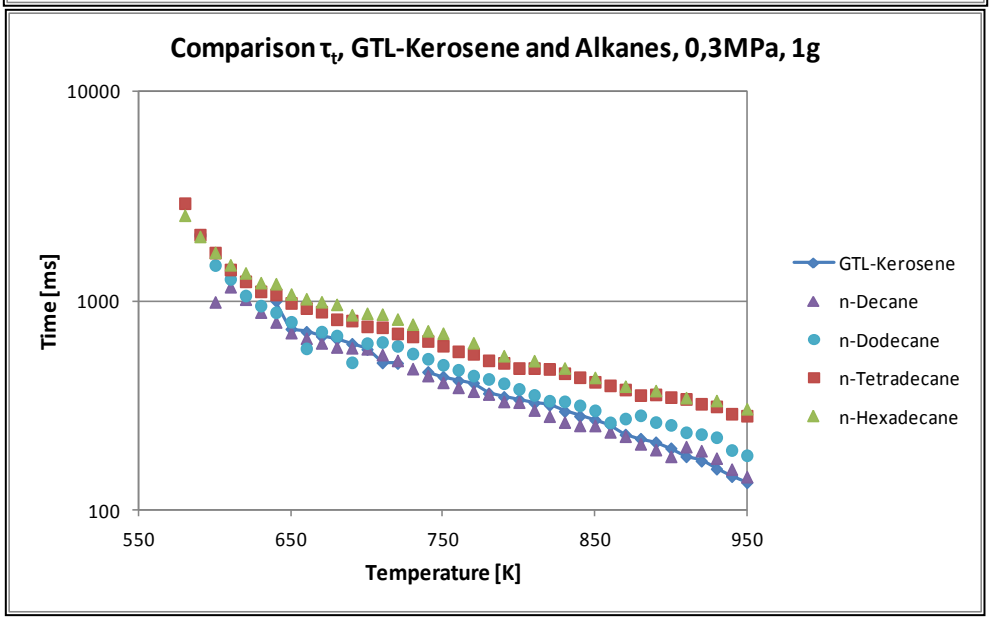
Comparison τt, GTL-Kerosene and Alkanes, 0,3MPa, 1g
10000
1000
100
Time [ms]
550
650
750
850
950
Temperature [K]
GTL-Kerosene
n-Decane
n-Dodecane
n-Tetradecane
n-Hexadecane

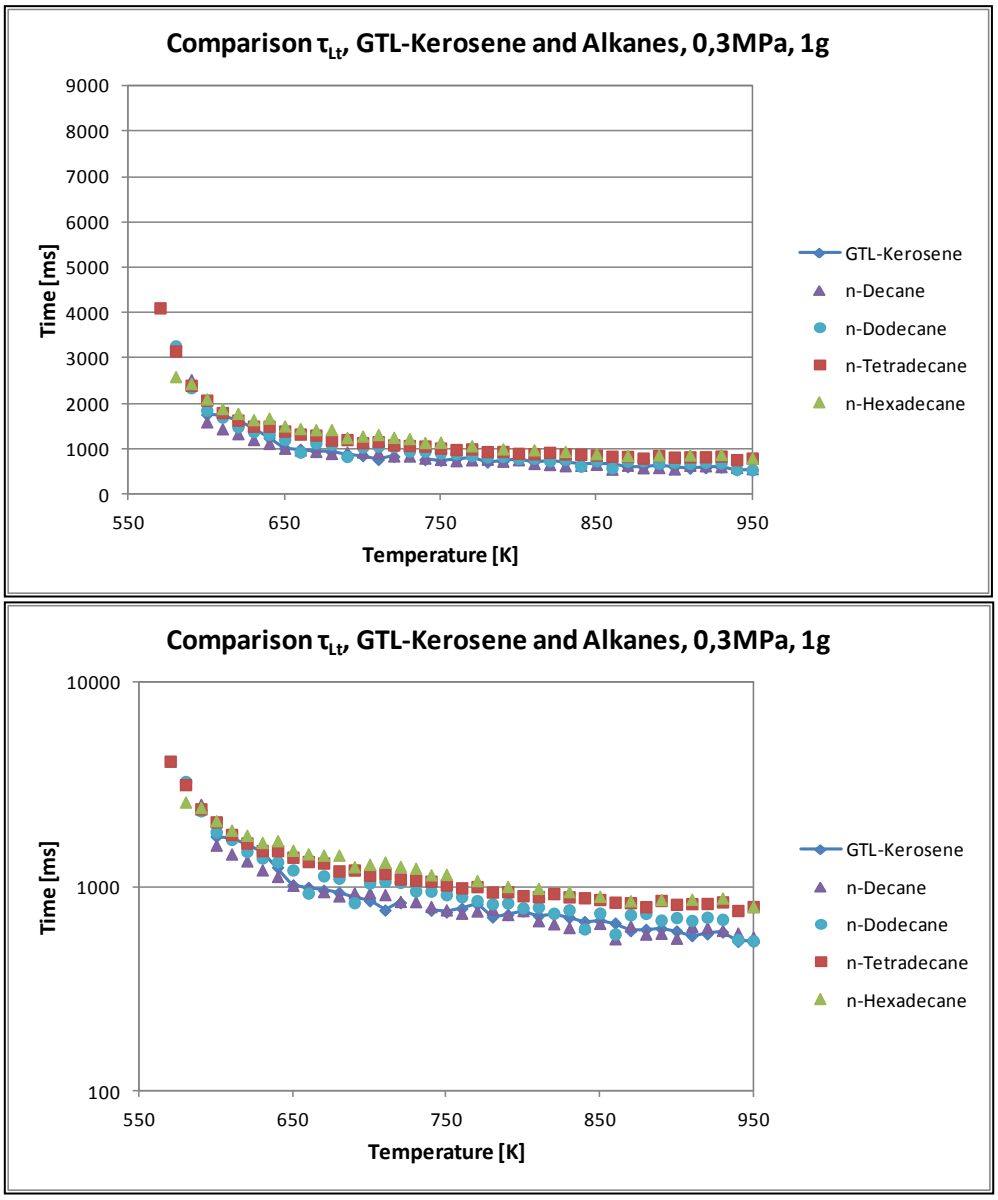

Fig. 113 - Comparison of the ignition delay times of GTL-Kerosene with selected alkanes (0,3 MPa, normal-g)

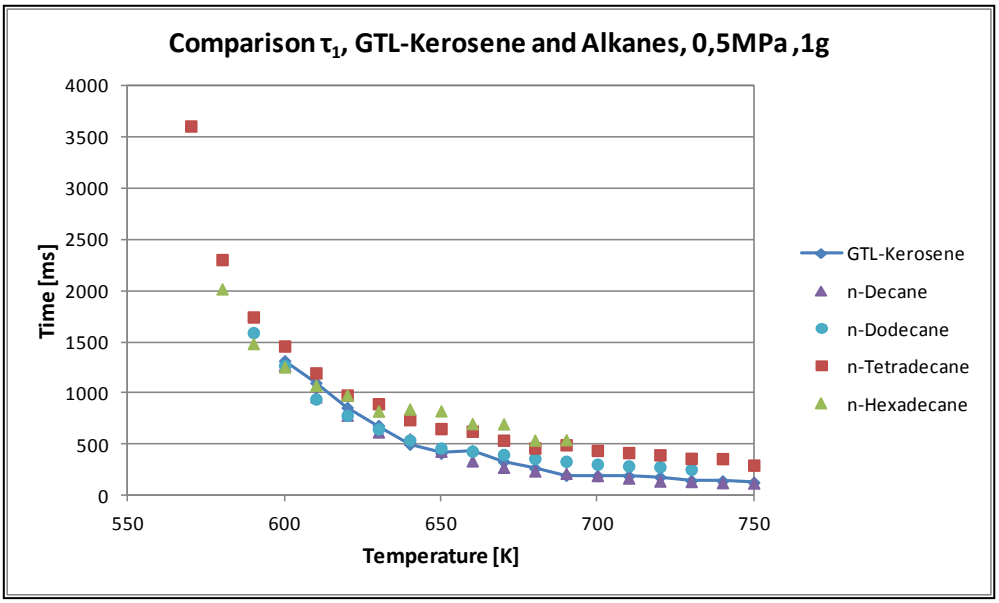

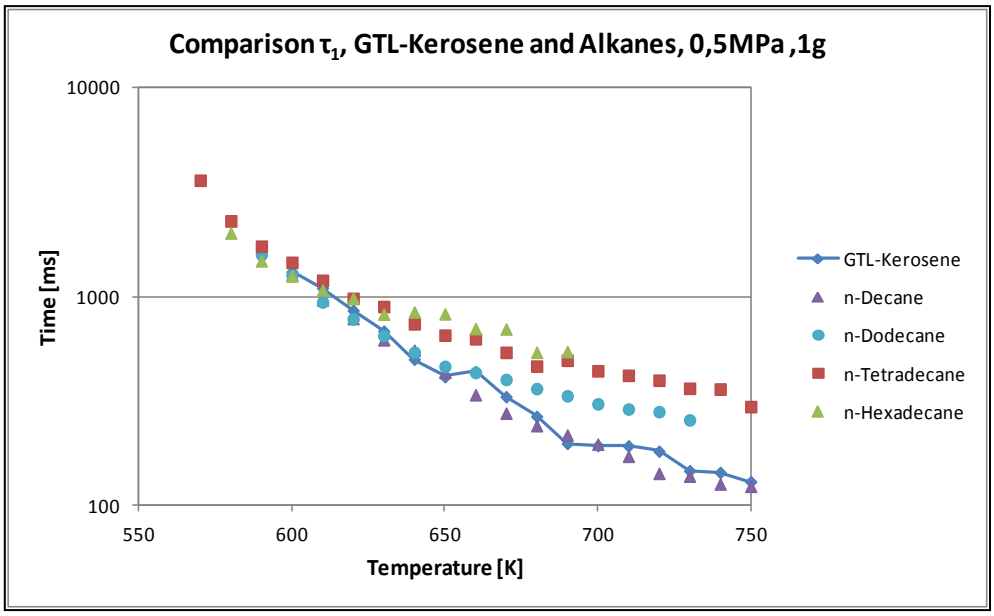
Comparison τ1, GTL-Kerosene and Alkanes, 0,5MPa ,1g
Time [ms]
10000
1000
100
550
600
650
700
750
Temperature [K]
GTL-Kerosene
n-Decane
n-Dodecane
n-Tetradecane
n-Hexadecane

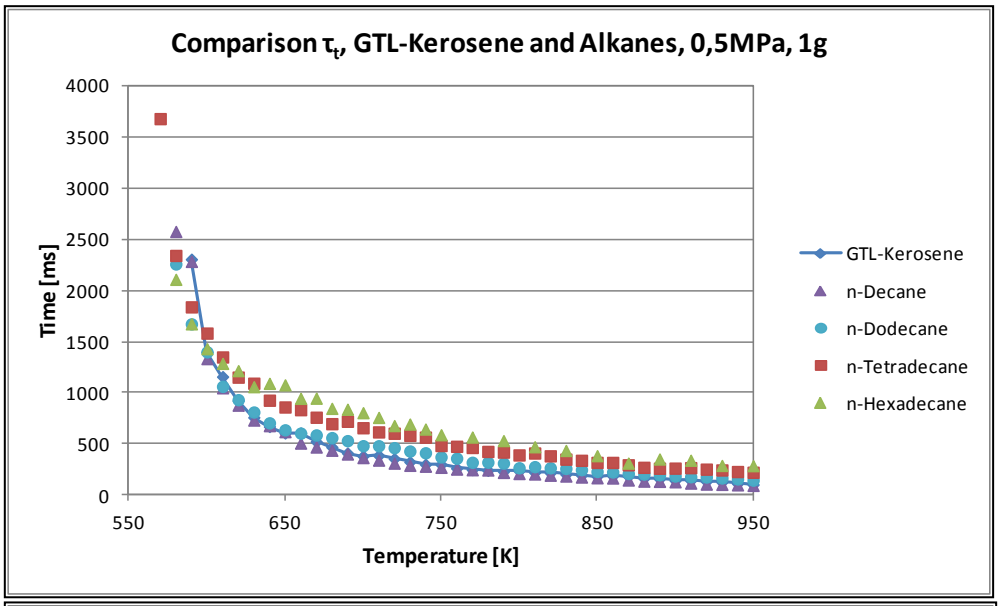
Comparison τt, GTL-Kerosene and Alkanes, 0,5MPa, 1g
Time [ms]
4000
3500
3000
2500
2000
1500
1000
500
0
550
650
750
850
950
Temperature [K]
GTL-Kerosene
n-Decane
n-Dodecane
n-Tetradecane
n-Hexadecane

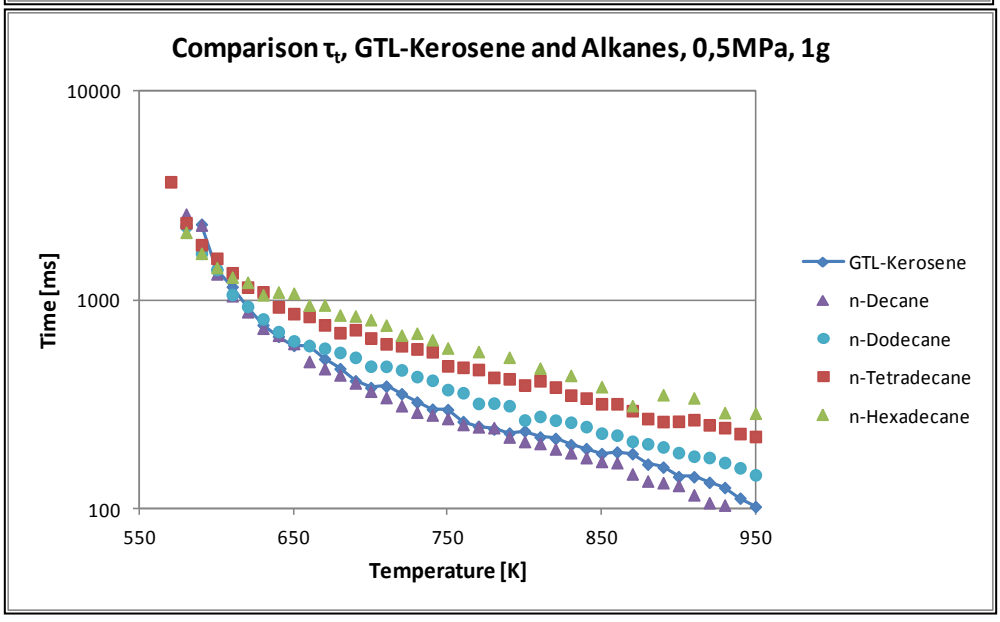
Comparison τt, GTL-Kerosene and Alkanes, 0,5MPa, 1g
Time [ms]
10000
1000
100
550
650
750
850
950
Temperature [K]
GTL-Kerosene
n-Decane
n-Dodecane
n-Tetradecane
n-Hexadecane

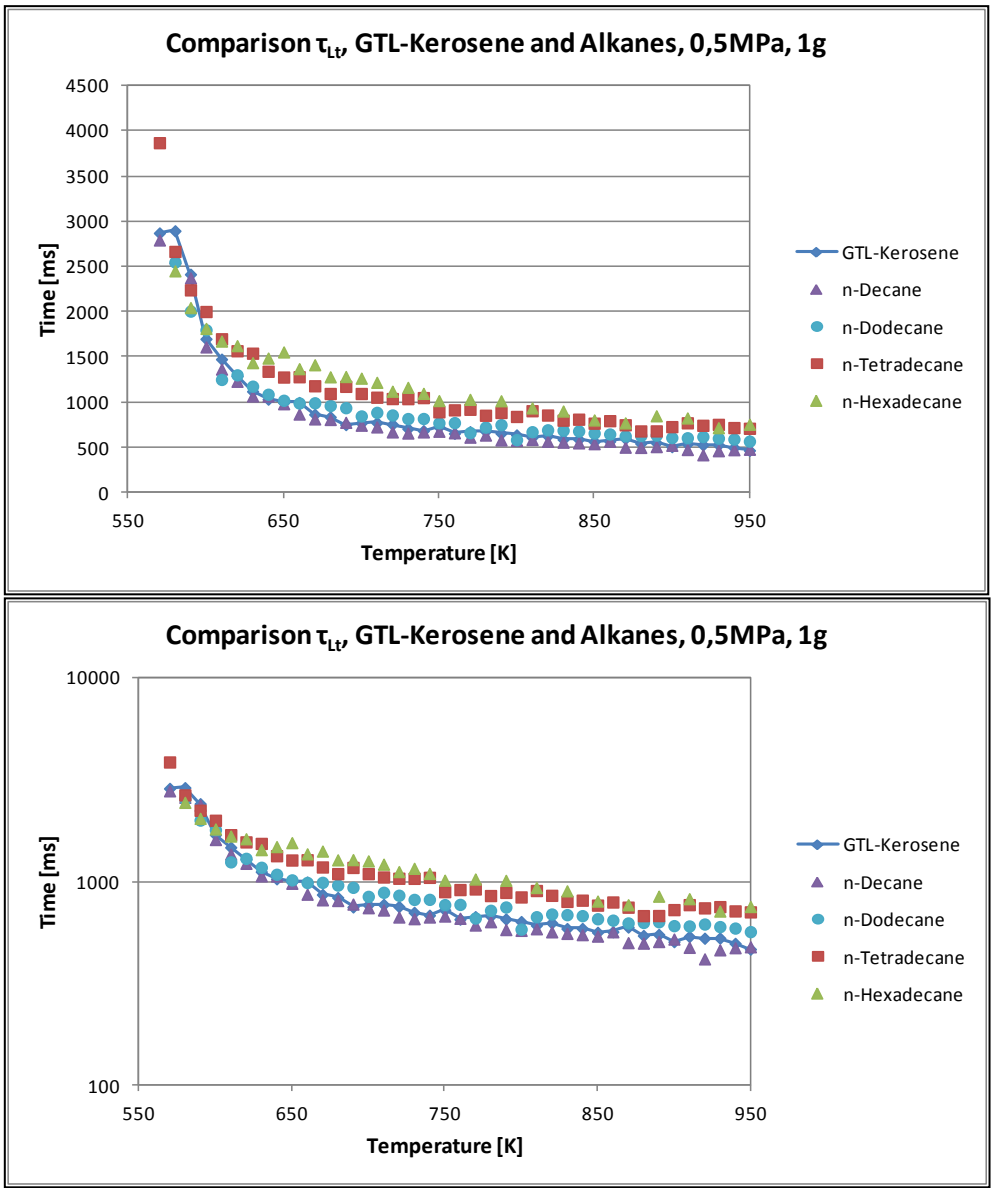

Fig. 114 - Comparison of the ignition delay times of GTL-Kerosene with selected alkanes (0,5 MPa, normal-g)

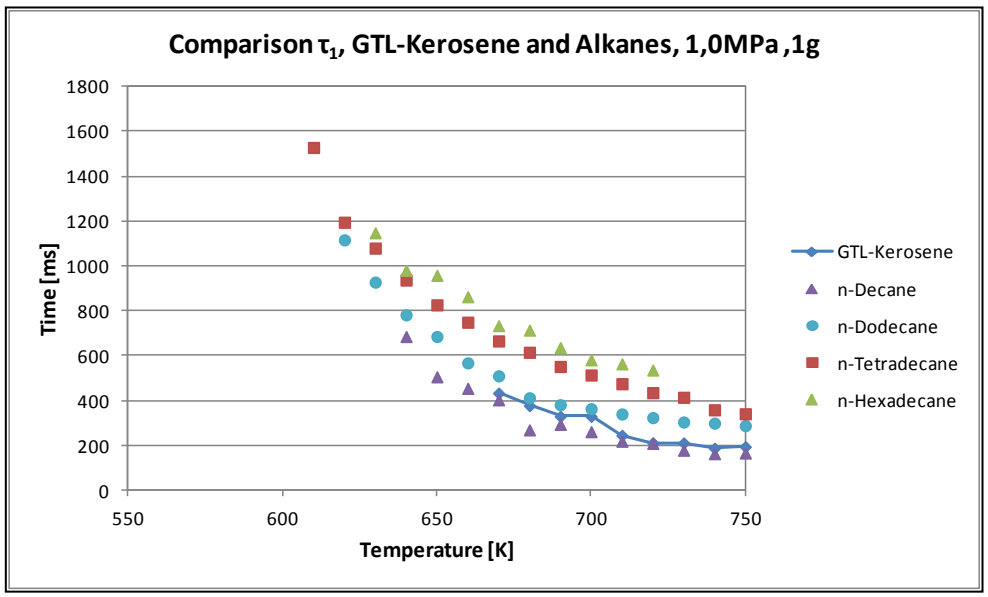

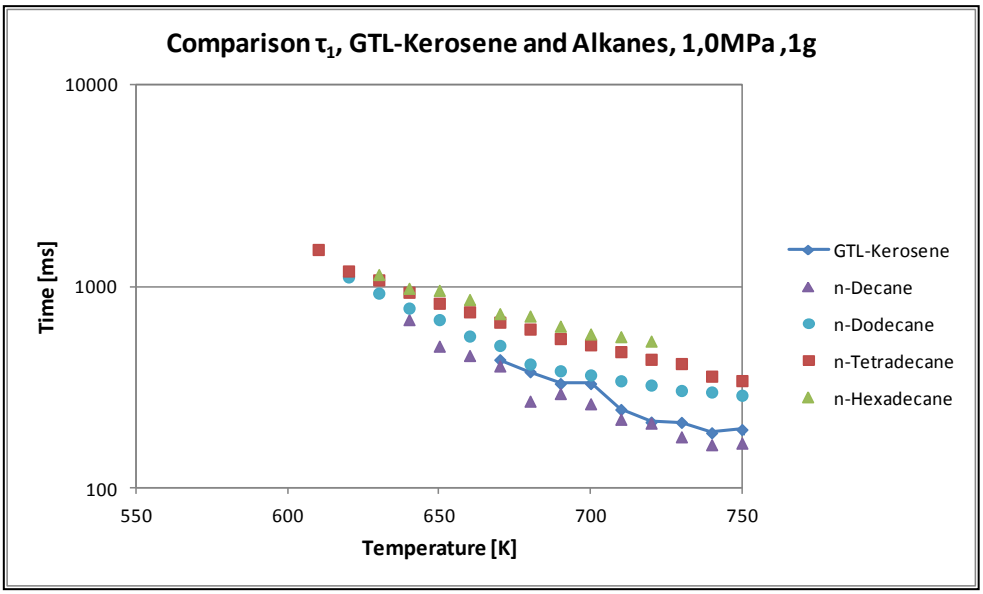
Comparison τ1, GTL-Kerosene and Alkanes, 1,0MPa ,1g
Time [ms]
10000
1000
100
550
600
650
700
750
Temperature [K]
GTL-Kerosene
n-Decane
n-Dodecane
n-Tetradecane
n-Hexadecane

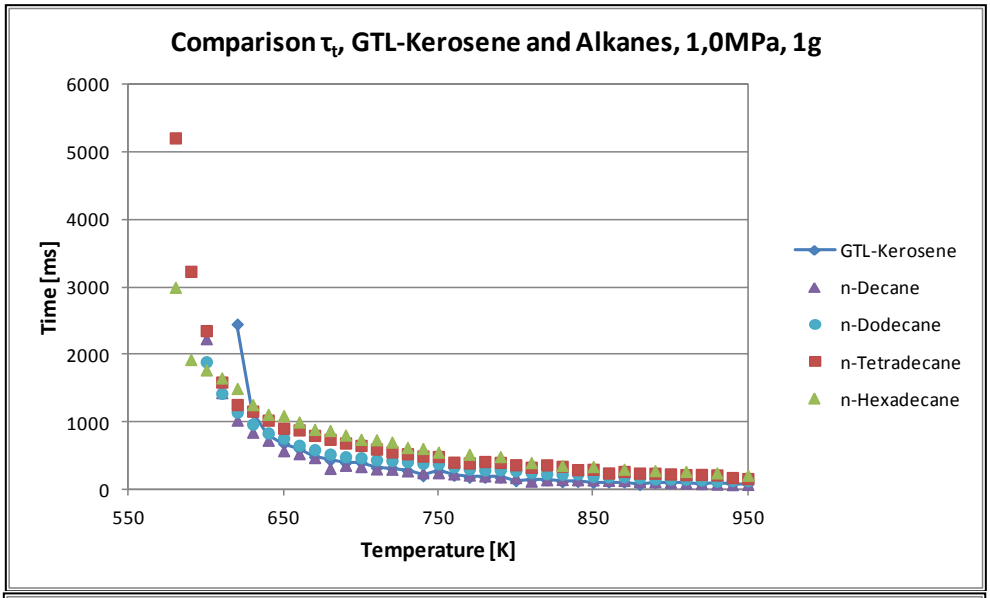
Comparison τt, GTL-Kerosene and Alkanes, 1,0MPa, 1g
Time [ms]
6000
5000
4000
3000
2000
1000
0
550
650
750
850
950
Temperature [K]
GTL-Kerosene
n-Decane
n-Dodecane
n-Tetradecane
n-Hexadecane

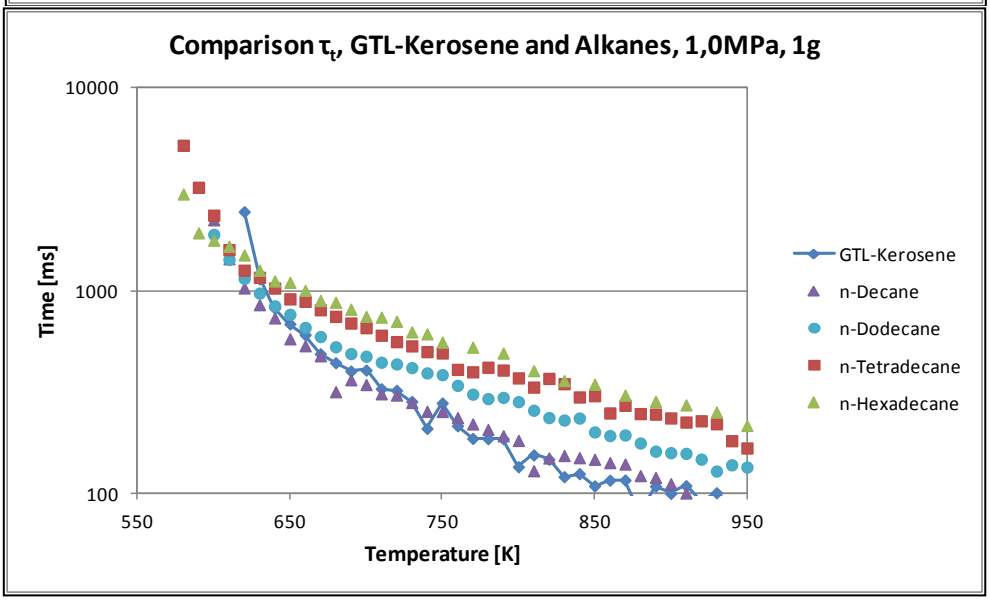
Comparison τt, GTL-Kerosene and Alkanes, 1,0MPa, 1g
Time [ms]
10000
1000
100
550
650
750
850
950
Temperature [K]
GTL-Kerosene
n-Decane
n-Dodecane
n-Tetradecane
n-Hexadecane

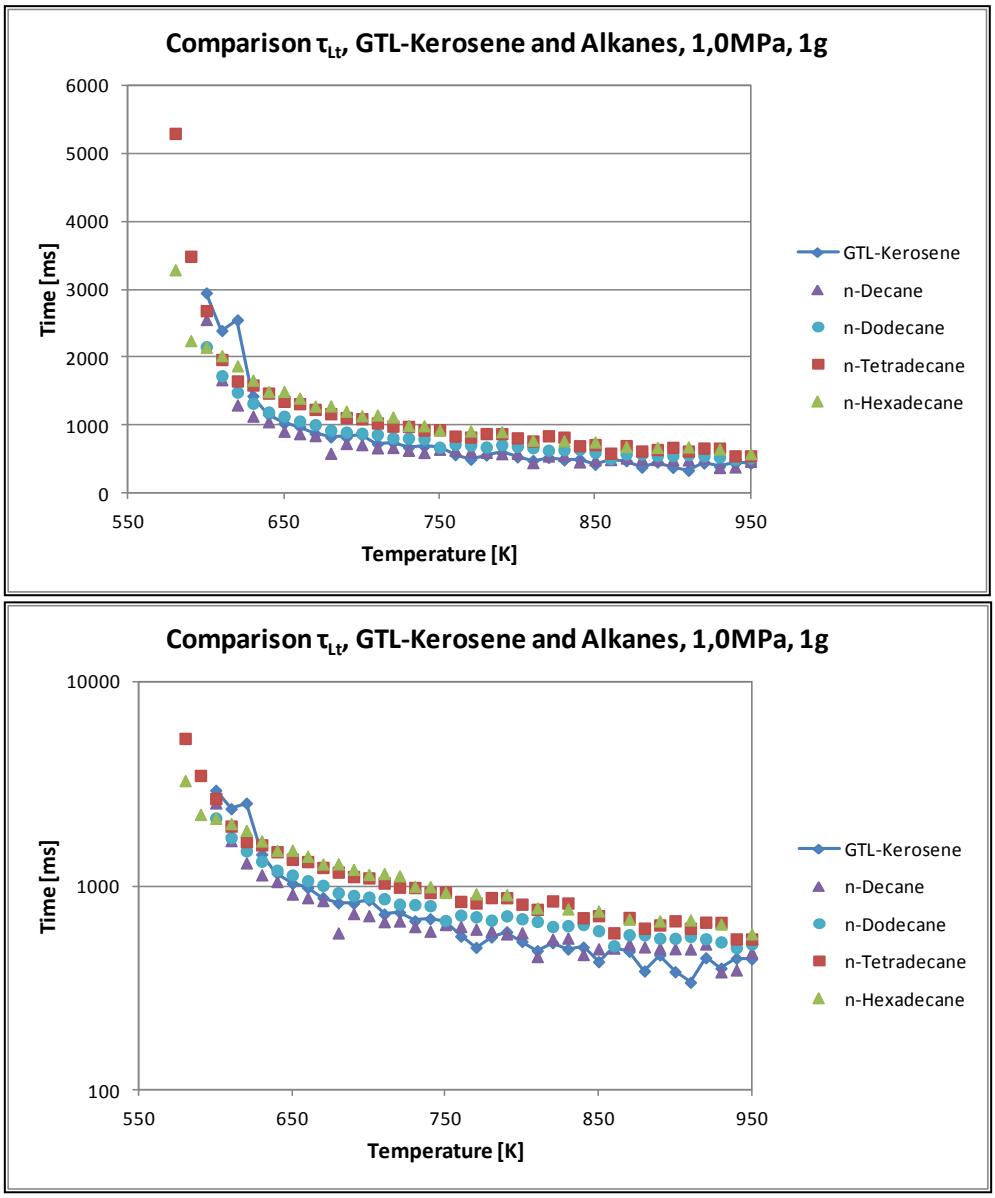

Fig. 115 - Comparison of the ignition delay times of GTL-Kerosene with selected alkanes (1,0 MPa, normal-g)

From the data shown in the previous diagrams, the following observations can be made:

- The extent of the detectable temperature range for the cool flame is larger for both n-Decane and n-Dodecane than for GTL-Kerosene at 0,3 and 1,0 MPa. For 0,5 MPa n-decane and GTL-Diesel show practically the same extent.
- The first hot flame is detected for GTL-Kerosene at higher temperatures for 0,3 MPa at 640 K, compared to 600 K for n-Decane.

The two candidate base components have a very similar behavior compared to GTL-Kerosene. For each induction time, τ_1, τ_t and also τ_{Lt}, (for a fixed pressure level) the average (first value) and the squared (second value) deviations are calculated using the GTL-Kerosene data as reference. These values are then averaged and the results used as a benchmark. These are summarized in the following table:

	n-Decane			n-Dodecane		
Pressure	τ_1	τ_t	τ_{Lt}	τ_1	τ_t	τ_{Lt}
0,3 MPa	0,25/0,08	0,03/0,01	0,02/0,01	0,54/0,36	0,14/0,04	0,10/0,02
0,5 MPa	0,07/0,01	0,09/0,01	0,06/0,01	0,25/0,15	0,21/0,07	0,10/0,02
1,0 MPa	0,10/0,02	0,14/0,04	0,13/0,03	0,43/0,26	0,48/0,35	0,17/0,07
Average	0,14/0,04	0,12/0,02	0,07/0,02	0,41/0,26	0,28/0,15	0,12/0,04
Total average	0,11/0,03			0,27/0,15		

Tab. 38 - Comparison of the deviations of the ignition delay times for n-Decane and n-Dodecane to GTL-Kerosene

As can be seen, n-decane shows the overall best values and thus is chosen as the base component for the surrogate fuel for GTL-Kerosene.

Selection of an Additive

The following diagrams show the experimental data on the autoignition of the different mixtures analyzed based on the components selected according section 2.1.5. The experimental parameters are analogous to the settings described in previous sections. The experimental data shown here is for 0,3 MPa ambient pressure. The following blends have been analyzed:

- n-Decane-50% - n-Dodecane-50%
- n-Decane-75% - n-Dodecane-25%
- n-Decane-50% - 1,3,5-Trimethylcyclohexane-50%
- n-Decane-75% - 1,3,5-Trimethylcyclohexane-25%
- n-Decane-50% - Cyclooctane-50%
- n-Decane-75% - Cyclooctane-25%
- n-Decane-50% - 2,2-Dimethyloctane-50%
- n-Decane-75% - 2,2-Dimethyloctane-25%
- n-Decane-50% - Propylcyclohexane-50%
- n-Decane-75% - Propylcyclohexane-25%

No ternary mixtures have been analyzed.

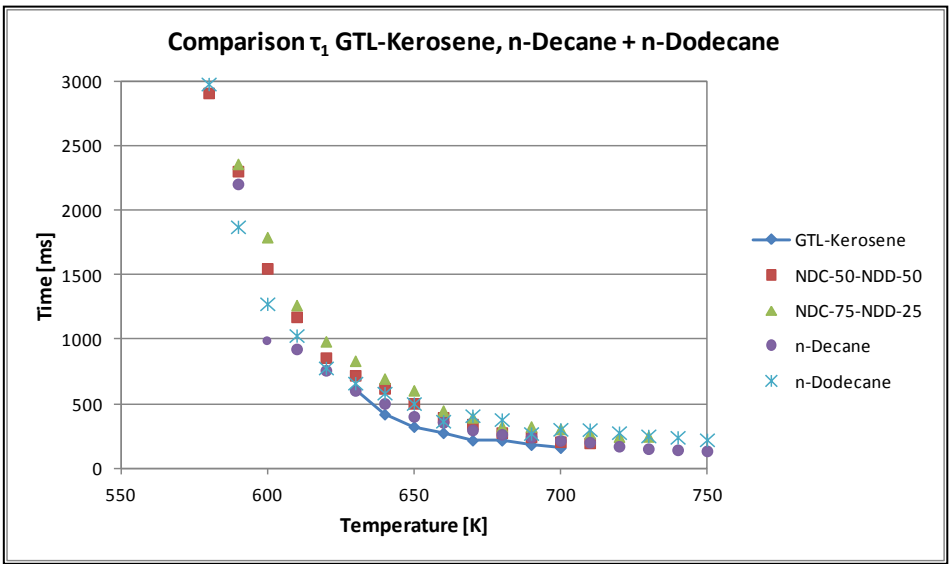

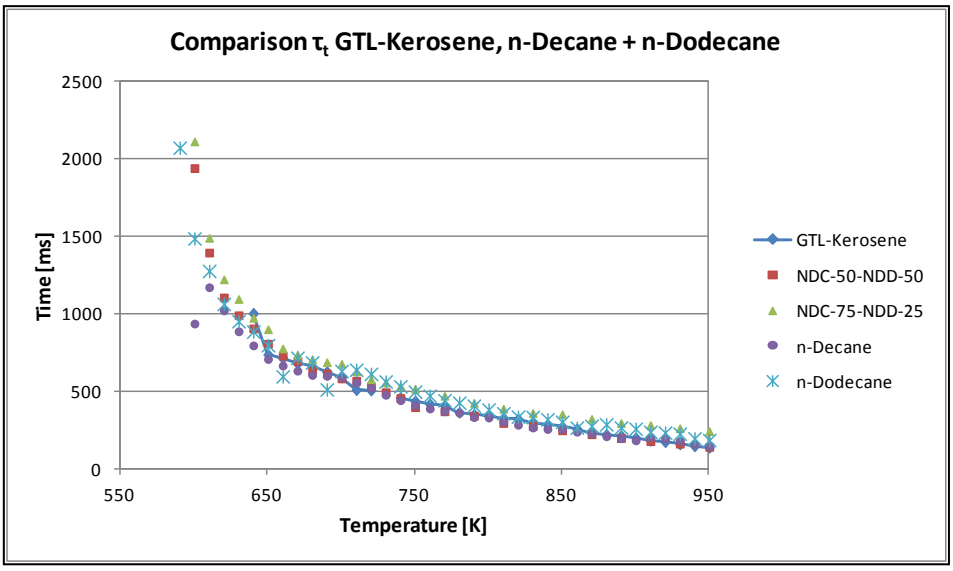
Comparison τ_t GTL-Kerosene, n-Decane + n-Dodecane
Time [ms]
2500
2000
1500
1000
500
0
550
650
750
850
950
Temperature [K]
GTL-Kerosene
NDC-50-NDD-50
NDC-75-NDD-25
n-Decane
n-Dodecane

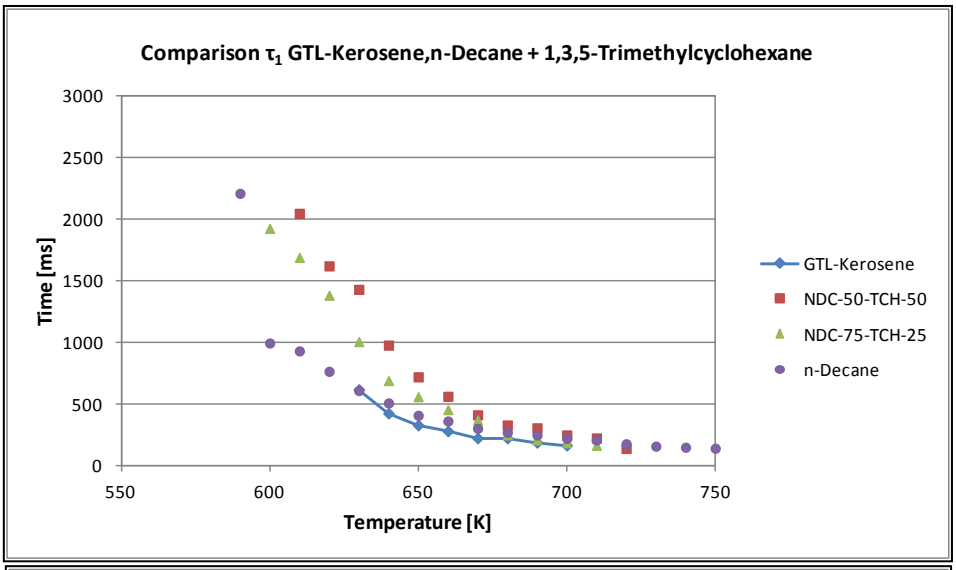
Comparison τ_1 GTL-Kerosene,n-Decane + 1,3,5-Trimethylcyclohexane
Time [ms]
3000
2500
2000
1500
1000
500
0
550
600
650
700
750
Temperature [K]
GTL-Kerosene
NDC-50-TCH-50
NDC-75-TCH-25
n-Decane

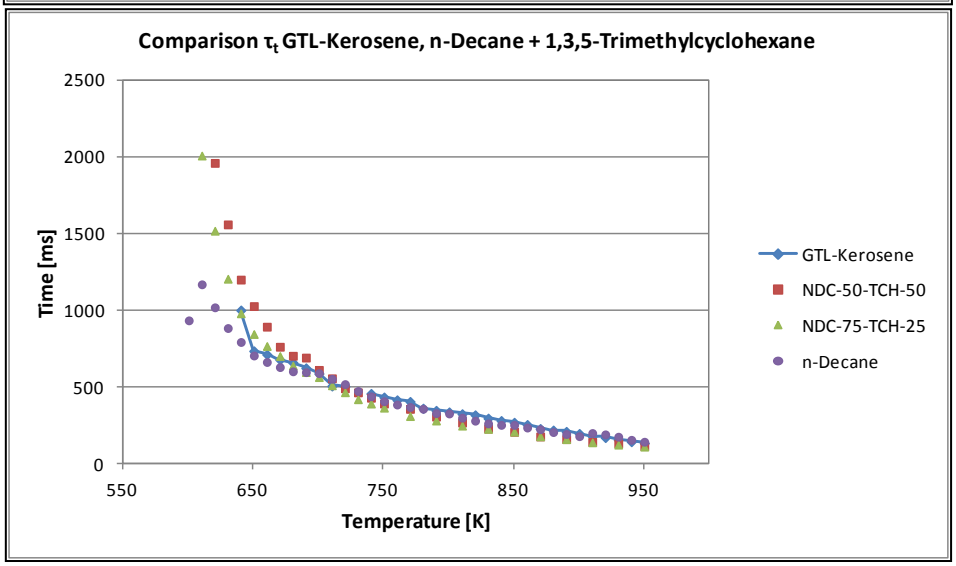
Comparison τ_t GTL-Kerosene, n-Decane + 1,3,5-Trimethylcyclohexane
Time [ms]
2500
2000
1500
1000
500
0
550
650
750
850
950
Temperature [K]
GTL-Kerosene
NDC-50-TCH-50
NDC-75-TCH-25
n-Decane

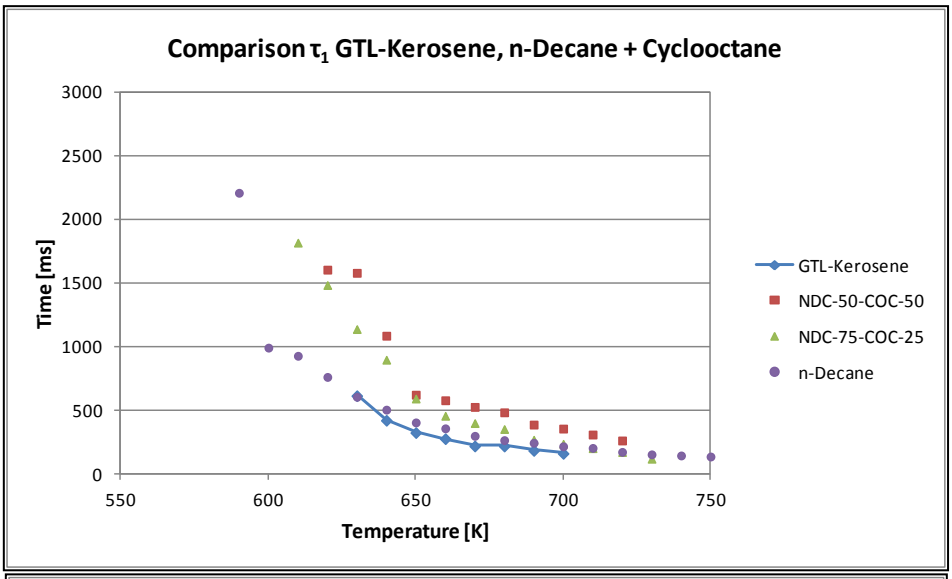
Comparison τ1 GTL-Kerosene, n-Decane + Cyclooctane
Time [ms]
3000
2500
2000
1500
1000
500
0
550
600
650
700
750
Temperature [K]
GTL-Kerosene
NDC-50-COC-50
NDC-75-COC-25
n-Decane

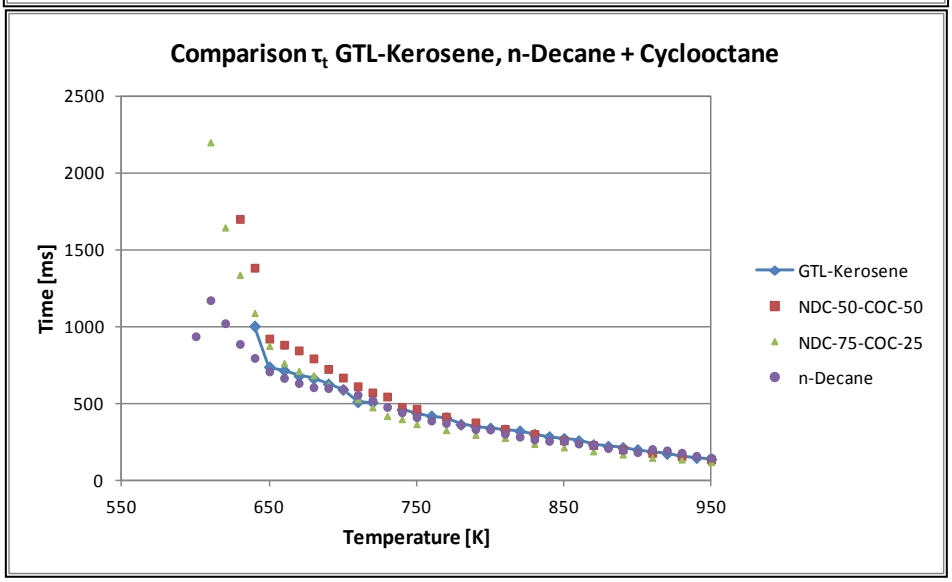
Comparison τt GTL-Kerosene, n-Decane + Cyclooctane
Time [ms]
2500
2000
1500
1000
500
0
550
650
750
850
950
Temperature [K]
GTL-Kerosene
NDC-50-COC-50
NDC-75-COC-25
n-Decane

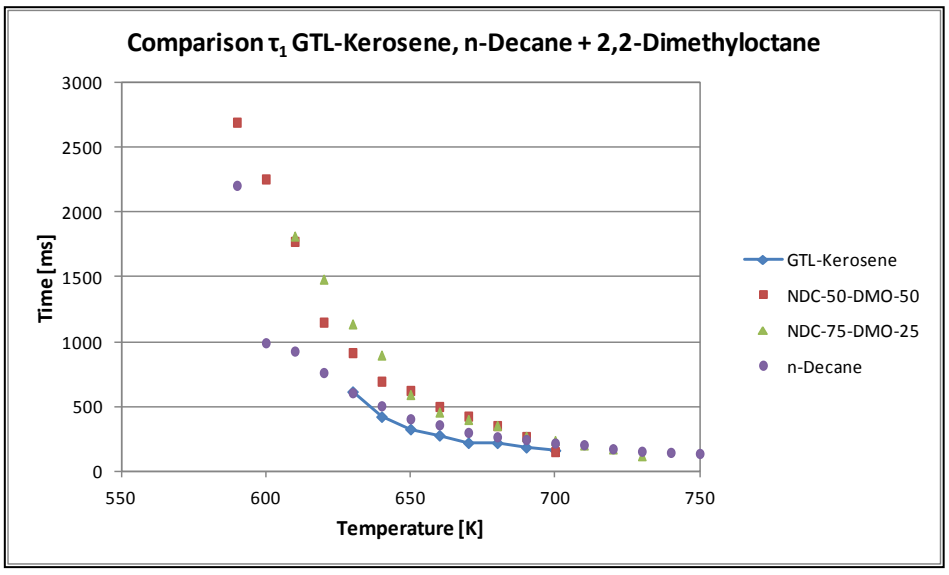
Comparison τ1 GTL-Kerosene, n-Decane + 2,2-Dimethyloctane
Time [ms]
3000
2500
2000
1500
1000
500
0
550
600
650
700
750
Temperature [K]
GTL-Kerosene
NDC-50-DMO-50
NDC-75-DMO-25
n-Decane

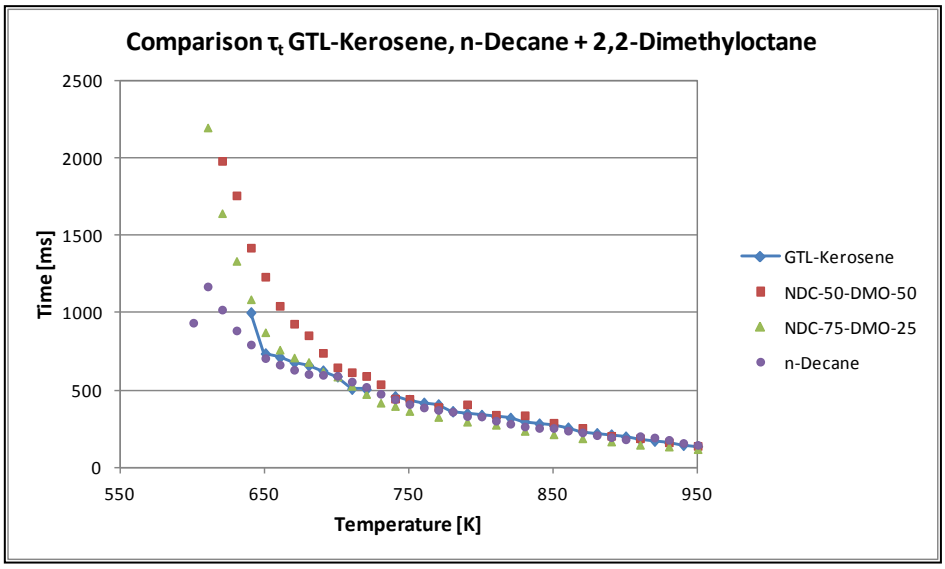

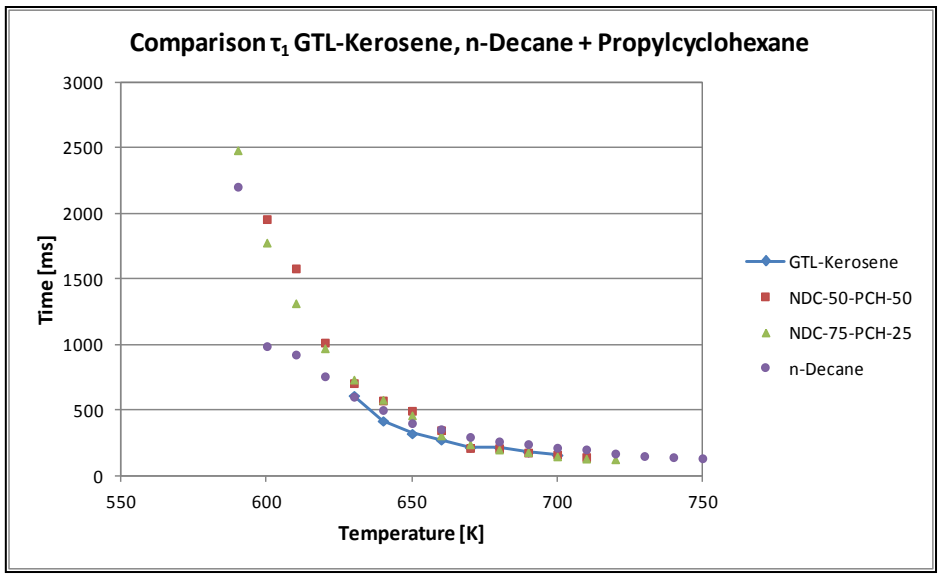

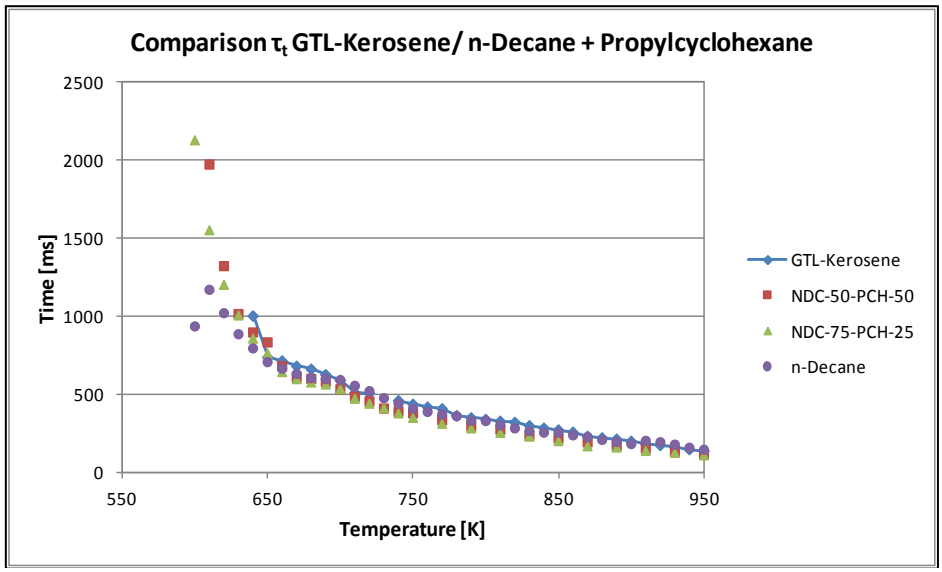

Fig. 116 – Experiments on the autoignition behavior of surrogate fuel candidates for GTL-Kerosene under normal-g for 0,3 MPa

Based on the previous diagrams, the following observations can be made:

- The mixtures of n-decane and n-dodecane have considerably larger detectable temperature ranges for first ignition delay time. The first appearance of a hot flame occurs at a lower temperature for the mixtures. The 50%-50% mixture shows a good representation of the hot flame ignition behavior.
- The addition of 1,3,5-Trimethylcyclohexane causes a retardation of the cool flame ignition and consequentially rather poor representation of the first ignition time. The 50%-50% mixture represents the total ignition time accurately.
- Cyclooctane as an additive also shows a cool flame retardant behavior and moderately good total ignition representation values as shown in the following table.
- The addition of 2,2-Dimethyloctane shows similar behavior as the two previous additives. The total ignition time representation is rather good, exemplified by the excellent value of the 75%-25% mixture.
- Adding Propylcyclohexane yields moderately good values for the first and total ignition delay times.

Surrogate fuel candidate	τ_l	τ_t	τ_{Lt}	Average
n-Decane-50% - n-Dodecane-50%	0,39	0,02	0,16	0,19
n-Decane-75% - n-Dodecane-25%	0,69	0,25	0,25	0,40
n-Decane-50% - 1,3,5-Trimethylcyclohexane-50%	0,93	0,03	0,10	0,35
n-Decane-75% - 1,3,5-Trimethylcyclohexane-25%	0,46	0,11	0,07	0,21
n-Decane-50% - Cyclooctane-50%	1,27	0,09	0,12	0,49
n-Decane-75% - Cyclooctane-25%	0,73	0,08	0,06	0,29
n-Decane-50% - 2,2-Dimethyloctane-50%	0,60	0,16	0,05	0,27
n-Decane-75% - 2,2-Dimethyloctane-25%	0,32	0,005	0,11	0,14
n-Decane-50% - Propylcyclohexane-50%	0,16	0,12	0,06	0,11
n-Decane-75% - Propylcyclohexane-25%	0,14	0,17	0,03	0,11

Tab. 39 - Comparison of the deviation of the ignition delay times for the surrogate fuel candidates compared to GTL-Kerosene

The best results are obtained in average for the n-Decane/Propylcyclohexane mixtures, with the 50%-50% showing a minimal better average. The total average value for the pressures analyzed (data not shown here) for this mixture is 0,17. Pure n-Decane reaches a better total average value for the pressures analyzed.

Validation of the Selected Surrogate Fuel Candidate in Microgravity

The selected surrogate fuel is n-Decane and is validated in µg and compared to GTL-Kerosene data. For 0,3 MPa the representation of GTL-Kerosene by the surrogate fuel is poor, as shown by the table at the end of this section. For 0,5 and 1,0 MPa the quality of the representation improves and shows excellent values for the total ignition time and good values for the first ignition time. The adjacent diagrams illustrate the results obtained:

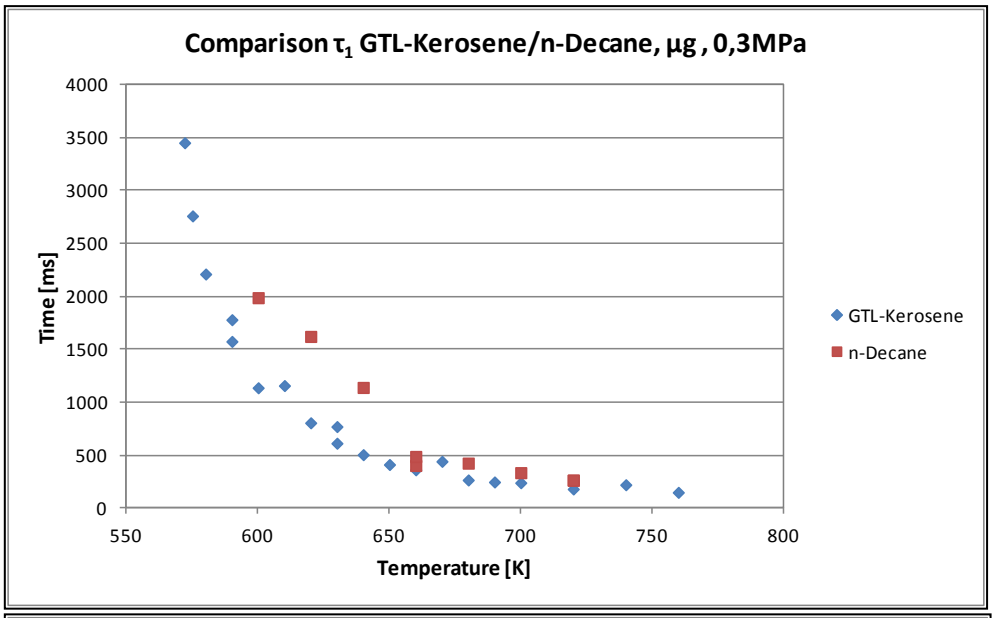
Comparison τ1 GTL-Kerosene/n-Decane, µg , 0,3MPa
Time [ms]
4000
3500
3000
2500
2000
1500
1000
500
0
550
600
650
700
750
800
Temperature [K]
GTL-Kerosene
n-Decane

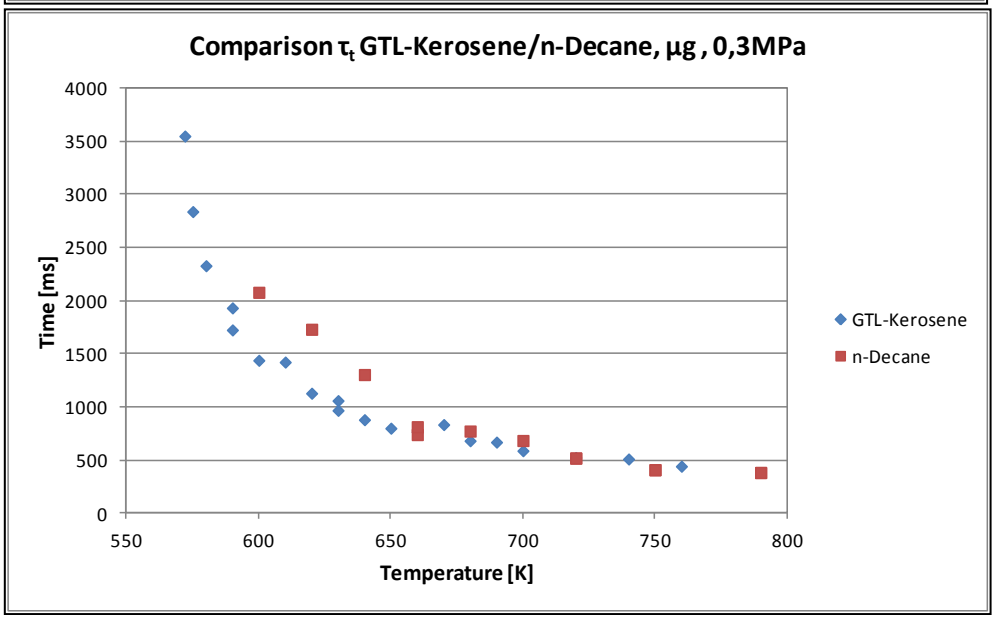
Comparison τt GTL-Kerosene/n-Decane, µg , 0,3MPa
Time [ms]
4000
3500
3000
2500
2000
1500
1000
500
0
550
600
650
700
750
800
Temperature [K]
GTL-Kerosene
n-Decane

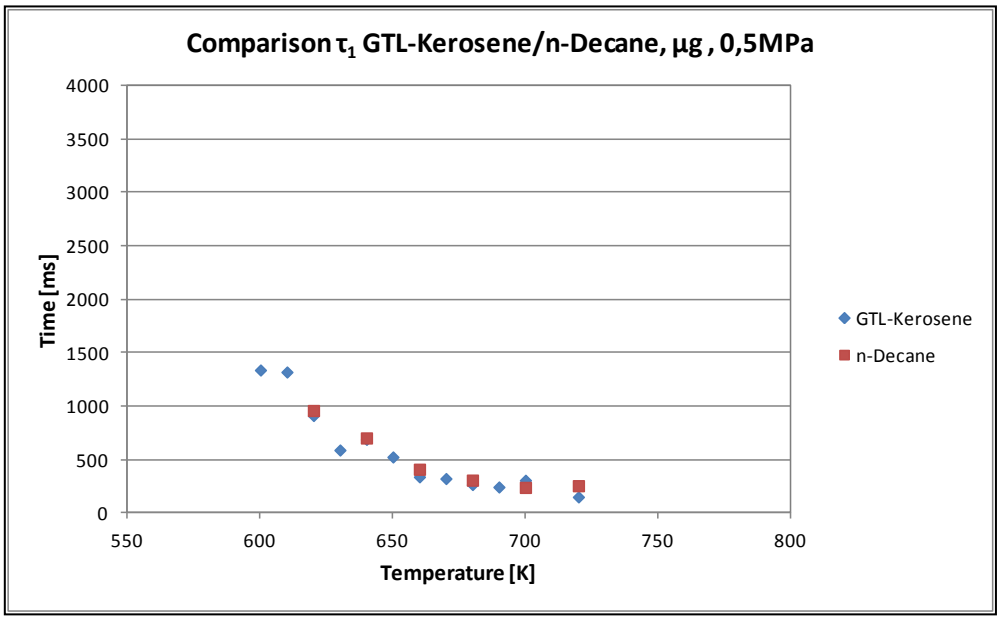
Comparison τ1 GTL-Kerosene/n-Decane, µg , 0,5MPa
Time [ms]
4000
3500
3000
2500
2000
1500
1000
500
0
550
600
650
700
750
800
Temperature [K]
GTL-Kerosene
n-Decane

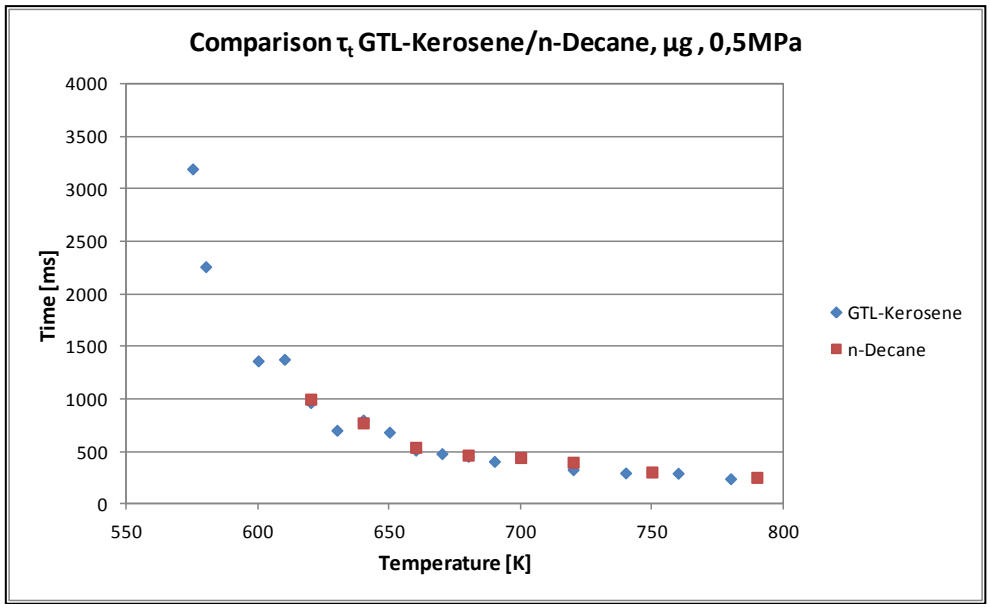

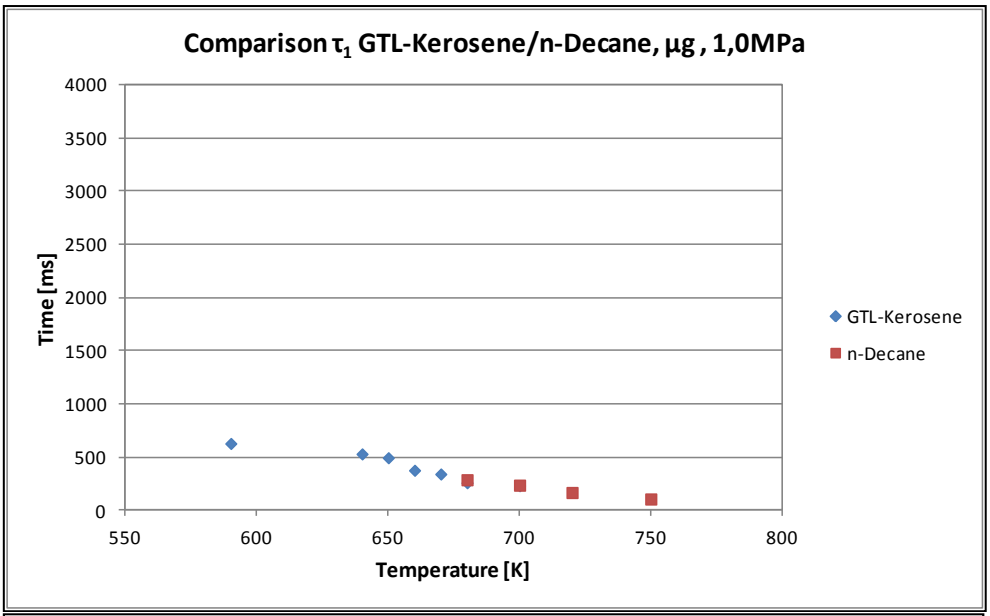

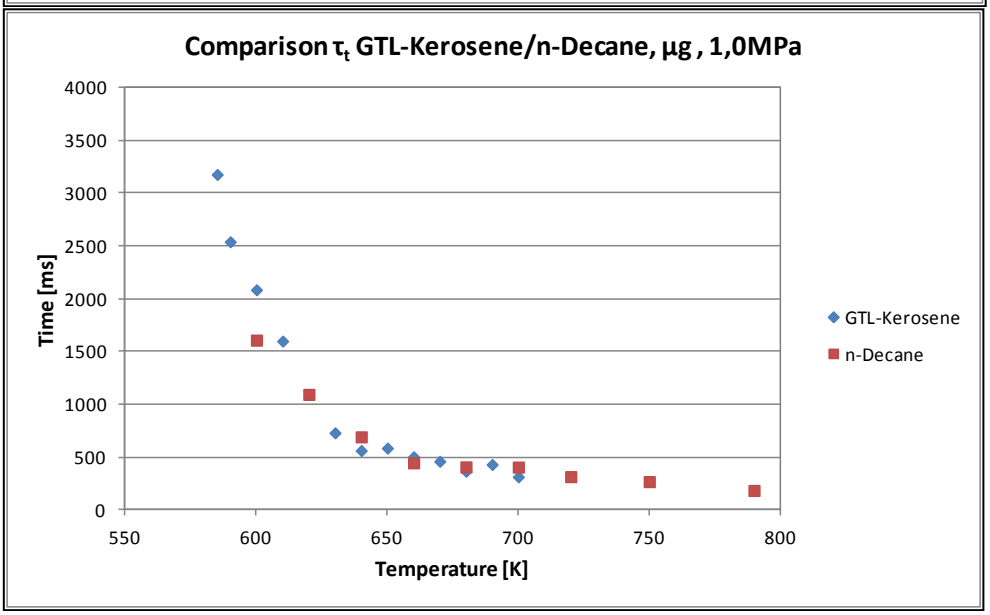

Fig. 117 - Comparison of the ignition delay times of GTL-Kerosene and n-Decane in µg for the pressure levels analyzed

Pressure	τ_I	τ_t	τ_{Lt}	Average
0,3MPa	0,67	0,25	0,29	0,40
0,5MPa	0,15	0,05	0,01	0,07
1,0MPa	0,06	0,06	-	0,06

Tab. 40 - Comparison of the deviation of the ignition delay times for n-Decane compared to GTL-Kerosene in µg

3.6.5. Evaporation Experiments

The experiments in this section are conducted with parameters analogous to section 3.5.5.

Evaporation Experiments of GTL-Kerosene

Normal gravity and microgravity evaporation experiments have been conducted for GTL-Kerosene. The regression of the droplet diameter through time for set ambient temperatures and pressures is presented in the following diagrams. The extracted evaporation rates are listed in the subsequent table.

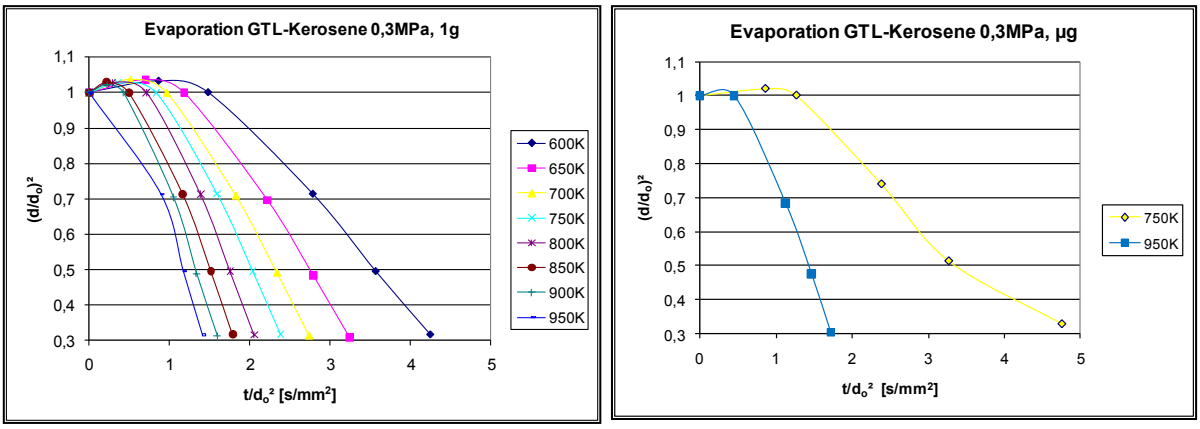

Fig. 118 - Droplet diameter regression for GTL-Kerosene for 0,3 MPa, 1g and µg

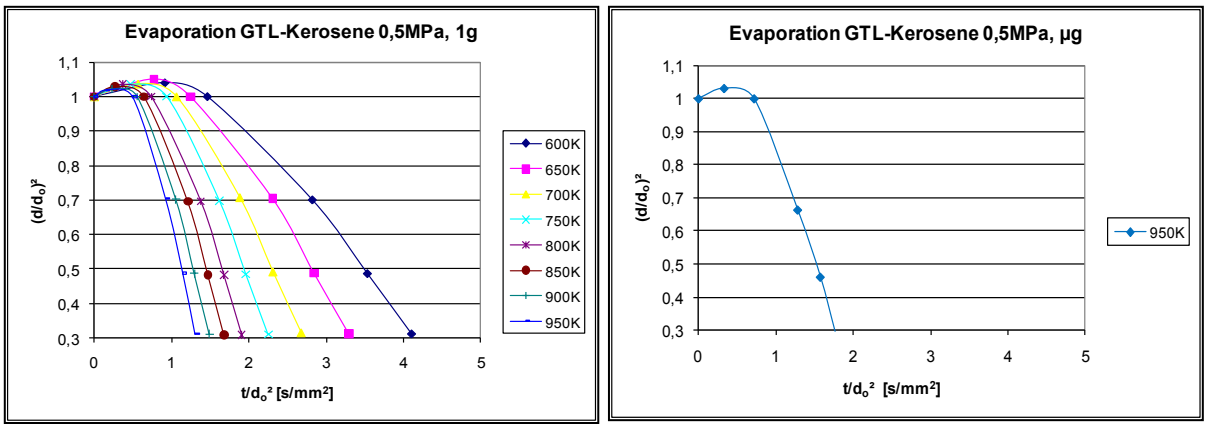

Fig. 119 - Droplet diameter regression for GTL-Kerosene for 0,5 MPa, 1g and µg

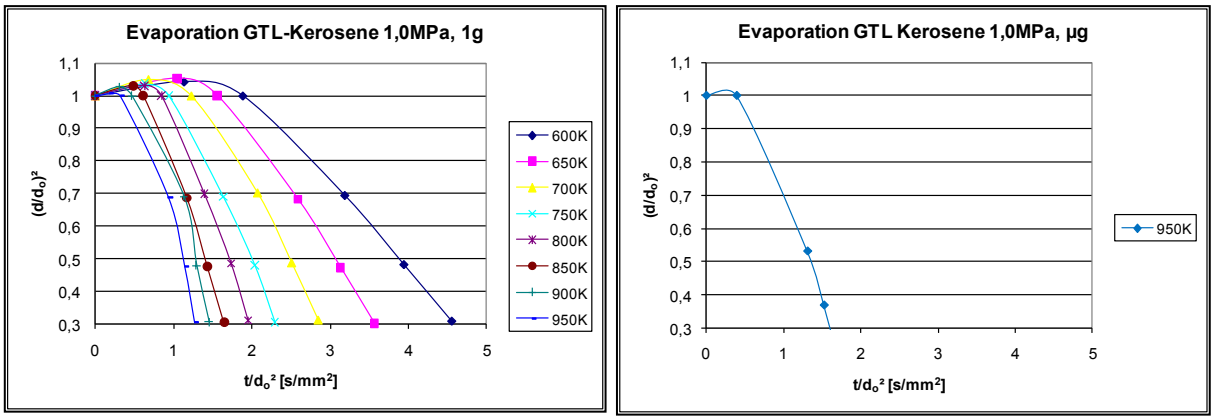

Fig. 120 - Droplet diameter regression for GTL-Kerosene for 1,0 MPa, 1g and µg

	Evaporation Rate, 1g		
Temperature	**0,3 MPa**	**0,5 MPa**	**1,0 MPa**
600 K	0,2474	0,2588	0,2586
650 K	0,3344	0,3337	0,3459
700 K	0,3856	0,4240	0,4204
750 K	0,4400	0,5236	0,5042
800 K	0,5070	0,5830	0,6118
850 K	0,5242	0,6589	0,6676
900 K	0,5879	0,7273	0,6683
950 K	0,7741	0,8398	0,6958
	Evaporation Rate, µg		
750 K	0,1938	N/A	N/A
950 K	0,5428	0,6640	0,5762

Tab. 41 – Evaporation Rates for GTL-Kerosene, 1g and µg

As shown in the previous diagrams and table, the evaporation rate of GTL-Kerosene increases with rising ambient temperature and pressure. Some notable exceptions are the lower values registered for 1,0 MPa at 900 and 950 K. The µg data available is scarce; nonetheless the data is presented for the sake of completeness.

A comparison of GTL-Kerosene and the developed surrogate fuel, n-Decane, is presented in the following diagram set:

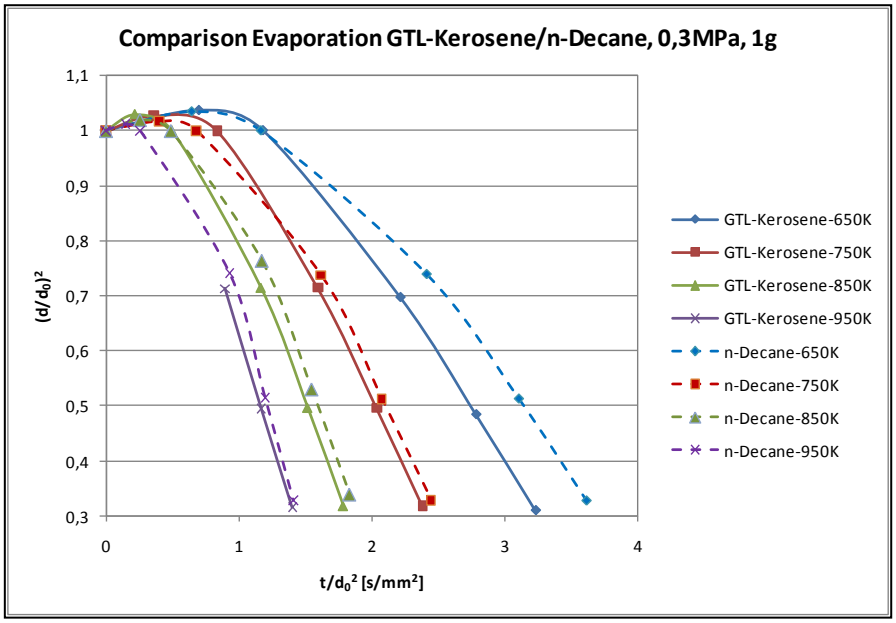

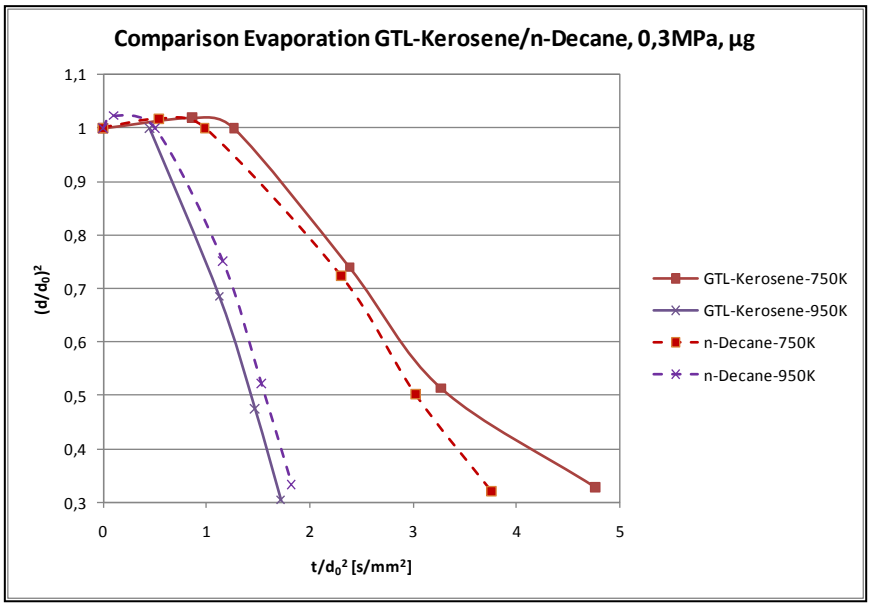

Fig. 121 – Comparison evaporation of GTL-Kerosene and n-Decane, 0,3 MPa, 1g and µg

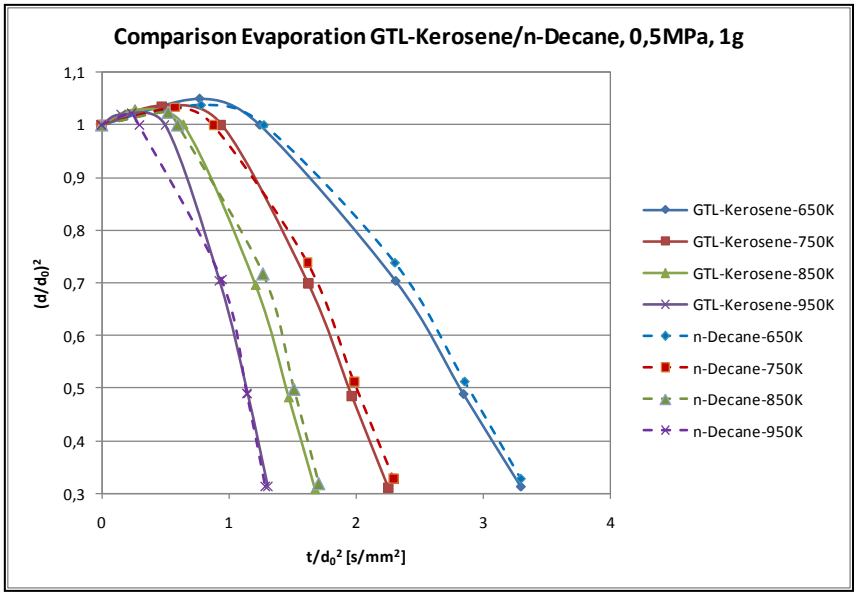

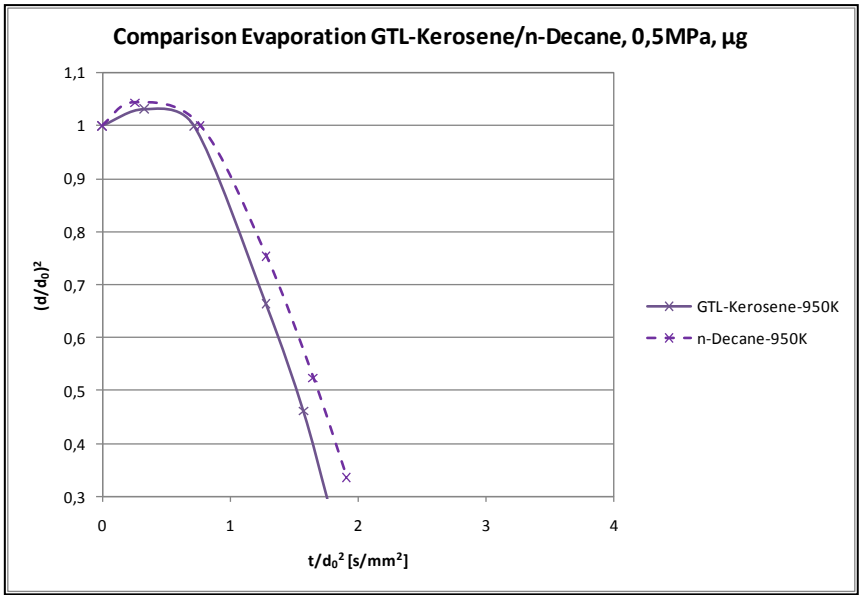

Fig. 122 - Comparison evaporation of GTL-Kerosene and n-Decane, 0,5 MPa, 1g and µg

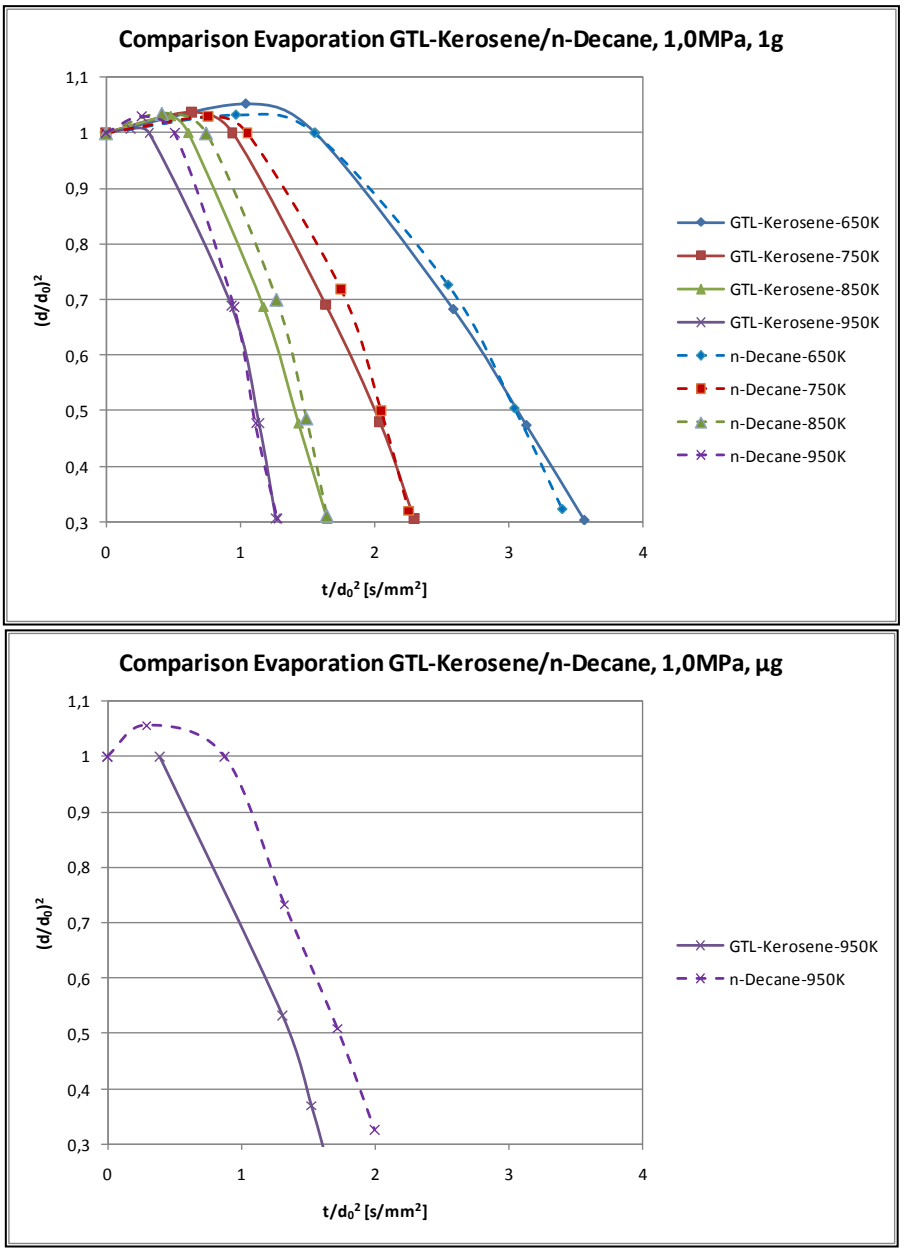

Fig. 123 - Comparison evaporation of GTL-Kerosene and n-Decane, 1,0 MPa, 1g and µg

Interestingly, GTL-Kerosene has overall slightly higher evaporation rates. With increasing pressure these differences become marginal. A notable exception is seen at 750 K in µg, where the evaporation rate of GTL-Kerosene is higher than the one measured for n-Decane. The following table lists the obtained evaporation rates for n-Decane:

	Evaporation Rate, 1g		
Temperature	**0,3 MPa**	**0,5 MPa**	**1,0 MPa**
600 K	0,2362	0,2344	0,2559
650 K	0,2710	0,3304	0,3606
700 K	0,3264	0,3987	0,4521
750 K	0,3764	0,4699	0,5479
800 K	0,4546	0,5507	0,6249
850 K	0,4866	0,5942	0,7437
900 K	0,5114	0,6587	0,8144
950 K	0,5650	0,6525	0,8985

	Evaporation Rate, µg		
750 K	0,2463	0,2382	0,3085
850 K	0,3822	0,4144	0,4255
950 K	0,5025	0,5772	0,5965

Tab. 42 - Evaporation rates for n-Decane, 1g and µg

3.7. Comparison of the Autoignition Behavior of GTL-Diesel and related Fuels

In this section, experimental data on the autoignition behavior of the Diesel family of fuels is presented and a comparative study is shown. The fuels (including surrogates) taken into consideration are:

- Fossil Diesel
- GTL-Diesel
- Bio-Diesel (RME)
- n-Heptane
- n-Tetradecane
- n-Tetradecane-75%-2,2,4,4,6,8,8-Heptamethylnonane-25%
- n-Tetradecane-50%-Alphamethylnaphthalene-50%

The experimental data on n-Heptane and n-Tetradecane-50%-Alphamethylnaphthalene-50% is taken from a previous study by Moriue [12] performed at ZARM. All data presented in this section was obtained using the same experimental facility, thus the comparability is ensured.

Normal Gravity Experiments

The following diagrams show the data obtained with the facility described in section 3.2 at normal gravity conditions and at 0,3 MPa ambient pressure. The experimental parameters and procedures are analogous to previous sections.

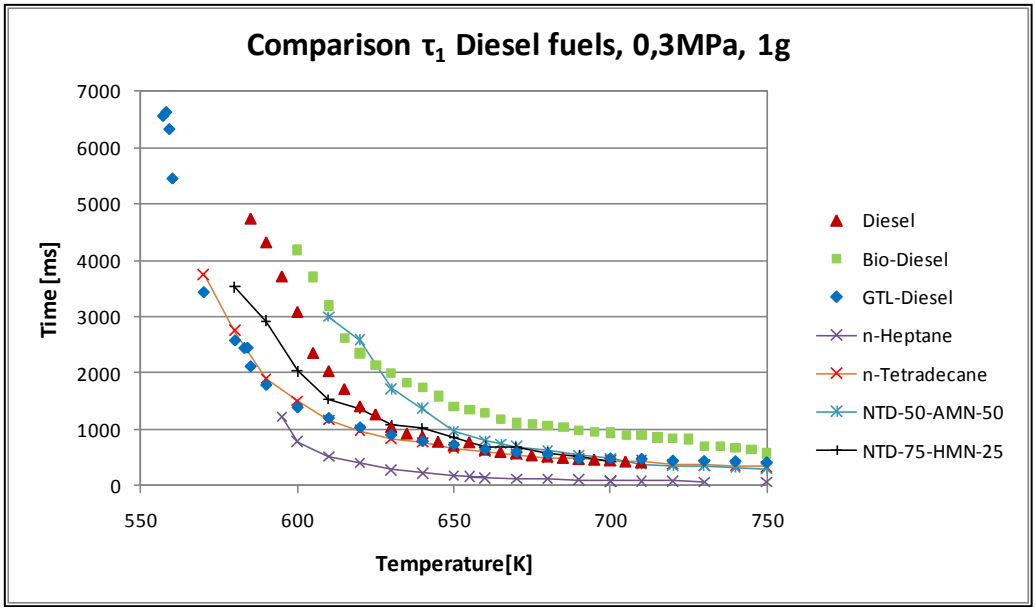

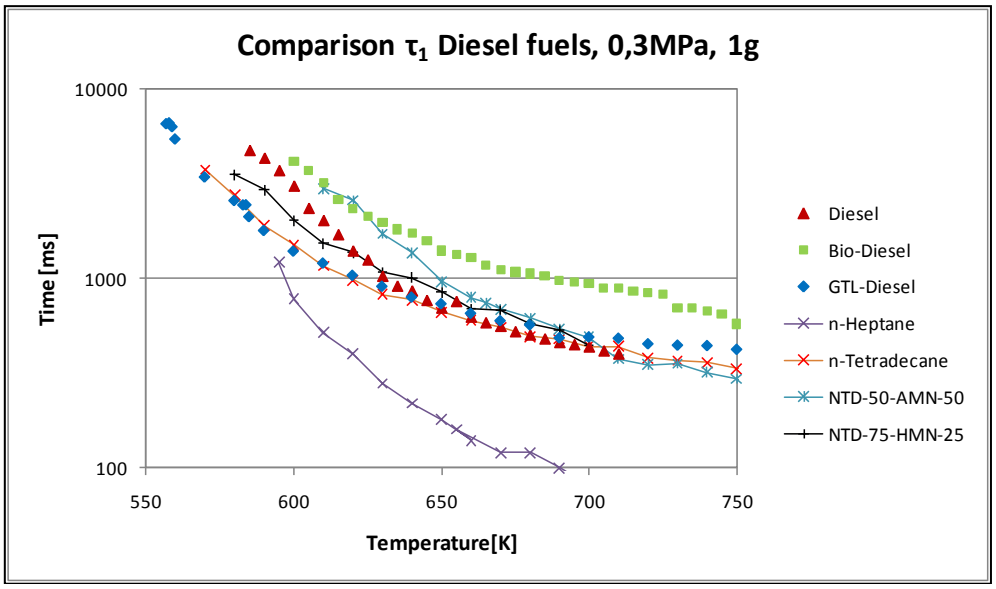
Comparison τ1 Diesel fuels, 0,3MPa, 1g
Time [ms]
10000
1000
100
550
600
650
700
750
Temperature[K]
Diesel
Bio-Diesel
GTL-Diesel
n-Heptane
n-Tetradecane
NTD-50-AMN-50
NTD-75-HMN-25

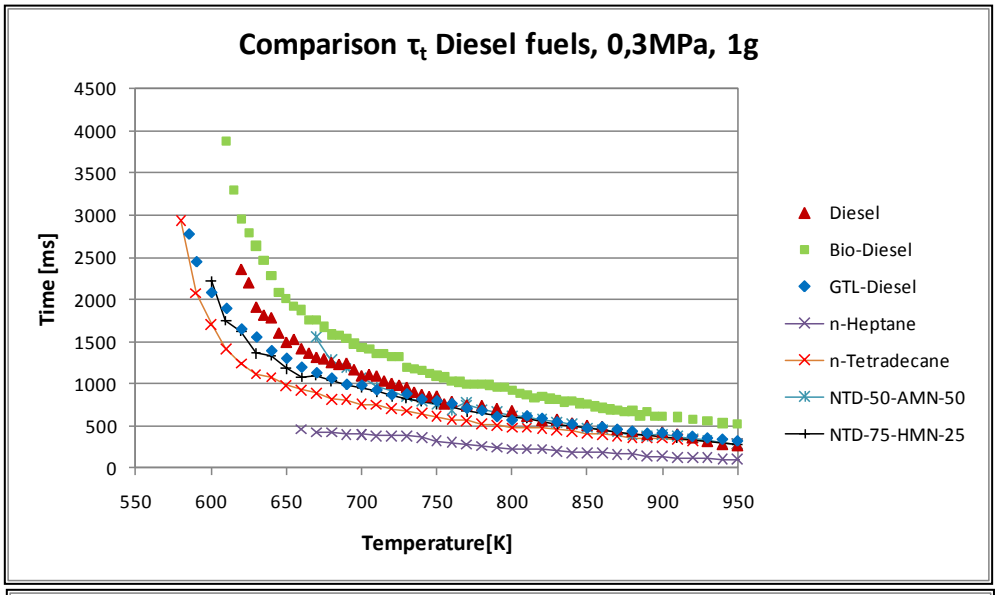
Comparison τt Diesel fuels, 0,3MPa, 1g
Time [ms]
4500
4000
3500
3000
2500
2000
1500
1000
500
0
550
600
650
700
750
800
850
900
950
Temperature[K]
Diesel
Bio-Diesel
GTL-Diesel
n-Heptane
n-Tetradecane
NTD-50-AMN-50
NTD-75-HMN-25

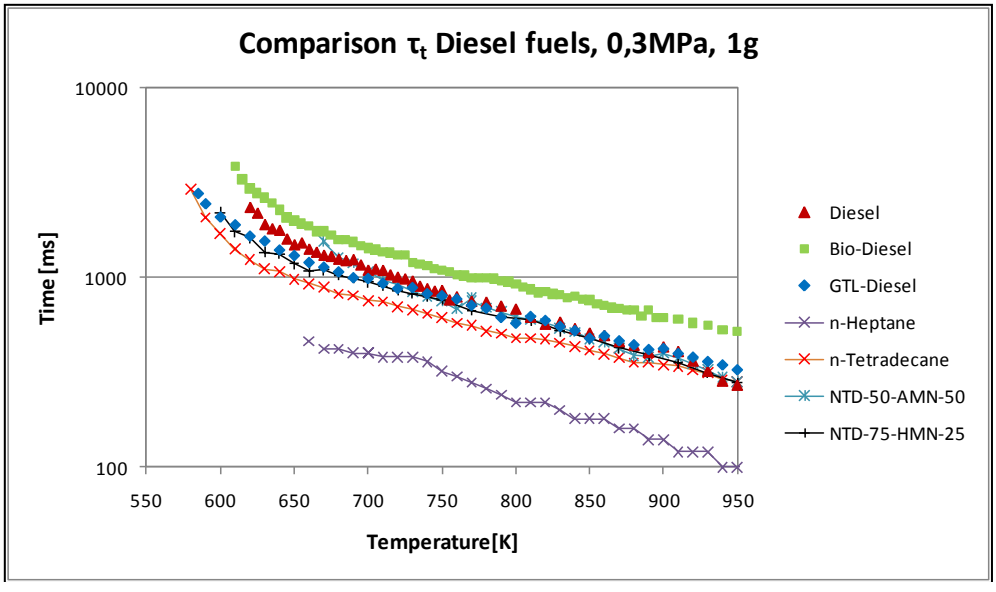
Comparison τt Diesel fuels, 0,3MPa, 1g
Time [ms]
10000
1000
100
550
600
650
700
750
800
850
900
950
Temperature[K]
Diesel
Bio-Diesel
GTL-Diesel
n-Heptane
n-Tetradecane
NTD-50-AMN-50
NTD-75-HMN-25

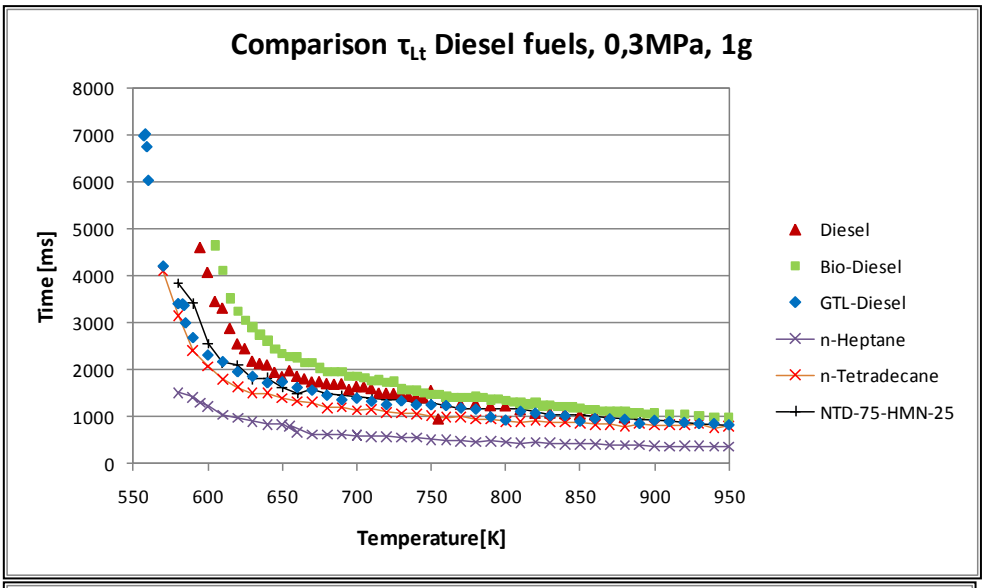
Comparison τ_{Lt} Diesel fuels, 0,3MPa, 1g
Time [ms]
8000
7000
6000
5000
4000
3000
2000
1000
0
550
600
650
700
750
800
850
900
950
Temperature[K]
Diesel
Bio-Diesel
GTL-Diesel
n-Heptane
n-Tetradecane
NTD-75-HMN-25

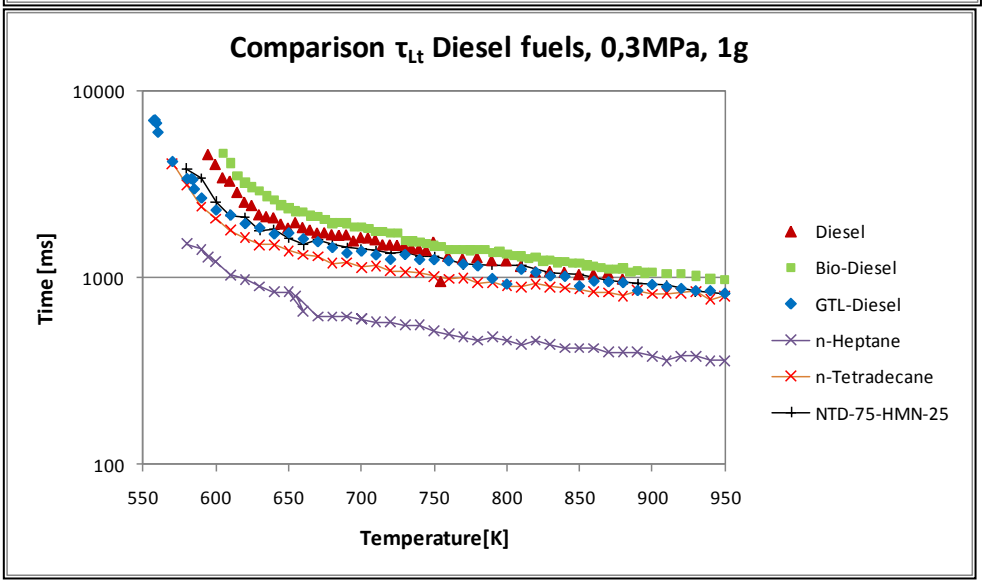
Comparison τ_{Lt} Diesel fuels, 0,3MPa, 1g
Time [ms]
10000
1000
100
550
600
650
700
750
800
850
900
950
Temperature[K]
Diesel
Bio-Diesel
GTL-Diesel
n-Heptane
n-Tetradecane
NTD-75-HMN-25

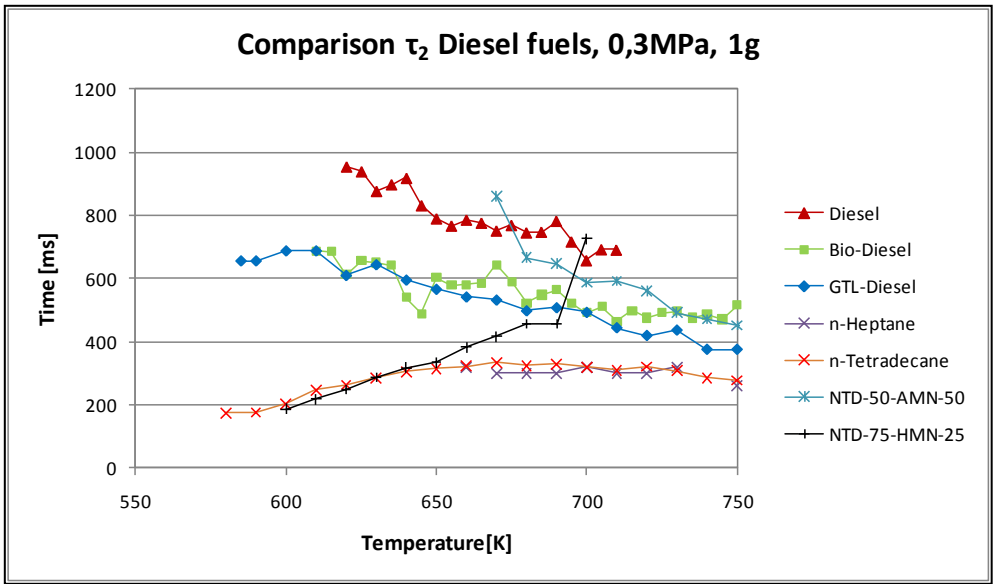
Comparison τ_2 Diesel fuels, 0,3MPa, 1g
Time [ms]
1200
1000
800
600
400
200
0
550
600
650
700
750
Temperature[K]
Diesel
Bio-Diesel
GTL-Diesel
n-Heptane
n-Tetradecane
NTD-50-AMN-50
NTD-75-HMN-25

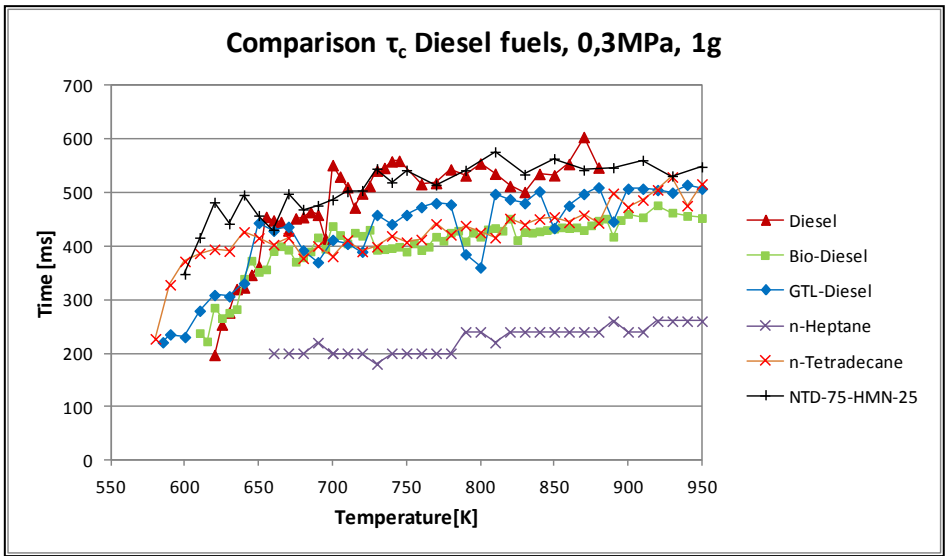

Fig. 124 – Experimental Data on the Ignition Delay Times for Diesel fuels at normal-g, 0,3 MPa

The following general observations can be made:

- Bio-Diesel is chemically a very different mixture of compounds compared to fossil Diesel and GTL-Diesel. Thus, as expected, it shows a different autoignition behavior. In general, ignitions occur later than in the other two Diesel variants, as shown in the first and total ignition delay times.
- Fossil Diesel and GTL-Diesel have for higher temperatures very similar ignition delay times.
- At low temperatures, below 640 K, each fuel shows a different cool flame behavior with Bio-Diesel having overall the largest and n-Heptane the smallest values for the first ignition delay time. Fossil Diesel has at these temperatures longer ignition delay times than GTL-Diesel.
- For temperatures higher than 640 K, fossil Diesel and GTL-Diesel show very similar behavior and values for τ_1. As shown in section 3.5.4, n-Tetradecane follows the τ_1 behavior of GTL-Diesel very accurately. As can be seen, the first detection of cool flames occurs for GTL-Diesel at lower temperatures (557 K) than for fossil Diesel (585 K).
- The NTD-75-HMN-25 surrogate fuel converges to the GTL-Diesel and fossil Diesel times at 640 K, the NTD-50-AMN-50 mixture at 650-660 K.
- The total ignition delay times show a similar behavior, with Bio-Diesel having the largest times and n-Heptane the smallest values.
- It can be inferred that the addition of an aromatic compound to a surrogate fuel acts as an ignition retardant at low temperatures (<650 K at 0,3 MPa), as shown by the first and total ignition delay diagrams.
- There is no data available on the droplet lifetimes of the NTD-50-AMN-50 mixture.
- The droplet lifetimes show an analogous behavior as the preceding ignition delay times. The difference between the highest delay times for Bio-Diesel and the times for fossil Diesel and GTL-Diesel becomes at temperatures higher than 750 K marginal. The droplet lifetime values for n-Heptane are less than 50% of the values encountered for the other Diesel variants and surrogates.
- The second ignition delay time diagram, which represents the duration of the cool flames shows for fossil Diesel the highest values. All fuels, except NTD-75-HMN-25

and the pure n-alkanes show a decreasing behavior for increasing temperatures. GTL-Diesel and Bio-Diesel have similar values, also n-Tetradecane and n-Heptane.

- The extent of the cool flame detection can also be inferred from this diagram. GTL-Diesel, Bio-Diesel and n-Tetradecane have a similar detection range. n-Heptane has a small range and the first detection occurs at 670 K.
- The τ_c diagram shows the duration of the hot flame combustion. The highest values are found for fossil Diesel and NTD-75-HMN-25. Bio-Diesel yields the lowest values for the Diesel variants. For all fuels, except n-Heptane, the values tend to reach a plateau around 500 ms in a band 200 ms wide. n-Heptane converges to a plateau at roughly 250 ms.
- NTD-50-AMN-50 is a usable surrogate fuel for fossil-Diesel, but has its weakness at lower temperatures. It cannot be used as a surrogate fuel for GTL-Diesel due to the presence of an aromatic compound which is absent in the GTL-Diesel composition.
- Bio-Diesel, as mentioned before, is chemically different compared to the other Diesel variants, thus requires a different type of surrogate fuel formulation, which can be found in literature. [29, 78-80]
- n-Heptane is a poor surrogate fuel for the autoignition behavior of Diesel and its related variants.

Microgravity Experiments

The diagrams in this section depict the autoignition behavior of Diesel variants and surrogates in microgravity. The experimental parameters are analogous to previous sections in this study and the ambient pressure is 0,3 MPa. There is no µg data available on n-Heptane and NTD-50-AMN-50.

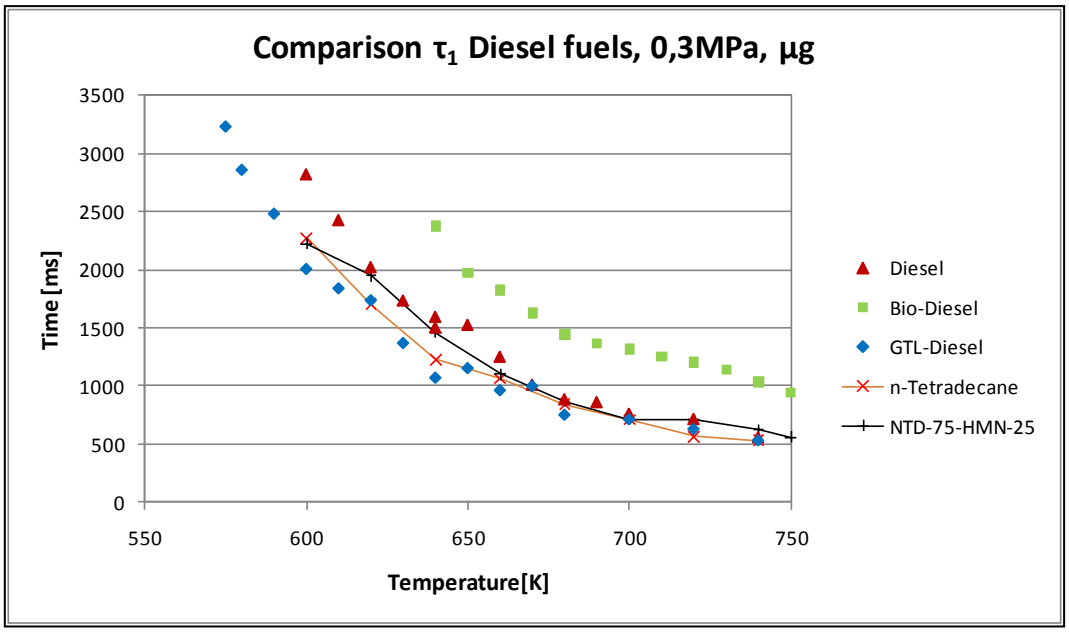

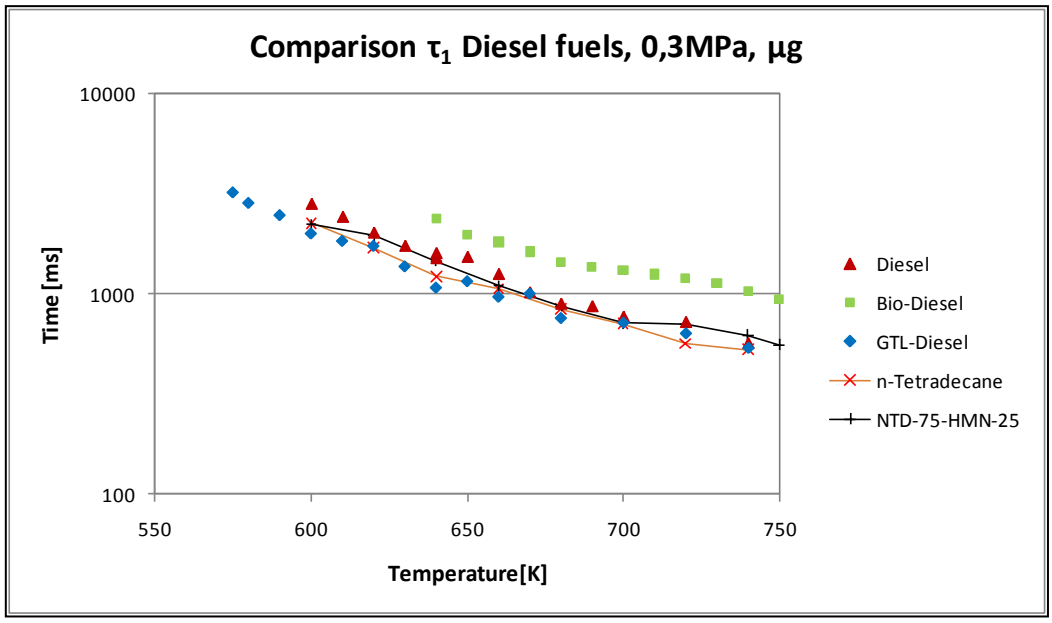
Comparison τ1 Diesel fuels, 0,3MPa, µg
10000
1000
100
Time [ms]
550
600
650
700
750
Temperature[K]
Diesel
Bio-Diesel
GTL-Diesel
n-Tetradecane
NTD-75-HMN-25

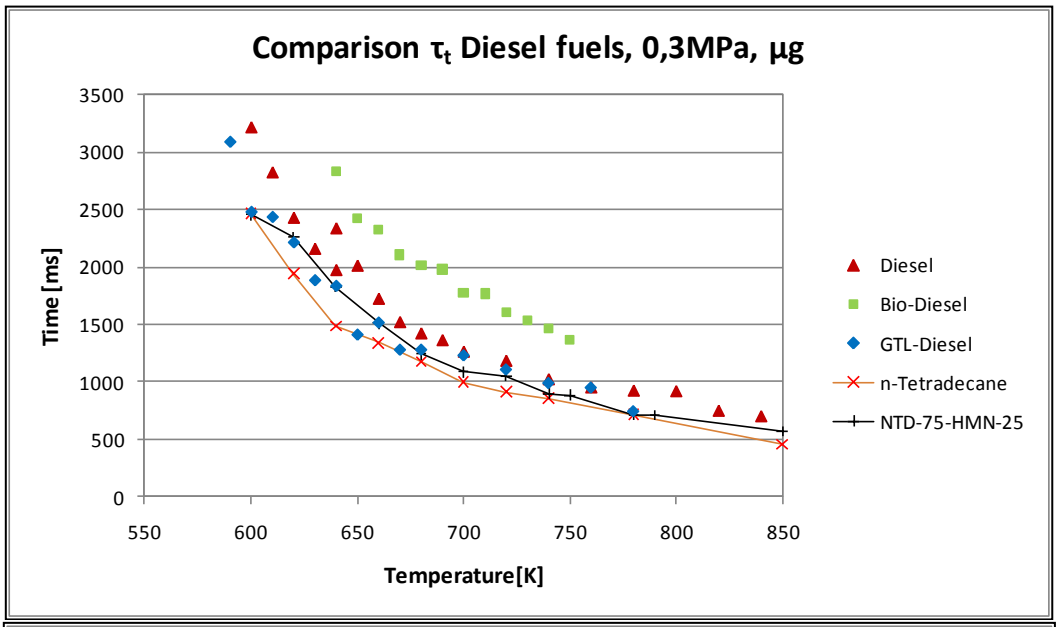
Comparison τt Diesel fuels, 0,3MPa, µg
3500
3000
2500
2000
1500
1000
500
0
Time [ms]
550
600
650
700
750
800
850
Temperature[K]
Diesel
Bio-Diesel
GTL-Diesel
n-Tetradecane
NTD-75-HMN-25

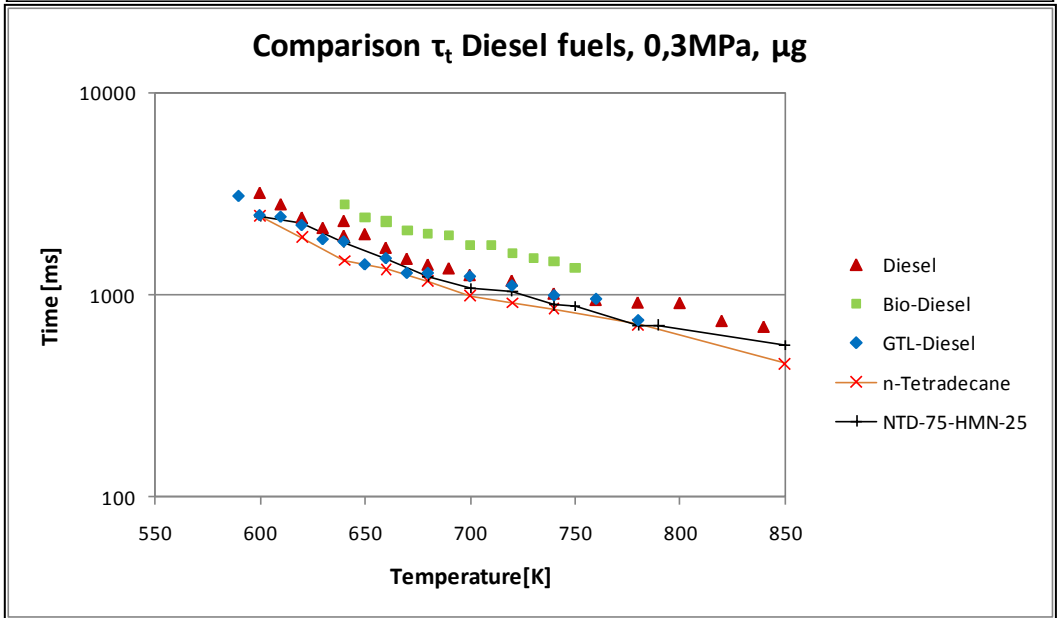
Comparison τt Diesel fuels, 0,3MPa, µg
10000
1000
100
Time [ms]
550
600
650
700
750
800
850
Temperature[K]
Diesel
Bio-Diesel
GTL-Diesel
n-Tetradecane
NTD-75-HMN-25

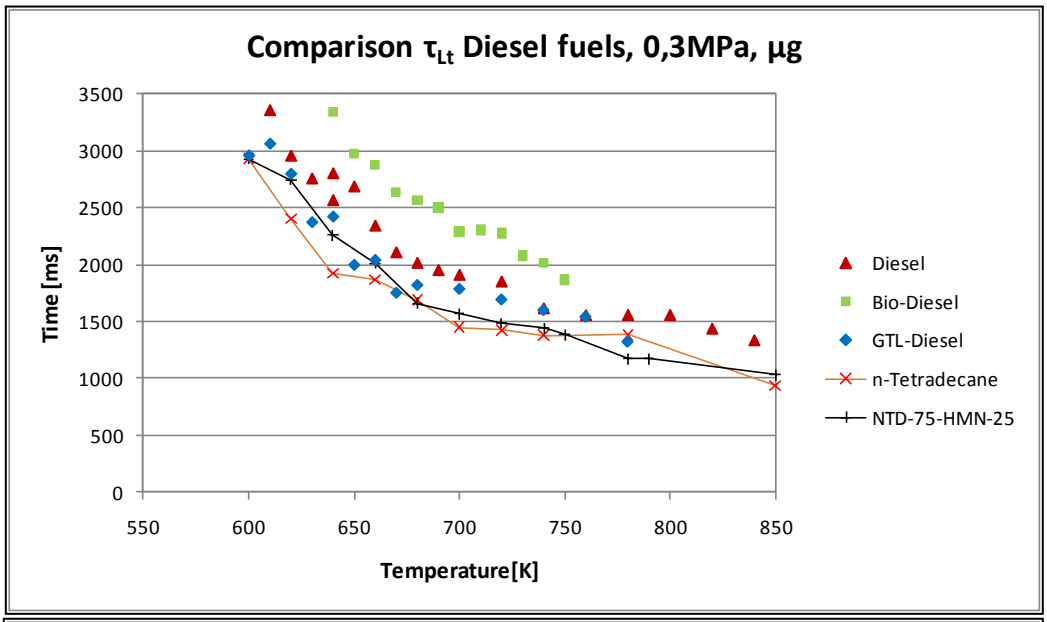
Comparison τLt Diesel fuels, 0,3MPa, µg
Time [ms]
3500
3000
2500
2000
1500
1000
500
0
550
600
650
700
750
800
850
Temperature[K]
Diesel
Bio-Diesel
GTL-Diesel
n-Tetradecane
NTD-75-HMN-25

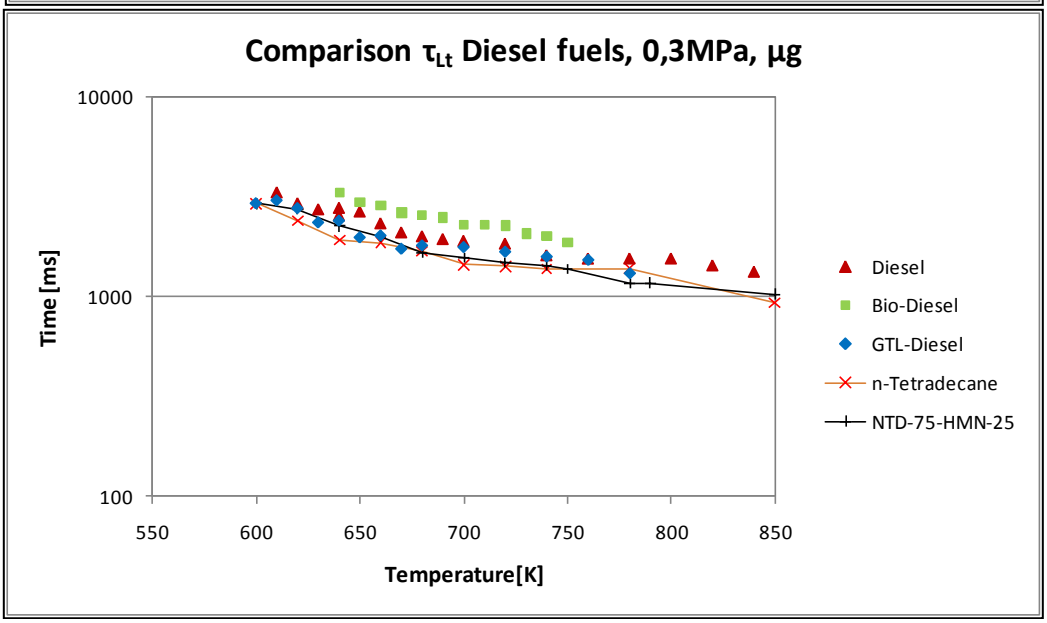
Comparison τLt Diesel fuels, 0,3MPa, µg
Time [ms]
10000
1000
100
550
600
650
700
750
800
850
Temperature[K]
Diesel
Bio-Diesel
GTL-Diesel
n-Tetradecane
NTD-75-HMN-25

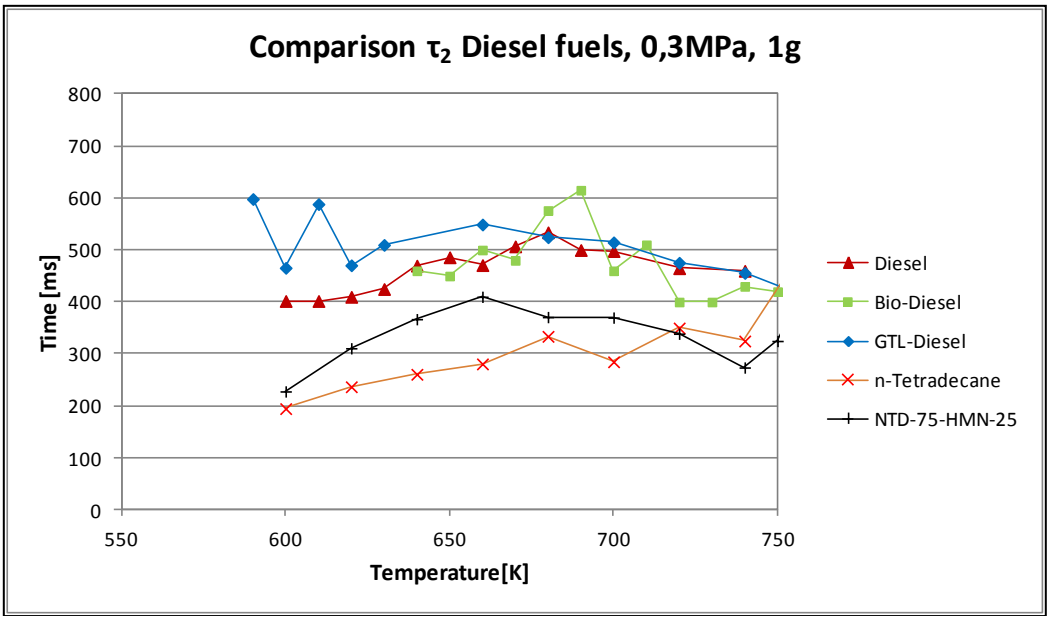
Comparison τ2 Diesel fuels, 0,3MPa, 1g
Time [ms]
800
700
600
500
400
300
200
100
0
550
600
650
700
750
Temperature[K]
Diesel
Bio-Diesel
GTL-Diesel
n-Tetradecane
NTD-75-HMN-25

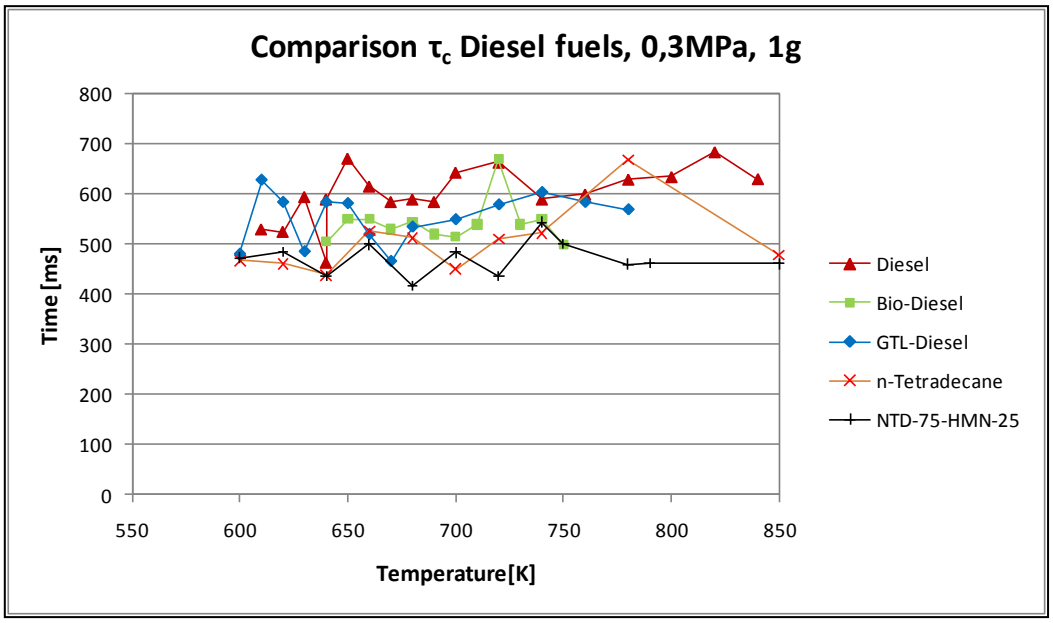

Fig. 125 - Experimental data on the ignition delay Times for Diesel fuels in µg, 0,3 MPa

The following observations can be inferred from the data presented:

- The first ignition delay time diagram shows for all fuels except Bio-Diesel similar values. Bio-Diesel has the highest values and the latest detection of a cool flame at 640 K. The earliest detections are observed for GTL-Diesel at 575 K. Fossil Diesel has slightly higher times compared to GTL-Diesel. n-Tetradecane shows a good representation of the τ_1 behavior of GTL-Diesel, as presented in section 3.5.4.
- The total ignition delay time diagram shows similar trends. Bio-Diesel has the highest total ignition delay times. There is only data till 750 K available for this fuel. The other fuels show similar times among each other, with fossil Diesel having the higher values.
- No pronounced ZTC or NTC are observed for the fuels.
- The droplet lifetimes show a similar behavior as the previous ignition delay times. The lowest values are encountered for n-Tetradecane and the surrogate mixture, the highest for Bio-Diesel.
- For the second ignition time, excluding some outliers, the Diesel variants show very similar values around 500 ms. The surrogate fuel and n-Tetradecane show lower times.
- For the hot flame combustion time, the values are in a band between 450 and 650 ms, with the surrogate fuel having the lowest and fossil Diesel having the highest times.

3.8. Comparison of the Autoignition Behavior of GTL-Kerosene and related Fuels

In this section, experimental data on the autoignition behavior of the Kerosene family of fuels is presented and a comparative study is shown. The fuels (including surrogates) taken into consideration are:

- Fossil Kerosene
- GTL-Kerosene
- n-Decane
- n-Decane-60%-1,2,4-Trimethylbenzene-40%

The experimental data on n-Decane-60%-1,2,4-Trimethylbenzene-40% is cited from a study by Moriue [12]. Except for GTL-Kerosene and n-Decane, no microgravity data is available for the other fuels. Only data acquired in normal gravity will be presented. The experimental parameters are analogous to previous sections and the ambient pressure is 0,3 MPa.

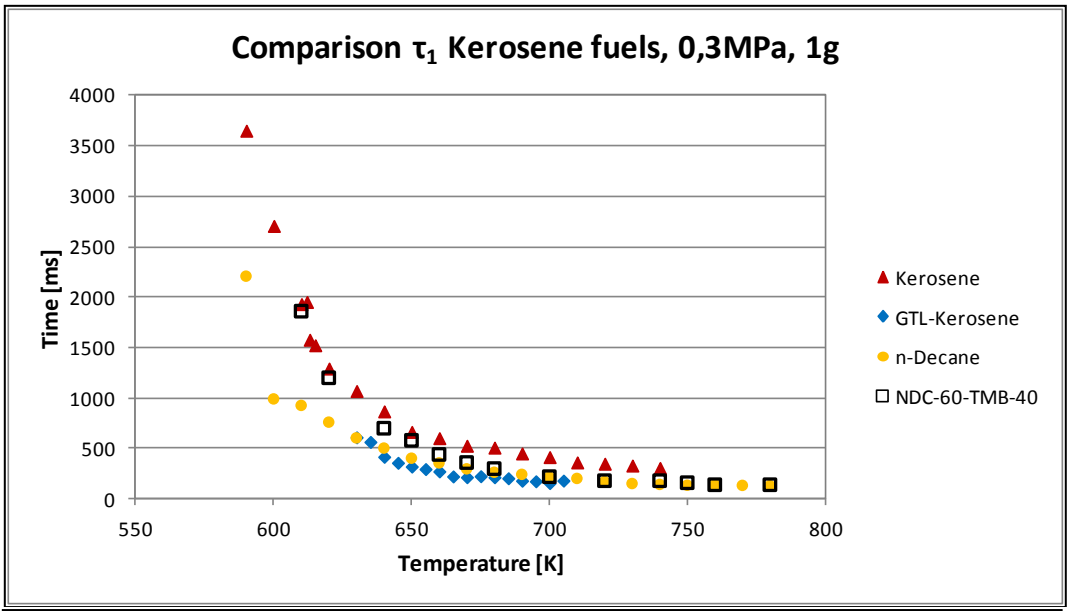

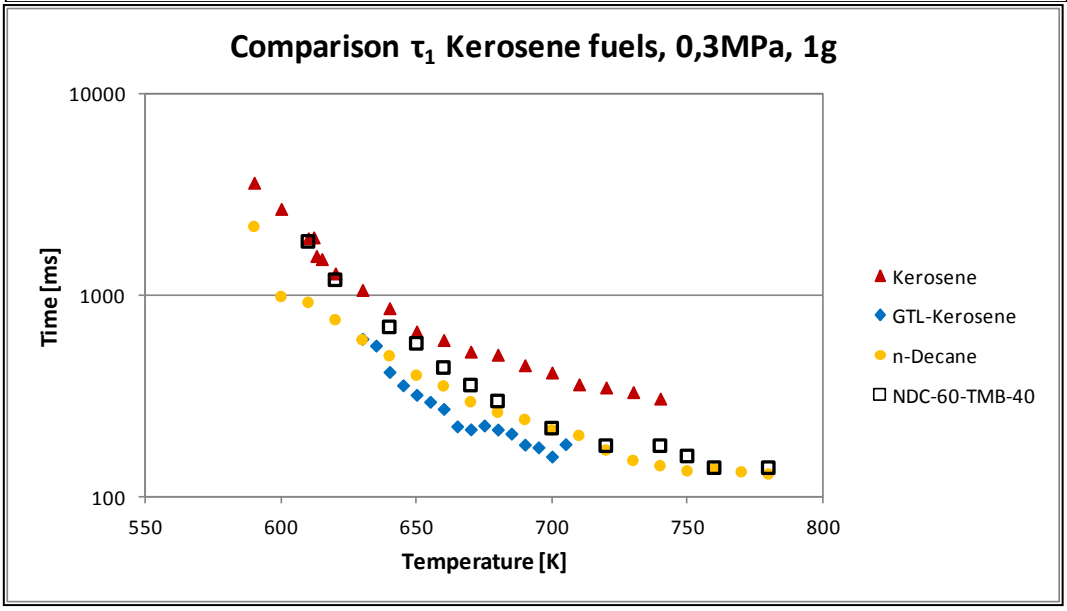

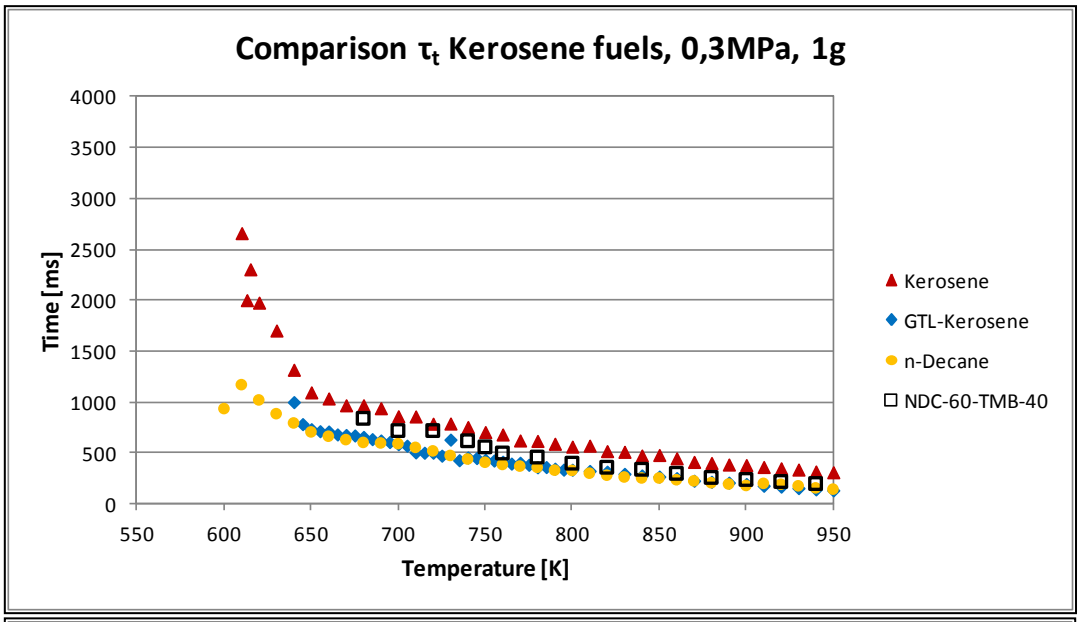
Comparison τt Kerosene fuels, 0,3MPa, 1g
Time [ms]
4000
3500
3000
2500
2000
1500
1000
500
0
550
600
650
700
750
800
850
900
950
Temperature [K]
Kerosene
GTL-Kerosene
n-Decane
NDC-60-TMB-40

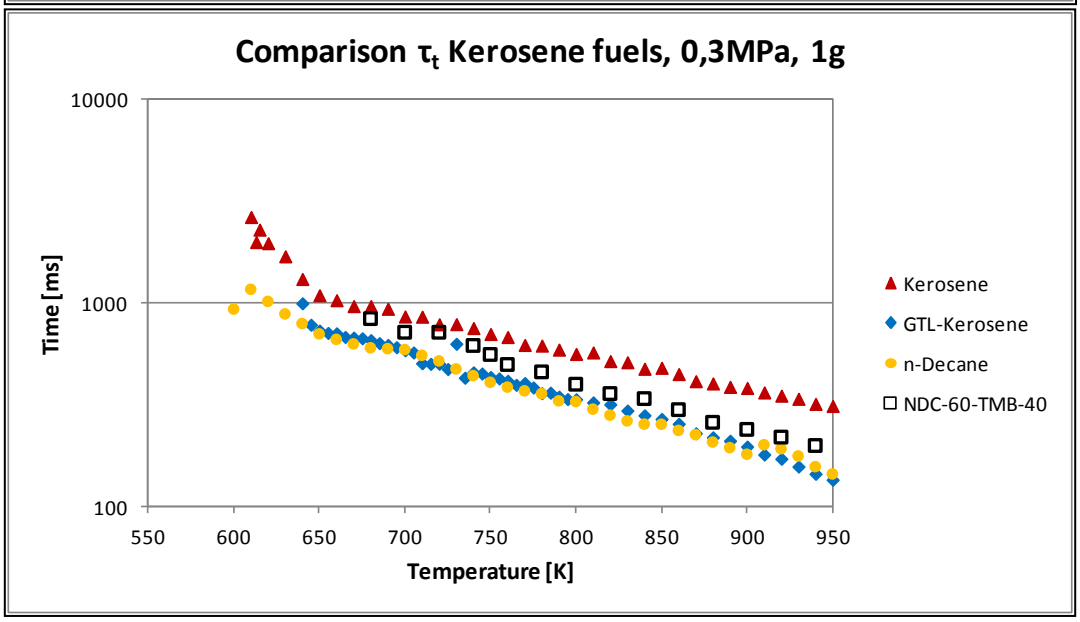
Comparison τt Kerosene fuels, 0,3MPa, 1g
Time [ms]
10000
1000
100
550
600
650
700
750
800
850
900
950
Temperature [K]
Kerosene
GTL-Kerosene
n-Decane
NDC-60-TMB-40

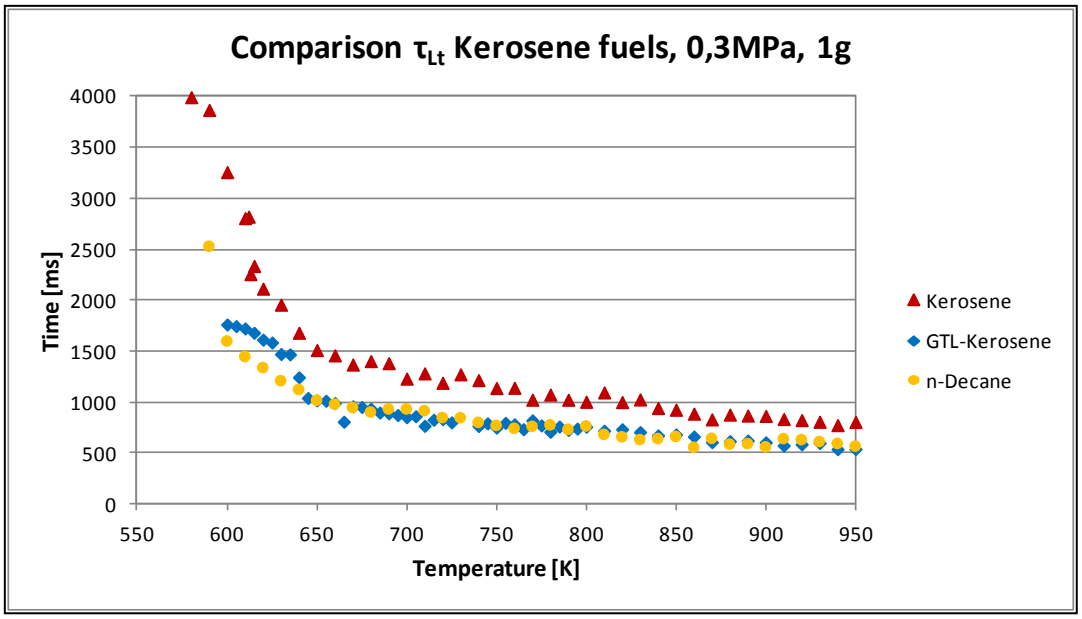
Comparison τLt Kerosene fuels, 0,3MPa, 1g
Time [ms]
4000
3500
3000
2500
2000
1500
1000
500
0
550
600
650
700
750
800
850
900
950
Temperature [K]
Kerosene
GTL-Kerosene
n-Decane

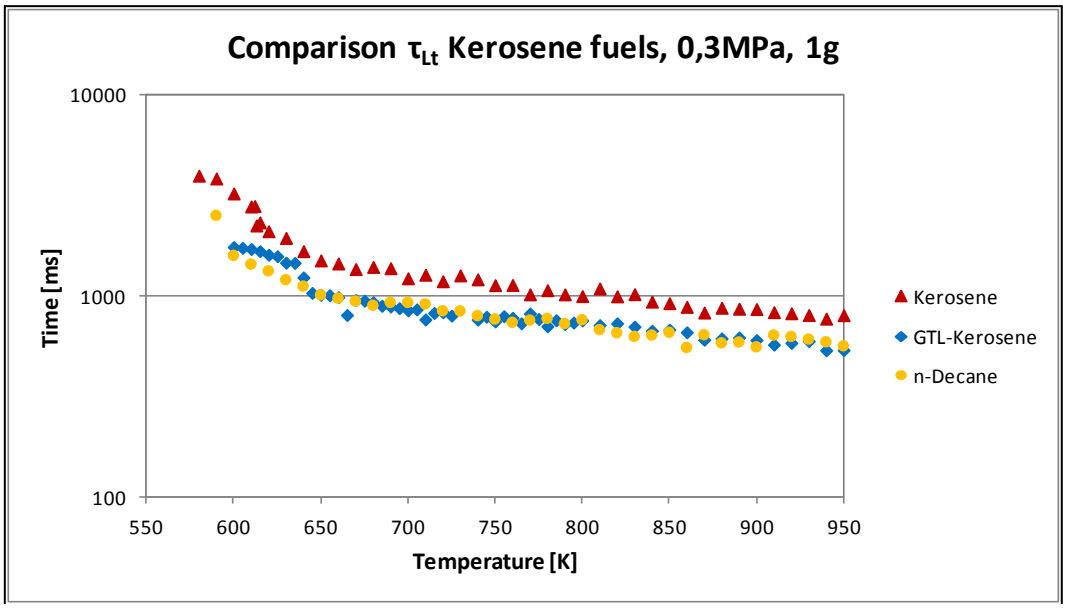

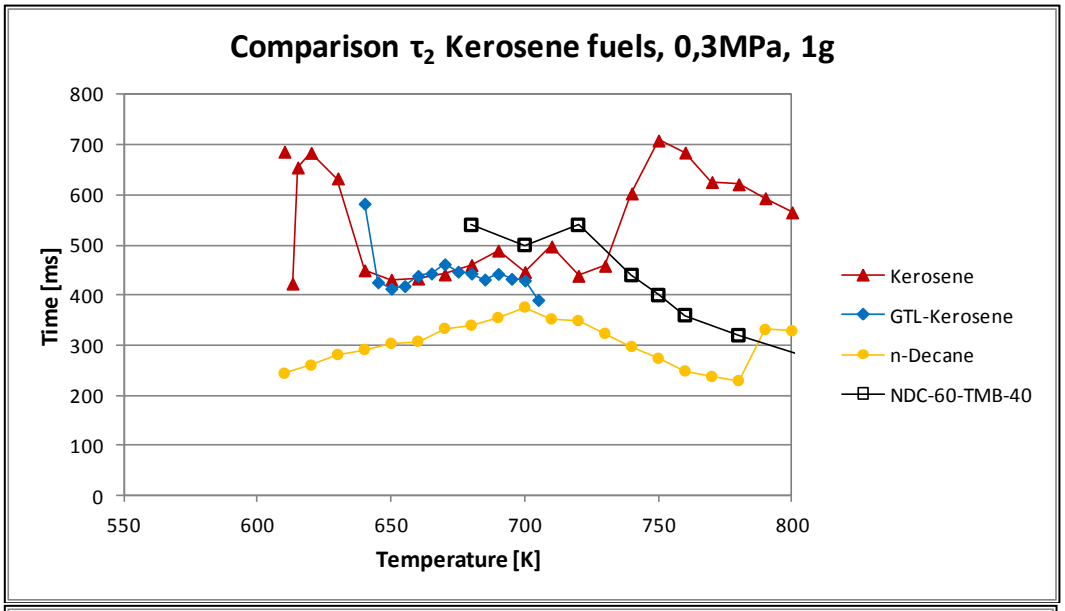

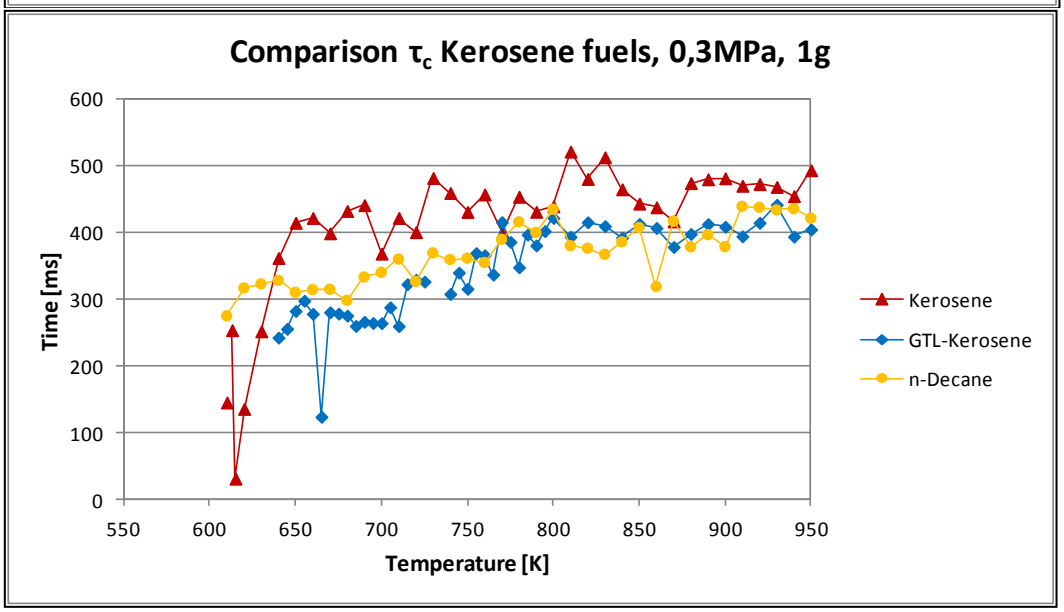

Fig. 126 - Experimental data on the ignition delay times for Kerosene fuels at normal-g, 0,3 MPa

General observations, based on the presented data, are as follows:

- The first induction times are the highest for fossil Kerosene and lowest for GTL-Kerosene. The extent of the cool flame temperature range shows large variations among the fuels. For GTL-Kerosene cool flames are detectable from 630 to 705 K, for fossil Kerosene from 590 to 740 K.
- The two surrogate fuels show a similar induction times starting at 670 K. Below this temperature the influence of TMB can be seen in the retardation of the cool flame (increase of the first induction time) compared to pure n-Decane.
- The total induction times diagram depicts for fossil Kerosene the highest induction times, being in the order of 50% higher than for GTL-Kerosene.
- As shown in section 3.5.4 n-Decane maps the total ignition behavior of GTL-Kerosene accurately. NDC-60%-TMB-40% has a good correspondence for fossil Kerosene, but at higher temperatures the two curves tend to diverge,
- There is no droplet lifetime data available for NDC-60%-TMB-40%, thus τ_c cannot be inferred for this mixture.
- The second induction time is in the range of 640-700 K rather equivalent for fossil and GTL-Kerosene. For higher temperatures there is no detectable cool flame for GTL-Kerosene, thus no τ_2 is defined. n-Decane show much shorter second induction times than the two Kerosene variants. For the surrogate mixture the small amount of data infers a similar behavior as fossil Kerosene at 670-720 K, and lower times at higher temperatures in contrast to the increasing times for fossil Kerosene.
- The τ_c data shows that the highest values are achieved by fossil Kerosene. GTL-Kerosene and n-Decane show roughly equivalent values. The three curves show the trend of converging at 450 ms in a band 100 ms wide.

4. Calculations and Modeling

The current chapter is based on work performed in the past years at the Aerospace Combustion Engineering Group at ZARM [13, 15-17, 82-89]. One of the aims of the experimental work is to validate and support the development of numerical codes. These codes enable the computational design and optimization of practical devices and apparatuses such as internal combustion engines and gas turbines. For this, detailed chemical kinetic models of the fuels in question are needed.

4.1. Description of the Physical Model

The numerical model is 1-dimensional for a spherical droplet and is based on the following assumptions:

- Low velocities of the gas, no pressure gradient
- Temperature gradient is sufficiently small, no thermal diffusion
- No radiative heat transfer
- No invasion of the gas in the liquid phase
- No chemical reactions inside the droplet
- Surface tension is neglected and its influence is assumed to be negligible for higher pressures

The model itself is fully transient and is composed of a one dimensional grid for the liquid and gas phase. The liquid phase has 21 nodes and the gas phase 71. The nodes of the grid in the gas phase are exponentially distributed since most of the chemical reactions and high gradients in the physical gas occur close to the droplet surface. The nodes in the liquid phase are linearly distributed. The following schematic depicts the numerical grid and the boundaries of the model.

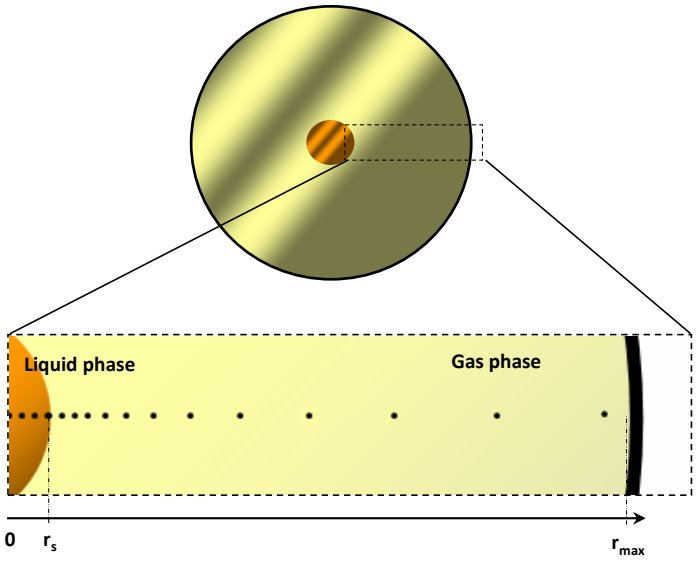

Fig. 127 – Schematic of the numerical grid and the boundaries [8]

The equations can be divided in three main sets, two for each phase and the boundary conditions. For the liquid phase continuity, heat flow and state equations are solved.

Liquid phase:

Eq. 36 – Equation of state

$$p = \rho Z \frac{R^0}{\mu} T$$

Eq. 37 – Mass conservation

$$\frac{\partial \rho}{\partial t} + div(\rho \boldsymbol{u}) = 0$$

Eq. 38 – Energy conservation

$$\rho c_p \left(\frac{\partial T}{\partial t} + u \cdot \nabla T \right) = div(\lambda \nabla T) + \frac{\partial p}{\partial t}$$

From the above equations it can be seen that the pressure in the liquid phase is assumed to be spatially constant but is allowed to vary with time. On the other hand, temperature is not only dependent on time but also location. This allows the surface layers closer to the gas phase boundary to become heated and a temperature distribution in the droplet to be established.

For the gas phase two sets of equations are solved, the first one treats the fluid dynamical properties such as state, continuity, species flow and heat flow (Eq. 39-43). The second set of equations is the reduced chemical reaction mechanism. The heat and species produced in the gas phase result from this mechanism, which is described in the subsequent section.

Gas phase:

Eq. 39 – Equation of state

$$p = \rho Z \frac{R^0}{\bar{\mu}} T$$

$$\bar{\mu} = \sum \mu_i X_i$$

Eq. 40 – Mass conservation

$$\frac{\partial \rho}{\partial t} + div(\rho \boldsymbol{u}) = 0$$

Eq. 41 – Components conservation

$$\rho \frac{\partial Y_i}{\partial t} + \rho \boldsymbol{u} \nabla Y_i + div(\rho Y_i \cdot \boldsymbol{u}_{Di}) = \dot{w}_i$$

Eq. 42 – Energy conservation

$$\rho \sum c_{pi} Y_i \left[\frac{\partial T}{\partial t} + u \cdot \nabla T \right] - \frac{\partial p}{\partial t} + \sum h_i \dot{w}_i + div(-\lambda \nabla T) + \rho \sum c_{pi} Y_i u_{Di} \cdot \nabla T = 0$$

Eq. 43 – Maxwell-Stefan model for multi-component diffusion

$$\nabla X_i = \sum_{j \neq i} \frac{X_i X_j}{D_{ij}} \left(\boldsymbol{u}_{Dj} - \boldsymbol{u}_{Di} \right)$$

Eq. 44 – Chemical reactions, concentration rate

$$\dot{w}_i = \mu_i \sum_{k_{reaction}} \left(v''_{i,k} - v'_{i,k} \right) A_k T^{n_k} e^{\frac{E_k}{R^0 T}} \prod_{j_{species}} \left(\frac{X_j p}{R^0 T} \right)^{v'_{j,k}}$$

The initial conditions are applied to the liquid droplet and the gas phase. These include equivalence ratio, temperature and pressure. The equivalence ratio within the liquid phase is always one.

Boundary conditions:

Centre of the droplet, point symmetry ($r = 0$)

Eq. 45 - No heat flux

$$\left. \frac{\partial T}{\partial r} \right|_{r=0} = 0$$

Eq. 46 - No mass flux

$$\boldsymbol{u}|_{r=0} = 0$$

Liquid-gas phase boundary ($r = r_s(t)$)

Eq. 47 – Temperature equilibrium

$$T_l|_{r=r_{s-}} = T_g\big|_{r=r_{s+}}$$

Eq. 48 - Fugacity equilibrium

$$f_i^l\big|_{r=r_{s-}} = f_i^g\big|_{r=r_{s+}} .., f_i = X_i \cdot \phi_i \cdot p$$

Eq. 49 – Mass conservation

$$\rho_l (u_l - \dot{r}_s)|_{r=r_{s-}} = \rho_g \left(u_g - \dot{r}_s \right)\big|_{r=r_{s+}} = \dot{m}$$

Eq. 50 – Components conservation

$$Y_i^l \cdot \dot{m}|_{r=r_{s-}} = Y_i \left(\dot{m} + \rho_g \cdot \boldsymbol{u}_{Di} \right)\big|_{r=r_{s+}}$$
$$Y_i^l = \delta_{i,fuel}$$

Eq. 51 – Energy conservation

$$-\lambda_l \cdot \nabla T_l|_{r=r_{s-}} + \dot{m} \cdot \Delta H_v = -\lambda_g \cdot \nabla T_g\big|_{r=r_{s+}}$$

Outer boundary ($r = r_{max}(t)$)

Eq. 52 – No heat flux

$$\frac{\partial T}{\partial r}\bigg|_{r=r_{max}} = 0$$

Eq. 53 – No mass flux

$$\boldsymbol{u}|_{r=r_{max}} = 0$$

4.2. Chemical Reaction Kinetics

The previous section presented the complex physical model for the autoignition of single droplets of fuel. In order to be able to obtain realistic and quantitative results a detailed chemical model is needed. This section presents a detailed chemical reaction mechanism for n-Decane, the n-alkane developed as a surrogate fuel for GTL-Kerosene. For GTL-Diesel and the developed components for the surrogate fuels, n-Tetradecane and HMN no detailed chemical model is currently available.

Chemical Reaction Kinetics for n-Decane

This reduced but nonetheless detailed reaction mechanism was developed by Bikas and Peters [90] and adapted by Schnaubelt [84]. It consists of 65 species and 580 reactions, with low and high temperature paths. Special attention has been given for the transition between the low and high temperature paths. The cool flame reactions are chemically lumped in a submechanism, a so-called autoignition mechanism, consisting of 30 reactions. The most important classes of elementary reactions that take place at both high and low temperatures are:

- Unimolecular fuel decomposition
- H-atom abstraction from the fuel
- Alkyl radical decomposition
- Alkyl radical + O_2 to produce olefin + HO_2 directly
- Alkyl radical isomerization
- Abstraction reactions from olefin by OH, H, O and CH_3
- Alkenyl radical decomposition
- Olefin decomposition
- Addition of alkyl radicals to O_2
- Alkyl peroxy radical isomerization ($RO_2 \rightarrow RO_2H$)
- RO_2H = olefin + HO_2 (radical site β to OOH group)
- Addition of RO_2H to O_2
- Isomerization of O_2RO_2H and formation of ketohydroperoxide and OH
- Decomposition of ketohydroperoxide to form oxygenated radical species and OH

As described by Bikas [90], the high-temperature mechanism describes the attack of radicals on n-Decane, the isomerization of the decyl radicals formed, the β-decomposition of the decyl radicals and the thermal decomposition of the fuel to form smaller alkyl radicals. This includes also a C_1 to C_4 submechanism completing the reaction mechanisms for the high-temperature oxidation of n-Decane.

The easily ignited fuels, such as n-alkanes, e.g. n-Hexadecane as the easily ignitable reference fuel in the cetane number, are according to Westbrook et al. [91] noteworthy for the extensive amounts of low temperature reactivity that they produce. Low temperature pathways are controlled by alkylperoxy radical isomerization, and low temperature reactivity is an essential part of their rapid, early ignition kinetics.

The low-temperature oxidation is initiated by reactions with molecular oxygen to produce the corresponding decyl radicals and HO_2. There are five different decyl radicals, but this model employs only two, which simplifies the calculations. The decyl radicals can then be decomposed by β scission of a C-C bond to produce an olefin and a smaller alkyl radical, which react with O_2 to produce an alkyl peroxy radical (RO_2). If the temperature increases the RO_2 radical will decompose back to the reactants. This leads to an inverse temperature dependence of the reaction, the NTC/ZTC or degenerate chain branching. The RO_2 radicals then will undergo abstraction of internal H atoms: $RO_2 \rightarrow$ QOOH, where QOOH is a corresponding alkylhydroperoxy radical with fuel structure. These alkylhydroperoxy radicals can then eliminate OH and produce cyclic ether, or decompose to a fuel olefin and HO_2, or react with a second O_2. Bikas [90] excludes the cyclic ether formation. The addition of a second O_2 is the only path leading to chain branching. The treatment of the decomposition of the O_2RO_2H radical formed in the last reaction follows Curran et al [92]. Bikas assumes that O_2RO_2H isomerizes, releasing OH and forming ketohydroperoxide (ORO_2H). One hydroxyl radical is formed during the production of ketohydroperoxide in the last reaction. The subsequent decomposition of the ketohydroperoxide molecule leads to another hydroxyl radical, a smaller alkyl radical, an olefin, CO and formaldehyde, which is a tracer of the cool flame regime. The reaction mechanism is depicted in the following schematic.

For a detailed listing of the chemical reactions and kinetic parameters used in this model please refer to Bikas et al. [90].

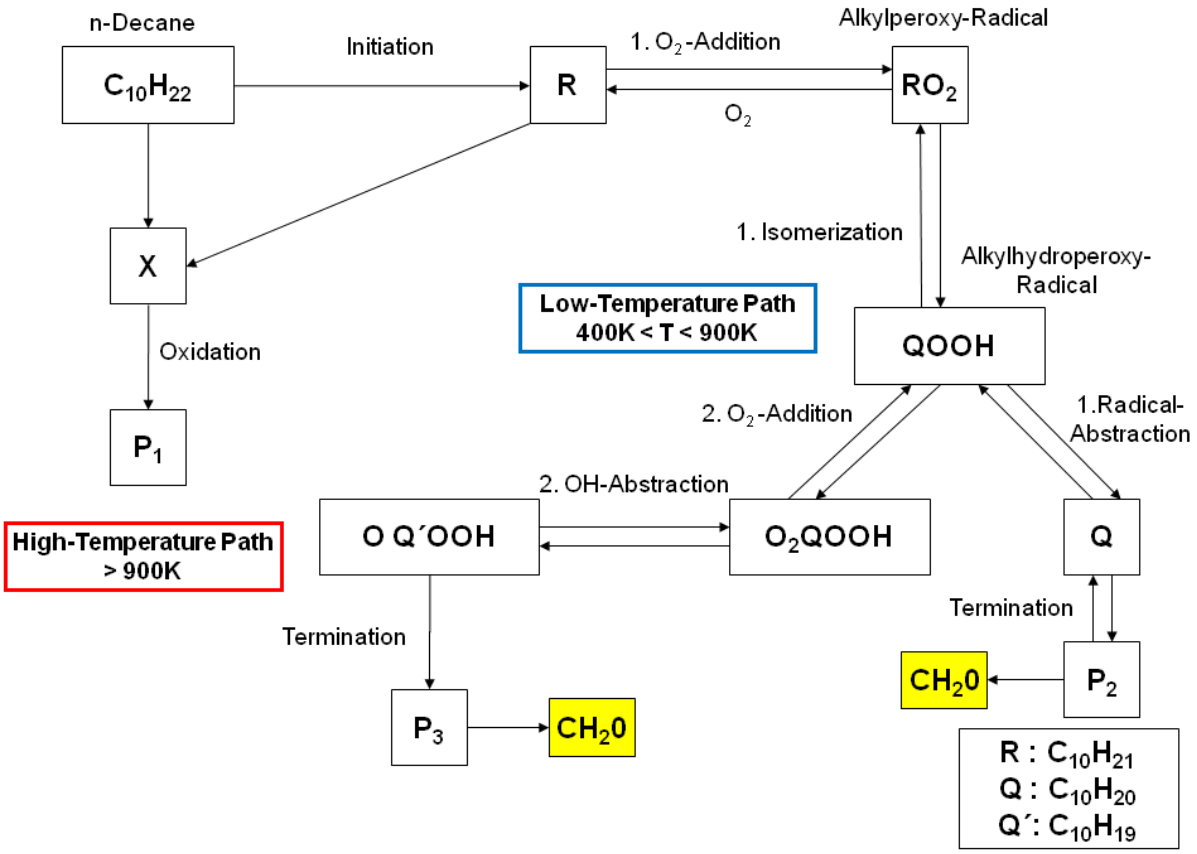

Fig. 128 - Detailed reaction mechanism for n-Decane with low and high temperature reaction paths [84, 90]

Ignition criteria

Schnaubelt defines for these calculations ignition criteria in order to establish the starting point for each stage of ignition, thus obtaining τ_l and τ_t. For τ_l the starting point is defined as the moment where a temperature gradient

Eq. 54

$$\frac{\partial T}{\partial \tau} \geq 10^4\ K/s$$

is observed. Similarly for τ_t the temperature gradient is defined as:

Eq. 55

$$\frac{\partial T}{\partial \tau} \geq 10^7\ K/s$$

Complementary to these definitions, a hot flame ignition is defined also as the moment where the gas phase reaches a temperature higher than 1300 K.

4.3. Comparison of Experimental Data and preliminary Numerical Simulations

This section presents preliminary numerical calculations with the n-Decane kinetic mechanism and the numerical code for the single droplet autoignition performed by Schnaubelt [84] and compares these results with experimental data obtained in this study for n-Decane and GTL-Kerosene.

The following diagrams depict the comparison of experimental and numerical data on the autoignition behavior of n-Decane in microgravity and under normal gravity conditions:

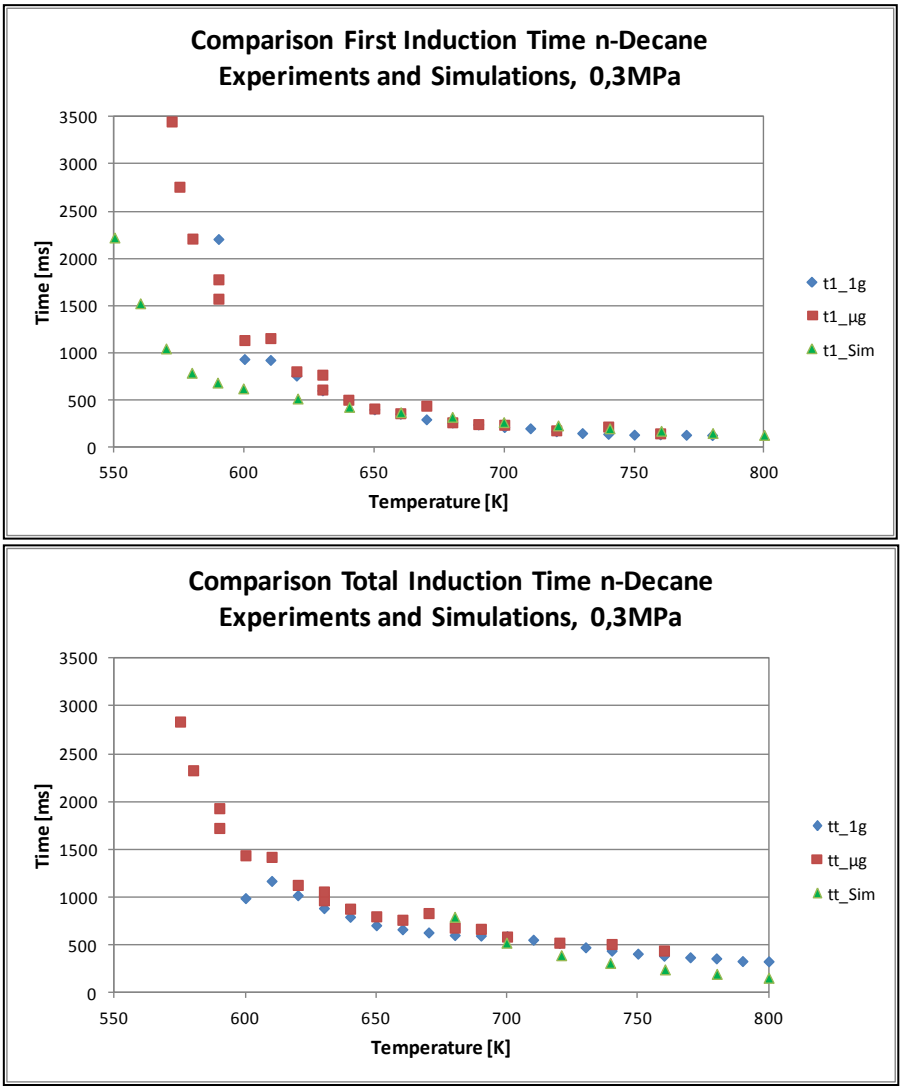

Fig. 129 – Comparison of the first and total ignition times for n-Decane, 0,3 MPa

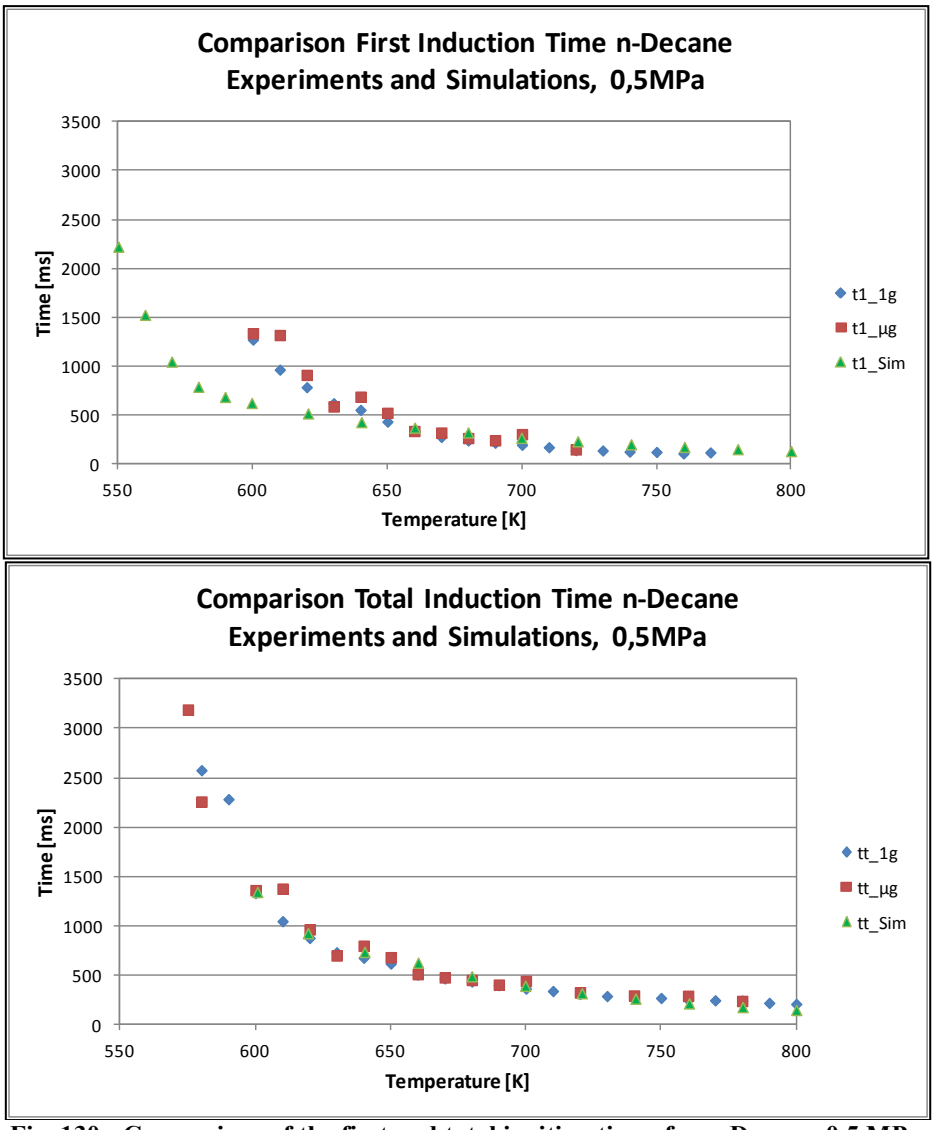

Fig. 130 - Comparison of the first and total ignition times for n-Decane, 0,5 MPa

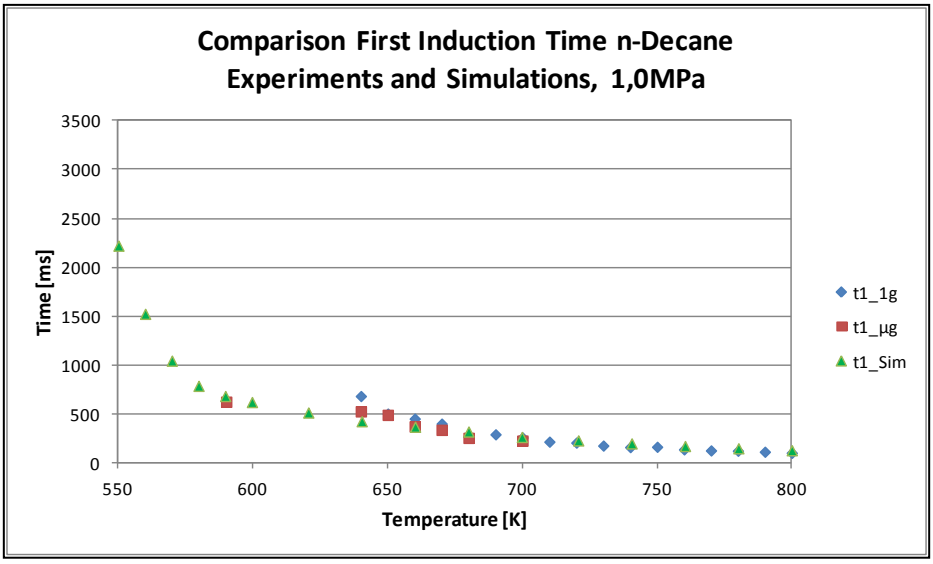

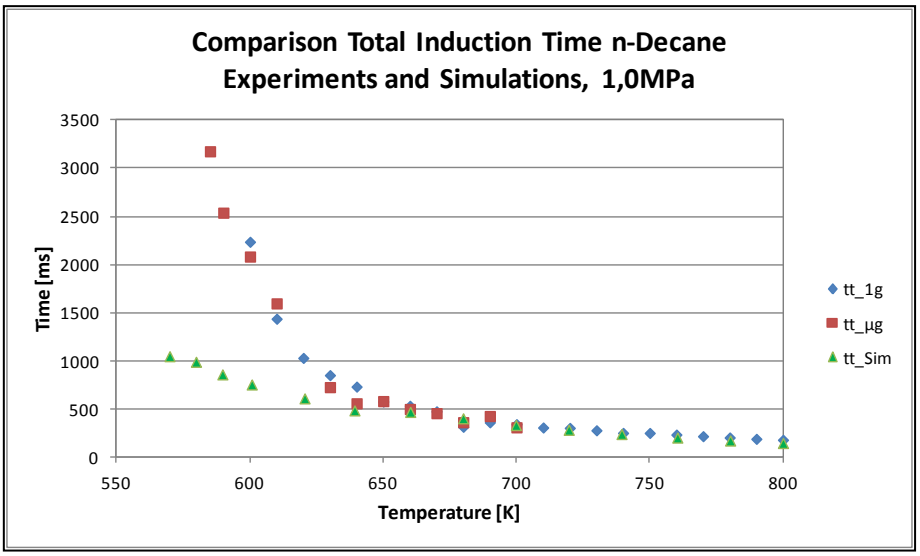

Fig. 131 - Comparison of the first and total ignition times for n-Decane, 1,0 MPa

As can be seen from the previous diagrams, the simulated first ignition delay times, denoted as "t1_Sim", show a good accordance with the experimental results for temperatures higher than 660 K. Below this temperature the calculated first ignition times are much lower than the detected ones, in some cases, (e.g. 0,3 MPa, 580 K, µg) amounting to only one third of the experimentally observed times. The pressure dependence of the first ignition time is for the simulations much weaker than the experimental data. Also the temperature range (550-800 K) for cool flame appearance remains unchanged for the calculated data.
The simulation yields total ignition delay times that are in relatively good correspondence with the observed times. In the case of 0,3 MPa the appearance of the first hot flame occurs in the simulation at a much higher temperature (680K) than in the experiments (575 K, µg / 600 K, 1g). The 0,5 MPa data show the best agreements between the experimental data and the simulation. For 1,0 MPa at lower temperatures (570-660 K) the simulated data does not follow the trend of the experimental data. For higher temperatures the simulation shows a good representation of the experimental data.

The following diagrams show the comparison of the experimental results on the autoignition behavior in microgravity and normal gravity conditions for GTL-Kerosene and the calculations by Schnaubelt with n-Decane as a surrogate fuel.

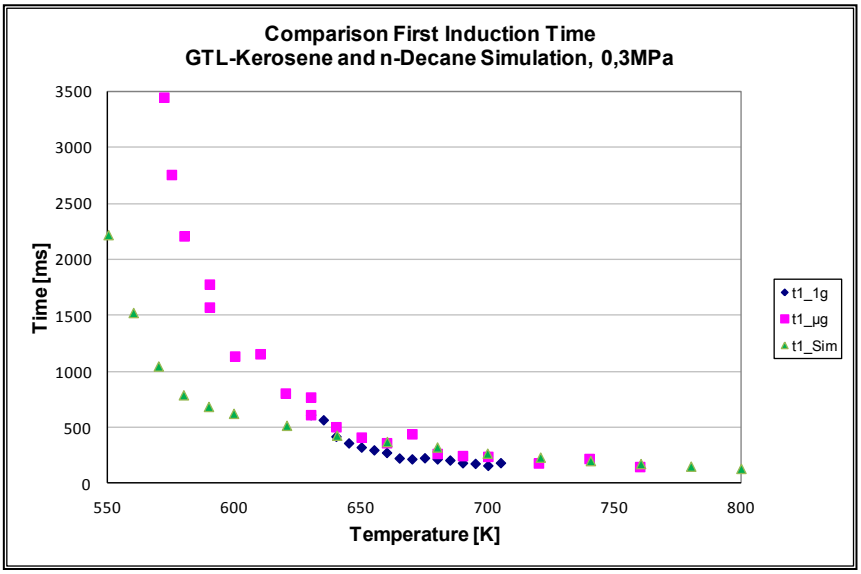

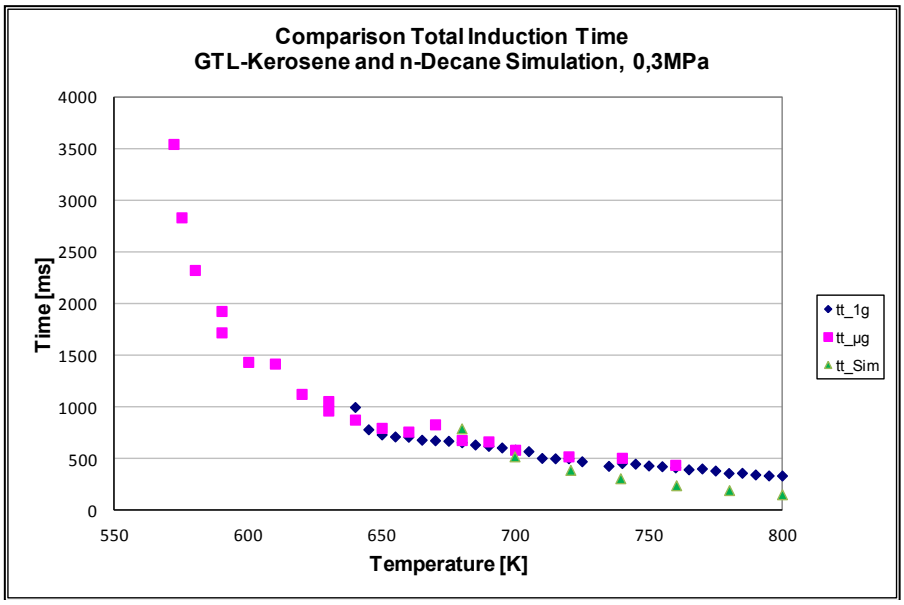

Fig. 132 - Comparison of the first and total ignition times of GTL-Kerosene and n-Decane, 0,3 MPa

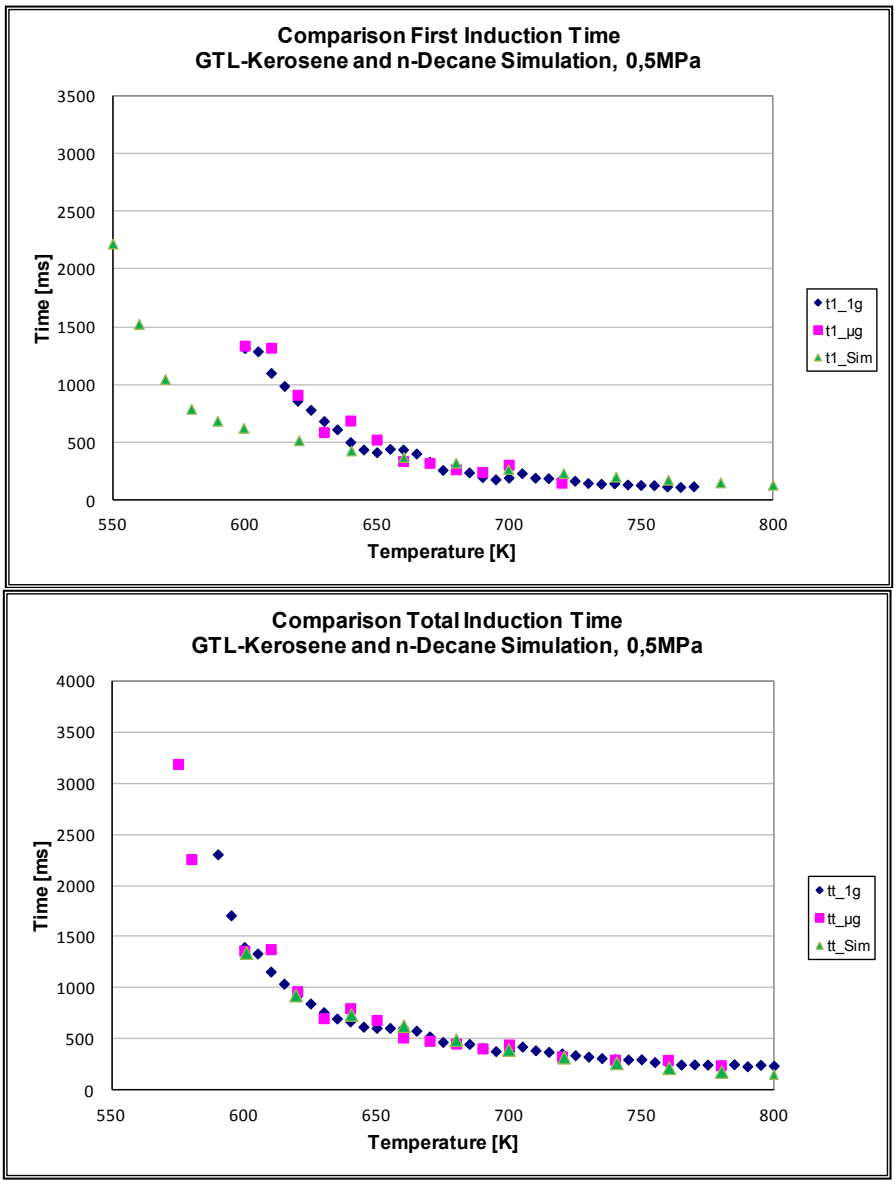

Fig. 133 - Comparison of the first and total ignition times of GTL-Kerosene and n-Decane, 0,5 MPa

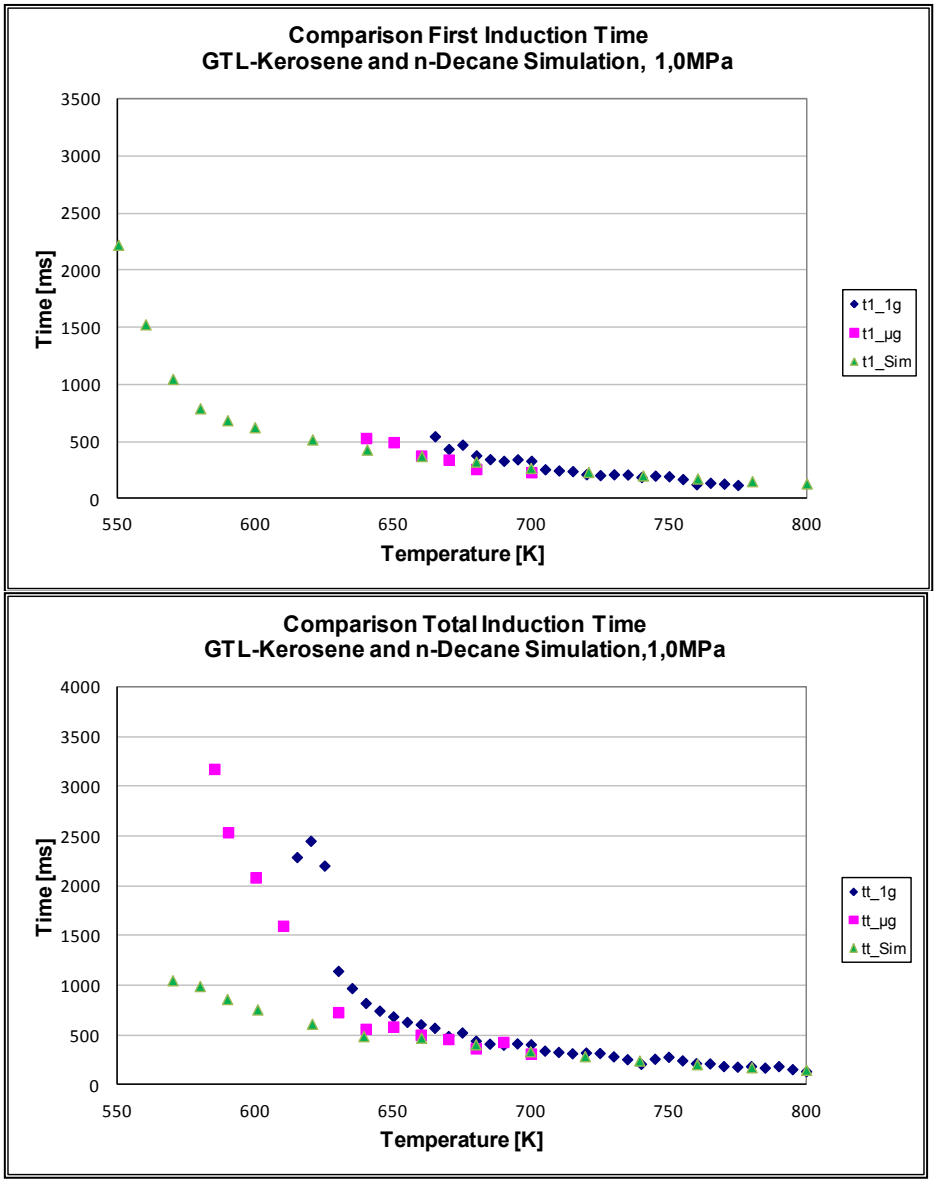

Fig. 134 - Comparison of the first and total ignition times of GTL-Kerosene and n-Decane, 1,0 MPa

Similar to the previous observations for n-Decane, the simulations show generally good representations of the experimental data for τ_1 for temperatures higher than 660 K. Nonetheless the experimentally detectable temperature range shows for cool flames large discrepancies. As stated previously, the simulated data shows the appearance of cool flames for the temperature range between 550 and 800 K for all pressure ranges shown. Experimentally, the ranges are generally smaller with the exception of 0,3 MPa, showing a good agreement. The comparison of the hot flame induction delay yields similar results as in the previous comparison with the experimental n-Decane data.

5. Conclusions and Outlook

Conclusions

The greater frame of these investigations is the reduction of the emission of CO_2 and other pollutant gases such as NO_x. Different strategies have been in the focus of research, such as CO_2 neutral fuels and improving combustion processes and engine efficiency.
Renewable liquid fuels based on biomass processing are gaining more and more the attention of producers and consumers. They allow the use and adaptation of current engine technology, which makes them, at least for a more or less longer transition period, a very important alternative to fossil fuels. So-called biofuels of the second generation, synthesized through the Fischer-Tropsch process, also provide the promise of a CO_2 neutral fuel.
For most technical applications, liquid fuels are used as sprays. Regarding the combustion of fuel sprays in internal combustion engines and gas turbines for power generation and aircraft propulsion, the reduction of NO_x emissions generated by the thermal nitric oxide formation process (Zeldovich-mechanism) is strongly connected to lowering of the combustion temperatures. Important here is not only the average temperature connected to the overall air/ fuel mixture ratio but the local temperatures that are in addition coupled to the homogeneity of the mixture. Assuming a lean overall mixture, the highest emissions are generated through non-pre-vaporized and non-premixed conditions, which for example are given by simply injecting a fuel spray into a flame. Vice versa, the lowest possible emissions will be generated from a perfectly pre-vaporized and premixed system representing “well stirred” conditions. As generally the NO_x emissions are the lower, the leaner the mixture ratio is, it is clear, that an overall mixture ratio close to the lean flammability limit can only be safely burned in “well stirred” conditions. An only partially premixed system will be richer than the lean limit in some places, producing more nitric oxides then ideally possible, and will be leaner than the flammability limit in other places forming pockets of unburnt gases. This will lead to emissions of nitric oxides (NO, N_2O and NO_2), unburnt hydrocarbons and partially burnt hydrocarbons e.g. HCOH.
Technically, fuel is injected into more or less adiabatically compressed air of elevated temperature. Aiming for high process efficiency the compression ratio is actually as high as 45 in actual aircraft engines aiming for compression ratios of 50 for future aero-engine concepts. In any case the dispersed fuel will undergo autoignition after a certain residence time. Therefore the aim for premixed conditions has to deal with autoignition, limiting the time available for droplet vaporization and turbulent mixing of the fuel vapor with air. Naturally the available time is the shorter, the higher the ambient temperatures are.
In this respect, knowledge about the behavior of spontaneous ignition processes of droplets and sprays is of great importance for the design and safe operation of premixed operated engines (HCCI) or gas turbines (LPP).
The basic and fundamental element of a spray is the single droplet. With the aid of investigations on the autoignition of single droplets, fundamental thermophysical properties concerning evaporation and mixture formation are obtained. The results of previous and current experiments help to establish a database on the autoignition of different fuels and mixtures supporting the development and validation of numerical codes.
The autoignition behavior of single droplets of GTL-Diesel and GTL-Kerosene under normal gravity and microgravity conditions has been characterized in this work. The temperature and pressure dependence of the ignition delay times has been studied and fitted with Arrhenius-type correlations. An improvement of the fitting quality to the experimental data has been shown by using two-term Arrhenius functions, as these correlate to the two-stage nature of the ignition phenomenon. Also the evaporation behavior has been studied separately, as this physical process plays a fundamental role and affects directly the induction times.

This data was used to develop suitable surrogate fuels that are needed for further work in the field of numerical simulations of the physical and chemical processes leading to the ignition of a droplet and subsequently from a spray. In this context, a surrogate fuel is, from its composition, a simplified mixture that shows similar autoignition behavior as for instance, a much more complicated fuel such as GTL-Diesel which is composed of more than 40 compounds. This simplified fuel allows a complete simulation of the chemical and physical processes in a timely manner. A general selection and formulation procedure for the development of surrogate fuels has been presented. This procedure had to be adapted, as an exact chemical composition of the fuels was not available and no permission for a detailed chemical analysis was given. The obtained surrogate fuels have been validated experimentally under normal and microgravity conditions. For GTL-Diesel a mixture of n-Tetradecane-75 vol% - 2,2,4,4,6,8,8,-Heptamethylnonane-25 vol% shows the best representation of the autoignition behavior of GTL-Diesel. For GTL-Kerosene good results were obtained with n-Decane.
Also data on related fuels, such as the mineral counterparts and other surrogates, has been compared and the results presented. GTL-Diesel and mineral Diesel show very similar behavior at higher temperatures. Bio-Diesel has considerably higher induction delay times than both mineral and GTL-Diesel. A widely used surrogate, namely n-Heptane, shows considerably shorter ignition delay times and therefore it is not a suitable surrogate fuel for autoignition studies of neither Diesel nor GTL-Diesel. For GTL-Kerosene the comparison with its mineral counterpart yielded higher induction delay times for mineral Kerosene.
A comparison with preliminary numerical calculations performed with n-Decane showed good agreements at temperatures higher than 660 K. Lower temperatures show poor correspondences with the simulated data having considerably shorter ignition delay times.

Outlook

As mentioned before, the single droplet is the fundamental element of a spray. Consequentially experimental investigation on the autoignition behavior of a multiple droplet array and furthermore on sprays of Fischer-Tropsch fuels should be conducted. Experiments with a multiple array should be conducted in the same pressure chamber as the experiments of this study in order to ensure comparability of the obtained experimental data.
Also quantitative measurements under µg of interesting trace species, such as formaldehyde with the aid of the ADL (Advanced Disk Laser) at ZARM should be performed in order to calibrate the numerical code. The deviations observed in the kinetic mechanism for n-Decane should be further investigated and corrected. A further development and implementation of chemical kinetic mechanisms for n-Tetradecane and interesting compounds such as HMN should be performed. This could be part of the development of a generalized modular chemical kinetics mechanism for n-alkanes and eventually its extension to related compounds such as iso- and cycloalkanes.

6. References

1. FAO, *The state of food and agriculture, Biofuels: prospects, risks and opportunities*. 2008, FAO: Rome.
2. S. Solomon, D. Qin, M. Manning, Z. Chen, M. Marquis, M. Averyt, M. Tignor and H. L. Miller, *IPPC Fourth Assessment Report: Climate Change 2007 Contribution of Working Group I: The Physical Science Basis* 2007, IPCC.
3. B. Metz, O. R. Davidson, P. R. Bosch, R. Dave and L. A. Meyer, *IPPC Fourth Assessment Report: Climate Change 2007 Contribution of Working Group III: Mitigation of Climate Change*. 2007, IPCC.
4. A. Eisentraut, *Second-Generation Biofuels: Potential and perspectives in major economies and developing countries*. 2010, IEA.
5. IEA, *Key World Energy Statistics*. 2010, IEA: Paris.
6. R. Sims, M. Taylor, J. Saddler and W. Mabee, *From 1st- to 2nd-Generation Biofuel Technologies: An overview of current industry and RD&D activities* in *IEA Bioenergy*. 2008, IEA, OECD.
7. D. Rajagopal and D. Zilberman, *Review of environmental, economic and policy aspects of biofuels*, in *World Bank Policy Research*. 2007, World Bank: Washington, DC.
8. P. Rickmers, *Experimental Investigation of the Spray Autoignition of n-Heptane in a Jet in Cross Flow Configuration and Comparison to Single Droplet Ignition Simulations* in *ZARM* 2010, University of Bremen: Bremen.
9. S. Schnaubelt, C. Eigenbrod and H. J. Rath. *Measurement of autoigntion characteristics of technical fuel sprays under machine-identical conditions in a hot windtunnel*. in *29th International Symposium on Combustion, WIPP*. 2002.
10. O. Moriue, C. Eigenbrod, H. J. Rath, J. Sato, K. Okai, M. Tsue and M. Kono, *Effects of dilution by aromatic hydrocarbons on staged igntion behavior of n-decane droplets.* Proc. Combust. Inst. , 2000. **28**: p. 969-975.
11. O. Moriue, M. Mikami, N. Kojima and C. Eigenbrod. *Numerical simulations of the ignition of n-heptane droplets in the transition diameter range from heterogeneous to homogeneous ignition*. 2005.
12. O. Moriue, *A Study of Spontaneous Ignition Process of a Multicomponent Fuel Droplet*. 2000, University of Tokio.
13. O. Moriue, C. Eigenbrod, H. J. Rath, M. Tsue, M. Kono and J. Sato, *Spontaneous Ignition of n-Alkane droplets with various volatility.* Trans. Japan Soc. Aero. Space Sci., 2004. **47**(157): p. 189-194.
14. M. Tanabe, *Spontaneous Ignition of a single Fuel Droplet in High Temperature and High Pressure Surroundings*. 1995, University of Tokio.
15. M. Tanabe, T. Bolik, C. Eigenbrod, H. J. Rath, J. Sato and M. Kono. *Spontaneous Ignition of liquid droplets from a view of non-homogeneous mixture formation and transient chemical reactions*. in *Twenty-Sixth International Symposium on Combustion*. 1996. Naples: The Combustion Institute.
16. M. Tanabe, M. Kono, J. Sato, J. Koenig, C. Eigenbrod, F. Dinkelacker and H. J. Rath, *Two Stage Ignition of n-Heptane Isolated Droplets.* Combustion Science and Technology, 1995. **108**: p. 103-119.
17. O. Moriue, K. Matsuo, E. Murase, S. Schnaubelt and C. Eigenbrod, *Verification of a Numerical Simulation Model of Fuel Droplet Ignition through Microgravity Experiments and its further application.* Journal of the Japan Society of Microgravity Application, 2007. **24**(3): p. 251-254.

18. T. Bolik, J. König, C. Eigenbrod and H. J. Rath. *Application of a new diagnostic method to observe pre-igntion phenomena of self igniting fuel droplets*. in *10th Int. Symp. Appl. of Laser techn. to Fl. Mech.* 2000. Lisbon.
19. C. Eigenbrod. *Experimental and numerical studies on the autoigntion process of fuel droplets*. in *Joint Meeting of the British, German and French sections of the Combustion Institute*. 1999. Nancy.
20. C. Eigenbrod, O. Moriue, P. Weilmünster and H. J. Rath. *Development of a simple model fuel for Kerosene droplet igntion*. in *28th Int. Annual Conference of Fraunhofer Institut Chemische Technologie*. 1997. Karlsruhe.
21. R. van Basshuysen and F. Schäfer. *www.motorlexikon.de*. 2010 [cited; Available from: http://www.motorlexikon.de/.
22. S. R. Turns, *Thermal-Fluid Sciences: An Integrated Approach*. 2006: Cambridge University Press.
23. ASTM. *ASTM Standards*. 2010 [cited; Available from: www.astm.org/Standards/index.shtml.
24. C. Wikimedia. *Wikimedia*. 2010 [cited; Available from: www.commons.wikimedia.org.
25. C. L. Yaws, S. D. Sheth and M. Han, eds. *Chemical properties handbook : physical, thermodynamic, environmental, transport, and health related properties for organic and inorganic chemicals* Handbooks, ed. C. L. Yaws. 1999, McGraw-Hill: New York.
26. AED, *Brochure - Diesel fuel Ignition Quality Tester IQT(TM), Advanced Engine Technology LTD.* 2009: Ottawa, Canada.
27. P. Ghosh, *Predicting the effect of cetane improvers on diesel fuels.* Energy and fuels, 2008. **22**: p. 1073-1079.
28. P. Ghosh and S. Jaffe, *Detailed composition-based model for predicting the cetane number of diesel fuels.* Industrial and Engineering Chemistry Research, 2006. **45**: p. 346-351.
29. P. Soltic, D. Edenhauser, T. Thurnheer, D. Schreiber and A. Sankowski, *Experimental investigation of mineral diesel fuel, GTL fuel, RME and neat soybean and rapeseed oil combustion in a heavy duty on-road engine with exhaust gas aftertreatment.* Fuel, 2009. **88**: p. 1-9.
30. W. J. Pitz and C. J. Mueller, *Recent progress in the development of diesel surrogate fuels.* Progress in Energy and Combustion Science, 2010: p. 1-21.
31. G. Knothe, *Biodiesel and renewable diesel: A comparison.* Progress in Energy and Combustion Science, 2010(36): p. 364-373.
32. A. Violi, S. Yan, E. G. Eddings, A. F. Sarofim, S. Granata, T. Faravelli and E. Ranzi, *Experimental formulation and kinetic model for JP-8 surrogate mixtures.* Combustion Science and Technology, 2002. **174**(11,12): p. 399-417.
33. C. Guerét, *Elaboration d'un modele cinetique pour l'oxydation du kerosene et d'hydrocarbures representatifs*, in *Chemistry*. 1989, University of Orleans: Orleans.
34. ExxonMobil, *World Jet Fuel Specifications*. 2008, ExxonMobil.
35. Shell, *Safety Data Sheet GTL-Kerosene*. 2007, Shell Co.
36. M. L. Huber, B. L. Smith, L. S. Ott and T. J. Bruno, *Surrogate mixture model for the thermophysical properties of synthetic aviation fuel S-8: Explicit application of the advanced distillation curve.* Energy and fuels, 2008. **22**: p. 1104-1114.
37. M. L. Huber, E. W. Lemmon and T. J. Bruno, *Surrogate mixture models for the thermophysical properties of aviation fuel Jet-A.* Energy and fuels, 2010. **24**: p. 3565-3571.
38. M. L. Huber, E. W. Lemmon, A. Kazakov, L. S. Ott and T. J. Bruno, *Model for the thermodynamic properties of a biodiesel fuel.* Energy and fuels, 2009. **23**: p. 3790-3797.

39. R. Span and W. Wagner, *Equations of state for technical applications. I. Simultaneously optimized functional forms for nonpolar and polar fluids.* International Journal of Thermophysics, 2003. **24**(1): p. 1-39.
40. M. L. Huber, E. W. Lemmon, V. Diky, B. L. Smith and T. J. Bruno, *Chemically authentic surrogate mixture model for the thermophysical properties of a coal-derived liquid fuel.* Energy and fuels, 2008. **22**: p. 3249-3257.
41. R. Lemaire, A. Faccinetto, E. Therseen, M. Ziskind, C. Focsa and P. Desgroux, *Experimental comparison of soot formation in turbulent flames of diesel and surrogate diesel fuels.* Proceedings Combustion Institute, 2009. **32**: p. 737-744.
42. S. Kook and L. Pickett, *Combustion and soot processes of conventional and surrogate jet fuels at high-temperature and high-pressure conditions*, in *US National Combustion Meeting*. 2009: Ann Harbor.
43. S. Kook and L. Pickett, *Soot volume fraction and morphology of conventional and surrogate jet fuel sprays at 1000K and 6.7MPa ambient conditions*, in *33rd International Symposium on Combustion*. 2010: Beijing, China.
44. R. Natelson, M. Kurman, N. Cernansky and D. Miller, *Experimental investigation of surrogates for jet and diesel fuels.* Fuel, 2008. **87**: p. 2339-2342.
45. F. Douce, N. Djebaili-Chaumeix, C. Paillard, C. Clinard and J. Rouzaud, *Soot formation from heavy hydrocarbons behind reflected shock waves.* Proceedings Combustion Institute, 2000. **28**: p. 2523-2529.
46. O. Mathieu, N. Djebaili-Chaumeix, C. Paillard and F. Douce, *Experimental study of soot formation from a diesel fuel surrogate in a shock tube.* Combustion and Flame, 2009. **156**: p. 1576-1586.
47. K. Mati, A. Ristori, S. Gail, G. Pengloan and P. Dagaut, *Experimental study in a JSR and detailed chemical kinetic modeling.* Proceedings Combustion Institute, 2007. **31**: p. 2939-2946.
48. H. R. Zhang, E. G. Eddings and A. F. Sarofim. *Criteria for selection of components for surrogates of natural gas and transportation fuels*. in *Combustion Symposium*. 2007: Elsevier.
49. Y. Ra and R. D. Reitz, *A vaporization model for discrete multi-component fuel sprays.* International Journal of Multiphase Flow, 2009. **35**: p. 101-117.
50. C. Eigenbrod, M. Reimert, P. Rickmers and H. J. Rath, *Autoignition of Droplets and Sprays*, in *4th China-Germany Workshop on Microgravity and Space Life Sciences*. 2009: Shanghai, China.
51. M. Reimert, G. Marks and C. Eigenbrod, *Diesel, Bio-Diesel, GTL-/BTL-Diesel, n-Heptane and n-Tetradecane / AMN: Experimental Comparison of the spontaneous ignition of single droplets*, in *24. Deutscher Flammentag, Verbrennung und Feuerung*, VDI-Wissensforum, Editor. 2009, VDI-Gesellschaft Energietechnik: Bochum. p. 97-102.
52. S. Honnet, K. Seshadri, U. Niemann and N. Peters, *A surrogate fuel for kerosene.* Proceedings Combustion Institute, 2009. **32**: p. 485-492.
53. U. Steil, M. Braun-Unkhoff and M. Aigner, *An experimental and modeling study on the autoignition of kerosene and surrogate fuel mixture.* American Institute of Aeronautics and Astronautics, 2008(AIAA 2008-973).
54. W. D. Schulz, *Oxidation products of a surrogate JP-8 fuel.* ACS Petrol. Chem. Div. Preprints, 1991. **37**: p. 383.
55. NIST. *NIST Scientific and Technical Databases*. 2010 [cited; Available from: http://www.nist.gov/index.html.
56. M. Murphy, J. Taylor and R. McCormick, *Compendium of Experimental Cetane Number Data*. 2004, National Renewable Energy Laboratory.

57. R. C. Reid, J. M. Prausnitz and B. E. Poling, *The properties of gases and liquids*. Fourth Edition ed. Chemical Engineering Series. 1988, Singapore: McGraw-Hill International Editions.
58. J. Dykyj, J. Svoboda, R. C. Willhoit, M. Frenkel and K. R. Hall, eds. *Vapor Pressure of Chemicals, Subvolume A*. Landolt-Börnstein, Numerical Dta and Functional Relationships in Science and Technology, ed. K. R. Hall. Vol. 20. 1999, Springer: Berlin Heidelberg New York.
59. Sigma-Aldrich, *Sicherheitsdatenblatt Dicyclohexyl*. 2008.
60. H. Yamamoto. *Pirika, Java and Chemistry Site*. 2011 [cited; Available from: http://www.pirika.com/index.html.
61. Sigma-Aldrich, *Sicherheitsdatenblatt Propylcyclohexane*. 2009.
62. Alfa-Aesar, *Sicherheitsdatenblatt Cyclooctane*. 2008.
63. ABCR, *Sicherheitsdatenblatt 1,3,5-Trimethylcyclohexane*. 2009.
64. J. Warnatz, U. Maas and R. W. Dibble, *Combustion: Physical and Chemical Fundamentals, Modeling and Simulation, Experiments, Pollutant Formation*. 1996, Berlin Heidelberg: Springer. 265.
65. D. I. Kolaitis and M. A. Founti, *On the assumption of using n-heptane as a surrogate fuel for the description of the cool flame oxidation of diesel oil.* Proceedings Combustion Institute, 2009. **32**: p. 3197-3205.
66. L. J. Spadaccini and J. A. TeVelde, *Autoignition characteristics of aircraft-type fuels.* Combustion and Flame, 1982. **46**: p. 283-300.
67. J. A. TeVelde and L. J. Spadaccini, *Autoignition characteristics of No.2 Diesel Fuel*. 1981, NASA.
68. N. A. Henein and J. A. Bolt, *Kinetic considerations in the autoignition and combustion of fuel sprays in swirling air.* ASME Paper No.72-DGP-8, 1972.
69. C. J. Mestre, L. Papathakos and P. Verbulecz, *Preliminary studies of autoignition and flashback in a premising-prevaporizing flame tube using JET-A fuel at lean equivalence ratios*. 1977, NASA.
70. F. W. Stringer, A. E. Clarke and J. S. Clarke, *The spontaneous ignition of hydrocarbon fuels in a flowing system.* Proc. Auto. Div. Institution of Mechanical Engineers, 1970.
71. G. M. Faeth, B. L. Karhan and G. A. Yanyecic, *Ignition and combustion of monopropellant droplets.* AIAA Journal, 1967. **6-4**: p. 684.
72. M. Tanabe, M. Kono, J. Sato, J. Koenig, C. Eigenbrod and H. J. Rath. *Effects of natural convection on two stage ignition of an n-dodecane droplet*. in *Twenty-Fifth Combustion Symposium*. 1994.
73. H. D. Ross, ed. *Microgravity Combustion*. 2001, Academic Press.
74. C. K. Law and G. M. Faeth, *Opportunities and challenges of combustion in microgravity.* Progress in Energy and Combustion Science, 1994. **20**: p. 65-113.
75. ZARM. *Official Website*. 2010 [cited; Available from: www.zarm.uni-bremen.de.
76. ZARM-FABmbH, *ZARM Drop Tower User Manual*. 2009: Bremen.
77. J.-R. Yang and S.-C. Wong, *On the discrepancies between theoretical and experimental results for microgravity droplet evaporation.* International Journal of Heat and Mass Transfer, 2001. **44**: p. 4433-4443.
78. O. Herbinet, W. J. Pitz and C. K. Westbrook, *Detailed chemical kinetic oxidation mechanism for a biodiesel surrogate.* Combustion and Flame, 2008. **154**: p. 507-528.
79. O. Herbinet, W. J. Pitz and C. K. Westbrook, *Detailed chemical kinetic mechanism for the oxidation of biodiesel fuels blend surrogate.* Combustion and Flame, 2010. **157**: p. 893-908.
80. J. Y. W. Lai, K. C. Lin and A. Violi, *Biodiesel combustion: Adcances in chemical kinetic modeling.* Progress in Energy and Combustion Science, 2011. **37**: p. 1-14.
81. STW, *Drucktransmitter A09 Datenblatt*. 2011.

82. S. Schnaubelt, C. Eigenbrod and H. J. Rath, *Numerical Analysis of the cool flame behavior of igniting n-heptane droplets.* Microgravity Science and Technology, 2004.
83. C. Eigenbrod, K. Klinkov and F. F. Fachini, *On the effect of pressure oscillations on droplet autoignition*, in *Proceedings ASME Turbo Expo 2011, submitted paper*. 2010, ASME: Vancouver, Canada.
84. S. Schnaubelt, *Numerische Analyse des Selbstzündverhaltens einzelner Brennstofftropfen*. 2005, University of Bremen.
85. C. Eigenbrod, J. C. Dittmer, O. Essmann and H. J. Rath, *Spraylets - a Way to simulate Spray Autoignition.* J. Jpn. Soc. Microgravity Appl., 2007. **24**(3): p. 213-219.
86. O. Moriue, S. Schnaubelt, C. Eigenbrod and H. J. Rath. *Numerical simulation of the ignition of a single fuel droplet in air with finite volume*. in *ICLASS, 9th Int. conf. on Liquid Automization and Spray Systems*. 2003.
87. S. Schnaubelt, O. Moriue, C. Eigenbrod and H. J. Rath, *Verification of detailed numerical simulations with complex chemistry for the multi-stage selfigntion process of n-decane droplets.* Microgravity Science and Technology, 2001. **12**(1): p. 20-23.
88. S. Schnaubelt, O. Moriue, C. T., C. Eigenbrod and H. J. Rath, *Detailed numerical simulations of the multi-stage self-ignition process of n-heptane isolated droplets and their verfication by comparison with microgravity experiments.* Proc. Combust. Inst., 2000. **28**: p. 953-960.
89. S. Schnaubelt, M. Tanabe, C. Eigenbrod and H. J. Rath. *Verification of detailed simulations for two stage ignition of single droplets by ignition radii*. in *Space Forum Proc. Drop Tower Days*. 2000.
90. G. Bikas and N. Peters, *Kinetic modelling of n-Decane Combustion and Autoignition.* Combustion and Flame, 2001. **126**: p. 1456-1475.
91. C. K. Westbrook, W. J. Pitz, O. Herbinet, H. J. Curran and E. J. Silke, *A comprehensive detailed chemical kinetic reaction mechanism for combustion of n-alkane hydrocarbons from n-octane to n-hexadecane.* Combustion and Flame, 2009. **156**: p. 181-199.
92. H. J. Curran, P. Gaffuri, W. J. Pitz and C. K. Westbrook, *A comprehensive modeling study of n-heptane oxidation.* Combustion and Flame, 1998. **114**: p. 149-177.